Low-Cost Real-Time Impedance Measurement System Based on Power Converter for Lithium-Ion Batteries

Chao Wu

Thesis submitted in accordance with
the requirements of the University of Liverpool for the degree of
Doctor of Philosophy
2021

Declaration

I declare that this thesis has been composed solely by myself and that it has not been submitted, either in whole or in part, in any previous application for a degree. Except where otherwise acknowledged, the work presented is entirely my own.

Chao Wu

July 2020

Abstract

Lithium-ion batteries are increasingly used as energy storage devices in electric power systems, transportation, and portable applications. An accurate monitoring of their state of charge and state of health is of paramount importance to guarantee an efficient, reliable, and safe operation of batteries. However, existing methods employed in commercial battery monitoring cannot provide complete information with regard to the complex electrochemical dynamics of the internal battery processes, and this often leads to inaccurate monitoring.

Electrochemical Impedance Spectroscopy (EIS) is a well-established and high-accurate diagnostic technique for the characterisation and monitoring of the battery dynamics in the frequency domain. Nevertheless, several limitations still impede the transfer of this technique from the laboratory to commercial applications, including the unaffordable and bulk instrumentation as well as the long measurement duration. This thesis is therefore devoted to the development of low-cost and small-size solution for commercial battery condition monitoring, based on the use of DC-DC power converter typically connected to the battery to create the current and voltage perturbations required to measure the battery impedance. To achieve this goal, this thesis proposes an embedded system (based on the BeagleBone Black board) that combines real-time digital signal processing with the high computational power and user-friendly interface of affordable off-the-shelf hardware. In more detail, the work focuses on the EIS measurements on

3.3-Ah 18650-size lithium-ion batteries, and it shows how the proposed hardware can control the converter, acquire measurable signals, properly process them in time and frequency domains, and estimate battery state by using a memory-efficient method based on battery equivalent circuit model.

Experimental results show that impedance measurements can be successfully obtained from the proposed system, with the measurement uncertainty of around 2 $m\Omega$ within the frequency range from 1.0 Hz to 1320 Hz. The accuracy of the prototype is validated by comparison to state-of-the-art laboratory equipment. Finally, feasible approaches to estimate the battery state of charge and state of health, based on the estimation of the solid electrolyte interface resistance and pure ohmic resistance, respectively.

Acknowledgements

I would like to express thanks to my supervisor, Dr Roberto Ferrero for his kind guidance and patient support during the program. In addition, I would like to express my gratitude to Dr. Lin Jiang for his technical insights and assistance.

I would like to thank my parents and XJTLU for founding the tuition fees and the University of Liverpool for their assistance in supporting me during my doctorate.

Many thanks to go to my colleagues at the G03 Laboratory for making the past years enjoyable. In particular, I would like to thank Mr. Sandschulte Arne helping me to get the access to do the tests at the Stephenson Institute and Dr. Neale Alex allowing me to do the tests with the BioLogic system.

This work would not have been possible if it were not for the discussion with my friend Mr. Yi Yang regarding programming issues, nor without the encouragement of my supervisor, parents and friends.

List of Abbreviations

BMS	Battery Management System
SOC	State-of-Charge
SOH	State-of-Health
DC	Direct Current
AC	Alternative Current
EIS	Electrochemical Impedance Spectroscopy
OCV	Open Circuit Voltage
EMF	Electromotive Force
EF	Kalman Filter
FPGA	Field Programmable Gate Arrays
DSP	Digital Signal Processor
ADC	Analog-to-Digital Converter
PWM	Pulse Width Modulation
PID	Proportional-Integral-Differential
BBB	BeagleBone Black
FS	Full-Scale
SQNR	Signal-to-Quantisation-Ratio
ASICs	Application-Specific Integrated Circuits
PRU	Programmable Real-Time Unit
HLOS	High Level Operation System

OS	Operation System
PRU-ICSS	Programmable Real-Time Unit and Industrial Subsystem
RISC	Reduced Instruction Set Computer
ISA	Instruction Set Architecture
IEP	Industrial Ethernet Peripheral
FT	Fourier Transfer
SAR	Successive Approximation Register
TSC_ADC	Touschscreen and Analog Digital Converter
FIFO	First Input First Output
IDLE	Ideal Configuration for ADC
$SOC_{\_ADC}$	Start of Conversion of ADC
$EOC_{\_ADC}$	End of Conversion of ADC
FMS	Fast Multiple Sampling
AIN0	Analog Channel 0 of ADC
AIN1	Analog Channel 1 of ADC
AIN2	Analog Channel 2 of ADC
IDE	Integrated Development Environment

List of Symbols

Li^+	lithium charge
Y	a surface site or arbitrary molecule fragment of the electrode materials
Y^-	negative charge of the electrode materials
t	time
$SOC(t)$	SOC with time variation
$SOC(t_0)$	SOC at initial time
$V(t)$	voltage with time variation
$I(t)$	current with time variation
Z	impedance
f	analog signal frequency
$V(f)$	voltage with frequency variation
$I(f)$	current with frequency variation
j	complex symbol
θ	phase
R_{ohm}	pure resistance
R_t	charge-transport resistance
C_{dl}	capacitance
w	angle speed
Z_w	warburg element
A_w	warburg coefficient

ΔV	voltage drop
ΔI	current drop
Δt	time difference
R	resistive performance or resistor
R_{ohm}	pure resistance
V_i	input voltage of the DC-DC converter
I_i	input current of the DC-DC converter
S	power switch of the DC-DC converter
L	inductor
D	diode
C	capacitor
I_o	output current of the DC-DC converter
V_o	output voltage of the DC-DC converter
V_L	voltage drop of inductor in the DC-DC converter
V_D	voltage drop of diode in the DC-DC converter
t_{on}	switch ON duration of the switch in the DC-DC converter
t_{off}	switch OFF duration of the switch in the DC-DC converter
d	duty cycle
I_{i_AC}	AC input current of the DC-DC converter
I_{i_max}	maximum amplitude of input current in the DC-DC converter
I_{i_min}	minimum amplitude of input current in the DC-DC converter
A	amplitude of signal
f_p	frequency of perturbation
V_{ac}	amplitude of perturbed voltage

$V_{batt-dc}$	DC voltage of battery
t_l	trigger time for AC perturbation
$I_{batt-dc}$	DC current base of battery
I_{ac}	AC current of perturbation
$I_{batt}(t)$	battery current signal with time variation
$V_{batt}(t)$	battery voltage signal with time variation
$Z_{batt}(f_p)$	the impedance at perturbed frequency
φ_V	phase of voltage of battery
φ_I	phase of current of battery
$y(t)$	output of system
$x(t)$	input of system
$e(t)$	time-variant error
$\mu(t)$	output of control
k	sample number
n	variation number
$e(n)$	error in discrete-time format
$x(n)$	discrete-time input
$y'(n)$	digitalised output by sensor
$y(n)$	discrete-time output
T	period
$x(nT)$	sampled input
T_{ADC}	ADC sampling period
$x_{analog}(t)$	input of ADC
$x_{ADC}(n)$	output of ADC
f_s	ADC sampling frequency
$x_{analog}(t)$	input of ADC
$x_{ADC}(n)$	output of ADC
f_s	ADC sampling frequency

$e_q(n)$	quantisation error
f_{system}	frequency of real-time system
N	number of samples for AC perturbation setting
K	iteration times
t_{system}	time interval of real-time system
t_1	time execution of reading data form ADC to PRU
t_2	time execution of PI algorithms
t_3	time execution of PWM
$t_{operation}$	operation time of function
n_{cycle}	number of PRU's clock cycle
t_{total}	total execution time of PWM or real-time system
k_{comp_on}	compensated time for ON state of PWM
t_{comp_off}	compensated time for OFF state of PWM
$X(f)$	Fourier transfer
N_{FT}	number of samples for FT
f_{sw}	switching frequency
R_{1_f}	No.1 resistor in voltage divider and filtering circuit
R_{2_f}	No.2 resistor in voltage divider and filtering circuit
$C_{\_f}$	capacitor in voltage divider and filtering circuit
V_{in_f}	input voltage of voltage divider and filtering circuit
V_{out_f}	output voltage of voltage divider and filtering circuit
R_{eq_f}	equivalent resistance of voltage divider and filtering circuit
f_c	cut-off frequency of the filter
X_{c_f}	capacitive impedance

t_d	latency of ADC sampling
φ_{t_d}	phase shift caused by sampling delay
N_{sample}	number of samples for the perturbation in PI control algorithm
$n_{frequency\_divider}$	the value of frequency divider
L	data length
$L_{data\_selection}$	data selection length
$t_{data\_selection}$	time of data selection
k_{target}	target number in Goerztel algorithm
f_T	frequency of AC targeted component
c_n	current time activity
P_0	current-time state parameter for Goerztel algorithm
P_1	last-time state parameter for Goerztel algorithm
P_2	last two-time state parameter for Goerztel algorithm
$coeff$	constant coefficient of Goerztel algorithm
$real$	real part of impedance
$imag$	imaginary part of impedance
φ	phase
$\varphi_{initial}$	initial phase of signal
$\varphi_{impedance}$	phase for impedance
M	measurement cycles
ΔV_o	output voltage variation of the DC-DC converter
ΔI_i	input current variation of the DC-DC converter
Δd	duty cycle variation of the DC-DC converter

V_{object}	the voltage of the object
$V_{measurement}$	the measured voltage
I_{load}	the load current
R_0	the pure resistance of the ECM
R_1	the resistance of the ECM for the positive electrode
R_2	the resistance of the ECM for the negative electrode
C_1	the capacitor of the ECM for the positive electrode
C_2	the capacitor of the ECM for the negative electrode
$R_{0(N)}$	the pure resistance of the ECM for a new cell
$R_{0(A)}$	the pure resistance of the ECM for an aged cell
U_{SOH}	the SOH uncertainty

Contents

Declaration iii

Abstract v

Acknowledgements vii

List of Abbreviations ix

List of Symbols xi

1 Introduction 1

2 Lithium-Ion Batteries and Impedance Measurements 9

2.1 Lithium-Ion Battery Discharging Chemistries 10

2.1.1 Lithium-Ion Battery Structural Composition 10

2.1.2 Lithium-Ion Battery Discharge Reactions 12

2.1.3 Lithium-Ion Battery Discharging Performances 14

2.1.4 SOC and SOH Estimations 16

2.2 Lithium-Ion Battery Impedance Characteristics 20

2.2.1 Impedance performance Caused by Mass-Transport Effects at Low Frequencies 22

2.2.2 Impedance Performance Caused by Charge-Transfer and Double-Layer Effects within Mid-Frequency Range 23

2.2.3 Impedance Performance Caused by Physical Effects at High Frequencies 25

2.3 Modelling Electrochemical Dynamics of Lithium-Ion Battery . . . 26

2.4 Impedance Measurement Techniques 31

2.4.1 Direct Current Resistive Measurement 31

2.4.2 AC Impedance Measurement 33

2.5 Chapter Summary 42

3 Cost-Efficient Impedance Measurement System for Lithium-Ion Battery **43**
3.1 EIS Measurement Method Based on a DC-DC Boost Converter . 44
3.1.1 DC-DC Boost Converter for Battery Voltage Step-up and Regulation 45
3.1.2 EIS Measurements for Lithium-ion Battery Based on the DC-DC Boost Converter 50
3.1.3 Control System for DC-DC Boost Converter 55
3.1.4 Requirements of Battery Impedance Measurement 60
3.2 Real-time Measurement System for Battery Impedance 63
3.2.1 Analog-to-Digital Conversion 64
3.2.2 Real-time Controller System 70
3.3 Real-Time Measurement and Control System Developed by BeagleBone Black 71
3.3.1 The PRU-ICSS Architecture 74
3.3.2 Programmable Real-time Units Activations 76
3.3.3 Time Counter of PRUs 77
3.3.4 Real-Time Control Functions in the PRU 79
3.4 Digital Signal Processing on Domain Transfer Algorithm 84
3.5 Single Tone Detection for Online Battery Impedance Measurement 92
3.5.1 Data Transmission between PRU and ARM in BBB 93
3.5.2 Single Tone Detection of Domain Transfer Algorithm . . . 96
3.6 Chapter Summary 98

4 Proof-of-Concept Implementation and Experimental Setup **101**
4.1 The Choice of Battery 102
4.2 Hardware Design and Implementation 104
4.2.1 DC-DC Boost Converter 105
4.2.2 Conditioning Circuits for Battery Voltage and Current . . 113
4.2.3 Onboard Analog-to-Digital Converter 120
4.2.4 Perturbation Setting Values for PI controller 129
4.2.5 Data Length Implementation for Single Tone Detection in Online Impedance Measurement 133
4.3 Experimental Prototype Setup 141
4.4 Chapter Summary 146

5 Experimental Prototype Results **147**
5.1 Measurement System Verifications 147
5.1.1 DC-DC Converter Performance of the Proposed Online Measurement System 148
5.1.2 Real-Time Controller Performances of Proposed Measurements 149
5.1.3 AC Perturbations for Impedance Measurements 155
5.2 Online Impedance Measurement Results 160

5.3 Equivalent Circuit Model 167
5.4 Dependency of Impedance Spectrum Characteristic on SOC, Aging and Current Rate 171
5.4.1 Impedance Spectrum Characteristic on SOC and Aging . . 171
5.4.2 Dependency of Impedance Measurement on Current Rate . 173
5.5 Impedance Measurement of Multiple Cells Connected in Series . . 175
5.6 Execution Time of Data Transfer and Processing 180
5.7 Chapter Summary 183

6 Performances on the Online Measurement System and Preliminary State Estimation 185
6.1 Comparison to a Commercial Measurement System 186
6.2 Possible Sources of Measurement Uncertainty 188
6.3 Comments on Data Selection 191
6.4 Battery State Estimations 193
6.4.1 Measurement Uncertainty 193
6.4.2 ECM Based State Estimation 196
6.5 Further Work 204
6.6 Chapter Summary 205

7 Conclusion 207

References 210

List of Tables

1.1 SPECIFICATIONS OF COMMERCIAL INSTRUMENTATIONS FOR EIS MEASUREMENTS 6

2.1 SOC ESTIMATION METHODS 16
2.2 SOH ESTIMATION METHODS 19

4.1 PANASONIC NCR18650B SPECIFICATIONS 102
4.2 PARAMETER VALUES OF AVERAGED STATE-SPACE MODEL 111
4.3 COMPONENT VALUES OF DIVIDER AND LOW-PASS FILTER FOR SINGLE CELL 117
4.4 COMPONENT VALUES OF DIVIDER AND LOW-PASS FILTER FOR MULTIPLE CELLS 117
4.5 MAXIMUM ClOCK SPEED FOR INTERFACING MULTIPLE ADCs 121

5.1 CONNECTION RESISTANCE FOR SINGLE CELL 161
5.2 VALUES OF COMPONENTS IN THE BATTERY CELL IMPEDANCE MODE 169
5.3 TIME PERFORMANCES IN THE TESTS 183

6.1 ECM PARAMETERS FOR SOC ESTIMATION 197
6.2 ECM PARAMETERS FOR SOH ESTIMATION 197

List of Figures

1.1 Schematic of Typical BMS Monitoring Functions 3
1.2 Photographs of Commercial Instruments for EIS Measurements . 6

2.1 Lithium-Ion Battery Structural Composition; (a) A Cylindrical Lithium-Ion Battery and (b) Cell Construction 11
2.2 Discharge of A Rechargeable Battery Represented as A Lithium-Ion Cell, with Electrons, Lithium Ions and Current Direction . . . 12
2.3 Typical Discharge Curve for 18650 Lithium-Ion Cell; The lithium battery discharges with a constant current rate (of 0.5 C) from the full Voltage (of around 4.1 V) to the cut-off voltage (of 2.5 V) under the room temperature of 25°C 14
2.4 Representation Nyquist Plot for Electrochemical Cell; Impedance variations caused by the discussed effects are characterised in the targeted frequency range (or time scale): 1) In the frequency range of below 1Hz (more than 1 second represented in time scale), a linear relationship between real and negative imaginary parts (of the impedance) is shown; 2) The semicircle within the mid frequency (from 1.0 Hz to 1.0 kHz, equalling the time variation from 1 millisecond s to 1 second) window is presented; 3) In the high frequency range, the positive imaginary part of the impedance increases with the frequency increasing, shown by a curve 21
2.5 Representation of Li-Ion Mass Transfer Phenomenal 22
2.6 Simplified Concept of Electrical Double-Layer Capacitance; (a) Liquid Double-Layer Capacitor for Lithium-Ion Battery (b) Connected Series Plate Capacitor (Wire Connection in Blue) 23
2.7 Simple Equivalent Circuits for a Lithium-Ion Battery Cell 27
2.8 Impedance Spectrum Based on the Randel Circuit 29
2.9 Impedance Spectrum of Randel Circuit (via Simulation) Presented by Bode Plot 29
2.10 Schematic Representation of a Current Pulse Applied to the Battery and Its Voltage Response 33
2.11 Diagram of EIS Measurements: (a) Offline Measurement Method; (b) Traditional Online Measurement Method 35
2.12 Proposed Online EIS Measurement System for Implementation . . 41

3.1 Basic Circuit Diagram of DC-DC Boost Power Converter 45
3.2 Two Statuses of Switch Operation in the Converter 47
3.3 Amplification of Output Voltage of DC-DC Converter 49
3.4 Illustration Diagram of Battery Impedance Measurement Methods 54
3.5 Closed-Loop (top) and Open-Loop (bottom) Controllers 56
3.6 Continuous-Time Mode of PI Controller Schematic 58
3.7 Conventional Discrete-Time System Digram with PI Digital Controller 60
3.8 The Proposed EIS Measurement System Based on DC-DC Boost Converter 61
3.9 Overall Diagram of the Proposed Measurement and Control System Architecture 64
3.10 Block Diagram of ADC 65
3.11 Example of Analog Signal and Discrete-time Signal $x(nT_{ADC})$ . . 65
3.12 Digital Samples by Using 2-bit Quantizer 68
3.13 Photograph of BeagleBone Black 71
3.14 AM335x Functional Block Diagram 73
3.15 PRU-ICSS Functional Block Diagram 76
3.16 Summary of Steps Involved in Deploying PRU-ICSS Program . . 77
3.17 Real-time Functions Operating in Series 80
3.18 Illustration of Two Optional Time Overlaps for Real-Time Functions 81
3.19 Twiddle factors for DFT, $N_{FT} = 8$ 87
3.20 Flow Graph of k^{th} Order Butterfly Computation 90
3.21 Computational Operations of N-point FFT and DFT 91
3.22 Data Transfer Diagram Between ARM and PRU 93
3.23 Line Buffer and Circular Buffer 94
3.24 LTI Filtering Process Based the Goertzel Algorithm 97

4.1 Photo of PANASONIC NCR18650B 102
4.2 Battery SOC Corresponds to Voltage for Single Lithium-Ion Cell in BioLogic VSP/VMP3 104
4.3 System Diagram of Battery Impedance Measurement 105
4.4 A Typical Circuit Diagram of A DC-DC Boost Converter, Inductor Resistance Included 105
4.5 A Typical Diagram of the Small Signal System for the DC-DC Boost Converter 111
4.6 The Proposed System Established via Simulink 111
4.7 Open-Loop and Closed-Loop Control-To-Output Frequency Response $I_i(s)/d(s)$ Plot 112
4.8 Voltage Divider and Filtering Circuit 116
4.9 Bode Plot for First-Order Low-Pass Filter, Showing Theoretical and Real Performances 118
4.10 Diagram of ADC Operation 123
4.11 Timing Diagram for Sequencer FMS 124

4.12 Timing of Clocks Across Three Active Channels of ADC 125
4.13 Voltage and Current Waveforms with A Relative Phase Difference 127
4.14 Settings for the PI Controller Based on I-V Conversion and 12-bit Perturbation Setting Values for the PI Controller 132
4.15 Flowchart for the impedance algorithm in ARM 134
4.16 Goertzel Algorithm vs FFT At Five Exampled Frequencies 137
4.17 Direct Form of IIR Filter Implementation Base on the Transfer Function in (3.54) 139
4.18 Flowchart of the Proposed Online Impedance Measurement System 142
4.19 Photographs of the Experiment Setup, Voltage Measurement in Blue and Current Measurement in Red 144

5.1 Measurements for Calculating Power Efficiency of the Bespoke Converter 148
5.2 Real-Time Control Based on Timing-Clock-Counting Method . . . 150
5.3 Counting PRU's Clocks in Five Tests for Different Functions: (a) Signal Acquisitions via ADC; (b) PI Controller; (c) PWM Compensation 152
5.4 Performance of Current-Mode PI Controller At Perturbation Frequency of 1.0 Hz; Sub-plots No.1 and 2 are used to represent the control in transient and state conditions; The sub-plot No.3 shows the different set on proportional parameter of the PI controller, $kp = 10$, where the integral parameter does not change. 153
5.5 Monitoring Battery Signals at Example Frequencies Under Different Measurement Conditions; (1) 60% and 0.5 C :(a) 0.05 Hz, (b) 1.0 Hz and (c) 1.32 kHz; (2) 20% and 0.5 C: (d) 0.05 Hz, (e) 1.0 Hz and (f) 1.32 kHz; (3) 60% and 0.3 C: (g) 0.05 Hz, (h) 1.0 Hz and (i) 1.32 kHz; All signals were monitored during battery steady-state operation (operating time exceeds 0.075 seconds) 156
5.6 Battery Current and Voltage Performance for Identifying Steady-State Operation, Monitored by NI USB-6366 161
5.7 Battery Current and Voltage Performance for Identifying Steady-State Operation, Monitored by NI USB-6366 162
5.8 Nyquist Plot of Impedance Measurements of a Single Lithium-Ion Battery at 60% SOC and 0.5 C, rebuilding the impedance spectrum with seventeen frequency candidates (marked by blue filled circles); The 5-point reconstructing method is shown here by orange circles; A shape-preserving interpolant algorithm is employed and the fitting result is presented by the dash line. 164
5.9 Battery Impedance Variations with Frequencies on the Amplitude (a) and Phase (b) 166
5.10 2-RC Full Battery Cell Impedance Model, Modified from [1, 2] . . 169
5.11 Point-Fitting Regression for Panasonic 18650 Cell at 60% SOC, 0.5 C170
5.12 Impedance Measurements at different SOCs and Ages 171

5.13 (a) Impedance Measured at 60% SOC and Different C-Rates of 0.3 C and 0.5 C; Comparisons on Magnitude (b) and Phase (c) in Bode Plot 174
5.14 AC Coupled Waveforms for Two Cells (Left) and Four Cells (Right) in Series Connection at around 1.0 Hz and 60% SOC, Monitored by NI USB-6366 176
5.15 Nyquist Plot for Two Series-Connected Cells Under 60% SOC, 0.5 C and Brand-New Measurement Condition 177
5.16 Comparison Between Different Measurements with Single Cell and Two Cells in Magnitude 178
5.17 Comparison Between Different Measurements with Single Cell and Two Cells in Real and Imaginary Magnitudes 179
5.18 The Time Performance of Different Samples Sent from PRU to ARM 181
5.19 The Mean Data Transfer Speed 182

6.1 Comparison of Prototype and the Bio-Logic VSP Under the Measurement Condition: 60% SOC, 0.5 C and Brand-New Cell 187
6.2 Comparison of Prototype and the Commercial Measurement Instrument on Magnitude (a) and Phase (b) at 60 % SOC and 0.5 C 189
6.3 Type-A Uncertainty (the coverage factor of 3 (99.7% probability), shown by circles) at Five Frequencies Under 60% SOC and 0.5 C Measurement Condition; (a) Type-A Measurement Uncertainty at Five Measurement Frequencies: 1 Hz, 10 Hz, 167 Hz, 440 Hz and 1320 Hz; (b) the Measurement Uncertainty for the ECM-Based State Estimation for Batteries (targeted frequencies in red filled circles) 195
6.4 The Fitting Performances (measured data and estimated data shown by blue filled circles and read filled circles, respectively); (a) and (b) for the measurement dependency on two SOC levels:20% SOC and 100% SOC under the measurement condition of 0.5 C and brand-new cell; (c) for the measurement dependency on the battery age; the Frequency Range of the Proposed Model (shown by purple filled circles) from 0.05 Hz to 1.32 kHz 198
6.5 ECM Parameter Sensitivities for SOC (dashed line – fitted, circle – applied) 200
6.6 ECM Parameter Sensitivities for SOH (dashed line – fitted, circle – applied) 202
6.7 Real Parts of the Impedance Measurement (circle) Obtained at 1320 Hz and Compared with the Fitting R_0 of ECM (filled circles); The frequency of interest expanded from 0.05 Hz to 10 kHz; . . . 204

Chapter 1

Introduction

Worldwide energy consumption has radically increased over the past decades [1–4], and traditional energy use currently faces several challenges. The paramount challenge has been the environment pollution by fossil fuels, which have been the most popular energy source since internal combustion engines became significant generators of the kinetic energy for machines in the early 20^{th} century [5]. Viable alternative energy sources have gradually replaced traditional energy sources, which has started to be a primary trend of energy revolution. It is also worth noting that with the widespread use of fossil fuels over past years, the emissions of greenhouse gases such as carbon dioxide and nitrous oxide in the earth's atmosphere have increased, with negative effects on our homes, agriculture, and well-being. As an effort to tackle this serious problem, more sustainable energy sources can be deployed [6, 7]. These energy sources play an important role to reduce greenhouse gas emissions.

Sustainable energy sources include wind, solar and tide, which can contribute to the generation of electricity without any pollution. Nevertheless, the generated electricity is not widely used on grids and electrical components because

of variable and unpredicted electricity generating and transferring conditions. To handle the unstable effects on electricity transformation, exploiting stationary energy storage and conversion systems is a possible solution.

In particular, electrochemical battery systems are economically viable and operationally effective for grid support in the transmission and distribution functions [8]. The properties of the electrochemical system are significantly determined by electrode and electrolyte materials. Different battery materials lead to differences in battery abilities in energy storage or conversion. On the market, universal electrolytes can be classified into three categories: liquid, solid and gas. According to the composition of electrolyte, traditional batteries can be sorted: lead-acid battery, fuel cells, nickel-metal hydride battery, and lithium-ion battery. These batteries have been broadly applied to several areas. For example, traditional and smart grid systems have benefited from the contribution of batteries on efficient energy storage [9].

Batteries are also utilised as the dominant power supply for the majority of portable applications, such as portable electronic devices, electric vehicles and mobile robots [10–14]. Popular implementations such as portable electronic devices (including mobile phones and laptops), are mainly powered by lithium-ion batteries [15]. This is due to lithium-ion batteries featuring higher energy conversion efficiency, light weight, low maintenance, and long service life [16]. In this case, lithium-ion batteries enable the mentioned above features to increase the lifespan for large scale battery applications, for example electric vehicles [16]. Therefore, for the coming years, the demand for lithium-ion batteries is expected to significantly increase in the UK and Europe (as well as in other countries or regions), in response to governments' policies of decarbonisation especially for transportations aimed at reducing the emissions of greenhouse gases (to zero in the UK and 20% in EU by 2050) by using electrical vehicles (EVs), instead of combustion engine cars [6, 17].

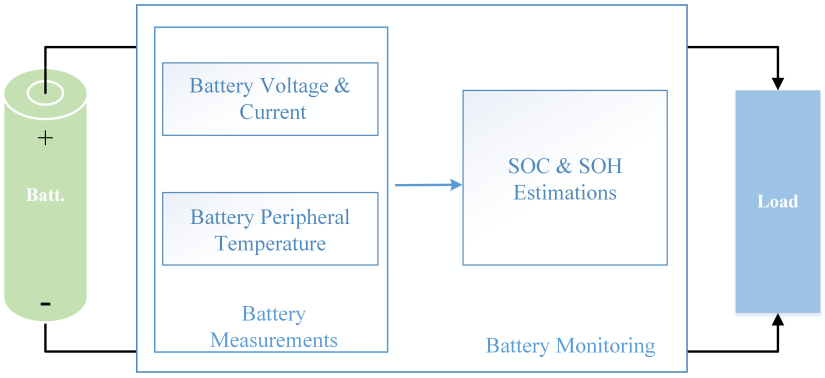

Figure 1.1: Schematic of Typical BMS Monitoring Functions

Despite the fact that lithium-ion batteries are increasingly required in many applications, the energy storage performance of batteries still needs further improvements to guarantee key aspects for commercial considerations, including efficiency, reliability, and cost. In past decades, the majority of efforts toward such improvements concentrated on battery structural design [18] and advanced material technology [19–23]. Nowadays, in-situ battery monitoring of battery management system (BMS) could be enhanced as batteries are used at a large scale. This is because the BMS is a real-time monitoring platform that can provide substantial information about battery operation as well as help detect trouble spots hidden in the battery system. For instance, the BMS of portable devices (powered by battery) is able to measure voltages, currents, and temperature for safety purposes and to monitor state-of-charge (SOC), state-of-health (SOH) and other metrics, as shown in Figure 1.1. In a commercial BMS, the DC voltage and current are measured and then used to estimate SOC. Additionally, the battery capacity degrades over time, which can be deployed to estimate SOH. Moreover, battery temperature is measured for safe and optimal performance where high temperatures resulting in fires, venting and electrolyte leakage must be avoided [24]. However, the traditional BMS employed in commercial applications cannot provide sufficient information on the cause of the battery degradation, so it cannot support an accurate prediction on the residual life of the battery.

To achieve accurate battery monitoring, a state-of-the-art BMS could be enhanced by monitoring techniques, such as updating SOC and SOH estimation algorithms [25–27], developing measurement methods for battery impedance [13], or detecting advanced monitoring parameters [28–30]. The impedance of a battery is a critical parameter that has been used to design batteries in the industry, and is capable of enhancing BMS behaviour to offer useful information on the performance of the battery and diagnosing operation faults hidden in the battery system.

Electrochemical impedance spectroscopy (EIS) is a popular impedance-based method for battery state estimation in the laboratory, which characterises the electrochemical dynamics of the battery. These dynamics can be used to accurately indicate battery performances, such as SOC and SOH [31, 32]. Thus, EIS would help existing battery monitoring systems to improve the monitoring accuracy in commercial or industrial applications. Its further development therefore focuses on the transfer of the EIS measurement technique from laboratories to commercial or industrial area.

EIS characterisations within a wide frequency range reflect small electrochemical changes inside a battery, mainly including mass-transport process, charge-transfer and double-layer reaction on the electrode/electrolyte interface, and physical capacitor and inductance growth of electrodes. In most advanced studies [31, 33–37], the non-invasive measurement approach of EIS has been applied to battery charge/discharge to measure specific response to injected AC perturbations at different frequencies. Besides, the studies report that a properly designed battery impedance model is usually needed in the EIS measurement, which can replace massive EIS data stored in the embedded BMS, saving large amounts of memory. Researchers over past years had studied EIS to deduce various valid methods on battery monitoring, based on either a partial or the whole

spectrum to predict SOC, and on specific changes of impedance to evaluate SOH and the battery operating temperature [35–37].

SOC estimation of a battery based on battery impedance is reported in the publications [2, 38–45], where authors collected the observed values of battery impedance in the whole or partial frequency range and then compared them to the figures in the impedance model or the ideal measurement to determine the SOC. The SOH is estimated with not only the effect of the battery impedance but also the influence of other factors, including temperature, aging, and cycle life [44, 45]. In this case, more measurement or monitoring elements are required in a BMS that create a challenge to current low-frequency data sampling of BMS.

Although EIS provides more details on the battery dynamics when compared to single DC voltage measurement and single current measurement, the use of EIS in real battery operations and commercial or industrial applications is still limited. The limitations are caused by not only sophisticated measurement techniques but also measurement instruments. The challenges of the measurement techniques are associated with the creation of high-quality AC perturbations, the simultaneous acquisition of a large number of battery signals, and the amplification of small AC voltage signals. In addition, the existing measurement instrumentations cannot be directly used for battery powering devices due to their large size and high cost, as shown in Table 1.1 and Figure 1.2 [46–48].

Table 1.1: SPECIFICATIONS OF COMMERCIAL INSTRUMENTATIONS FOR EIS MEASUREMENTS

Instrument	Measurement Type	Basic Cost (£)[1]	Size (W x D x H)
Bio-Logic VSP	Potentiostat/Galvanostat	14,088	435 x 335 x 95 mm
EIS Box	Potentiostat	12,500	415 x 457 x 133 mm
WaveDriver 200	Potentiostat/Galvanostat	10,343.09	160 x 324 x 255 mm

(1) Prices are obtained by the 'require a quote' service of official websites [46–48] and exchanged from US dollar to pound at the rate of 0.81 on 24th April, 2020.

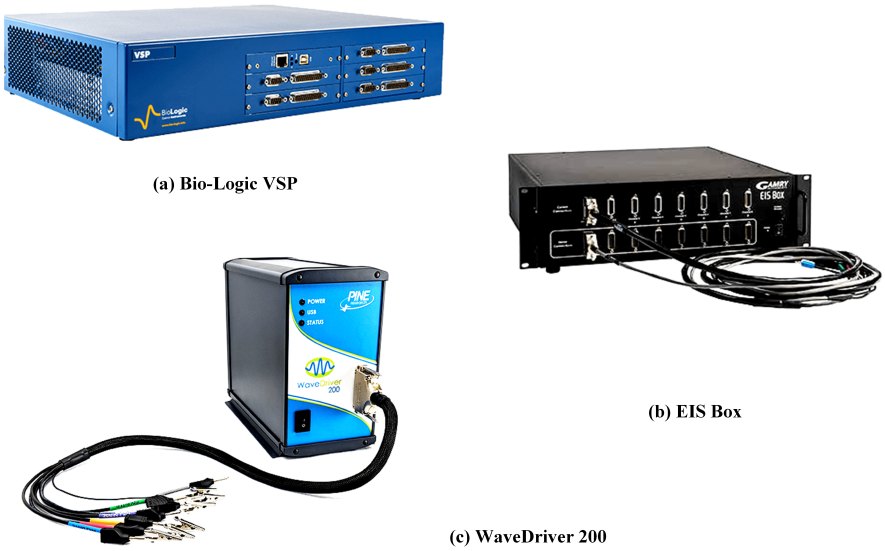

Figure 1.2: Photographs of Commercial Instruments for EIS Measurements

Fortunately, the aforementioned challenges can be partially solved by developing techniques. For instance, switch-mode power converters have become a feasible solution in recent years to measure the EIS under real battery operating conditions (for online measurement), as well as to implement the EIS in commercial applications at a lower cost [13], whereas additional hardware is required to provide specific control strategies to the converter (this consists of a real-time

control system that asks to integrate real-time performance into the impedance measurement programme and operate in parallel with non-real-time functions, such as the signal processing and impedance calculation), which creates other potential challenges to commercialise a user-friendly EIS measurement. Thus, even though the use of power converter is able to tackle the AC perturbation generation and the measurement during battery normal operation, the measurement instrumentations for acquiring online signals and calculating impedance are still barriers for small-scale battery powering devices.

Overall, the implementation of EIS measurement in commercial BMS is limited by expensive and bulk EIS instrumentations, slow impedance measurement speed (due to long measurement duration), and complicated control strategy (real-time control implementation for the power converter).

Therefore, this thesis aims to develop an affordable and user-friendly online EIS measurement platform for lithium-ion batteries. The platform is based on a DC-DC boost converter, allowing to measure EIS over a wide frequency range from millihertz to kilohertz during battery normal operation. It consists of the whole measurement process (including generating perturbations, measuring battery signals and calculating battery impedance) for single-cell (potentially expanding to 7-cell) applications. In addition, it could provide a solution for integrating EIS converter-based measurement system into cost-efficient development board (such as BesgleBone Black), in this way reducing cost of the measurement system, as well as size of measurement device. As a benefit from this work, EIS techniques could be ultimately applied to enhance the functionality of existing BMS on battery state estimations in battery powering devices. The remainder of the contents is organised as follows:

- In Chapter 2, the structural base of lithium-ion battery and the discharge

processes inside the battery are described; Also, battery discharge dynamics, battery impedance models, and impedance measurements are described;

- The proposed measurement method based on the low-cost and small-size hardware are explained in Chapter 3;
- The configurations of hardware and integrated circuits as well as the EIS measurement system design are shown in Chapter 4;
- Chapter 5 illustrates the performance of an innovative controller for the switch-mode power converter, and the results of multiple dependencies of EIS measured by the proposed method. In addition, the appropriate battery impedance model is presented in the same chapter;
- Chapter 6 focuses on analysing the measurement error and discussing the performance of the online fast SOC and SOH estimations;
- In Chapter 7, a brief conclusion is presented.

Chapter 2

Lithium-Ion Batteries and Impedance Measurements

Lithium-ion batteries have been used in a broad range of portable electronic devices in our daily life. The use of the lithium-ion battery in technological applications is wide-spread because of their high energy density, long cycle and shelf life. During battery discharge, internal electrochemical changes influence specific parameters of the voltage, current, temperature and internal impedance. To better understand these activities, in this chapter, the lithium-ion battery structure, the chemistry behind discharging and electrical dynamics behind the chemical reactions are described. Next, the performance of battery impedance spectrum in response to electrochemical changes is discussed. Furthermore, modelling impedance characteristics based on the battery equivalent circuit method is depicted. Finally, the impedance-based measurement techniques used to develop the proposed measurement are reviewed.

2.1 Lithium-Ion Battery Discharging Chemistries

Lithium-ion batteries are facing an ever-increasing demand for portable electronic applications [49]. Technological improvements in lithium-ion batteries are being driven by this demand in order to enhance battery properties regarding energy density, lightweight design and lifespan. In general, these critical properties are associated with battery compositions and structure, which is described in the following section.

2.1.1 Lithium-Ion Battery Structural Composition

Figure 2.1 shows the components of a cylindrical lithium-ion battery, anode, cathode, electrolyte, separators and a cell can. The anode is made of natural or synthetic graphite or hybrid carbons, and the cathode uses lithium metal oxide in modern lithium-ion batteries. Separators are always set between electrodes to split chemical oxidation-reduction processes into two parts: oxidation (anode) and reduction (cathode); this is due to the separators only allowing lithium ions to transport. The electrolyte is a salt solution that bathes the anode and cathode, supporting ion transport to maintain charge balance. Finally, the collectors (shown in Figure 2.2) enable the transport of electrons to and from the electrodes. Collectors are typically made of metals (aluminium for the cathode and copper for the anode) in contact with the electrodes, while the collectors cannot react with the electrodes.

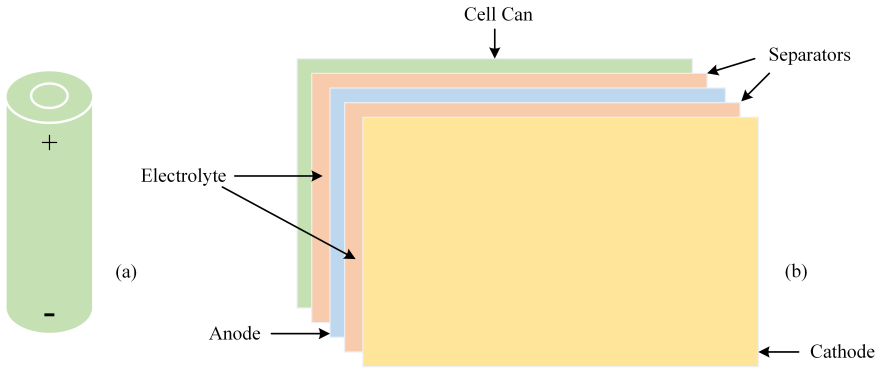

Figure 2.1: Lithium-Ion Battery Structural Composition; (a) A Cylindrical Lithium-Ion Battery and (b) Cell Construction

The properties of lithium-ion battery have been improved in past decades as battery materials have developed over time. For example, low-crystallinity carbon-based materials used at the anode in 1990 [19]. However, these materials are prone to low power capacity, so they are not ideal for long-time usage batteries. In order to prolong operating time and improve compactness for lithium-ion batteries, graphite with advantages such as lightness and high-power capacity has been gradually used since the mid 20^{th} century [50]. Nevertheless, engineers began to find that the power capacity of the lithium-ion battery is dominated by the cathode material rather than the anode one in the late 20^{th} century. Thus, more and more investigations moved from anode to cathode. For instance, the cathode was firstly utilised by pure lithium in the 1980s but was taken off on the market in 1989 [19]. This design caused safe operating problems, such as growing instabilities of metallic lithium electrode and lithium losses [51].

Besides, the energy storage ability and cycle life of lithium batteries would deteriorate due to the chemical instability of the pure metal cathode. Fortunately, since the first commercial rechargeable lithium-ion battery was produced by the Canadian company Moli in the late 1980s [19], the energy storage ability of lithium-ion batteries has been improved by advanced cathode materials. Lithium

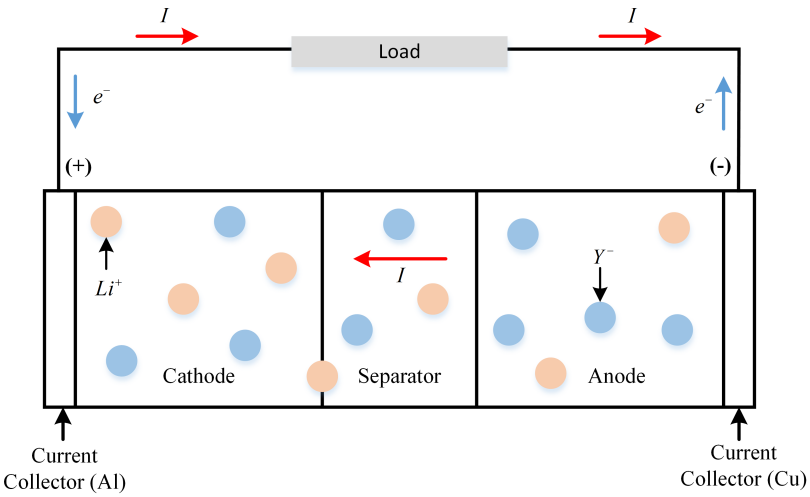

Figure 2.2: Discharge of A Rechargeable Battery Represented as A Lithium-Ion Cell, with Electrons, Lithium Ions and Current Direction

cobalt oxide (LiCoO2, LCO) and lithium iron phosphate (LiFePo4, LFP) are popular elements in composition, increasing specific energy to 180 Wh/kg and 160 Wh/kg, respectively. When compared with the cathode composed of pure lithium, the energy capacity of a multi-metal oxide cathode can be significantly increased [52]. Also, the cycle life has been increased from an initial value of fewer than 1000 cycles in mid last century to a maximum value of 20000 cycles in recent years [53, 54]. Consequently, the service life of lithium-ion batteries is able to last for over 5 years [54].

2.1.2 Lithium-Ion Battery Discharge Reactions

Discharge reactions of the lithium-ion battery are closely related to battery active materials, such as positive and negative materials. These materials work reversibly in the battery, moving or inserting into a host without a significant structural change to it. During the discharging process of the battery, the negative (anode) material is oxidised, and the positive (cathode) material is reduced.

Mainly, oxidation and reduction processes are characterised by electron donation and acceptance in electrochemical reactions, shown as below:

$$Anode : LiY \rightarrow Li^{+} + Y + e^{-}$$
$$Cathode : Y + Li^{+} + e^{-} \rightarrow LiY$$

Where Y (Y^{-} as the negative charge format is shown in Figure 2.2) denotes a surface site or an arbitrary molecule fragment of the electrode materials; for example, graphite carbon and lithium metal oxide [53]. When a lithium-ion battery discharges, lithium ions are intercalated into the positive material and de-intercalated from the negative electrode and migrate across a lithium salt electrolyte in the separator, as shown in Figure 2.2. However, electrons are stopped from free movement in the battery due to the separator, which only permits the transport of ionic charge carriers. By contrast, the oxidation reaction at the anode releases electrons; therefore, different numbers of positive and negative ions gather at the electrodes. As a result, a potential difference occurs between electrodes due to an unbalanced ionic distribution. This is the essential reason that lithium-ion batteries have terminal voltages.

The battery discharge process is actually reducing this potential difference. Theoretically, electrons in a larger concentration should rearrange themselves to compensate for the places where fewer electrons are gathering. The only place is the cathode of the battery because fewer electrons are left at the cathode after the initial electrons of the cathode have been used in the reduction reaction. However, the specific separators stop the electrons going straight from the anode to cathode [55]. In this situation, if a load connects electrodes, electrons can move along the conductor and arrive at the cathode. As a consequence, the current can flow along the load from cathode to anode, as the red arrow (outside of battery) presented in Figure 2.2.

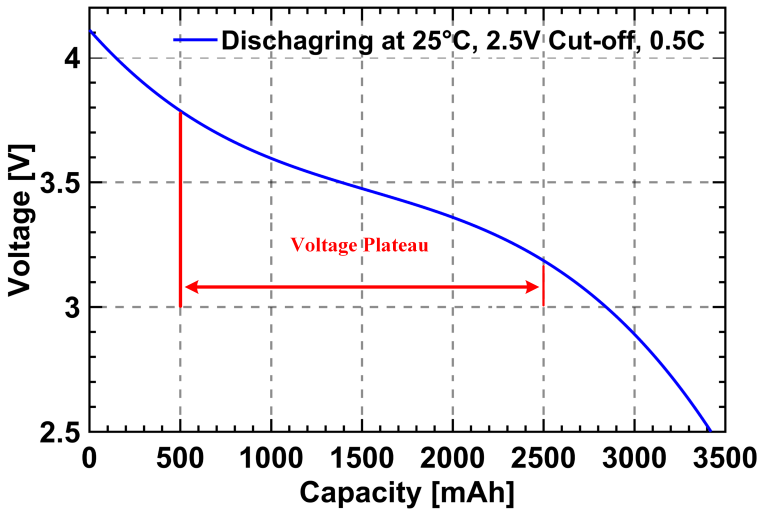

Figure 2.3: Typical Discharge Curve for 18650 Lithium-Ion Cell; The lithium battery discharges with a constant current rate (of 0.5 C) from the full Voltage (of around 4.1 V) to the cut-off voltage (of 2.5 V) under the room temperature of 25°C

2.1.3 Lithium-Ion Battery Discharging Performances

The discharge process of lithium-ion battery is complicated because the battery has elements such as capacitors. In most battery dynamic systems, when the current and ambient temperature act as inputs, the systematic outputs can be battery terminal voltage, core temperature and states [56]. When a load is connected to a battery, electrons at the cathode are able to move; meanwhile, the battery discharge process is launched. As shown in Figure 2.3 [57], the power is transmitted from the battery into the load profile during the discharge process. If a constant discharge rate (current rate in mAh) is considered, the discharge voltage of a lithium-ion cell drops observably at the beginning, and then reaches a voltage plateau where voltage reduces slightly. However, when the power consumption approaches to the maximum capacity (from 2500 to 3300 mAh), the terminal voltage of the battery decreases radically until the voltage moves to a cut-off value.

Additionally, the battery internal temperature rises in the discharge process due to the thermal evolution of current heating and oxidoreduction reaction. High battery temperatures (above 80°C), which accelerates heat generation due to solid electrode interface decomposition (that break down exothermic reactions) and electrolyte melting (including an internal short circuit [58]) could result in unsafe performances, including fires, venting and electrolyte leakage [24].

In order to protect battery discharge from overdischarge and high operating temperature, the BMS tracks battery discharge dynamics in real time [59–63]. The state of charge is the parameter showing how much energy remains in the battery and the state of health is the term describing the performance of the battery relative to its new state. However, the state of charge and state of health cannot be directly measured. These two states are generally estimated by measuring battery terminal voltage, current and temperature, as discussed in Section 2.1.4. Besides, the changes of the states during battery discharge not only depend on the time variation but also are applicable to calendar parameters, such as discharge cycles [59] and aging [60].

Battery states always change with the internal electrochemical dynamics during discharge. Electrochemical influences are mainly created by internal ion propagations and specific structural properties [61]. According to different time performances during battery discharge, electrochemical influences can be sorted into short-term history and long-term history. The short-term history ones contain electric and magnetic effects, electric double-layer effects and mass transport effects, which can last from microseconds to seconds. In contrast, the effects related to aging, reversibility and cycling influences last from a few minutes to several years. During a battery's entire life, electrochemical effects are fully contained in most of the electrochemical models. These mentioned effects are

Table 2.1: SOC ESTIMATION METHODS

Categories	Estimation Methods
Current-based estimation	Coulomb counting method
	Modified Coulomb counting method
Voltage-based estimation	Open circuit voltage method
	Terminal voltage method
Impedance-based estimation	Impedance method
	Impedance spectroscopy method

also considered as modelling parameters in power management systems in order to provide an accurate dynamic performance for the simulation.

2.1.4 SOC and SOH Estimations

Many SOC estimation methods have been proposed, as shown in [60–63], [64–67] and [68–72]. Three kinds of SOC estimation approaches in the citations are mainly discussed, called current-based estimation, voltage-based estimation, and impedance-based estimation, as shown in Table 2.1.

Firstly, current-based estimations in [61, 63] divide SOC in two parts: capacity and energy. In current-based estimations, capacity accounting and energy accounting methods are usually deployed. The former method focuses on coulomb counting. In this method, the SOC is defined by the ratio between the stored charge capacity and the total charge capacity. The SOC calculation can be derived from the charge consumption through calculating discharge current over a time variation [73]. The coulomb-counting method is straightforward to implement, but its accuracy suffers from an unknown initial SOC value (due to battery capacity loss) and error accumulation in the integration process. In order

to improve coulomb-counting accuracy, the modified method can be adopted, as shown in [63]. The method establishes that the discharge current can be modified with the corrected current by a quadratic relationship. Ultimately, this modification optimises the SOC expression that combines accurate current to improve SOC estimation.

The other current-based estimation mechanism for SOC is associate with energy usage. The mechanism applies the power behaviour (the multiplication of voltage and current within a certain time) to link SOC numerical performances. A conventional combination between SOC and power activity relies on the ratio between the retained energy and total energy. During battery discharge, the energy transferred to a load can employ the counting voltage ($V(t)$) and current ($I(t)$) method. In this method, voltage and current should be measured in a time-continuous mode in term of recording energy dynamics without interruption. Therefore, to express the SOC associated with the energy consumption one needs: energy transferred from initial time (0) to a recent time (t) and energy recorded by a full discharging (the time lasts from 0 to $total$), as shown in (2.1). Notably, the energy counting method is used to estimate current $SOC(t)$ roughly because of the uncertain initial value ($SOC(t_0)$) of SOC:

$$SOC(t) = SOC(t_0) - \frac{\int_0^t V(t)I(t)dt}{\int_0^{total} V(t)I(t)dt} \tag{2.1}$$

Secondly, estimating SOC of a battery depends on a voltage-based relationship. Such the authors reported in [63, 64, 74, 75]. There are two main types of voltage discussed in studies, called terminal voltage and open circuit voltage (OCV). Battery terminal voltage performance (terminal voltage drops) can reflect the electromotive force (EMF), which results approximately linearly proportional to the SOC [63]. Therefore, the numerical performance of SOC is linked with voltage measurements that can be used for battery powering applications. For

instance, an approximate linear relationship between the SOC and open-circuit voltage (of the battery) was implemented for lead-acid batteries [74]. On the contrary, the OCV relationship with SOC for the lithium-ion battery, is non-linear [64].

Even though several dependencies need to be taken into account in the SOC equilibrium in a complicated non-linear system, the SOC-VOC method is still reported by many authors [64–66, 74]; this is because some developing techniques can boost the estimation performance of the method. For example, the dual Kalman filter (KF) employed with more parameters (than the OCV method) to optimise the SOC algorithm, thereby improving the accuracy of the SOC estimation [65].

Additionally, the artificial network algorithm reported in [67] provides a further accurate process for the factors of SOC in the KF algorithm, so the desired SOC estimation can be obtained. Nevertheless, KF has the drawback that it linearises the non-linear behaviour of SOC, which may result in potential errors, especially for high dynamic load profiles [66].

Thirdly, the magnitudes of several parameters provided by impedance measurements may relate to the SOC of battery [68, 69]. A given battery could rely on impedance-SOC relationship to estimate the SOC in a wide range of impedance measurements. However, ongoing research is required to develop high-accurate relationships between the variations of impedance and the dependencies, such as degradation, operating temperature and cycle life [70–72].

The SOH of battery indicates how well a battery system is functioning relative to its nominal and end-life states. The battery energy storage is significantly affected by capacity fade and resistance deterioration. According to many relative contributions for the SOH estimation, the applied methods can

Table 2.2: SOH ESTIMATION METHODS

Categories	Estimation Methods
Model-based estimation	Electrochemical models
	Electrochemical impedance spectroscopy models
	equivalent circuit models
Data-driven estimation	Neural networks
	Support vector machines
	Gaussian process regression
	Dynamic Bayesian networks

be classified into two main categories: model-based methods and data-driven methods [70, 76–82], as shown in Table 2.2. The model-based methods are always applied with parameters of battery, such as load condition, material properties and degradation, to estimate SOH, while the data-driven methods usually depend on mathematical algorithms to analyse data and give an evaluation for battery health states without a manual model process. Since the SOH estimation methods are developed in the frequency domain, the electrochemical impedance spectrum has become an accomplished calibration method to validate battery degradation [35, 70, 72, 78]. This is due to the fact that irreversible losses (fade and deterioration) inside of batteries cause a typical reflection of impedance increment.

When compared to SOC and SOH estimations with a time parameter, the impedance-based methods track battery state changes in the frequency domain by impedance specific variations, which solves the problem of obtaining initial values for SOC and SOH. To better understand this tracking mechanism in the frequency domain, the battery impedance is described in the next section.

2.2 Lithium-Ion Battery Impedance Characteristics

As discussed in Section 2.1.3, battery discharge dynamics are significantly influenced by short-time and long-time effects, including mass-transport effects, charge transfer effects and physical effects (magnetic and electric). In particular, these effects can be characterised by the impedance spectrum, where they result in observations of battery AC impedances over a frequency range from millihertz to kilohertz. During battery AC impedance tests, AC excitations are injected to a battery amid regular operation in which DC constant components and AC variables are simultaneously contained.

The battery complex impedance (Z) at a given frequency (f) uses the amplitude and phase of the AC component of the voltage ($V(f)$) and current ($I(f)$) at the same frequency:

$$Z(f) = \frac{V(f)}{I(f)} e^{j\theta(f)} \tag{2.2}$$

where the phase ($\theta(f)$) is the phase shift between the voltage and current of the battery. The impedance values include a real part, an imaginary part, absolute value, and phase, and they are capable of characterising the electrochemical dynamics of a battery. According to the duration of electrochemical effects, the electrochemical processes characterised by the EIS can be segmented into three frequency regions [34, 61, 83], as demonstrated in the Nyquist plane in Figure 2.4. These processes include slow physiochemical processes, such as mass-transport, with a time constant slower than 1.0 second. Also, they contain fast processes like charge transfer with a time constant in the range between 1.0 millisecond to 1.0 second. For even faster processes, physical inductive and capacitive responses have a time constant faster than 1.0 millisecond.

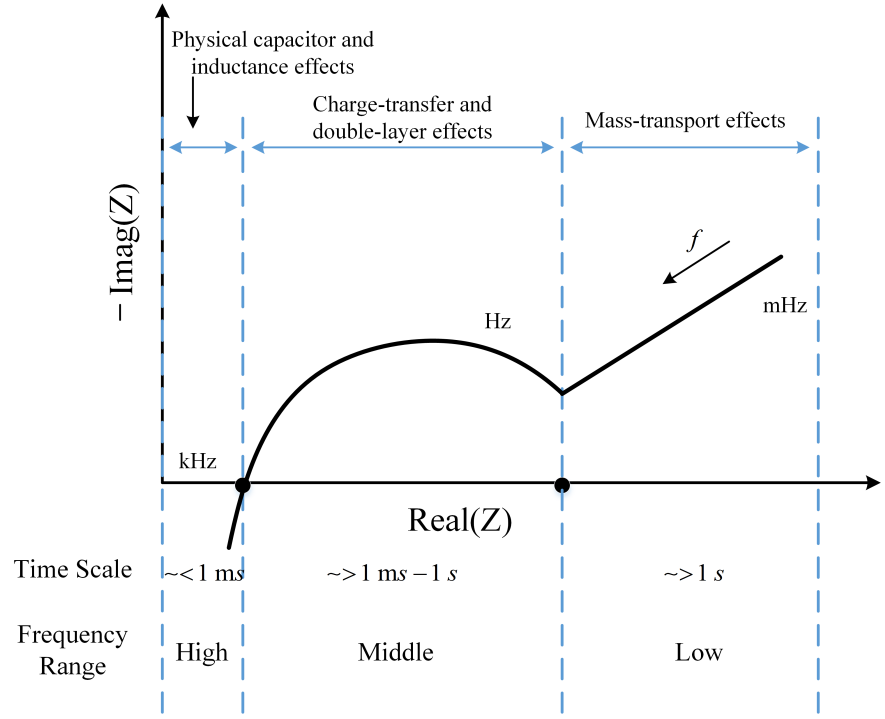

Figure 2.4: Representation Nyquist Plot for Electrochemical Cell; Impedance variations caused by the discussed effects are characterised in the targeted frequency range (or time scale): 1) In the frequency range of below 1Hz (more than 1 second represented in time scale), a linear relationship between real and negative imaginary parts (of the impedance) is shown; 2) The semicircle within the mid frequency (from 1.0 Hz to 1.0 kHz, equalling the time variation from 1 millisecond s to 1 second) window is presented; 3) In the high frequency range, the positive imaginary part of the impedance increases with the frequency increasing, shown by a curve

2.2.1 Impedance performance Caused by Mass-Transport Effects at Low Frequencies

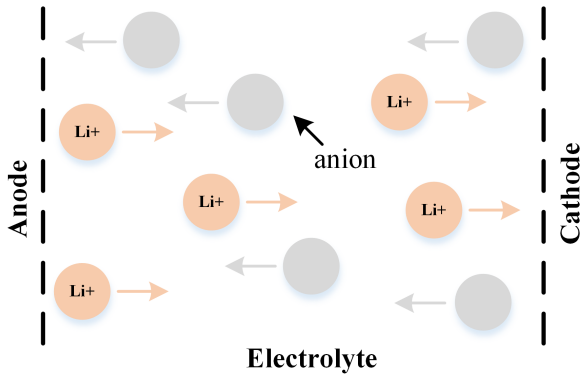

Figure 2.5: Representation of Li-Ion Mass Transfer Phenomenal

The mass-transport effects are caused by the lithium-ion transport in the electrolyte from anode to cathode, as shown in Figure 2.5, due to an ohmic potential difference over the electrolyte. In contrast, anions in the electrolyte diffuse from cathode to anode and create a concentration phenomenon; thereby an additional potential difference is generated in a discharge of a cell as studied by [84–86]. Battery impedance behaviours in low frequency range are generated by Faradic current and potential difference. The diffusion creates Faradic current and potential difference expressed by linear equations in [33]. These equations show that if a small sinusoidal signal is injected, the variables of the current and the potential are sinusoidal as well. Accordingly, the quantification of Faradic impedance is reported by the variations for the unit surface area of electrodes in [33]. The frequency response of Faradic impedance cover a wide bandwidth, of which the maximum value is around 1.0 Hz. In particular, the impedance spectrum characteristics in response to SOC variations mainly occurs in this low-frequency range [87, 88], which reflects the transport of ions having a significant effect in transforming the energy from electrical energy to chemical energy or vice versa.

2.2.2 Impedance Performance Caused by Charge-Transfer and Double-Layer Effects within Mid-Frequency Range

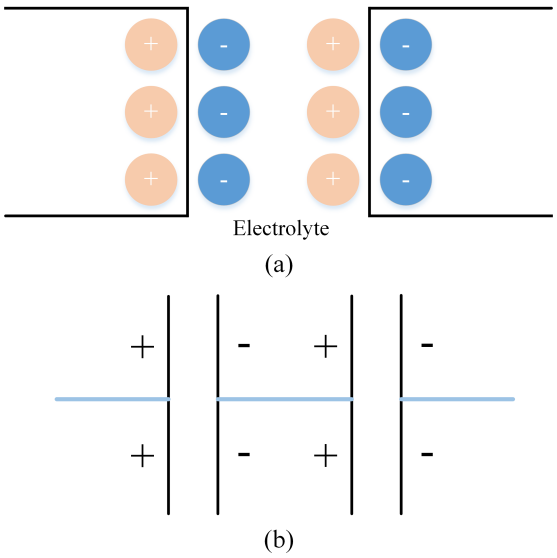

Figure 2.6: Simplified Concept of Electrical Double-Layer Capacitance; (a) Liquid Double-Layer Capacitor for Lithium-Ion Battery (b) Connected Series Plate Capacitor (Wire Connection in Blue)

As for battery discharges, the current flowing in the battery leads to unbalance distributions of positive and negative ions in a cell. The cathode has more positive ions than the anode, while the anode owns a more significant number of electrons. These electrons would gather around separators and absorb ionic charge carriers on the surface of the separator (which can be described on the surface of the electrodes as well). As a result, an electric field is created between the electrolyte which negative ions distribute on the cathode's surface, and positive ions allocated on the anode's surface, as shown in Figure 2.6(a). This arrange of ions around the electrode's and the separator's surfaces creates a typical capacitive performance, where the equivalent performance can be seen as two actual capacitors connected

in series, as shown in Figure 2.6(b). Consequently, a double-layer capacitive effect is caused, and the equivalent capacitors work in parallel in the discharging process. It is noteworthy that the capacitance would have a larger value in rechargeable batteries than in non-rechargeable batteries because the structure of the former is designed with a larger surface area and shorter distance between electrodes.

In the mid-frequency range, the dominant impedance variances come from equivalent capacitances, which had been justified by an analytical equation presented in [89]. The area of the plate and surface density of the electrodes determine the capacitance in its numerical performance. The frequency range of a double-layer effect is of interest for researchers. Kularatna presents a time range for electrochemical effects in the literature [90]. The time-varying range for double-layer effects can be read from the illustration: approximately, from milliseconds to minutes (in hertz: from millihertz to kilohertz). Likewise, Moya points out that the characteristics of the double-layer effect can approach a frequency of 1.0 kHz [91]. A common view is gained from the literature that a frequency of 1.0 kHz can be used as a maximum frequency for double-layer effects during battery impedance investigation.

Electrode's surface characteristically varies within this frequency range, causing an observed impedance rise [92]. In most cases, the rise of this response is used to indicate battery aging process due to the surface variations (especially the solid electrolyte interface film growth) mainly depending on the battery cycle life.

2.2.3 Impedance Performance Caused by Physical Effects at High Frequencies

When compared to the long-time effects of mass transport and the electrochemical double layer, physical effects cause impedance changes with a shorter time constant. Physical phenomena can be classified into three aspects: ohmic resistance, inductance, and capacitance.

The ohmic resistance for each cell is the sum of multiple resistances, including electrolyte resistance, the current collector resistance, the electrode resistance and the transition resistance between electrodes and the current collector [93], which does not significantly change over frequencies.

For the inductance behaviour, this is caused by the geometry of the cell; inductance performance is closely related to the cell's size [94]; the smaller size a cell has, the more obvious effect of inductive components will be caused. Besides, capacitive components are created by the change of the specific structural parameter (such as penetration depth of the ions [94]) that causes both electrodes behaving like flat surfaces. Therefore, a pair of flat surfaces become a pure plate equivalent capacitor when the frequency exceeds 1.0 kHz.

It worthy noting that the battery looks inductive at high frequency in EIS-based researches because the capacitive reactance which is inversely proportional to frequency is less than the inductive reactance which is proportional to the frequency. With the frequency increasing (over 1.0 kHz), this inductive reactance of battery becomes the dominant effect on the impedance variation [2, 95].

2.3 Modelling Electrochemical Dynamics of Lithium-Ion Battery

Electrochemical dynamics can be numerically identified by a lithium-ion battery model. In the literature [1, 33, 96–100], lithium-ion battery models mainly consist of two categories: physiochemical and electrochemical-based impedance ones.

In the former type, battery electrochemical behaviours at the structural compositions are quantified by differential equations. In order to ensure an accurate performance of the battery model, the primary cell model consisting of the main effects (for examples, Faradaic currents and potentials for electrodes) cooperates with sub-models where some possible effects are covered, such as humidity, battery temperature and battery aging [60, 96, 98, 101–103]. Although multi-physical conditions are considered into models to describe the battery internal dynamics accurately, these models for the lithium-ion battery are complex and not easily followed by non-chemical researchers due to the difficulty of understanding complex dynamics. Therefore, only a few research purposes suit the physical models, such as investigations on thermal and aging [101, 102].

In the second category, the electrochemical-based impedance model is a good way to study battery internal characteristics on the impedance responses [1, 33, 99, 100]. As the discussion shown in [33], the impedance expression delivers electrochemical processes of lithium-ion battery within a frequency range in which the previous electrochemical effects are contained. This model enables the tracked parameters (including constant parameters and dynamic parameters [33]) to be used as a metric of battery impedance. In fact, the electrochemical-impedance models are similar to the physiochemical ones that require a high-level understanding of battery physical properties and mathematical skills to derive differential equations.

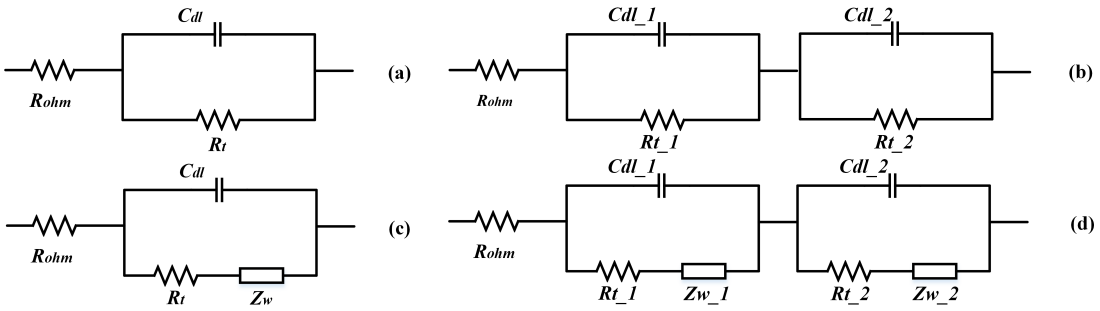

Figure 2.7: Simple Equivalent Circuits for a Lithium-Ion Battery Cell

On the other side, in most of the efforts to evaluate the performance of battery impedance in an efficient way, the equivalent circuit models (ECM) as illustrated in Figure 2.7 have been widely deployed [1, 43, 74, 90, 99, 100]. For instance, the simple models presented in Figure 2.7(a) and Figure 2.7(b), include resistive (R_{ohm} and R_t) and capacitive (C_{dl}) performances in order to model battery electrochemical activities, which are popularly used to investigate battery state changes of EVs [43, 74]. Figure 2.7(c) and Figure 2.7(d) illustrate slightly more complex models for lithium-ion batteries that include battery internal ion behaviour (diffusion and transportation) via a Warburg element (Z_ω). Historically, Randle et al. created this element to describe the effects caused by lithium ion activity related to internal impedance dynamics of batteries. In the applied Randle models, the Warburg element is connected to a RC network (R_t and C_{dl}) and then together connected to a pure resistor (R_{ohm}) in series, as shown in the illustration (the first-order model is shown in Figure 2.7(c) and the second-order model is shown in Figure 2.7(d)). For complex models, such as the ones using high-order RC circuits (3-order, 4-order and so on, which are excluded in the illustration) and inductive elements (also excluded in the illustration), they can be employed for large-scale battery storage (such as electrical grid storage) with sufficient accuracy [43, 90]. For the Warburg element presented in Figure 2.7(c) and Figure 2.7(d), a common understanding is that this element represents ion diffusion dynamics from mass-transport effects and the pure resistor serves

as the resistive phenomenon, which dominants the effects in the low-frequency range. In addition, the first-order RC network is fundamentally used in the ECM to stand for the effects of double layers, as shown in Figure 2.7(c). In this case, the total battery impedance (Z) can be derived with a frequency variety (ω):

$$Z = R_{ohm} + (R_t + Z_\omega) \parallel \frac{1}{j\omega C_{dl}} \tag{2.3}$$

The Warburg impedance is expressed as:

$$Z_\omega = \frac{A_w}{\sqrt{\omega}} - j\frac{A_w}{\sqrt{\omega}} \tag{2.4}$$

where A_w is the Warburg coefficient.

It is worth addressing that the model shown in Figure 2.7(c) has a specific name: the Randle model. The complex impedance visible in the Nyquist plot of a lithium-ion battery can be characterised by the Randle model, as shown in Figure 2.8. In the low-frequency range from millihertz to hertz, the value of impedance increases linearly in a capacitive manner. As expressed in (2.4), the increase ratio of the Warburg impedance in the low-frequency zoom is 1.0. At middle frequencies, the spectrum shows a capacitive semicircle which poses the maximum of the real part at the value $R_{ohm} + R_t$ and the minimum real part occurs at R_{ohm}. Besides, the peak of the imaginary part reaches the frequency of $1/2\pi R_t C_{dl}$. At a high frequency around kilohertz, the spectrum only represents a resistive behaviour (R_{ohm}). For further development at much higher frequencies (over kilohertz), the spectrum would cross the real axis and tend to the imaginary infinity, which specifically delivers its inductive property (not presented in the illustration). Other complex equations in response to complex models are not considered in this thesis, but can be found in [43, 90]

Apart from presenting the impedance spectrum in the Nyquist plot, the

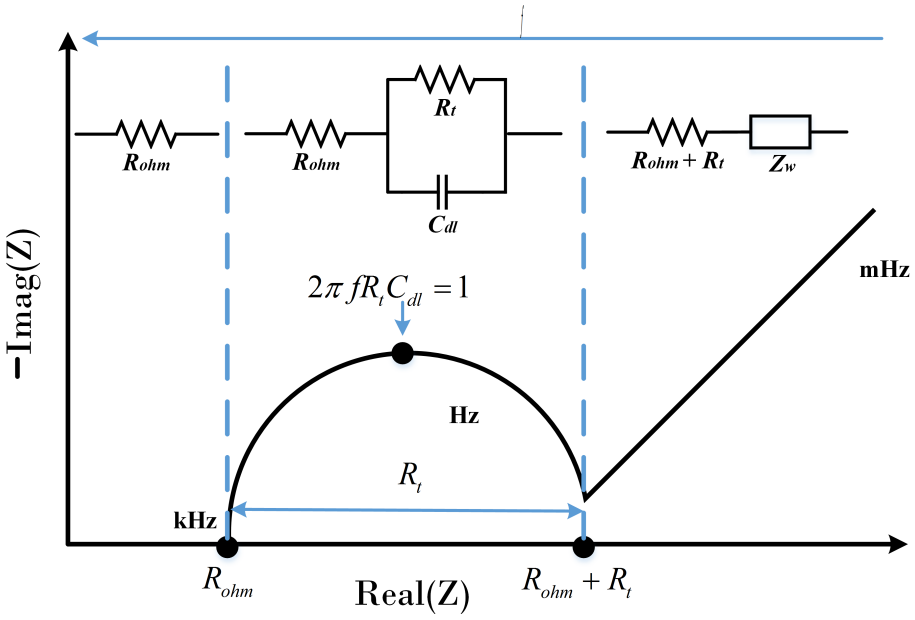

Figure 2.8: Impedance Spectrum Based on the Randel Circuit

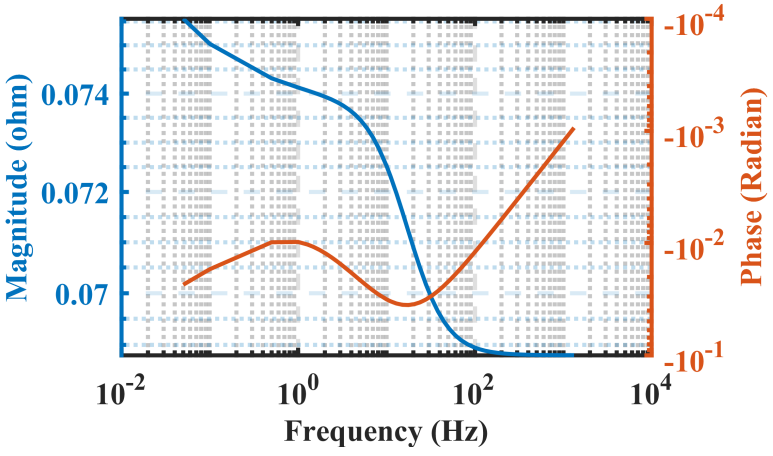

Figure 2.9: Impedance Spectrum of Randel Circuit (via Simulation) Presented by Bode Plot

magnitude and phase representations (Bode Plot) are usually used to obtain a little more insight into the impedance variation with respect to the frequency. As studied in[104, 105], the magnitude shown in Figure 2.9 suffers a gradual decline in the frequency range from millihertz to around kilohertz, while the phase curve in the illustration experiences a complex change in that frequency region, which can be described into three parts. Phase slowly moving occurs at low frequencies below hertz. Next, with the value of the frequency moving toward hertz, the value of the phase decreases. Finally, an increase of the phase is observed as the frequency rises from hertz to kilohertz.

Even though the Randle model allows researchers to gain electrochemical dynamics in an efficient way, its results impede the application of designing high-performance battery management systems. This is the result of a lack of a direct relationship to explain battery's internal physiochemical properties. In order to tackle this issue, researchers have attempted to boost the performance of the Randle model with more physiochemical effects [1, 100, 106], which should be related to electrochemical changes. As Li and the other authors reported in [1], they put forward a cell model to reflect the electrical equivalents of physical electrochemical processes. Also, a structure-based version of battery impedance mode was unveiled. The model provides a clear combination between the impedance spectrum and the battery composition (including anode, cathode and electrolyte). Furthermore, the extended circuit consists of an inductor to represent the charge-transfer effect and two RC networks in order to indicate impedances of the anode and cathode, respectively. When compared with the models (shown in Figure 2.7(a) and Figure 2.7(b)) based on partial battery dynamics [100, 106], the fulfilled effects (especially involving film impedance arising from electrode reactions) reported by Li et al. are well covered in the model. As a result, the model may be possibly used to improve the accuracy of BMS.

In these years, lithium-ion battery models have been slightly modified by [1, 99] in order to become user-friendly. Recently, ECM has focused on high-performance properties in mapping EIS data, aimed at benefiting EIS techniques to battery online applications, such as battery state estimations [2, 44].

2.4 Impedance Measurement Techniques

As mentioned before, battery impedance-based methods have been employed to model battery electrochemical dynamics in order to forecast battery discharging performance and improve the accuracy of SOC and SOH estimations. Battery resistive characterisation in general consists of two performances: DC performance and AC performance. The direct current causes the DC performance of impedance and the alternative elements result in the AC performance of impedance. Several studies have delivered impedance measurement techniques [13, 44, 102, 103, 107, 108]; these measurements can be sorted into two types: DC resistive measurement and AC impedance measurement.

2.4.1 Direct Current Resistive Measurement

Batteries have an internal resistance (R), which is the target of direct current resistive measurement. When a battery is connected to a load profile, the power of the battery is automatically transferred to the load. Figure 2.10 shows that the voltage drop (ΔV) is obtained as a discharge current pulse (ΔI) is applied with a long duration (Δt). The main cause of voltage drop is due to the fact that DC resistive performance (R) consumes the majority of power. Thus, based on

Ohm's law, the DC resistance of the battery can be expressed as:

$$R = \frac{\Delta V}{\Delta I} \tag{2.5}$$

Therefore, the first technique for obtaining battery DC resistance consists in applying a current pulse to the battery and to measure the resulting voltage drop during battery discharge, as reported in [13, 34, 44]. The battery DC resistance (DCR) is always mentioned in most battery impedance measurement to stress the battery transient response [44]. However, DCR cannot fully describe the electrochemical dynamics and depends on the battery current, which limits its application; for instance, using the DC resistance to only estimate SOC with the OCV method [13]. Besides, the DC voltage variation not only contains voltage drop on the internal resistance of the battery but also consists of a variation in the electromotive force (EMF) (a long-time measurement causes a change in the lithium surface concentration of the active mass particles, which leads to a change of EMF that is included in the total voltage drop, as studied in [44]), which cannot be easily distinguished in the DC resistance measurement. In this case, the measurement would obtain a lager DC resistance than the truth value. Besides, the time duration of the DCR measurement always lasts for a quite long time in order to obtain transient settlements. Such a specific period of 10 seconds was set to the measurement in [44], and a longer time (up to 2.0 h) was configured in [13]. Thus, the time durations are not consistent in the mentioned works, which would result in a difference in the DCR measurement, leading to an incorrect estimation.

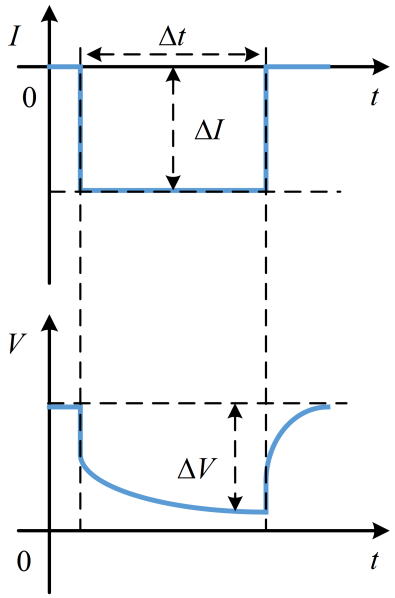

Figure 2.10: Schematic Representation of a Current Pulse Applied to the Battery and Its Voltage Response

2.4.2 AC Impedance Measurement

On the other hand, battery AC impedance characteristics have been introduced in three different frequency ranges. These characterisations can be modelled by the equivalent circuit method used to investigate electrochemical dynamics. In order to measure AC impedance in the mentioned frequency range, the AC signal injection method can be adopted. This is because batteries are DC power sources that cannot independently create AC signals for impedance measurements. In these measurements, AC injections are usually superimposed to the operating voltage or current of a battery. There is no specific limitation for DC signals (as batteries work under safe conditions) during the measurements; however, for AC excitations the method addresses that only a small AC current or voltage signal is allowed to superimpose to battery operation given that the negative effects of large AC injections may result in possible damages and durability decrease on lithium-ion batteries [95]. Also, the linear response of a battery (either current or voltage) can be introduced by the small AC excitation. Finally,

the ratio between responded AC excitation (current or voltage) and AC injection (voltage or current) is calculated in terms of the values of battery impedance, as shown in (2.2). Conventionally, an AC impedance measurement requires essential functions: an AC signal generator creating AC excitations at given frequencies, signal acquisitions collecting the battery current and voltage signals, and a microprocessor processing collected signals and calculating impedances. Here, a typical AC impedance measurement is presented by the most popular EIS measurement.

Electrochemical Impedance Spectroscopy Measurement

EIS is able to characterise sophisticated electrochemical dynamics involved in the change of the impedance spectrum within a broad frequency range. To obtain the impedance spectrum, a proper EIS measurement is needed. Several EIS measurement methods have been shown in [2, 40–44, 103, 107–112]. The EIS measurement methods can be divided into two main categories: offline measurement [43, 103, 108, 109] and online measurement [2, 107]. In the offline measurement method, as illustrated in Figure 2.11(a), the battery is extracted from real operating circuits and tested by using an electrochemical instrument. The common feature of using these devices is to provide an ideal measurement conditions in which the SOC of battery is maintained. Hence, battery power storage (SOC) performs consistently during the whole measurement process, which can eliminate the influence of SOC variation on the impedance measurement. However, it is worth addressing that electrochemical instruments are expensive and not user-friendly for portable applications, such as EIS box, Bio-Logic VSP, or impedance analyser, as shown in Figure 1.2.

In the measurement of using an electrochemical instrument, the instrument supplies key functions, including creating AC excitations, acquiring battery

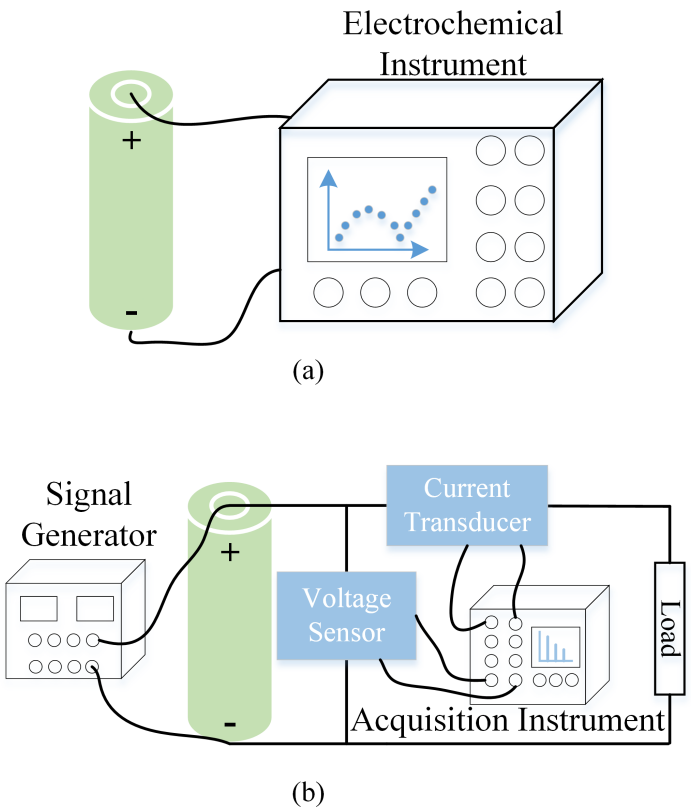

Figure 2.11: Diagram of EIS Measurements: (a) Offline Measurement Method; (b) Traditional Online Measurement Method

signals and calculating impedances, which are embedded by an integrated program using the aforementioned instruments. For example, the instrument named Bio-Logic VSP offers an integrated impedance measurement platform in which the AC injection can be flexibly configured in amplitude and phase, and the measurement frequency range can be set with maximum and minimum frequencies. Besides, the impedance calculation works with a mean measurement algorithm to reduce the influence of noise. Although the offline measurement delivers easy-to-use and high-level accuracy properties, it is very expensive and the battery needs to be removed from the current.

An online measurement method can be employed due to battery impedance measurement performing in a regular battery operation. As illustrated in Figure

2.11(b), in a traditional online measurement, the battery can regularly work with a load profile [13, 107]. At the same time, the impedance measurement works with an AC signal generator in order to create AC excitations for the battery operating circuit, and with a signal acquisition (or a frequency analyser) device to acquire battery signals (such as voltage, current, and surface temperature). If an acquisition instrument is used in the measurement, impedance calculations can be included in the acquisition system or built from the acquired data with the help of external software. Notably, battery signals cannot be sensed directly by the acquisition device. Thus, the voltage sensor and current transducer are used to sense signals on voltage and current, respectively. If a frequency analyser, alternatively, completes the online impedance measurement, additional current transducer and voltage sensor may be not required. However, the drawback of using these instruments is that the complexity and cost of impedance measurements would increase significantly.

Developed Techniques of Online EIS Measurement

In recent years, online EIS measurement techniques have been developed, which is going to meet the requirements demanded by potential markets in terms of requiring a proper measurement instrument with the features, such as lower-cost, user-friendly, smaller size and high-accuracy [2, 13, 40–43, 103, 107, 108, 113]. Here, the cost of online EIS measurement is the first challenge in the technical transition process from laboratory to commercial application, which determines whether the EIS technique can be used broadly in commercial applications or not [40].

The vast majority of existing online impedance measurements focuses on hardware and software parts to improve performances of the measurement system, such as how to develop a circuit to create current excitation for online

impedance measurements [13, 107, 108, 113], or improve performance of SOC and SOH estimation algorithms [40–42, 114, 115]. From the hardware side, the initial target is reducing the measurement cost in AC signal generator because AC signals over a wide frequency range are generally created by the generator that leads to additional cost during the measurement. Recently, the implementation of AC signal generator have been replaced by using a cost-efficiency switch-mode power converter with a proper control theory [13, 40, 107]. For example, the power converter method was reported in [13, 40–42, 107, 114]. Huang's team used a DC-DC power converter to create a sinusoidal perturbation of the voltage (or the current) at different frequencies [13, 40, 114]. The converter was properly controlled in the measurement based on the duty-cycle/current control theory (where a sinusoidal reference was set in the control system of which details will be discussed in Chapter 3) [13, 40, 114]. Moreover, the effort on measuring EIS based-on the power converter during the discharge and charge processes was taken by Qahouq's team [107]. They focused on the use of a bidirectional power converter (DC-DC buck-boost converter) while batteries are in operation. The same sinusoidal control theory was deployed in the measurement to create sinusoidal excitations over a wide frequency range. So the implementation of the power converter in the mentioned studies gives an opportunity to create the desired excitations in EIS measurement, potentially resulting in a low and small measurement platform for commercial applications (Another benefit of using a power converter in battery operation is regulating the voltage for the specific requirement of the output, which will be explained in Section 3.1).

Although Huang and Qahouq have utilised a lower cost switch-mode converter to replace the AC signal generator and reached a wide frequency measurement range, expensive and sophisticated acquisition instruments cannot be ignored in their measurements. However, in [2], Din et al. devoted to decrease further investment in the measurement by adopting a comprehensive method. In

this method, a comparable lower-cost microprocessor (field-programming gate array (FPGA)) was deployed to control a power converter and deal with measurable signals by an integrated conditioning circuit and a MATLAB platform.

An general online impedance measurement technology has been reported by [2] to verify the achievements on the accurate and wide-frequency range measurement. FPGA is discussed in the publication, which can provide a compatible option to take over additional functions to the point where some are now marked as a full system on chips. However, a hardware description language of FPGA is complicated, so high-level programming skills would be required, which adds complexity to the design. Even though the discussed methods based on the power converter shown in [2, 13] seem promising to enable an uninterrupted AC impedance measurement of a battery during battery discharge or charge, as well as without additional AC signal generations, they still need to face the battery state variations caused by a long-term measurement.

Related studies in [2] and [13] allow only one AC frequency for the impedance measurement at a time, which means that measuring an impedance spectrum over a broad frequency range from millihertz to kilohertz would need to be sequential. It is worth mentioning that continuous measurements require batteries to operate continuously, which would cause changes on the battery operating state such as voltage, SOC (shown in Chapter 5) and temperature [24]. Those state changes would lead to impedance variation during a long-term measurement. To reduce the measurement duration, multi-frequency measurement approaches have been used. For example, in [44], a single perturbation was constructed by a fundamental component and nine odd harmonic components to the impedance measurement, in which a total number of ten corresponding responses can be obtained at the same time. The impedance spectrum in the citation can be partially constructed at the given frequencies.

Other examples are shown in [103, 108] where the multi-frequency method only replies on a few numbers of frequencies, such as Dotelli et al. employing five individual frequencies for low frequencies and another five components (including a fundamental frequency and four harmonics for high frequencies to investigate the effects of current ripple at low-frequency range and high-frequency range, respectively) [108]. In a word, the multi-frequency measurement method benefits from harmonic performances of a DC-DC converter in which several impedance responses can be fetched simultaneously at the specific frequencies (including a basic switching frequency and the numbers of harmonic frequencies). Typically, several frequencies of the harmonics are fixed at integer times the switching frequency of the converter, which are characterised at high frequency above 10 kHz. In fact, one of the challenges in the electrochemical impedance measurements by using the DC-DC converter consists in the difficult to cover the frequency range from around millihertz to kilohertz (a common frequency range of interest in this thesis ranges from 50 mHz to 2.0 kHz [1, 2, 13, 43, 94, 116–118], but some works can reach a maximum frequency of around 10 kHz [2, 13] or even 100 kHz [117]).

On the one hand, at lower frequencies of approximately 10 mHz, only a few studies reported their findings in [116, 119]. This is due to the negative effect of a long measurement duration, which would lead to battery states to vary significantly. On the other hand, the impedance spectrum performs within a much higher frequency range (more than 2.0 kHz), which would be an impossible mission for the online EIS measurements because the high-frequency impedance requires a much faster sampling rate to acquire high-frequency voltage and current signals. Apart from the previous concern for high frequencies, the higher frequency range should be comprehensively considered along with the switching frequency of the power converter and the filtering elements in the power circuit, which are requirements not easy to satisfy at higher frequency margin.

Starting from the review on the development of online EIS measurements

[2, 13, 40–43, 103, 107, 108, 113], the measurement cost has been decreased efficiently by using a switch-mode converter. A further reduction in the investment of the measurement method is achieved by reasonable lower-cost measurement devices, such as FPGA. Besides this, the online measurement time is shortened by the single multi-point injection in a single measurement. Despite their efforts to ensure that the properties of the measurement are cost-efficiency and with fast responses, there is still an implementation gap between experimental attempts and commercial requirements due to instrument size and user-friendly programming. In this case, relevant applications based on the EIS measurement, such as battery state monitoring (SOC and SOH) and degradation detection, cannot be used to further improve the accurate of the measurements in commercial products.

Overall, the challenges to develop an EIS measurement system for commercial implementations are manifold:

- The measurement instrument needs to be of low-cost and small size.
- The system is required to measure the relevant signal, support the controller for a switch-mode power converter and allow fast data transfer.
- The implementation of the system should be capable of being undertaken with low-level programming skills.

This work will present a modified method which allows EIS measurements to be done at a lower cost and with smaller size chip than commercial EIS instrumentations. A high-level block diagram of the proposed system is shown in Figure 2.12. In the proposed system architecture, a fully embedded solution for the converter control, signal acquisition and impedance calculation is depicted, entirely based on a low-cost off-the-shelf hardware system. The system highlights the multiple combinations to potentially commercialise online EIS measurement:

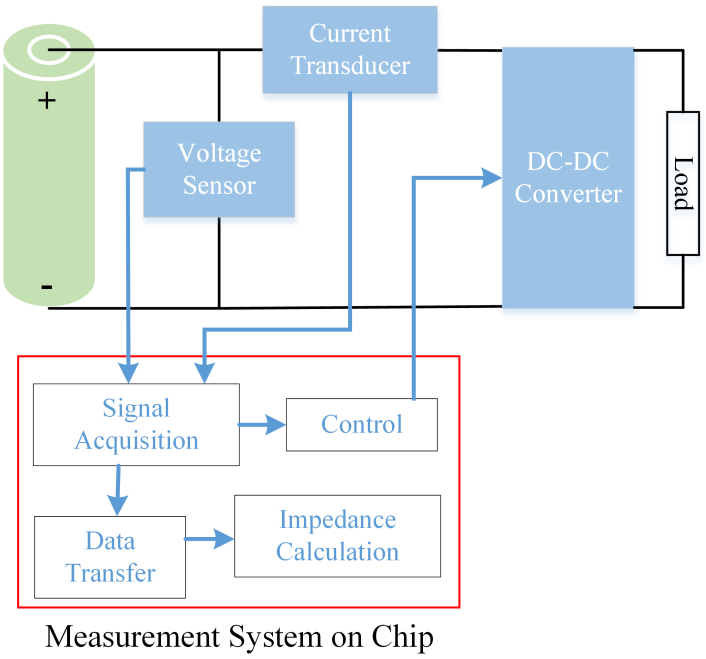

Figure 2.12: Proposed Online EIS Measurement System for Implementation

- Between real-time signal generation and acquisition;

- Between real-time signal acquisition and DC-DC converter control;

- Between real-time operation and non-real-time operation for data transfer.

Moreover, the system uses an innovative DC-DC converter control strategy and a control algorithm to assess the synchronised measurement at high frequencies. Finally, the system has the potential not only to allow high-speed SOC and SOH estimations based on the multi-frequency spectrum but also to diagnose the fault of battery operation depending on the variation of the battery impedances.

2.5 Chapter Summary

This chapter focuses on the material technique, state monitoring, modelling and impedance measurement developments of lithium-ion batteries. The estimation of the battery state of charge and state of health are critical aspects of battery monitoring systems. The most common state of charge and state of health estimation methods are reviewed, concentrating on the use of electrochemical impedance spectroscopy (EIS). The EIS is a non-invasive detection that tracks the battery internal dynamics based on the battery internal signal measurement, which can reflect battery state variations sensitively in the frequency domain. Lithium-ion battery models are reviewed in this chapter, which quantify internal dynamics in a memory-saving way. EIS measurement techniques are developed in the direction of the online measurement based on DC-DC power converters. Recent research developments in this area are reviewed and current limitations requiring further research are identified.

Chapter 3

Cost-Efficient Impedance Measurement System for Lithium-Ion Battery

In this chapter, a novel cost-efficient and small-size impedance measurement method is described. The method was evolved from one of the existing online impedance measurement approaches that uses a switch-mode DC-DC boost converter to generate AC perturbations required for the impedance measurement. A low-cost credit-card-sized device, BeagleBone Black (BBB), was creatively employed, which provides a combination between a general-purpose processor and programmable real-time units to which real and non-real time processes for impedance measurements can be integrated. In this way, the low cost and small size purpose of this work can be reached. In the proposed impedance measurement, an onboard analog-to-digital converter acquisition and a real-time switching controller were firstly put forward to acquire and generate AC signals at high frequencies (over 1 kHz). The measurement allows the synchronous behaviour between signal acquisition and switching control. Additionally, a

dynamic data transfer tube was created to combine real-time and non-real-time operation environments, and a time-saving domain transform algorithm was used to achieve a fast impedance calculation.

3.1 EIS Measurement Method Based on a DC-DC Boost Converter

Electrochemical impedance spectroscopy (EIS) is a popular method employed to characterise the impedance performance of a lithium-ion battery over a wide frequency range. Impedance characteristics show an accurate response to internal electrochemical dynamics in that frequency range. These dynamics can be applied to diagnose battery operations and predict battery states [2, 13, 31, 33–37]. Therefore, the developing technique of EIS measurement aims to move the diagnostic and predictive implementation from the laboratory to commercial and industrial applications, helping battery monitoring systems to reach a more accurate performance.

Notably, DC-DC converters are used in most battery applications. The reason behind the wide use is to regulate the output voltage to meet the load demand due to low voltage of the battery. In the past few years, EIS applications based on the power converter have been put forward by many researchers [1, 2, 13, 103, 107, 108, 113, 116, 117, 120]. Currently, affordable EIS measurement systems are being developing to improve the performances of the conventional BMS. With the same research proposal to seek a reliable solution to commercialise EIS measurement, the DC-DC boost converter is introduced.

AC excitations can be created automatically by a proper control (such as single sinusoidal-control method method that sets a sinusoidal reference for the

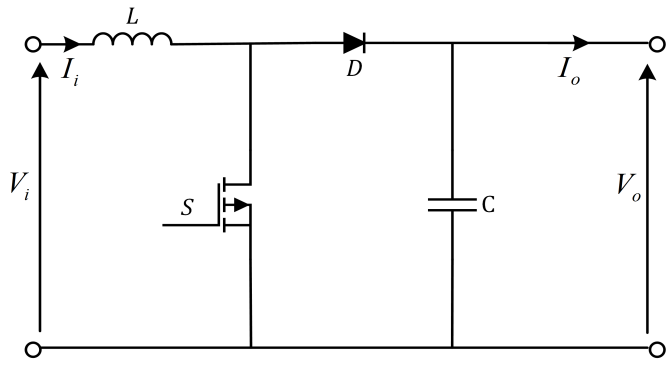

Figure 3.1: Basic Circuit Diagram of DC-DC Boost Power Converter

control system of the power converter, which will be discussed in the following section). As a benefit from generating AC perturbations, the signal generator can be replaced in the EIS measurement. Thus, the investment on the battery impedance measurement could be reduced.

3.1.1 DC-DC Boost Converter for Battery Voltage Step-up and Regulation

A switch-mode DC-DC boost converter is normally used with DC power sources, such as batteries. The advantage of employing DC-DC boost converter to the proposed measurement are not only to meet the research proposal under a cost-efficient condition but also to satisfy the requirement related to batteries driving loads on a higher voltage (than battery terminal voltage) with low energy transmission losses. Therefore, when a DC-DC boost converter contributes to the impedance measurement, a boosted voltage (compared with the original output voltage of the battery) can be obtained and then it can be used to drive a higher voltage (than the battery terminal voltage) load.

The basic circuit diagram of a traditional DC-DC boost converter is shown

in Figure 3.1. Four main electronic components are contained in the diagram. The semiconductor switch S is connected to an inductor L, and in parallel with the series connection of the free-wheeling diode D and the capacitor C. The outputs (in voltage and current) of converter have different characteristics due to the different switch states. Next, the output characteristics are introduced in two switch states: switch-on and switch-off.

When the switch (S) turns on, and the converter circuit acts as two parts, shown in Figure 3.2(a), the input current through the load is shortened. In this case, the voltage drop V_L, across the inductor, conducting the input current I_i, equals the input voltage V_i. Thus,

$$V_i = V_L = L\frac{dI_i}{dt} \tag{3.1}$$

Consequently, the current in the inductor increases linearly in time, and it is derived by the input voltage and the inductor's coefficient from (3.1).

$$\Delta I_i = \frac{V_i}{L} t_{on} \tag{3.2}$$

where t_{on} stands for the duration of the ON state of the switch.

As the status of switch changes to OFF state, displayed in Figure 3.2 (b), the input current decreases. If a resistor R is used as an active load, the current in the switch-off situation induces three voltage drops across the inductor, the diode D, and the load resistor. The voltage drop V_R through the resistor is identical to the output voltage V_o. Analysing the output current I_o in the switch-off condition is similar to analysing the input current under the switch-on condition. The output current decrement in the switch-off time is opposite to the input current rise during the switch-on duration. A typical ripple behaviour can be obtained since the output peak-to-peak current ripple ΔI_o has a linear relationship

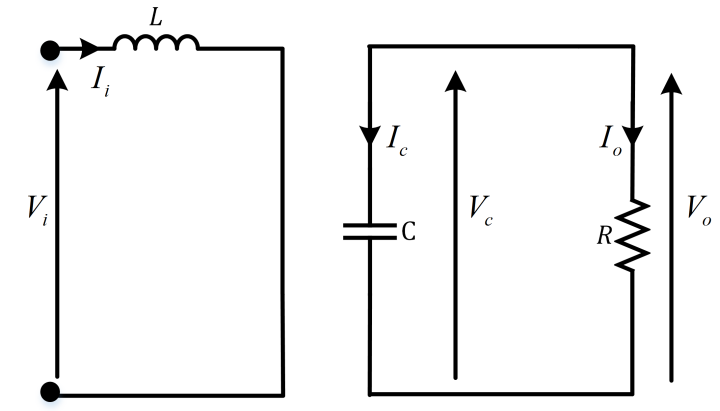

(a)

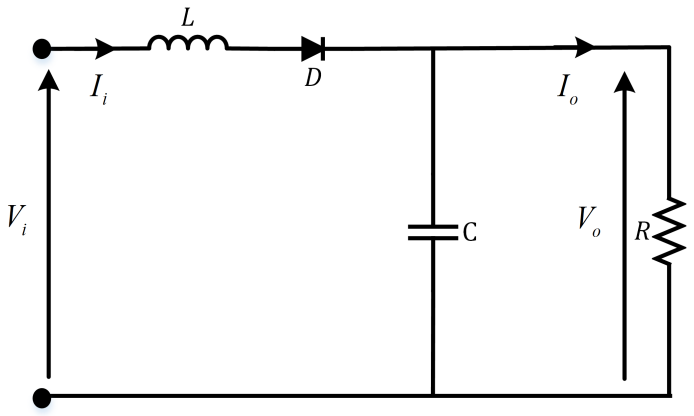

(b)

Figure 3.2: Two Statuses of Switch Operation in the Converter

(a) switch on and (b) switch off

with the switch-off duration (t_{off}). That relationship can be expressed with the input voltage, diode forward voltage stresses V_D, output voltage and inductance coefficient.

$$\Delta I_o = \frac{V_o + V_D - V_i}{L} t_{off} \tag{3.3}$$

During the steady-state operation, the mean input current is constant. Even though the slopes of the current during the switch-on and switch-off phases are different, the peaks and valleys of the current ripple are still maintained. Therefore, the derivative of the output voltage can be expressed by identifying the current increment in the switch-on time and decrement in the switch-off time:

$$V_o = \frac{V_i(t_{on} + t_{off})}{t_{off}} - V_D \tag{3.4}$$

Ideally, voltage drops across the diode (V_D) are simplified or even neglected when their values are negligible. As a result, the output voltage is merely determined by the time intervals (t_{on} and t_{off}):

$$V_o = \frac{V_i(t_{on} + t_{off})}{t_{off}} \tag{3.5}$$

Notably, the output voltage regulation is related to the input voltage and the duration of the switch state. If the input voltage is fixed during applications, the switch operating time can be used to control the output voltage. This digital control signal with a fixable period is popularly known as Pulse Width Modulation (PWM). PWM is the process of modifying the width of the pulse in a pulse train, in direct proportion to a small control signal. In particular, it tracks an average value of the converter's outputs [121], including current and voltage. In this case, a typical stage is needed to identify the width of pulse, the so-called the duty cycle d. In the derivation of (3.6), the duty cycle is used here to obtain the formula of

the output voltage:

$$V_o = \frac{V_i}{1-d} \tag{3.6}$$

where the duty cycle is modified as

$$d = \frac{t_{on}}{t_{on} + t_{off}} \tag{3.7}$$

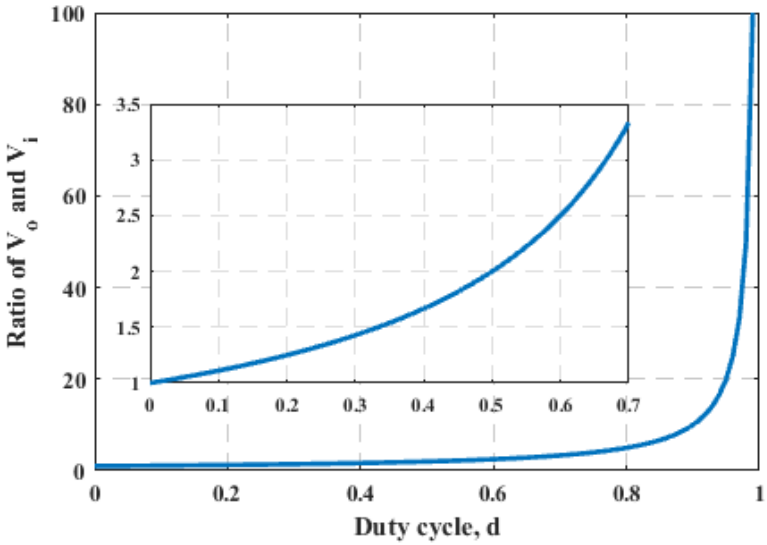

Figure 3.3: Amplification of Output Voltage of DC-DC Converter

When assuming that the power converter is only used to create the high voltage for the output (V_o), a variable duty-cycle (d) could be used to amplify the output voltage at different levels, as presented in Figure 3.3. The theoretical ratio of voltage amplification can span from 1.0 to infinity (the practical operating area of converter is shown by a sub-plot in Figure 3.3).

In steady-state conditions, the input current and output voltage of the converter contain a high frequency ripple at the switching frequency (of the converter), which is not sinusoidal (for example input current is triangular), and so it involves harmonic components. What matters here is that the frequency

content is at the switching frequency and above. Therefore, the filter elements are normally designed to eliminate those high frequency components (discussed in Section 4.2.2).

3.1.2 EIS Measurements for Lithium-ion Battery Based on the DC-DC Boost Converter

Several requirements for the developed measurement can be met by the implementation of the power converter, including size reduction of the measurement system and feasible voltage regulation for load profiles [13, 120]. EIS measurements demand AC excitations to perturb the normal operation of batteries (given that batteries are a DC power source). As mentioned earlier, AC voltage or current responses can be obtained from a properly controlled power converter. In this condition, received AC responses can be seen as perturbations for battery normal operations, so an additional AC signal generator is not required for battery EIS measurements. Consequently, instruments for impedance measurement demand a smaller space, which reduces the size of the whole measurement system.

In these years, a wide-use approach for the impedance measurement by controlling a DC-DC converter properly to create desired AC perturbations has been adopted [13, 107, 122].

However, the biggest challenge for converter-based EIS measurement is how to control the converter to create perturbations at various frequencies. Unlike the control implementation with a fixed reference (such as the DC voltage/current reference to keep output voltage/current constant), the proposed control of the measurement needs to combine measurable signals (of the battery) in real time, and then implement a proper modification to meet the AC voltage/current reference (for AC perturbations to keep output voltage/current periodic change).

The real time function is required to define frequencies for AC perturbations (discussed in Section 3.2.2).

In many related works, two control strategies, voltage-model control and current-model control, have been reported [13, 15, 107]. Those control strategies are developed from the basic control method on the duty cycle [13, 107]. The voltage-mode control mechanism is described in [13, 107], in which the output voltage is targeted and compared to the voltage reference for the control panel. After this comparison, the control algorithm can determine the corresponding value of the duty cycle for the switch operation.

Similarly, in the current-mode control strategy [15], the current in the measurement circuit is compared to a current reference while the duty cycle corresponds to the comparison and is given by the control algorithm.

A conventional design process for the control uses three steps. Firstly, clarify an individual control target; secondly, set a control reference for the target; finally, develop an appropriate control algorithm for the power converter. The control reference offers a sinusoidal waveform for the proposed measurement in response to the single-frequency measurement strategy. Sinusoidal excitations are created by a properly controlled power converter, as shown in Figure 3.4. It is possible to produce a waveform of which the average item varies sinusoidally for AC impedance measurement. In references [13, 107], the control voltage strategy was used to induce a perturbed voltage into impedance measurements.

Same papers [15, 113] have unveiled a current control strategy for the EIS measurement. For the current control, there is no need to concern about oversized currents taking place in the measurement, which efficiently avoids dangerous issues caused by a large current. As Jaber A. Abu reported [107], the duty cycle control was applied to the converter in order to create a corresponding

voltage at the given frequency. When the safe operation of the battery and current dependence are taken into account in the impedance measurement, the proposed method of work utilises current control in the real-time condition to obtain a characterised Ohm's response from the battery. The real-time control strategy for the converter aims to guarantee that AC perturbations are generated at the desired frequencies; in this way, the battery impedance can be obtained at given frequencies. How to choose a suitable control system depends on the research target of the EIS measurement. When considering a safe work condition for the battery and investigating a relationship between the discharge current and the SOC, discharge current control would be a better choice. If the DC values (including voltages, currents and duty cycle) are considered during the battery operation, the output elements (output voltage and current) are theoretically determined by the input elements (input voltage and current) and the duty cycle, as shown in (4.1).

During an EIS measurement, a small AC sinusoidal current (I_{i_AC}) is superimposed to the DC base (I_{i_DC}). Therefore, the value of mixed current should vary periodically between the maximum amplitude ($I_{i\_max} = I_{i\_DC} + A$) and minimum amplitude ($I_{i\_min} = I_{i\_DC} - A$). The frequency of variation is given by f_p, and the amplitude of the AC component A ($A > 0$), is presented in (3.9):

$$I_i = I_{i\_DC} + I_{i\_AC}(t) \tag{3.8}$$

$$I_{i\_AC}(t) = A\sin(2\pi f_p t) \tag{3.9}$$

Since such AC perturbations are injected to the discharge current, the battery can reflect those current variations in voltage due to the Ohm's response of the electrochemical system. In consequence, the terminal voltage of the battery is perturbed by a sinusoidal voltage component, as shown in Figure 3.4(b). Here, a linear performance is assumed for the electrochemical cell since a sufficiently

small change of the current is injected to the system. It is worth mentioning that the amplitudes of voltage responses only depend on the amplitude of current perturbations, which cannot be defined prior to the impedance measurements.

The proposed measurement has been introduced based on AC impedance techniques [13, 107, 113], as reported in Chapter 2. Figure 3.4(a) shows a diagram of the DC-DC boost power converter with the single-frequency AC impedance measurement approach. In this method, a sinusoidal current perturbation can be generated at a given frequency by the power converter. The DC current I_{batt_dc} is shown in the diagram since the battery is powering a resistive load profile.

When the measurement time approaches t_l, the current perturbation I_{ac} is superimposed to the DC current I_{batt_dc}, which triggers the voltage response in the battery power system. If a linear battery power system is assumed for the measurement, the amplitude of perturbed voltage (V_{ac}) has a proportional relationship with the amplitude of the injected current perturbation.

Moreover, a corresponding perturbed voltage (V_{batt_ac}) to the DC voltage base (V_{batt_dc}) during the measurement. Nevertheless, the voltage perturbation in response to the AC current injection can not be predicted. Here, V_{batt_ac} is used to represent the amplitude of the voltage response; from this, the voltage performance of the battery in the measurement system can be obtained according to (3.11).

Importantly, the amplitude of AC perturbation should be carefully considered in the measurement. Some papers [95, 108, 123, 124] have pointed out the adverse effects that AC perturbations may create on electrochemical devices. These undesired effects are an increase in the power losses and the possibility of damages, as well as decrease the durability. Although all hazard phenomena of batteries caused by the impacts have not been fully understood and there is not

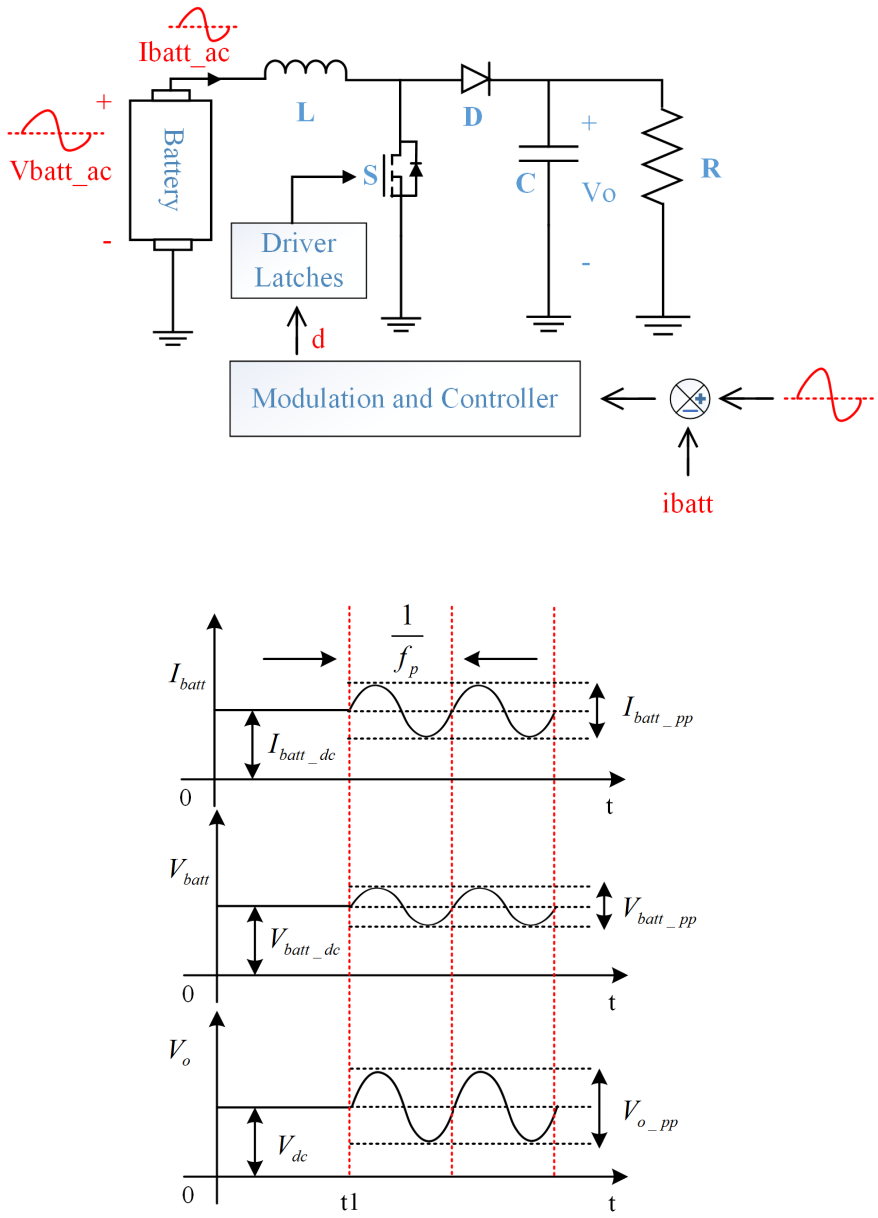

Figure 3.4: Illustration Diagram of Battery Impedance Measurement Methods

Single-perturbation-cycle closed-loop sinusoidal function online EIS measurement method employed in this thesis (top) and the corresponding waveforms of the battery voltage responses (bottom); The waveform of V_o is sinusoidal when the perturbation frequency is less than the filtering frequency (about 231 Hz) of the DC-DC converter.

an acceptable indication of the maximum allowed perturbation, a reasonable excitation amplitude that can be used around 10% peak-to-peak of the rated current [15, 125].

In equations (3.11) and (3.12), the symbols for battery voltage and current are V_{batt} and I_{batt}, respectively. All perturbed signals (voltage, current, and duty cycle) perform with the same excitation frequency f_p. By transforming the time-domain values of battery voltage and current to the frequency domain during some perturbation cycles, the magnitude of the battery AC impedance at the frequency f_p can be expressed as in (3.12). As a phase shift exists between the battery voltage and the battery current, the phase at the same frequency is given by (3.13), where φ_V is the phase of the battery voltage, while the battery current phase is denoted by φ_I:

$$I_{batt}(t) = I_{ac}\sin(2\pi f_p t + \varphi_I) + I_{batt\_dc} \tag{3.10}$$

$$V_{batt}(t) = V_{ac}\sin(2\pi f_p t + \varphi_V) + V_{batt\_dc} \tag{3.11}$$

$$|Z_{batt}(f_p)| = \frac{V_{ac}}{I_{ac}} \tag{3.12}$$

$$\angle Z_{batt}(f_p) = \varphi_V - \varphi_I \tag{3.13}$$

3.1.3 Control System for DC-DC Boost Converter

Closed-loop and Open-loop Control Systems

Using the online measurement method based on the power converter introduced previously, to achieve desirable AC perturbations during the measurement, the converter (included in the plant, as shown Figure 3.5) needs a proper control. In general, there are two classifications of control systems to be considered, called closed-loop control system and open-loop control system, shown in Figure 3.5.

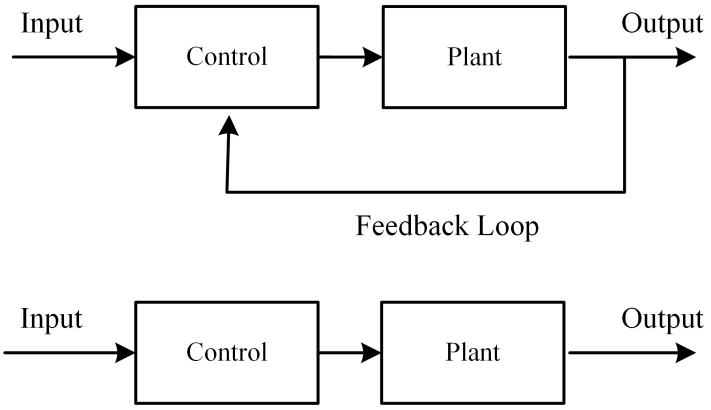

Figure 3.5: Closed-Loop (top) and Open-Loop (bottom) Controllers

Open-loop control systems, in which the output does not influence the input to the control process, have advantages such as simple construction, fast response and dramatic stability. They are popularly used in traffic lights and TV remote controls.

When considering most electrical or electronic control systems, those systems need to combine the control behaviour with the measurable signals or and the processed signals. So, in these systems, controls demand an accurate performance in order to reach the control purpose. One way that can be accurately used to control the process is by monitoring the system's output and feeding it back to compare it with the desired output. In this way, the control error can be reduced, and the system brings the output back to the expected level. The value of the output, which is measured and brought back to the system is called the feedback signal, and this control system is named the closed-loop control system.

With the feedback contribution, the main characteristics of the closed-loop control system consist in reducing control error, reforming stability of the unstable system, and producing reliable and repeatable performance. When compared with the open-loop control system, the closed-loop control system can be used for the proposed measurement in order to minimise the control errors and stabilise the

system. In Figure 3.5, the control object flows into the system. At the output terminal, the closed-loop control system can monitor the outputs directly and send them to the control system feedback loop. In the feedback loop, the control difference between the setting level and the output can be strictly quantified. When compared with the output performance within open-loop control systems, the output level of closed-loop control is mainly modified by the feedback process. Besides, unlike open-loop control without any output combination, closed-loop controllers modify the output performance for every single input, so the result of control performance can reach the proposed level effectively and accurately.

Closed-loop PI Controller

The boost DC-DC converter is always used to enhance the voltage outputs. This is because the output voltages can be controlled by the switch operation of the power converter. Additionally, in the proposed measurement, the power converter's switch responds to the control setting. The switch operates periodically in the measurements, and the switching frequency can reach megahertz. A fast-switching frequency can minimise the effect of ripples when the parameters of input voltage, inductance and duty cycle are fixed, as shown in (3.2). It should be noted that the switching frequency determines the upper limit of the frequency range for the AC perturbations, due to the fact that the AC perturbation frequency must be at least ten times lower than the switching frequency. Besides, the control performances, such as rise time and steady-state error, are closely associated with control strategy and algorithm. However, different control strategies have different algorithms to calculate the duty cycle for the power converter. As a result, to define a pseudo sinusoidal duty cycle for the measurement, choosing controller strategy is a top priority.

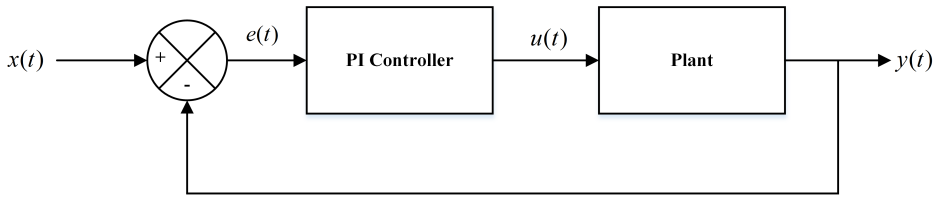

Figure 3.6: Continuous-Time Mode of PI Controller Schematic

Several controller categories have been included in industrial implementations, such as adaptive controller, and proportional-integral-differential (PID) controller. Adaptive controllers are able to deal with non-linear systems that strongly affect process disturbances and uncertainties [126]. PID controllers, are a more conventional control scheme, widely used in industries due to its straightforward implementation. During the EIS measurement, a PI controller was chosen for stability and ease of implementation.

The duty cycle is defined by a traditional linear PI controller in the measurement system. PI controllers are used as a fundamental closed-loop control technique in many applications, especially in electronic controls [127].

A PI controller structure in the continuous-time model contains two crucial parts that are proportional, as well as integral items. The PI controller is mainly concerned with the disparity between the measured process variable ($y(t)$) and the setting point ($x(t)$), which is involved in both items, as shown in Figure 3.6. Therefore, an expression for the controller's time-variant error can be obtained:

$$e(t) = x(t) - y(t) \tag{3.14}$$

Hence, the corresponding PI controller representation is

$$\mu(t) = k_p e(t) + k_i \int e(t)dt \tag{3.15}$$

where $\mu(t)$ is the output of the controller and $\int e(t)dt$ represents a discrepancy on the present error (it also is an accumulation of the past error).

In a traditional continuous-time mode of a PI controller, the error is determined without any interruption. Conversely, in the discrete-time controller model, measured variables are acquired with a constant time resolution. In this case, the difference between the reference and measurement will be updated with the same time resolution. Thus, the discrete-time controller mode is more suitable than the continuous time used for the proposed measurement due to sampling signals.

The impedance definition (3.12) shows a relationship with current and voltage signals. In the signal classification, current and voltage signals are a kind of analog signals. To obtain these during the measurement, they need to be converted into digital signals. In this case, the system can use them to calculate the battery impedance.

In practice, an analog-to-digital converter (ADC) is needed to convert analog signals to digital ones, in agreement with the requirement of the impedance identification. Depending on the discrete-time behaviour of the ADC, all measured values for the controller are firstly sampled with a configured time resolution before they are injected into the control system. The transition of the PI controller from the continuous-time model to the discrete-time model entails a proportional operation denoted by the discrete expression $e(n)$ in (3.16). For the integral item, it changes to a discrete summation (I_{err}), as presented in (3.17):

$$e(n) = x(n) - y'(n) \tag{3.16}$$

$$I_{err} = \sum_{k=1}^{n} e(k) \tag{3.17}$$

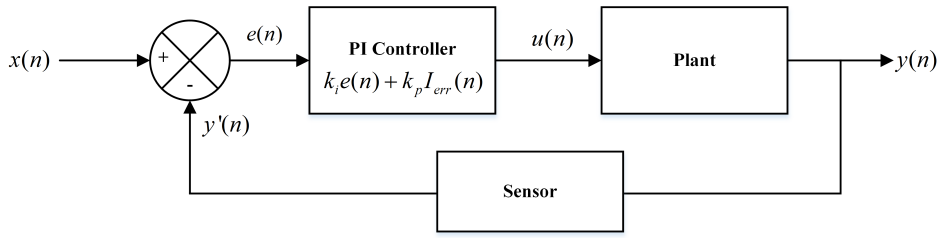

Figure 3.7: Conventional Discrete-Time System Digram with PI Digital Controller

where $y'(n)$ is the output of the sensor. From Figure 3.6, measurable variables and the setting value in continuous-time mode are converted to the discrete-time format. These are shown as $y(n)$ and $x(n)$ in Figure 3.7. Here, n equals the multiplication of the sample number k. It should be noted that measurable signals would require sensors to acquire their values, so a sensor mode is embedded in the digital control diagram.

When considering the PI controller algorithm, two adjusted gains for the proportion and the integration influence the controller. These gains pertain to the controller activities particularly to the transient response, the rise time, the setting time steady-state error and the overshoot. For more details, the gain effects of PI controller on the controller behaviour are discussed in Section 4.2.1 along with an explicit model (where battery, converter and PI control are included).

3.1.4 Requirements of Battery Impedance Measurement

A proper battery impedance measurement system requires several conditions to fully meet the measurement purposes, including a frequency range from millihertz to kilohertz and a proper operating frequency for the PI controller. Initially, to satisfy the measurement ranges of battery impedance, covering from millihertz to kilohertz, the switching frequency of the power converter must be much larger (around ten times) than the maximum measurement frequency of the battery

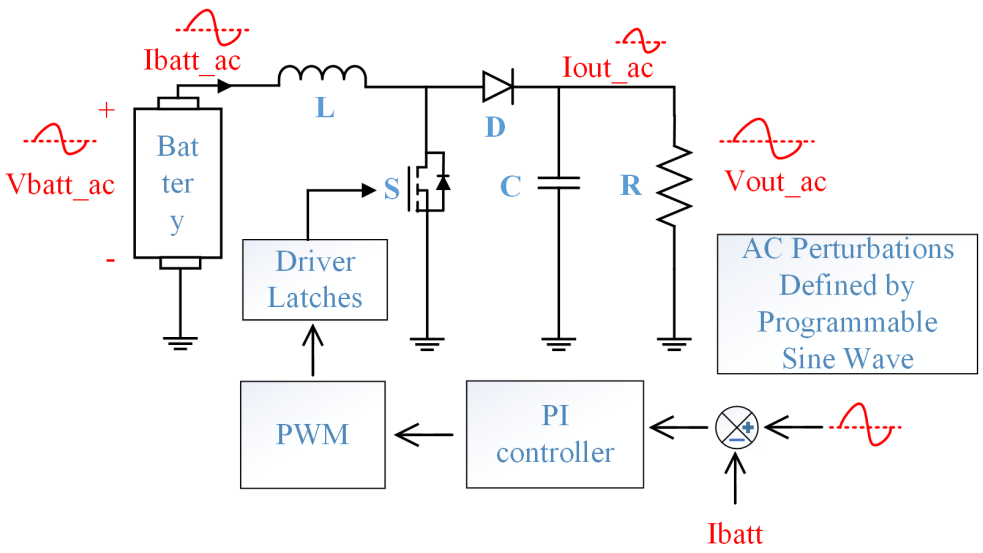

Figure 3.8: The Proposed EIS Measurement System Based on DC-DC Boost Converter

impedance. For example, 100 ksps set to measure the impedance at the frequency of 10kHz [13]. Under this condition, current ripples can be distinguished at perturbed frequencies and harmonic frequencies. Thus, a wide frequency gap between perturbation frequency and the switching frequency would be obtained under this condition, which makes the design regarding the cut-off frequency of the low-pass filter easier (shown in Section 4.2.2). Next, PI controllers involve both features of the P controller and the I controller, which can be used to the measurement system to control the proposed signal efficiently and precisely. The control needs to operate with a specific frequency, which performs synchronously with the switching frequency.

Traditionally, the PI control is programmed in a microprocessor. In the proposed PI control system, as shown in Figure 3.8, the defined duty cycle (d) should be passed to the switch without any data loss. It requires that signal acquisition and control operation are synchronous, which means that the operating frequencies of controller, PI algorithm and signal acquisition must

be identical. The same operating frequency phenomena is well known as a synchronous operation. To meet the synchronous requirement, hardware devices should have the ability to provide a compatible operating environment, in which the PI algorithm, controller and signal acquisition can work at the same time, as well as allowing the work duration to be accounted.

The operating time of the PI control is used to verify the control frequency. A short execution time of the instruction guarantees a fast control frequency. In particular, if there is a restrictive time consideration for executing a single instruction, it should introduce the real-time processing firstly. Real-time processing features a fixed time for every single instruction occurring in a specific unit. The execution time for instruction relies on the performance of the unit; a shorter execution time represents a faster speed of the unit. Accordingly, the proposed measurement is able to employ a real-time function to force a precise operation time for the control. Therefore, the operating time of PI control can be configured accurately.

Finally, the measurement needs multiple-channel and fast ADC to acquire several analog signals simultaneously. As previously discussed on the synchronisation, the frequency of updating duty cycle of the PWM signal is the same as the switching frequency, updating duty cycle once every switching period. Notably, the definition of duty cycle is based on control inputs and settings, as given by (3.18). Based on this constant time resolution, the sampling frequency of the ADC can be determined. In particular, the ADC sampling rate will be set identically to the control and switching frequencies, in agreement with [13]. In the control platform, the ADC sends the acquired data to duty cycle determination. The updating duty cycle has been configured similarly with the switching frequency in order to ensure that all data used in the calculation. When considering the requirement for ADC on the acquiring data frequency for the same measurement purpose, the sampling rate should be set at the synchronised frequency. In

summary, the requirements for the proposed synchronised measurement are next listed:

1. A high switching frequency (over10 kHz) for the DC-DC power boost converter and the control system, at least ten times larger than the excitation frequency of the AC perturbations.
2. A clear and fixed control frequency that can be identified within a real-time operation by a specific unit.
3. A fast sampling rate ADC, which can meet the frequency of the switch and control system.

3.2 Real-time Measurement System for Battery Impedance

The real-time operating condition is considered in the measurement system to capture current perturbations at specific frequencies, as shown in Figure 3.9. Real-time systems impose a hard restriction on the response time to one or more events. In a conventional real-time system, systematic events always consist in the arrival of new inputs or in the requirement that new outputs have to be generated; new inputs in the time-constrained system are captured periodically. For instance, in the system of perturbed signal injection with the DC-DC boost converter, AC perturbations would be pre-sampled by the number of samples. Then, their amplitudes in mathematical representation are calculated. On the other hand, their frequencies correspond to the period T, which depends on the frequency of the real-time system. In the proposed battery impedance measurement system, the desirable frequency of the perturbed signal is defined by the operating system period under a real-time condition.

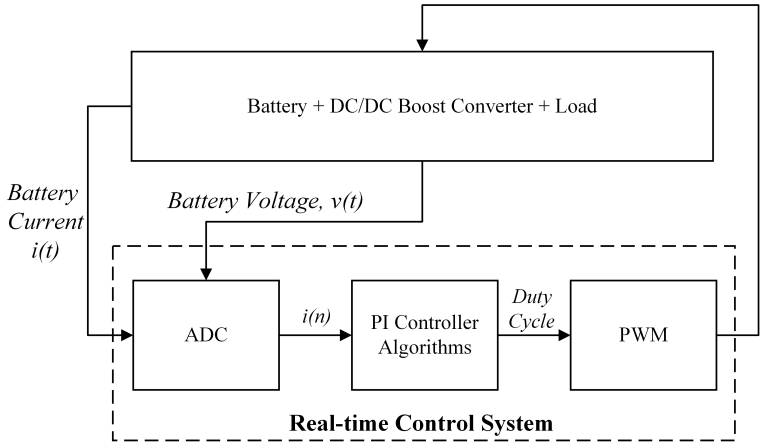

Figure 3.9: Overall Diagram of the Proposed Measurement and Control System Architecture

3.2.1 Analog-to-Digital Conversion

In order to monitor signals in the proposed impedance measurement system, continuous-time voltage and current are converted into digital signals. The process of converting analog signals to digital ones is called analog-to-digital conversion and is usually performed by an analog-to-digital converter (ADC), as shown in Figure 3.10.

Digital information differs from its continuous counterpart in two critical aspects: sampling and quantisation. Sampling is the digitisation in time and quantisation digitalises the amplitude. If sampling and quantisation are represented by the x-y axes, they generate different polarisations (the horizontal pole normally denotes time and the vertical pole usually represents the amplitude, which affect the information that the input signal delivers, such as signal real-time acquisition speed and amplitude. A more detailed discussion of sampling and quantisation will now follow.

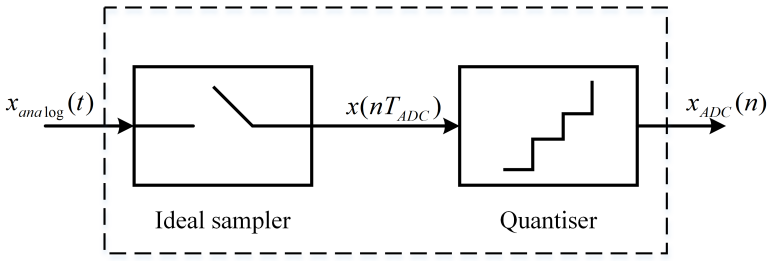

Figure 3.10: Block Diagram of ADC

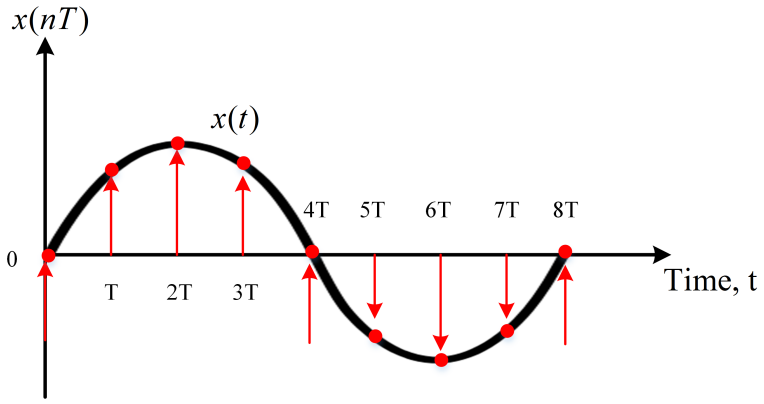

Figure 3.11: Example of Analog Signal and Discrete-time Signal $x(nT_{ADC})$

Sampling

In the illustration, the analog signal $x_{anaolg}(t)$ first passes through a sampler and quantiser in sequence; then, the signal is converted to the digital signal $x_{ADC}(n)$. During the process of sampling, the amplitude $(y-axis)$ of the analog signal is presented with a sequence of values, but in time scale $(x-axis)$, several samples are fetched with an identical time interval (T_{ADC}).

When those samples are used to restructure the analog signal, the reconstruction of an analog signal is discrete in the time region. For example, an analog sinusoidal signal is sampled with an 8-point sampling, resulting from a restoration of the signal shown by red dots in Figure 3.11.

The intermediate signal is a discrete-time one with a continuous value

at the discrete-time nT_{ADC}, $n = 0, 1, 2 \ldots 7$. In the mathematical definition of the sampling frequency, an ideal sampler can be considered as a switch that periodically opens and closes every T_{ADC} seconds. The sampling period is defined as

$$T_{ADC} = \frac{1}{f_s} \tag{3.18}$$

where f_s is the sampling rate (or sampling frequency) in hertz (or cycles per second).

The sampling frequency has a significant impact on the reconstruction of analog signals. When an unsuitable sampling rate is set to ADC, the digitalised signal cannot recover the analog signal. The result of the mismatched situation is essentially caused by the sampling frequency, called aliasing. Therefore, in practice, to represent an analog signal $x_{analog}(t)$ by a discrete-time signal $x(nT_{ADC})$ accurately, two conditions must be satisfied:

1. The analog signal, $x_{analog}(t)$, must be limited by the bandwidth of the signal f.

2. The sampling frequency, f_s, ought to be at least twice the maximum of the frequency component in the analog signal f, that is

$$f_s > 2f \tag{3.19}$$

This is Shannon's sampling theorem and is normally deployed to acquire signals in the real word at a higher-level (the sampling rate is slightly larger than two times of the maximum frequency of the targeted signal). For example, in the proposed measurement, AC signals will vary in the frequency range from millihertz to kilohertz; that means that the sampling rate should be just above than twice of the kilohertz. Under this consideration, approximately a hundred

thousand samples per second are desired, which cannot lead to an aliasing problem for signal acquisition.

It should be noted that switching frequency components will be filtered in the proposed measurement so there is no need to set the sampling rate to meet the sampling theorem in order to sample switching frequency components.

In the proposed measurement, multiple signals of the battery (including voltage, current, and temperature signals) should be sampled by the ADC. There are two possible sampling options for multi-channel ADCs: simultaneous sampling can be achieved with a separate ADC for each channel; alternatively, the use of a multiplexer allows using an ADC (which is cheaper), but introduce time delay between active channels. Nevertheless, the time delay would result in an apparent phase shift between the measurable signals of the battery, which has a negative effect on the measurement accuracy and will be discussed later.

Quantisation and Encoding

The quantisation is the second stage of signal processing shown in Figure 3.10, which aims to represent the amplitudes of quantised signals corresponding to stair-stepped digitalisation. If the discrete-time signal $x(nT_{ADC})$, as depicted in Figure 3.13, is considered to have an infinite number of bits, the quantified amplitudes of the signal will correspond exactly to original values of continuous-time signals.

Nevertheless, in real DSP applications, the quantisation is always driven by a finite number of bits to represent the discrete-time signal as a binary number. This process of exhibiting binary numbers is called quantisation and encoding. Figure 3.12 displays an example with the 4-level quantisation of unipolar ADC. Six samples are acquired periodically, and the corresponding signal amplitudes in

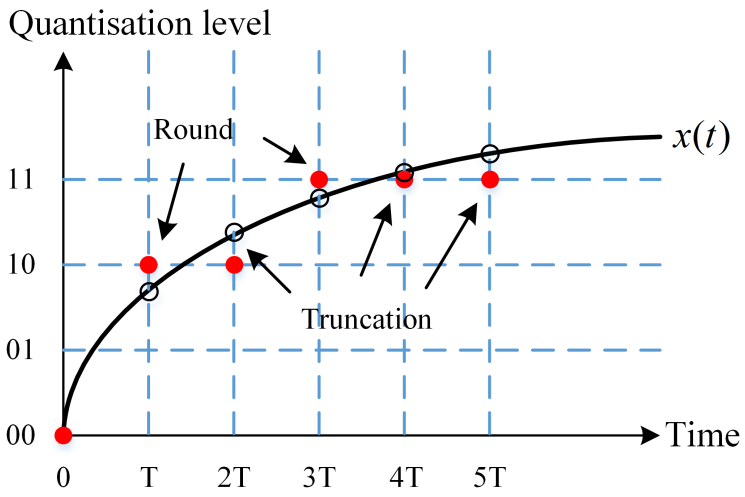

Figure 3.12: Digital Samples by Using 2-bit Quantizer

Symbol 'o' stands for discrete-time value $x_{ADC}(n)$ and the quantified value is marked by red filled cycle.

the same numbers are quantified. Between consecutive quantisation levels, the spacing is named the quantisation width, step or resolution.

When compared with the discrete-time value $x(nT_{ADC})$, represented by the symbol 'o', the digital signal marked by the red filled circle has the observed difference on signal quantisation. The difference of quantisation results is called the quantisation error. Conventionally, there are two different types of quantisation errors, called round and truncation, both shown in the illustration. Round happens if $x_{ADC}(n)$ is replaced by the value of the nearest quantisation level and truncation occurs when the smaller value of the level is used to quantify $x_{ADC}(n)$.

If an average value is located between two close quantisation levels, the value of the signal exceeding the mean value is assigned to the higher quantisation level; on the other hand, the signal value that does not exceed the value is allocated to a lower quantisation level. Therefore, the maximum varying range can be

obtained and can be derived from the quantisation resolution (Δ) as:

$$|e_q(n)| \leqslant \frac{\Delta}{2} \tag{3.20}$$

where $e_q(n)$ denotes the quantisation error.

It is worth noting that the quantiser is uniform in the spacing between quantisation levels. The resolution of a quantiser is identified by the ratio of full-scale (FS) range and the number of levels 2^B, where B denotes the weight of a particular bit of ADC. The resolution can be expressed in terms of $2^B - 1$ (because the quantisation levels vary from 0 to $2^B - 1$):

$$\Delta = \frac{FS}{2^B - 1} \tag{3.21}$$

Recalling that the quantisation error aims to consider the noise performance of ADC's output, the quantisation error is a discrepancy between the quantised value and the real value of the analog signal. Specifically, tt appears in ADC outputs as noise and thus, is also called quantisation noise. The quantisation noise is assumed to be a random variable that is uniformly distributed. When a B-bit ADC is used, the signal-to-quantisation-ratio (SQNR) as the signal quality indicator is approximated by

$$SQNR \approx 6B \text{ dB} \tag{3.22}$$

The unit dB is the an abbreviation of decibel, which expresses the power ratio between variance of the domain signal and quantisation error. The bigger SQNR is, the higher quality of the signal is obtained. Accordingly, the quantisation error can be reduced in the signal conversion as ADC is implemented with a larger bit. For the effect of quantisation error, it would result in unavoidable measurement

differences in amplitude, and is better to discuss with experimental results, as well as seen in Chapter 6.

During the proposed measurement, it should note that the DC components of the measurable signals (of the battery) are much bigger than the AC components (less than 5% of the DC base is used for the AC amplitude configuration). This means that the AC targets will cover only a very small part of the ADC range. On the other hand, the relatively high sampling frequency and the cost constrains limit the maximum number of bits so a common choice of quantisation level of around 12-bit will be considered in this work, in agreement with the references [2, 107, 128].

3.2.2 Real-time Controller System

As mentioned before, the frequencies of AC perturbations injected to the measurement are defined by the real-time system. In a complete measurement system for battery impedance, the measurement circuit and the controller system are involved. Measurement circuits include a power source, a power converter and a load profile, as shown in Figure 3.9.

Normally, the power source and load file have a negligible effect on small time variations, while the time performance of the control system is necessarily considered for the converter's high-speed control. The control system includes three parts: ADC (signal acquisitions), PI controller scheme and PWM. The control process starts from reading ADC values, via operating PI controller computation and ends with the PWM behaviour. Therefore, the execution time of the real-time system should be accounted from data reading to the end of PWM.

In order to achieve an accurate time performance of the system, the

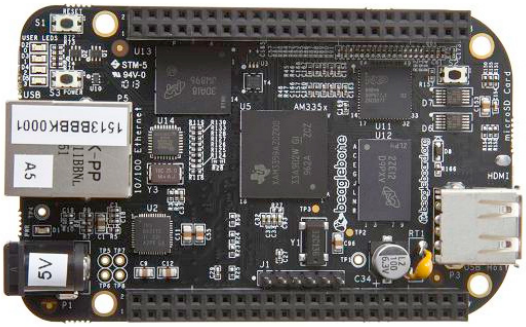

Figure 3.13: Photograph of BeagleBone Black

microprocessor must allow to account the system operating time. In this way, the operation period for the controller system can be obtained, so the period (or frequency) can be used to determine the flexible frequencies of AC perturbations.

3.3 Real-Time Measurement and Control System Developed by BeagleBone Black

BeagleBone Black (BBB) is a well-known open-source prototyping platform (shown in Figure 3.13), which is used as a central control unit for many embedded control implementations such as robotics and 3D printers. BBB is a low-cost (around £36) development single-board computer, which features portability due to its small size. When compared with other low-cost and low-power chips, such as Raspberry Pi and Arduino, BBB has high-frequency real-time processing. The real-time action of BBB is primarily required for the project while Raspberry Pi does not have a real-time function. Besides, analog signals cannot be directly measured by Raspberry Pi due to the lack of onboard ADC. When considering the implementation of Arduino, although it has a real-time processor, its real-time complex system performance is reduced by the processor specification. When

BBB is compared to some building high-performance devices, such as application-specific integrated circuits (ASICs), digital signal processors (DSPs) and field-programmable gate arrays (FPGAs), BBB does not demand a long duration to access its programming language. It is worth noting that BBB features its simpler ARM architecture and data communication, as well as its a more energy-efficient way that favours acceptable real-time activities to the battery impedance measurement under a lower power consumption and cost condition, when compared with the implementations of DSP and FPGA for the proposed measurement.

The particular advantage of the BBB for the proposed battery impedance measurement consists in that it favours desired real-time configurations within two existing "programmable real-time units" (PRUs). The on-board microprocessor AM335x is the core that includes PRUs and other subsystems, as shown in Figure 3.14. Before PRUs are called to reach a time-constrained measurement, the microprocessor should be introduced in advance. The AM355x processor is developed from the ARM Core-A8 core and widely used in image and graphics processing, as well as in industrial real-time interfaces. The processing ability of the processor can reach 1.0 GHz. Moreover, the processor is capable of working with high-level operation systems (HLOS). For example, Linux is an open-source OS available for free.

Figure 3.14 also provides more information on the subsystems of the AM335x processor [129], which will contribute to the measurement. For all the presented subsystems, PRU-ICSS is the most primary subsystem, which offers a time-critical condition where the execution time for introductions can be recorded.

The low-cost purpose of this work has introduced. One of the methods is deployed in which DC-DC boost converter creates AC perturbations to battery

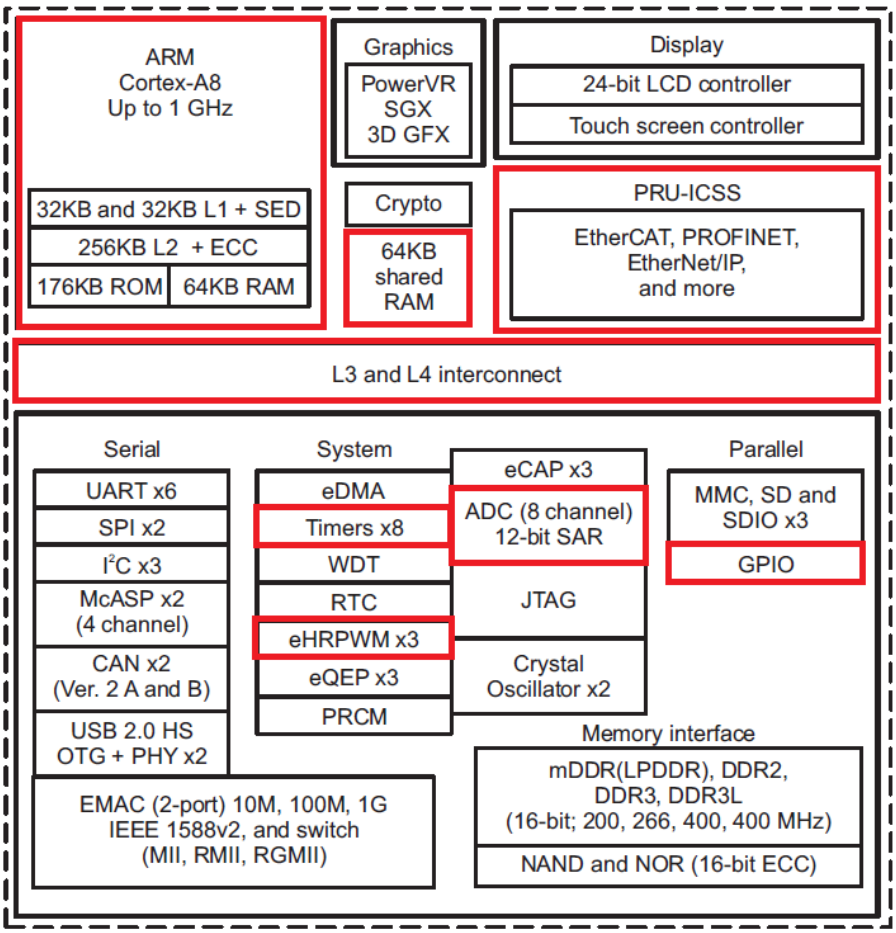

Figure 3.14: AM335x Functional Block Diagram

Red rectangles present the requirements of the proposed measurement on signal acquisitions, controller scheme and PWM.

operations. Another cost-effective enhanced approach focuses on the affordable device, named BeagleBone Black, which is used to acquire analog signals with ADC and generate PWM via embedded hardware PWM (eHRPWM or GPIO), as shown in Figure 3.14. Advantages of implementing BBB for the impedance measurement are:

1. Two decent PWM modes that can be invoked to control the converter's switch, up to 200 MHz;
2. Two individual real-time units that are assembled on the board and embedded within PRU-ICSS, with a real-time processing frequency of up to 200 MHz (5 nanoseconds);
3. The overall sampling rate of the on-board ADC is 200 ksps and the ADC channels are multiplexer.

In particular, all real-time functions, including ADC signal acquisition, the PI algorithm and PWM, would be contained by the PRU-ICSS environment in terms of measuring execution time of functions. In this case, the requirement regarding the frequency of the control system can be defined. The following section will focus on BBB's typical architecture used to deliver the root of EIS measurement system based on the real-time performance.

3.3.1 The PRU-ICSS Architecture

The programmable real-time unit and industrial communication subsystem (PRU-ICSS) on the AM335x processor contains two 32-bit 200MHz RISC (Reduced Instruction Set Computer) cores, where the instruction set architecture (ISA) allows them to use few cycles per instruction, which can be used as the real-time indicator. PRUs' individual memories are allocated separately from the

core processor. Importantly, the specific performance of the PRU is allowing independent operation and clocking for decent efficiency and flexibility. The time interval in PRUs is constrained to 5 nanoseconds per cycle, meaning that a flexible time-critical platform can be established and capture a theoretical frequency of up to 200 MHz. Additional peripheral interfaces and real-time protocols are capable of being implemented with PRUs.

The PRU-ICSS architecture also allows data transfer, which would contribute to the impedance calculation for the on-line impedance measurement. In the PRU-ICSS functional block diagram outlined in Figure 3.15 [130], two independent 32-bit RISC PRU cores (PRU0 and PRU1) are involved. Each of them are connected to 8 KB of program memory and 8 KB of data memory. The program memory mainly stores instructions that are required to be executed in the PRU, while the data memory is primarily used to save temporary data that is obtained from data arrays, indicators, etc. For data storage in the PRU, there are two data memories: Data RAM0 and Data RAM1, contributing to PRU0 and PRU1, respectively. However, there is a drawback of having separated data memory for the PRU; data stored in different PRUs cannot be transferred mutually. Therefore, only a single PRU would be used to save experimental data in real-time operation. For data saved in ARM, a 12 KB general-purpose shared RAM is activated to resolve the data transfer between PRU and ARM, as shown in Figure 3.15. The shared RAM is employed as a communication bridge between PRU and ARM core (Host), which can offer significant support for measurement applications in non-real-time operation, such as battery impedance determination and state estimation.

Essential developments for the proposed measurement occur in real-time conditions. PRUs are primary time restrictive chips, and the way to invoke them to count the measurement program duration is discussed below.

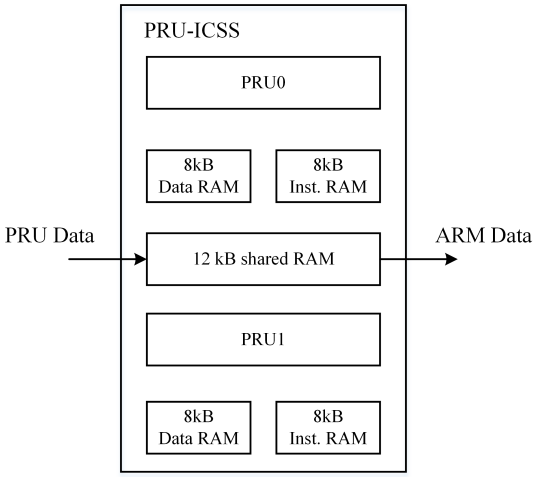

Figure 3.15: PRU-ICSS Functional Block Diagram

3.3.2 Programmable Real-time Units Activations

The real-time measurement system for battery impedance operates via BBB's host processor (ARM) creating an appropriate executive event to wake up the PRU and then let the PRU work following the memory-storage instruction. How to activate and execute the program for PRU is shown in Figure 3.16. Generally, BBB enables on-board functions and Input/Output pins for all applications via device tree overlays. Therefore, a customer device tree overlay presented in the illustration is initially active.

Real-time applications require ARM to manage PRU's operation; thus, there are two code files (for single PRU implementation) allocated to ARM and PRU, named host code file and PRU code file. The host code file is normally written in a high-level programming language, such as the C language. This file contains a primary program to invoke the PRU and allows it to operate the instructions that are written in the PRU code file. Next, once the host program (.c) and the binary PRU program (.p) are created, they can be compiled or assembled in the core processor (ARM). The compiling and assembly actions aim to translate the programming language into instructions that BBB can use.

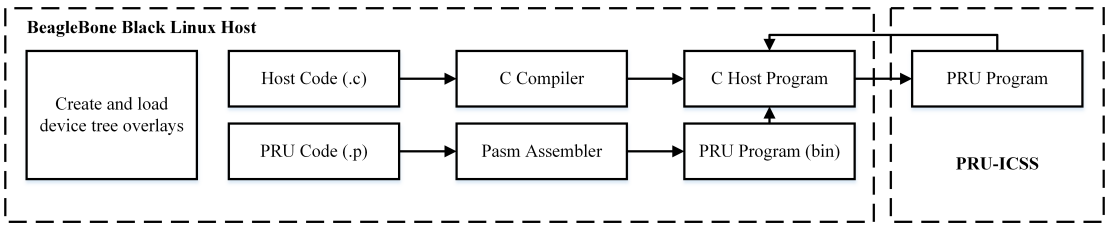

Figure 3.16: Summary of Steps Involved in Deploying PRU-ICSS Program

Afterwards, the compiled PRU programme in binary format can be loaded to the C host program and passed to the PRU-ICSS. During this process, the host program acts as the communications bridge between the PRU and the ARM within Linux OS. For further applications on the data transfer between PRU and the host core, the communication bridge is improved significantly. For more details regarding the data transfer technique, these will be introduced in Section 3.5.

3.3.3 Time Counter of PRUs

Regarding the time-critical implementation, time counters of PRUs are traditionally used to count the execution time of the system. PRUs have several counters, such as clock cycle counter, microsecond counter, millisecond counter and so on. Among these counters, the clock cycle counter is a straightforward counter (also a minimum counter in time scale) to deploy. The PRU's clock cycle counter is a 32-bit time indicator, which merely shows the number of clock cycles since the operation approaches counter instruction. It should be mentioned that the clock cycle counter does not work to drive an infinite number of clock cycles because the counter cannot be wrapped automatically. The threshold time is around 20 seconds since the maximum number n of clock cycles used in the PRU (5 ns per clock cycle) is $2^{32}-1$, as shown in Figure 3.18. When the counter reaches the threshold, it stops immediately. However, for the proposed impedance measurement system

for lithium-ion batteries, the power converter requires a fast-switching frequency to reduce ripple effects; in general, the value of the switching frequency is not less than 10 kHz (100 microseconds). Since the system operating time is much shorter than 20 seconds, then the PRU cycle counter can sufficiently meet the requirement related to the recoding system executive time. If a high-level cycle is needed in PRUs, an optimised method with the Industrial Ethernet Peripheral (IEP) can be implemented to wrap a large number of clocks automatically [131].

Particularly, the frequency (f_p) of an AC perturbation has a close relationship with the real-time system operating frequency (f_{system}). The switching frequency synchronises with the control system frequency, which is much larger than the perturbation frequency (f_p). The system should spend time to match the perturbation period. In practice, the frequency ratio method is employed to obtain AC perturbations at different frequencies.

Analytically, the time interval t_{system} between two cycles of the system is $1/f_{system}$ seconds. When a fixed number (N) of samples are contained by the perturbation, all samples read by the real-time system will require N/f_{system} seconds. As an assumption, the value of the fundamental frequency f_p equals f_{system}/N Hz; this means that once a single period of perturbations includes N samples, the period of N/f_{system} seconds can be fetched. If the N-sample system is repeated K times, the period duration of the perturbation is extended K times. Consequently, a new frequency is created for the perturbation with value $(1/K) \times (N/f_{system})$. In this case, feasible frequencies for the N-sample perturbations are given by f_p/K Hz, where k takes the values 1, 2, 3 and so on. The maximum frequency for the AC perturbation in this case is f_{system}/N Hz, but there is no limitation for the minimum frequency due to a wrapped clock cycle implementation to measure the operating time in the PRU.

3.3.4 Real-Time Control Functions in the PRU

The real-time control-relative functions have been discussed previously, which consist of ADC signal acquisition, PI control algorithm and PWM. These functions require an accurate operating time record in terms of the measurement system working with a single frequency under real-time condition. The execution time in the PRU is recorded by the number of clock cycles. As discussed about the real-time controller, the proposed controller must run within certain execution time in order to define values of the frequencies for AC perturbations.

Figure 3.17 illustrates the real-time controller established by a single PRU. The PRU has the behaviour of a fixed execution time for a single instruction. Typically, a single instruction of PRU only uses a single clock cycle of 5 nanoseconds (in Hertz, 200 MHz) for execution. In the illustration, three functions contained by the real-time system are considered. The ADC execution time (t_1) includes the ADC acquiring individual data from the measurement circuit and passing the data to the data array (shown in Section 3.5). In the second time period (t_2), the duty cycle for PWM is calculated. The last quantity (t_3) denotes the period of the PWM.

A simple relationship between the function operating time ($t_{operation}$) and PRU's clock cycle (n_{cycle}) in nanoseconds is

$$t_{operation} = 5n_{cycle} \tag{3.23}$$

Thus, the frequency of the measurement system can be defined by the total execution time.

$$f_{system} = \frac{1}{t_1 + t_2 + t_3} \tag{3.24}$$

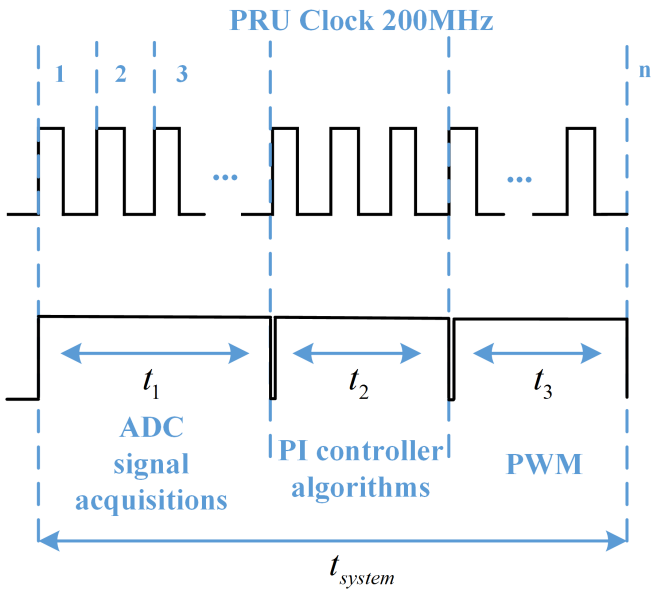

Figure 3.17: Real-time Functions Operating in Series

Even though the frequency of the measurement system can be obtained from (3.26), it cannot guarantee a synchronous frequency for all real-time functions (ADC signal acquisitions, PI controller algorithms, and PWM). This is because the execution time of the functions are independent and sequent; as a result, it is impossible to obtain an identical operating time between the system (t_{system}) and PWM (t_3): $t_{system} = t_3$, as shown in Figure 3.18. In more detail, if the operating durations of ADC and PI algorithm are constant, the total execution time ($t_1 + t_2$) of ADC and PI algorithm is therefore fixed. When an additional execution time (of PWM, not equal zero but also fixed) is added to the system, it means the previous fixed time (of ADC and PI algorithm, $t_1 + t_2$) would be extended, resulting equal to $t_1 + t_2 + t_3$. In this situation, the frequency of the system becomes much slower than the frequency of PWM. Unfortunately, the synchronous frequency cannot be achieved.

How to tackle execution time for obtaining a synchronous performance among real-time functions is the second challenge in this work. As previously discussed on the time allocation for real-time functions, a possible solution is to

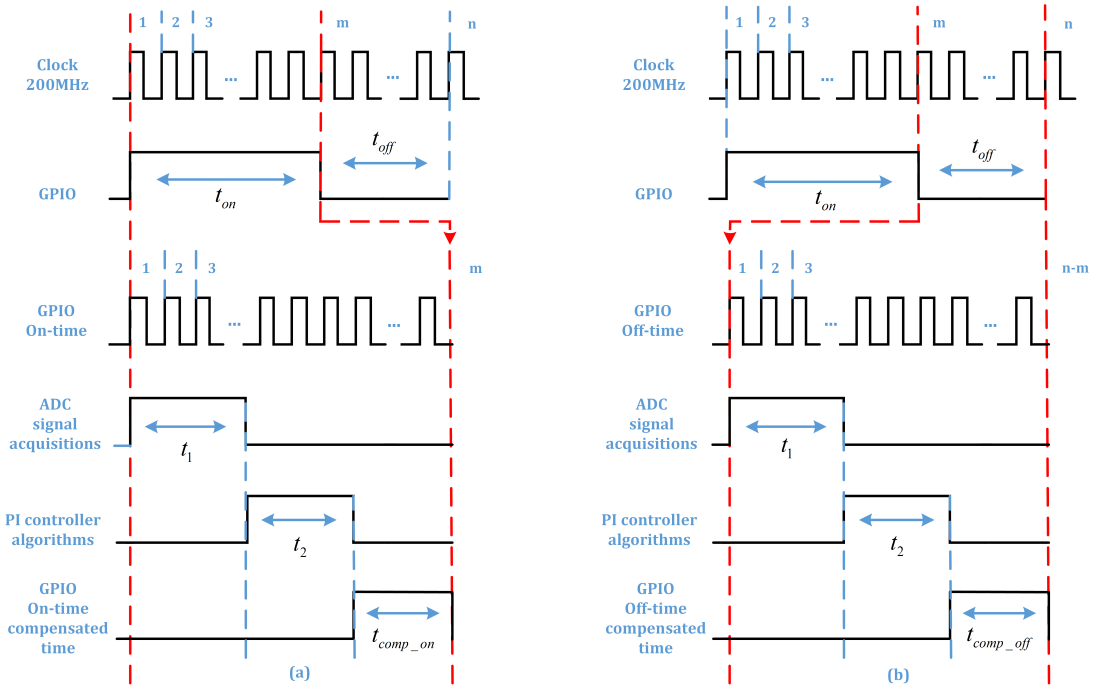

Figure 3.18: Illustration of Two Optional Time Overlaps for Real-Time Functions

(a) The execution time of ADC and PI controller algorithm overlap with the on-time region of GPIO; (b) The operating period of ADC and PI controller algorithm is covered in the off-time region of GPIO.

use a functional management to put one of the execution durations into the other ones. This means that two of the real-time functions (ADC signal acquisitions and PI algorithm) operate in series and the PWM function would work entirely or partially in parallel with the ADC acquisitions and the PI algorithm. Fortunately, a flexible PWM mode, named software mode (GPIO), can be developed with the BBB, which allows the execution of each real-time function in parallel in the time domain.

Based on this method, the execution time of the PWM imposes a parallel performance with the ADC and PI control functions, as shown in Figure 3.18. There are two reasons to employ a parallel execution. On the one hand, PWM activities involve ON and OFF states, which have time gaps between

states; this provides a chance to insert functions in order to share the operating time simultaneously. On the other hand, the software mode completes PWM performance through GPIO techniques, which indicates that a single digital pin can operate in the ON (high-voltage output) and OFF (low-voltage output) states with a timer periodically and flexibly. During the ON or OFF state, the ADC acquisition and control algorithm can be allowed to operate with ON (or OFF) state at the same time. On the BBB, the hardware PWM model is included by the enhanced high-resolution pulse-width modulator (EHRPWM), and seven individual EHRPWMs in total can be exploited. The modulator is programmed by a single function, which cannot provide independent ON state (or OFF state) to contain the ADC and PI algorithm functions. According to above explanations, the time "contained" method is put forward, which can be used to handle the functions of the ADC and PI algorithms operating with PWM in parallel.

The time-contained method is employed, depending on the flexibility of the software PWM mode. The software PWM mode drives a general-purpose input/output (GPIO) pin, which is activated periodically at two states on output voltages of 3.3 V and 0 V. A single GPIO pin is configured in the software mode, which performs with a fast nanosecond-level I/O in the PRUs. It should be mentioned that the activated GPIO output varies periodically at either the high output (3.3 V) or the low output (0 V). In this case, the GPIO outputs present a similar performance with the traditional PWM (regarding high and low behaviours). Additionally, using PRU clock cycles to set the time allocation for ON state (t_{on}) and OFF state (t_{off}) in the software, PWM is the same configuration as the setup of the duty cycle in the traditional PWM. Using the time-contained method, a flexible execution time of the PWM can be used in the

programme:

$$t_{total} = t_{on} + t_{off} \tag{3.25}$$

$$f_{system} = \frac{1}{t_{on} + t_{off}} \tag{3.26}$$

$$t_{total} = \frac{1}{f_{system}} \tag{3.27}$$

where the period of the system being t_{total} and the frequency of the system f_{system}.

Next, to implement the PWM execution time overwrite ADC and that PI algorithm operating times, two strategies regarding time ranges are considered due to the duty cycle: on-time range and off-time range.

Figure 3.18 shows the time-contained method for different GPIO operating states. In the illustration, the left plot shows the ADC and PI algorithm functions covered in the on-time range. The system spends t_1 seconds reading ADC data and t_2 seconds to complete the PI algorithm. Since the duty cycle (d) is determined by the ratio of t_{on} and t_{total} ($t_{on} + t_{off}$), then on-time compensation (t_{comp_on}) would be superimposed to PWM because there is a possibility for t_{on} to ask for additional time (t_{comp_on}) in order to compensate the time difference between t_{on} and real execution time $t_1 + t_2$, as shown in (3.29). In this situation, the ratio of the on-time duty cycle is initialised by a small value (due to the small sum of t_1 and t_2 being larger than zero), which never reaches a zero value:

$$t_{on} = t_{total} \times d \tag{3.28}$$

$$t_{comp\_on} = t_{on} - t_1 - t_2 \tag{3.29}$$

Another time-contained strategy focuses on the off-time region of GPIO. Different from the aforementioned on-time range approach, the off-time filed involves reading ADC data and running the PI algorithm; this is illustrated in

Figure 3.18(b). As the PI algorithm defines the duty cycle, the value of the duty cycle is used to allocate the GPIO on-time duration directly. On the contrary, the GPIO off-time duration (t_{off}) is given by the difference between the total time (t_{total}) and the on-time (t_{on}), shown in (3.30). As a result, the off-time compensation (t_{comp_off}) is a discrepancy between the off-time t_{off} and the sum ($t_1 + t_2$) of the ADC and PI algorithm presented in (3.31):

$$t_{off} = t_{total} - t_{on} \tag{3.30}$$

$$t_{comp\_off} = t_{off} - t_1 - t_2 \tag{3.31}$$

When compared those two time-contained strategies, the former (on-time strategy) implies a minimum duration t_{on} (in which the minimum value of duty cycle is limited), whereas the latter (off-time strategy) results in a minimum duration t_{off} (which means a limit on the maximum value of the duty cycle). The off-time strategy is, therefore, more appropriate as the converter does not normally work with a very high duty cycle.

3.4 Digital Signal Processing on Domain Transfer Algorithm

Digital signal processing (DSP) is used on digital representation of signals to analyse, modify, store or extract information from measured signals. In battery impedance measurements, the equation for the impedance (3.12) is concerned with two measurable signals: terminal voltage and discharge current of the battery. These signals change continuously in the time domain. However, time-continuous signals cannot be used directly for impedance calculations. In general, they should be properly processed by the ADC, which digitalises the signals to a discrete-time

format (well-known as samples), as discussed in Section 3.2.2. Obtained samples perform with a fixed time resolution and their amplitudes are quantified by 2^B bits.

As the previous discussion about the real-time controller, measurable signals of battery need to be converted to digital signals, and then they can be processed by the microprocessor. Here, two categories of DSP operating conditions are considered in practice, called real-time and non-real-time. The real-time controller functions (ADC, PI algorithm and PWM) are involved in the time-constrained condition to generate required AC excitations. By contrast, the aspects of battery impedance computation with the domain transfer algorithm and SOC estimation, have no specific requirement for the constrained time. Therefore, the non-real-time operation in the RAM is considered.

So far, the measurable voltage and current are shown as functions that depend on time, given by (3.10) and (3.11). Besides, impedance expressions related to the voltage and current measurements are displayed in (3.12) and (3.13), which need to transfer measurable data into the frequency domain. Analytically, for the continuous-time signals, such as voltage and current, they consist of a range of frequencies, which can be transferred from the time domain to the frequency domain via a Fourier transform (FT, $X(f)$). According to [132], the FT algorithm over the time range $(-\infty, \infty)$ is given by

$$X(f) = \int_{-\infty}^{\infty} x(t) e^{-j2\pi ft} dt \tag{3.32}$$

$$x(n) = \sum_{k=0}^{N_{FT}-1} c_k e^{-j2\pi kn/N_{FT}}, k = 0, 1..., N_{FT} - 1 \tag{3.33}$$

The discrete-time signal $x(n)$ is transformed into a sequence by the

discrete-time Fourier transform (DFT):

$$X(k) = \sum_{n=0}^{N_{FT}-1} x(n)e^{-j2\pi kn/N_{FT}}, k = 0, 1..., N_{FT} - 1 \tag{3.34}$$

where the analog signal is denoted by a continuous-time format $x(t)$, while $x(n)$ is the discrete-time counterpart; here, j stands for the unit imaginary number.

According to the expression (3.32), a Fourier transform delivers an essential connection between time-domain and frequency-domain. In addition, the FT offers critical information: two signal formulae in different domains are equivalent if they are obtained with the same measurement circumstances, such as the sampling rate. This said, in the proposed battery impedance measurement platform, the observed continuous-time signals must be sampled and quantised by the unipolar ADC; the latter, supports signal acquisitions that guarantee the measurement under the same sampling rate and quantisation level. In response to discrete-time performance for ADC samples, a discrete-time Fourier transform is therefore deployed.

The DFT is the discrete-time equivalent of the continuous-time Fourier transforms. As the derivation for discrete Fourier series is shown in (3.33) and (3.34), where the number of samples of the signal are N_{FT} and c_k denotes the Fourier series coefficients, the DFT performs a sum to obtain the amplitudes for all samples. When the number of samples increases, the sum requires more amplitude elements, resulting in a longer operation. In practice, the number of samples are taken into a DFT depends on several aspects, such as the frequency of the measurable subject, the sampling rate and the measurement duration.

Additionally, the DFT defined in (3.34) can be represented with the

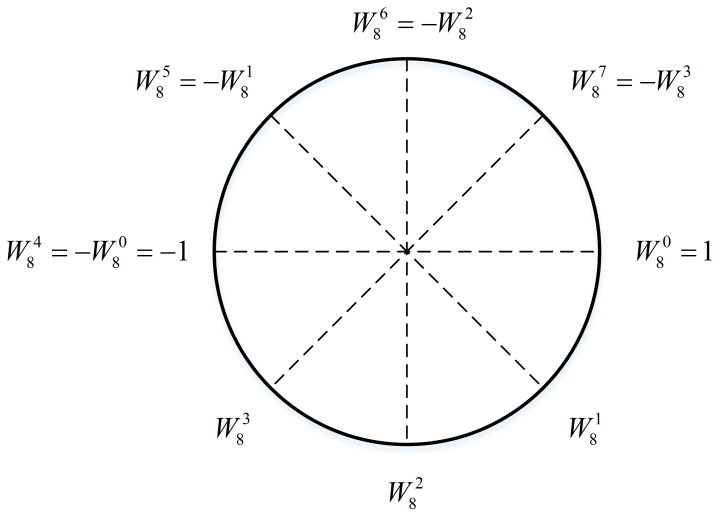

Figure 3.19: Twiddle factors for DFT, $N_{FT} = 8$

twiddle factor [132]:

$$X(k) = \sum_{n=0}^{N_{FT}-1} x(n) W_{N_{FT}}^{kn}, k = 0, 1..., N_{FT} - 1 \tag{3.35}$$

where

$$W_{N_{FT}}^{kn} = e^{-j2\pi kn/N_{FT}}, k = 0, 1..., N_{FT} - 1 \tag{3.36}$$

The parameter $W_{N_{FT}}^{kn}$ is known as the twiddle factor. The twiddle factor is a periodic and symmetric function which period can be found by $W_{N_{FT}}^{N_{FT}} = e^{-j2\pi} = 1$ and its symmetry is a consequence of the $e^{-j\pi}$ (equalling -1), as shown in Figure 3.19. The illustration exhibits the periodic and symmetric characters of the twiddle factor in an 8-point DFT. It can be proved that the symmetry of the twiddle factor is $N_{FT}/2$ and its periodicity is N_{FT}.

$$W_{N_{FT}}^{k+(N_{FT}/2)} = -W_{N_{FT}}^{k}, 0 \leqslant k \leqslant (N_{FT}/2) - 1 \tag{3.37}$$

$$W_{N_{FT}}^{k+N_{FT}} = W_{N_{FT}}^{k} \tag{3.38}$$

For DFT implementations, the DFT coefficients are equally spaced on the unit circle with the frequency intervals of f_s/N_{FT} or $2\pi/N_{FT}$. This means that, in the frequency domain, the resolution of two close frequency components of DFT are identical and the value is the frequency intervals. Therefore, the frequency sample f_k can be obtained as

$$f_k = k\frac{f_s}{N_{FT}}, k = 0, 1, ..., N_{FT} - 1 \tag{3.39}$$

However, the DFT is an expensive floating-point computation. If N_{FT} points are required by DFT to calculate each $X(k)$, there are N_{FT} complex multiplications and N_{FT} complex additions in the definition (3.34). Yet, for computing the N_{FT} samples of $x(k)$, as k varies from 0 to $N_{FT}-1$, about N_{FT}^2 complex computations and $N_{FT} \times (N_{FT} - 1)$ complex sums are needed. When considering four real multiplications included and two real additions in a complex multiplication, the number of arithmetic operations of computing N-point DFT is as large as $4N_{FT}^2$.

As N_{FT} becomes larger, the computation would last for a longer time, which causes a very low speed to measure battery impedance. In this case, to overcome the issue of DFT's requirement on long-term computations, an efficient algorithm called the fast Fourier transform (FFT) can be adopted. Historically, FFT was put forward by Cooley and Tukey in the mid-twentieth century [132]. With developments in the past several decades, FFT algorithms have become popularly and been applied to most frequency domain presentations. This is because FFT only requires $N_{FT}log_2N_{FT}$ operations, which replaces teh number of large operations for DFT as N_{FT} samples are referred. Notably, the Cooley-Tukey algorithm consist in dividing the transfer into two pieces of size of $N_{FT}/2$ at each step and is therefore limited to power-of-two sizes. There is a clear computational comparison if N_{FT} is valued at 1024, FFT needs about 10^4 operations, while the DFT requires 10^6. Statistically, FFT only demands 1% of DFT operations to complete the same sample computation. This computation

normally occurs under non-real-time conditions (in microprocessors). Fewer actions of the microprocessor indicate shorter time for the execution. Afterwards, this work focuses on how FFT decimates the operating time efficiently. FFT also requires the number of samples to meet the fast calculation algorithm. The recommended number of samples (N_{FT}) for FFT is power of two, $N_{FT} = 2^r$, where the integer r can be calculated as

$$r = log_2 N_{FT} \tag{3.40}$$

In the FFT algorithm, the signal $x(k)$ is split into two $N_{FT}/2$ samples that are categorised as an odd item $x_o(k_o)$ and an even item $x_e(k_e)$. For these odd and even elements, they consist of the identical signal samples, which can use a $(N_{FT}/2) \times 1$ transposed matrix [132], where n stands for an integer varying from 0 to $N_{FT}/2$:

$$x_e = [x(0), x(2), ..., x(2n)]^T \tag{3.41}$$

$$x_o = [x(1), x(3), ..., x(2n-1)]^T \tag{3.42}$$

The basic idea of the FFT is based on the DFT definition (3.34), which can be expressed in terms of odd and even parts:

$$\begin{aligned} X(k) &= \sum_{n=0}^{(N_{FT}/2)-1} x(2n) W_{N_{FT}}^{2kn} + \sum_{n=0}^{(N_{FT}/2)-1} x(2n-1) W_{N_{FT}}^{k(2n-1)} \\ &= X_e(k) + W_{N_{FT}}^{-k} X_o(k) \end{aligned} \tag{3.43}$$

From here the even part $X_e(k)$ can be obtained:

$$\begin{aligned} X_e(k) &= \sum_{n=0}^{(N_{FT}/2)-1} x(2n) W_{N_{FT}}^{2kn} \\ &= \sum_{n=0}^{(N_{FT}/2)-1} x(2n) W_{N_{FT}/2}^{kn} \end{aligned} \tag{3.44}$$

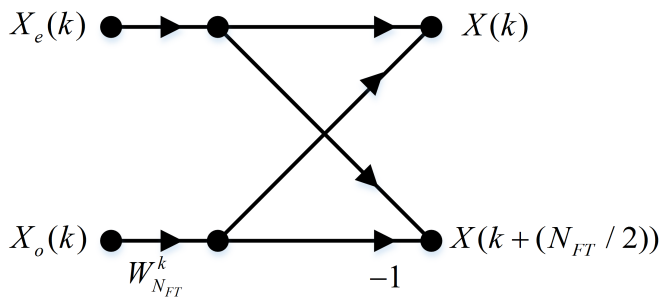

Figure 3.20: Flow Graph of k^{th} Order Butterfly Computation

Notice that the factor $W^{2kn}_{N_{FT}}$ appears in both odd and even sequences (3.43) and it only requires to be computed once. Furthermore, when the programmable FFT is driven by a microprocessor, the appeared factors are usually precomputed and stored in the random-access memory (RAM). For the coefficients of the FFT, they are obtained by combing the odd and even sequences using these formulae:

$$\begin{aligned} X(k) &= X_e(k) + W^k_{N_{FT}} X_o(k), k = 0, 1..., (N_{FT}/2) - 1 \\ X(k + (N_{FT}/2)) &= X_e(k) - W^k_{N_{FT}} X_o(k), k = 0, 1..., (N_{FT}/2) - 1 \end{aligned} \tag{3.45}$$

As the periodic property is governed by the factor $N_{FT}/2$, $X_e(k)$ and $X_o(k)$ are not changed as k increases with integer multiples of $N_{FT}/2$. Consequently, the simplified formulae (3.48) take the following form (where needs $0 \leqslant k \leqslant (N_{FT}/2) - 1$):

$$Y(k) = W^k_{N_{FT}} X_o(k) \tag{3.46}$$

$$X(k) = X_e(k) + Y(k) \tag{3.47}$$

$$X(k + (N_{FT}/2)) = X_e(k) - Y(k) \tag{3.48}$$

In the above simplifications, a temporary variable is used to reduce the number of complex multiplications from two to one. Notably, the simplified

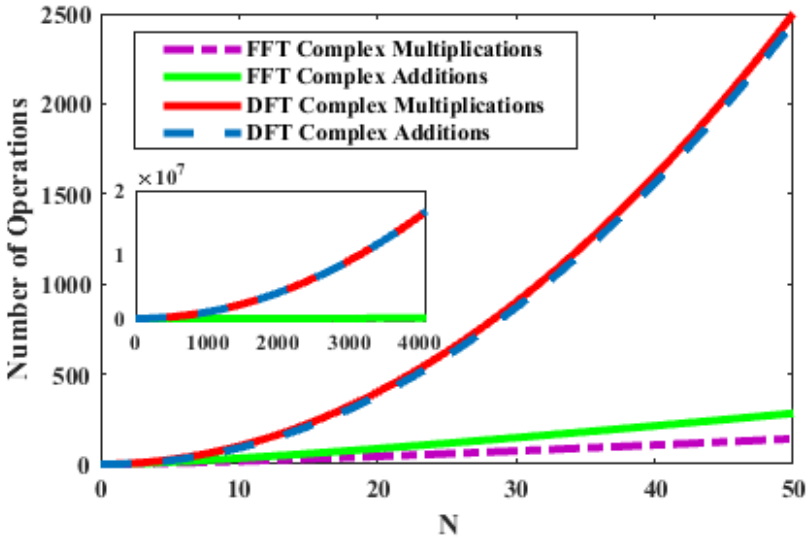

Figure 3.21: Computational Operations of N-point FFT and DFT

computations in (3.47) and (3.48) are used for a k^{th} order butterfly. This name comes from the computational representation of (3.47) and (3.48): schematically, the computations can be imagined as a 'wing' of a butterfly [132], which is shown in Figure 3.20.

As an assumption, given N_{FT} samples applied to the FFT computation, there are N_{FT} butterflies per stage with a total of $log_2 N_{FT}$ stages. Each butterfly owns one complex multiplication and two complex additions. Thus, a total number of $(N_{FT}/2)log_2 N_{FT}$ complex multiplications and $N_{FT} log_2 N_{FT}$ complex additions are involved by the FFT. When the FFT is compared to the DFT on computational operations (see Figure 3.21), a substantial saving occurs as the number N_{FT} is larger than 20, but for computational operations driven by microprocessors, the significant time saving that would be observed as N_{FT} is larger than 2000.

Therefore, in the battery impedance measurement system, FFT is used to fully support the frequency domain representations to transform battery voltage

and its discharge current from the time domain to the frequency domain given that it contributes to a fast operation. Depending on the desired operational efficiency of the FFT, that systemic requirement on the operation time can be decimated decently even though if a high-speed processor drives the FFT.

Consequently, with the FFT computational effort, the aim of this thesis to boost the performance of the BMS on fast SOC estimations can be guaranteed. However, if the AC perturbation is sinusoidal and its generation is perfectly synchronised with the sampling (which is the case in the proposed design), then it is always possible to acquire and process an integer number of cycles of the AC perturbation. This means that there is no need to calculate all the points of the Fourier spectrum, but only one point is required by the measurement.

Therefore, an efficient transfer algorithm, named the Goertzel algorithm, is required to calculate only one point of Fourier spectrum. In this way, a fast online impedance measurement system can be achieved. In the following section, a fast-online measurement method is implemented with two supportable techniques, dynamic data transfer and Goertzel transfer algorithm.

3.5 Single Tone Detection for Online Battery Impedance Measurement

A simple tone detection for the online impedance measurement method for electrochemical batteries, such as lithium-ion batteries, is discussed in this section. Based on the impedance expression (3.13) of battery, the impedance at the specific frequency is defined, depending on the single-frequency consideration. This is because the proposed approach on the impedance measurement applies a single perturbation to trigger the battery Ohm's response, so the main target

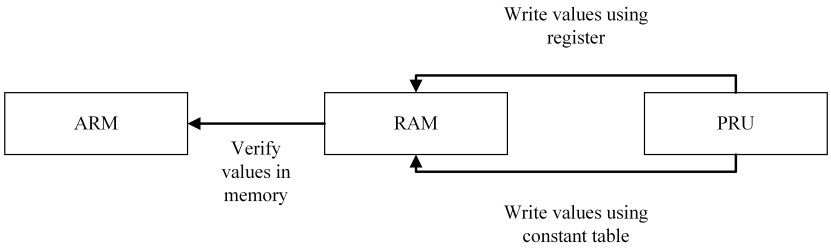

Figure 3.22: Data Transfer Diagram Between ARM and PRU

frequency is important in this work. Furthermore, in order to guarantee a fast response on the domain transfer calculation, the targeted frequency (also called tone detection) algorithm is used in the non-real-time operation environment to efficiently transfer measurable data from the time domain to the frequency domain. In this case, the concepts of online impedance measurements are divided into two main parts: data transfer and single tone detection of domain transfer algorithm.

3.5.1 Data Transmission between PRU and ARM in BBB

Onboard data transfer was developed to support impedance calculation and battery state estimations. Fortunately, the ARM 335X architecture provides a possibility for fast data communication between PRUs and ARM. PRUs enable the time restriction to process real-time tasks, while the ARM mainly deals with tasks within a non-real-time environment. In the real-time environment, target signals in battery impedance measurements are acquired periodically by the ADC, and then 12-bit (quantified by the ADC) data is stored synchronously with an ADC sampling frequency in the PRU's RAM. There are two categories of memory margins, one for data and anther for instructions. So, the names for these two margins are called Data RAM and Instruction RAM, respectively.

In the diagram of the underlying interaction among ARM, memory and

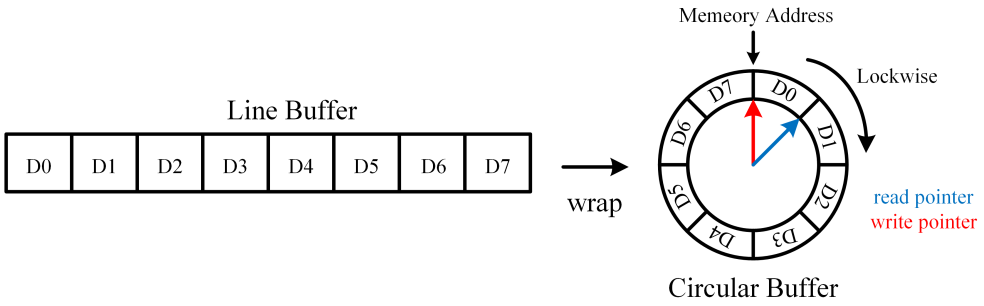

Figure 3.23: Line Buffer and Circular Buffer

PRU, as shown in Figure 3.22, RAM is employed here as a communication tube to transit stored data from the PRU to the ARM. Currently, this tube transmission is a convenient way to meet the high-speed requirement of online battery impedance measurement as compared to the implementation of GPS data acquisitions and phaser measurement applications [133]. Besides, register-based memory addresses and global addresses pointed by entries in the constant table are accessed by the RAM; where the address memory of Data RAM has an address in both the local data memory map and global memory map. Notice that RAM memory is mapped to PRUs in a slightly different way between PRU0 and PRU1. If PRU0 is used to execute a real-time program, the corresponded function *prussdrv_map_prumem*() for RPU0 will be active [134], which identifies the address of the PRU memory map using a pointer. Pointer operations can be used to read data from the specific PRU memory directly only when the correct PRU is called.

A circular buffer (also called ring buffer) as a memory-saving contributor is used for onboard data transfer. Due to BBB assembling with only 8 kB size of RAM Data memory, it is impossible to store massive data in a line buffer individually in the memory. In this case, when the buffer is wrapped as a circle, the stored data in the buffer can be overwritten in such a way that data can fill the buffer until it is full. Subsequently, the new data can be allowed to fill the buffer again from the initial position as the buffer is fulfilled and the saved data is read.

Figure 3.23 shows how an 8-element line buffer wraps into a circular buffer. When a circular buffer is built, the way is employed importantly. In the implementations of circular buffers, array and pointer are always customised to indicate data and memory addresses, respectively. For instance, an array $D[8]$ is called into the data storage program in the C language, and it has two critical meanings. Firstly, $D[8]$ means that 8 elements are involved in this array, and these elements are ordered by integer numbers from 0 to 7, shown in Figure 3.23. Secondly, with an address symbol (&) ahead of a specific portion of an array, the memory address of this element can be indicated. In other words, an array is used not only as a data indicator but also as an address pointer. To avoid the confusion related to indicate data or memory address, different pointers specifying memory addresses can be deployed. There are two conventional pointers, read and write pointers, used to indicate data reading and the data writing in the buffer at the pointed address. In practice, for battery discharge signal acquisitions in the proposed system, data writing occurs under real-time conditions, and the data is written in the buffer in a clockwise direction, starting form the initial address of the array. Besides, the frequency of data writing would be the same as the frequency of the established real-time system of battery impedance measurement.

On the other hand, the data reading works in the ARM, where non-real-time operation environment is provided. Importantly, the speed of the data reading process is faster than the data writing's one because the processing ability of the ARM is more powerful than PRUs'. Therefore, the speed for data reading and writing should be fully considered to avoid the saturation that the data in the buffer is overwritten before reading it. To handle asynchronous saturation between data reading and data writing, a comparison between read and write pointers is carried out every time in the data writing program. If the read pointer is the same as the write pointer, the buffer is empty, which means all data in the buffer has been read already. In this case, the read pointer should hold its current

value and wait for the next comparison. On the contrary, if the write pointer is located ahead of the read pointer, data reading is executed continuously in a non-real-time environment.

3.5.2 Single Tone Detection of Domain Transfer Algorithm

The concept of domain transfer algorithms has been discussed in the previous section. In spite of FFT and the DFT reducing the time necessary to obtain a spectrum at several frequencies, there is still some operating time wasted as single points of the DFT (by the single AC injection technique) are computed via the FFT and DFT algorithms. To efficiently calculate the impedance at a single frequency component, the single tone detection algorithm is adopted [135, 136]. The tone detection, named Goertzel algorithm, utilises much less ARM horsepower than other Fourier transforms, such as the FFT and DFT, so that impedances at specific frequencies can be calculated within a short duration [137].

The single tone detection operates by generating individual DFT coefficients for the target frequency component, which mainly reduces vast calculations, while the FFT algorithm calculates input components and gives the amplitudes of all components in the frequency domain. There is an example that can be used to compare the different calculating activities of the DFT, the FFT and the Goertzel algorithm. If an 8 samples are used to the FFT algorithm, the frequency components should be computed in this order $k = 0, 1, 2, 3, ..., 7$. Totally, $8log_2 8 = 24$ complex multiplications are involved in the FFT computation.

The Goertzel algorithm, only requires 8 real multiplications and a single complex multiplication since an 8-point signal is used. About one-third of the

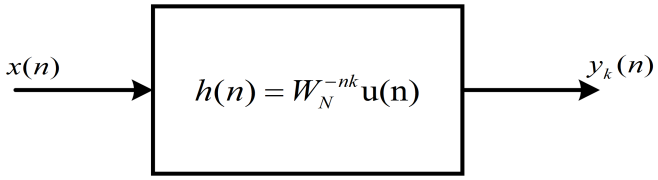

Figure 3.24: LTI Filtering Process Based the Goertzel Algorithm

computations for the FFT are required for the Goertzel computation. To find out the reason why the Goertzel algorithm is an efficient method for computing $X(k)$ with a given k, the details of the Goertzel algorithm are introduced next. The derivation of the algorithm is obtained from the expression (3.34) for the DFT and grows when the display is convoluted to gain its time-invariant performance. Initially, a simple expression is developed form the symmetry property of the phase factor (see equation (3.36)), where $W_{N_{FT}}^{-N_{FT}} = 1/e^{-j2\pi} = 1$, given as:

$$X(k) = \sum_{n=0}^{N_{FT}-1} x(n) W_{N_{FT}}^{-k(N_{FT}-n)} \tag{3.49}$$

Again, simplify (3.49) in convolution:

$$X(k) = (x(n) * W_{N_{FT}}^{-nk})|_{n=N_{FT}} \tag{3.50}$$

Finally, if an impulse is applied to equation (3.50) to characterise a system performance, which does not change the form of the equation, $X(k)$ can be expressed as:

$$X(k) = [x(n) * (W_{N_{FT}}^{-nk} \mu(n))]|_{n=N_{FT}} \tag{3.51}$$

In particular, (3.51) can be obtained as signal $x(n)$ through a linear time-invariant (LTI) filter with the impulse response $h(n) = W_{N_{FT}}^{-nk} \mu(n)$ evaluating the result, $y(n)$, at $n = N_{FT}$. This filtering process is illustrated in Figure 3.24. When represented the impulse response $h(n)$ by the z-transform method, the transfer

function is obtained for the filtering theory:

$$H(Z) = \sum_{n=0}^{\infty} W_{N_{FT}}^{-mk} Z^{-m} \tag{3.52}$$

This can be simplified to:

$$H(Z) = \frac{1}{1 - W_{N_{FT}}^{-k} Z^{-1}} \tag{3.53}$$

Alternatively, another equivalent performance (3.53) is referred to the proposed algorithm in the programmable application when normalise the denominator of $H(z)$ with its conjugate, $1 - W_{N_{FT}}^{k} Z^{-1}$. Hence, as studied in [137], a new expression can be obtained

$$H(Z) = \frac{1 - W_{N_{FT}}^{k} Z^{-1}}{1 - (2\cos\frac{2\pi k}{N_{FT}})Z^{-1} + Z^{-2}} \tag{3.54}$$

Therefore, according to the transfer function (3.53), only the output of the filtering process is evaluated at $y_k(N_{FT})$, where the factor $-W_{N_{FT}}^{k}$ only need to be calculated at $n = N_{FT}$. With this in mind, the proposed Goertzel algorithm requires a total of N_{FT} real multiplications and a single complex multiplication to compute the target frequency. In particular, the programmable implementation of the proposed tone detection is given by the effort of alternative equation (3.54), which will be discussed in the following chapter.

3.6 Chapter Summary

The proposed EIS measurement system is developed with a DC-DC power converter and a low-cost embedded device (BBB) in this chapter. The use of a DC-DC power converter offers a chance to measure battery impedance during battery normal operation. Besides, the required AC excitations of the impedance

measurements can be generated by controlling the converter in the real-time condition. Three real-time functions implemented in the BBB are discussed, including the acquisition of measurement signals, the execution of the PI control algorithm and the generation of the PWM signal to control the converter. The proposed implementation method, based on software PWM, allows to achieve the synchronisation of all three functions. An additional non-real-time function is used to transform the measurement signals to the frequency domain, in order to calculate the battery impedance. For this part, the Goertzel algorithm is used to minimise the time required to complete the domain transfer calculation, based on the fact that the AC perturbation contains a single frequency component.

Chapter 4

Proof-of-Concept Implementation and Experimental Setup

In this chapter, the proof-of concept implementations in the proposed measurement, such as the design of the DC-DC boost converter and the model based on the averaged state-space method, are discussed. Besides, the definition and the configuration of the sampling rate for the onboard ADC are described. The concept of this chapter also includes the SOC determination, which is used as one of dependencies of the impedance measurement. Apart from this, other dependencies, such as battery ageing and discharge currents, are taken into account as well. Furthermore, conditioning circuits for battery signals are used to properly process these signals for BBB-based signal acquisitions. A domain transfer algorithm is needed to transfer data from the time domain to the frequency domain. In practice, the single tone detection of the Goertzel algorithm with a flexible data length is employed. Finally, the experimental prototype of the online impedance measurement system is presented.

4.1 The Choice of Battery

Panasonic NCR18650B lithium-ion batteries are used in this thesis due to the cost efficiency. The main specifications of the battery are shown in Table 4.1 [57]. In the prototype (shown in Figure 4.16), several battery operating variables, such as SOC and internal temperature, are considered during the measurement, which would affect the impedance results of the battery.

Figure 4.1: Photo of PANASONIC NCR18650B

Table 4.1: PANASONIC NCR18650B SPECIFICATIONS

Nominal voltage	3.6 V
Cut-off voltage	2.5 V
Full charge voltage	3.9 V
Nominal capacity	3350 mAh
Maximum discharge/charge	1.0 C/0.5 C

Firstly, the discharge current is related to the battery full discharge duration directly. According to the battery impedance measurement with variable discharge currents, two common current levels of 0.3 C and 0.5 C are used. Much higher current rates (more than 0.5 C) are not employed because those current rates plate lithium metal at the negative electrode, which may cause rapid cell capacity fade [138]. Here, it should be noted that the C-rate is a measurable rate

on the current. For example, 0.5 C rate indicates that the battery discharges with 0.5 current rate continuously. The total discharge time lasts about two hours (in theory). So the current rate can be seen as a constant discharge current is approximately 1.7 A for 3350 mAh lithium-ion batteries. Secondly, when the SOC dependence of the proposed measurement is considered, different levels of SOC should be set. However, the SOC cannot be directly acquired from the measurement. Many SOC estimation approaches have been discussed in the papers [66, 139–141], such as the ampere-hour counting method, discharge test based on remaining capacity method, measurement of the electrolyte's physical properties method and open-circuit voltage method. Among mentioned SOC estimation approaches, the open-circuit voltage method is deployed by the electrochemical instrumentations to measure SOCs. In practice, the SOC levels used for the proposed measurement are identical to the SOC levels defined by the electrochemical instrumentation (BioLogic VSP/VMP3). The SOC-OCV relationships are shown in Figure 4.2.

In Figure 4.2, the curves of SOC- OCV are represented for the single-cell under the condition where the discharge rate is 0.5 C and the ambient temperature is around 21-23 ℃. The instrumentation (BioLogic VSP/VMP3) provides an integrated measurement system to measure the battery SOC from full charge (100%) to the nominal lowest level (20%). The minimum value of SOC is taken into account for the healthy and safe operation of the battery.

In the SOC-OCV illustration, five levels of SOCs (100%, 80%, 60%, 40% and 20%) are indicated by five terminal voltages of the battery: 3.90 V, 3.70 V, 3.55 V, 3.38 V and 3.18 V, respectively. The range of SOC below the cut-off voltage of 2.5 V is avoided in order to prevent irreversible damage.

On the other hand, the SOC application for multiple cells in a series connection were developed with the linearity method. In this method, the total

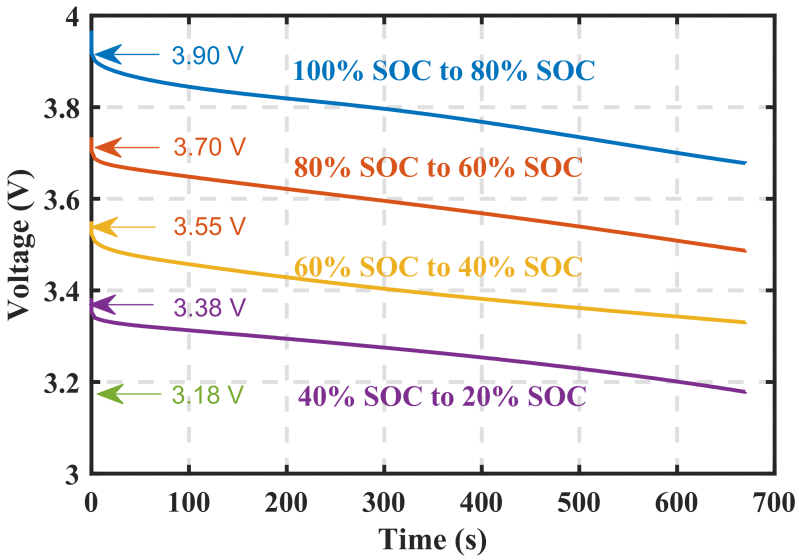

Figure 4.2: Battery SOC Corresponds to Voltage for Single Lithium-Ion Cell in BioLogic VSP/VMP3

terminal voltage of the series-connected cells is only related to the number of cells (assuming that all cells are in consistency), meaning that the total terminal voltage increases with the increase in cell number. For example, if two of the same cells are connected in series in a battery pack, the total voltage of the two cells are obtained at 7.8 V, 7.40 V, 7.10 V, 6.76 V and 6.36 V, corresponding to five SOC levels at 100%, 80%, 60%, 40% and 20%, respectively.

4.2 Hardware Design and Implementation

The boost power converter is to step up output voltage for the battery and generate desirable AC perturbations at multiple frequencies. A single board computer BBB is used to process signal conversions, digital PI controllers and data transfers in real-time conditions. Moreover, other necessary efforts of electrical components to improve the measurement quality for lithium-ion battery AC

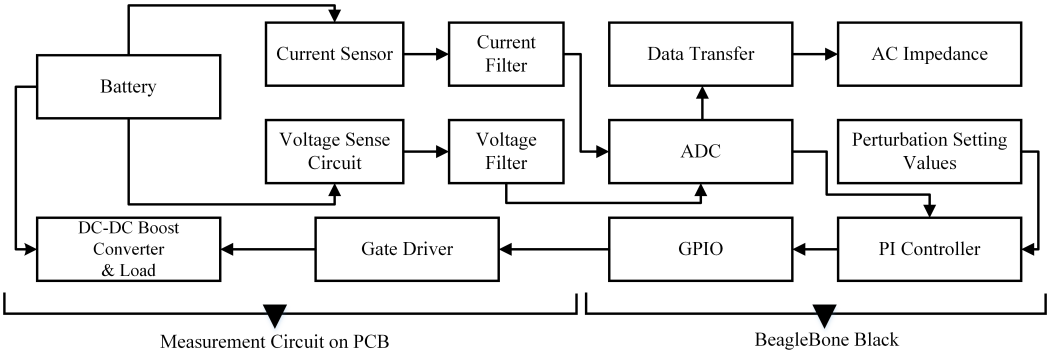

Figure 4.3: System Diagram of Battery Impedance Measurement

impedances, such as conditioning circuits and current sensors, will be explained in the following section. The system for measuring battery AC impedance is illustrated in Figure 4.3.

4.2.1 DC-DC Boost Converter

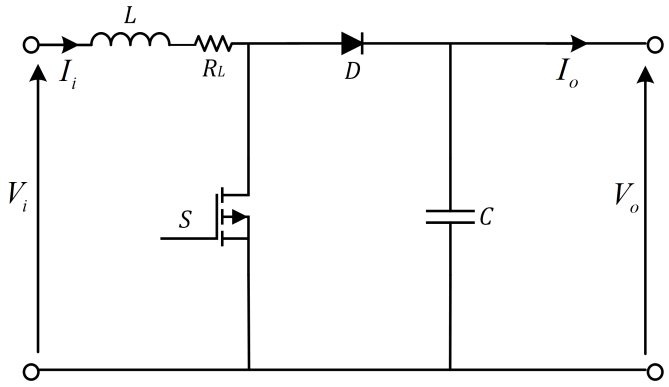

Figure 4.4: A Typical Circuit Diagram of A DC-DC Boost Converter, Inductor Resistance Included

The circuit diagram of a DC-DC boost converter is shown in Figure 4.4. The battery is used as a power supply and powers a resistor (R) in the diagram. Here, the PWM operation of the converter is taken into account for the proposed measurement. During this operation, if the duty cycle varies slowly, the power

converter introduces specific components (the harmonic of which frequencies are related to the power converter's switching frequency). Those components' frequencies are equal to integer multiples of the switching frequency f_{sw}.

The selection of the reactive components (input inductor L and output capacitor C) relies on the battery operating characteristics (including terminal voltage and discharge current), the peak-to-peak ripple amplitudes of the input current (ΔI_i) and the output voltage (ΔV_o), as well as the converter switching frequency and the duty cycle. Notably, the peak-to-peak amplitude of the current is presented by the conventional formula for the DC-DC boost converter:

$$\Delta I_i = \frac{V_i}{f_{sw}L} d \tag{4.1}$$

Additionally, the peak-to-peak amplitude of the output voltage is given by:

$$\Delta V_o = \frac{(1-d)d}{f_{sw}C} I_i \tag{4.2}$$

In (4.3), all output ripples of the current are assumed to flow through the capacitor. Based on this assumption, the peak-to-peak magnitude of the output voltage is maximised. Nevertheless, the ripples cause undesired influences on the battery. For example, large ripples might cause potential negative effects on the battery lifespan, such as loss increases, possible damages and durability decreases [95, 123, 124, 142, 143]. Thus, the amplitude of the current ripple needs to be properly restricted. According to the band value of the current ripple which researchers have used in related tests, as discussed in [13, 95], the maximum 5% amplitude (peak-to-peak amplitude is 10%) of the rated current can be configured, which provides reliability on both aspects: safe and healthy operation of the battery.

Based on above mentioned assumptions, when a 1.7 A rated current

(working with the terminal voltage of 3.55 V) and a switching frequency of 10 kHz are used in the inductance calculation [143], the maximum inductance can be calculated as the maximum duty cycle is taken into account (the maximum duty cycle is 0.7 which will be explained in Chapter 5):

$$L = \frac{V_i d}{f_{sw} \Delta I_i} = \frac{3.55 \times 0.7}{10^4 \times (2 \times 10\%)} = 1.24mH \tag{4.3}$$

In order to calculate the output capacitance, the peak-to-peak value of the voltage ripple should be restricted. Normally, this restriction is related to the DC base (voltage) during the measurement. Here, the rated nominal voltage of 0.72 V (20% of the nominal voltage [144], $20\% \times 3.6V = 0.72V$) is employed. Therefore, the maximum capacitance C of 69 μF can be calculated via the quadratic equation (4.2) when the duty cycle of 0.5 is taken.

In the DC-DC boost converter design, the filtering effect is considered for analysing perturbation influence on the load. It can be evaluated via low-pass filter method when the rest of the circuit behaves as a current source at ripple frequency is assumed. Under the assumption, the cut-off frequency can be calculated via capacitor (C) and resistor (R): $\frac{1}{2\pi \times 10 \times 69 \times 10^{-6}} = 231Hz$ when the resistance of the load is 10 Ω. In practice, the frequencies of perturbations (of interest in this thesis) vary from 0.05 Hz to 1.32 kHz. However, the filtering influence only works at frequencies of over 231 Hz, meaning that some perturbations (whose frequencies are less than 231 Hz) still exist at the output of the converter. It should be noted that the components of harmonic (related to switching frequency) can be entirely removed in this case, which lead to significant interferences when compared to other factors (such as lower-frequency components).

The unfiltered perturbations at lower frequencies may have a negative

impact on the load, which can be easily eliminated (discussed in Section 6.5) by using two DC-DC boost converters [107].

Modelling Boost Converter By State-Space Averaging

This subsection discusses a state-space averaging technique in order to model a boost converter in order to explain control dynamics and stability issues. The boost converter works with periodical changing configurations due to the inherent switching operation (ON and OFF states), as described in Section 3.1.1.

Each configuration is expressed in that section with separate equations. However, it is difficult to solve these equations in sequence for transient analysis and control design [145]. The state-space averaging technique can simplify the separate equations to a single equation by using a linearly weighted average, which may be a solution to this problem.

Figure 4.4 shows a detailed circuit DC-DC converter where an inductor's resistance (R_L) is taken into account, resulting in more accurate converter's performances when compared to its real behaviours. In this situation, the state-space equations of the converter are given as:

$$\begin{bmatrix} \frac{dI_i}{dt} \\ \frac{dV_o}{dt} \end{bmatrix} = \begin{bmatrix} \frac{-R_L}{L} & 0 \\ 0 & \frac{-1}{RC} \end{bmatrix} \begin{bmatrix} I_i \\ V_o \end{bmatrix} + \begin{bmatrix} \frac{1}{L} \\ 0 \end{bmatrix} V_i \tag{4.4}$$

$$\begin{bmatrix} \frac{dI_i}{dt} \\ \frac{dV_o}{dt} \end{bmatrix} = \begin{bmatrix} \frac{-R_L}{L} & \frac{-1}{L} \\ \frac{1}{C} & \frac{-1}{RC} \end{bmatrix} \begin{bmatrix} I_i \\ V_o \end{bmatrix} + \begin{bmatrix} \frac{1}{L} \\ 0 \end{bmatrix} V_i \tag{4.5}$$

where (4.5) and (4.6) present the ON and OFF states, respectively. Besides, the inductor current (I_i) and the output capacitor voltage (V_o) are the two elements

of the state vector, whilst the input voltage (V_i) is the single state element of the input vector. The state-space averaged equation of the converter is, therefore, derived by the equations (4.5) and (4.6) with the weighted state parameters (which are derived by the duty cycle, d for the ON state and $1-d$ for the OFF state in a switching cycle) as:

$$\begin{bmatrix} \frac{dI_i}{dt} \\ \frac{dV_o}{dt} \end{bmatrix} = \begin{bmatrix} \frac{-R_L}{L} & \frac{-(1-d)}{L} \\ \frac{1-d}{C} & \frac{-1}{RC} \end{bmatrix} \begin{bmatrix} I_i \\ V_o \end{bmatrix} + \begin{bmatrix} \frac{1}{L} \\ 0 \end{bmatrix} V_i \tag{4.6}$$

It can be seen that the averaged state-space equation is linear as I_i and V_o are the state vectors and V_i is the input vector. Here, the symbols of state vectors in the averaged equation (4.7) may be seen as averaged state vectors, which are different from their meanings in equations (4.5) and (4.6).

Current-Mode Control

In order to properly control the converter to create AC perturbations for the EIS measurements, the input current of the converter is regulated by closing a feedback loop as discussed in Section 3.1.3, which is specifically designed for batteries. A linear relationship between the state variables is expressed in (4.7), whilst the input current state variation has a non-linear relationship with the duty cycle variables. To derive this non-linear relationship, the small-signal variation is conventionally used. A small sinusoidal variation is superimposed on a constant current base, then this mixed current is used to compare the measured current, as shown in the EIS measurement diagram (see Figure 3.8). When the small state variations are taken into account, the averaged state-space equation (4.7) with

them can be expressed as:

$$\begin{bmatrix} \frac{d(I_i+\Delta I_i)}{dt} \\ \frac{d(V_o+\Delta V_o)}{dt} \end{bmatrix} = \begin{bmatrix} \frac{-R_L}{L} & \frac{-(1-(d+\Delta d))}{L} \\ \frac{1-(d+\Delta d)}{C} & \frac{-1}{RC} \end{bmatrix} \begin{bmatrix} I_i + \Delta I_i \\ V_o + \Delta V_o \end{bmatrix} + \begin{bmatrix} \frac{1}{L} \\ 0 \end{bmatrix} V_i \qquad (4.7)$$

where ΔI_i, ΔV_o and Δd denote the input current variation, the output voltage variation and the duty cycle variation, respectively. Here, the input voltage variation is not considered due to a constant input voltage under an ideal modelling scenario. The small-signal model can be simplified by the state equations: $0 = V_i - R_L I_L - (1-d)V_o$ and $0 = (1-d)I_L - V_o/R$, as given by:

$$\begin{bmatrix} \frac{d(\Delta I_i)}{dt} \\ \frac{d(\Delta V_o)}{dt} \end{bmatrix} = \begin{bmatrix} \frac{-R_L}{L} & \frac{-(1-d)}{L} \\ \frac{(1-d)}{C} & \frac{-1}{RC} \end{bmatrix} \begin{bmatrix} \Delta I_i \\ \Delta V_o \end{bmatrix} + \begin{bmatrix} \frac{V_0}{L} \\ \frac{-I_L}{C} \end{bmatrix} \begin{bmatrix} \Delta d \end{bmatrix} \qquad (4.8)$$

When combining those two state equations with (4.9) again, the state vectors V_o and I_L can be expressed by V_i. Hence, the control-to-output (for the current-mode control measurement system where the input current is controlled by the duty cycle) transfer function ($H(s)$) can be given by using the Laplace transform:

$$H(s) = \frac{I(s)}{d(s)} = \frac{(sRC+1)(1-d)RV_i}{((1-d)^2R + R_L)(s^2LRC + sRCR_L + (1-d)^2R)} \qquad (4.9)$$

where 's' is the symbol of the Laplace transform.

When the PI controller (the transfer function $C(s)$ of the PI control: $C(s) = k_p + \frac{k_i}{s}$) is set to control the converter, the typical system of controlling small signals (based on the DC-DC boost converter for EIS measurements) is established, as shown in Figure 4.5.

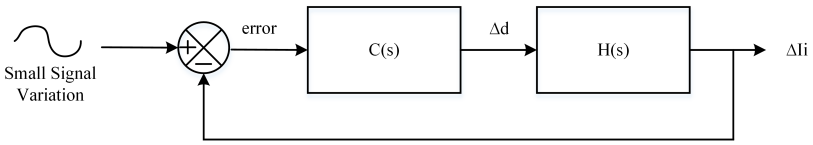

Figure 4.5: A Typical Diagram of the Small Signal System for the DC-DC Boost Converter

Table 4.2: PARAMETER VALUES OF AVERAGED STATE-SPACE MODEL

Parameter	Value
V_i	3.55 V
d	0.5
R	10 Ω
C	69 uF
L	1.24 mH
R_L	0.216 Ω

Table 4.2 shows the parameter values of the passive components (inductor L, capacitor C, and resistor R, referring to the calculation results and nominal operating conditions). Besides, the nominal duty cycle of 0.5 is employed in the model. As a result, all parameters of the transfer function $H(s)$ are given and then the established system including the PI controller can be obtained, as shown in Figure 4.6.

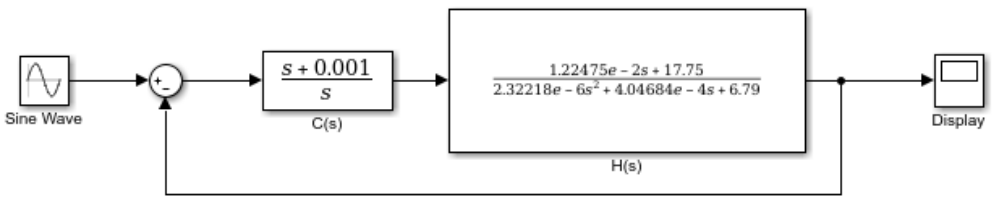

Figure 4.6: The Proposed System Established via Simulink

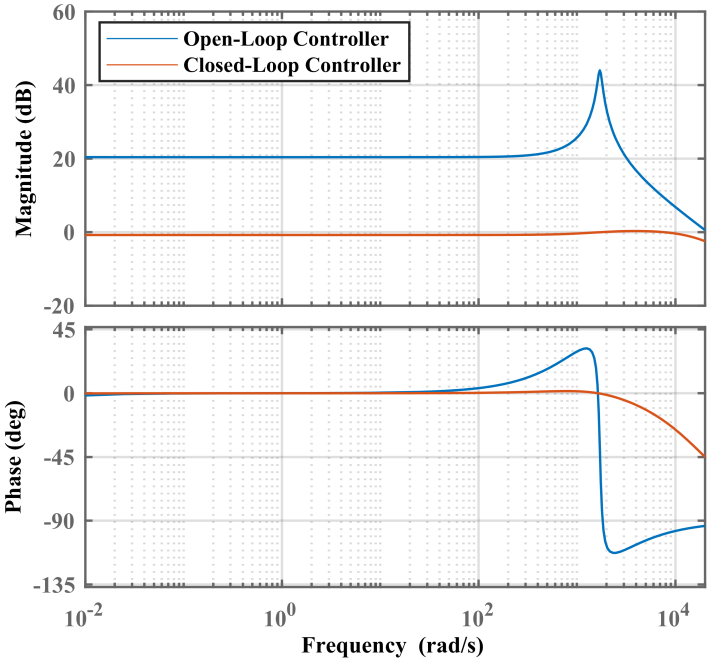

Figure 4.7: Open-Loop and Closed-Loop Control-To-Output Frequency Response $I_i(s)/d(s)$ Plot

There are two ways to obtain the frequency response of the control in MATLAB: coding or implementing Simulink. In Simulink, analysing control dynamics and stability of the converter can employ the linear analysis tool. For the linear analysis, the output of $C(s)$ is chosen as an open-loop input and the output of $H(s)$ is used as an open-loop output. The open loop control-to-output frequency response $\Delta I_i/\Delta d$. Alternatively, coding the transfer functions ($C(s) \times H(s)$ and $\frac{C(s)\times H(s)}{1+C(s)\times H(s)}$ for open-loop and closed-loop systems, respectively) in Matlab is preferred in this work. The difference between the two controllers is shown in Figure 4.7. As expected, the closed-loop provides more efficient control of the converter, especially of the magnitude. In the proposed measurement frequency range (from 0.05 Hz (equalling 0.314 rad/s) to 1.32 kHz (equalling 8289.6 rad/s)), the magnitude of the control object (input current) performs at around 0 dB. In addition, the stability of the system in the range has a reasonable

phase margin of approximate 135 °, resulting in a control bandwidth of around 3 kHz.

By contrast, when the open-loop control is employed in the system, it leads to instability with increasing frequencies, such as large overshot and insufficient phase margin [2].

It is worth addressing that the continuous-time controller gains of k_p (proportional gain) and k_i (integral gain) are used in the above conditions at 1.0 and 1/900, respectively. Those parameters of the controller were obtained from tests, according to the control performance of the current amplitude of 5% DC current base. A sufficient bandwidth results in a reasonable controller performance for the proposed impedance measurements.

4.2.2 Conditioning Circuits for Battery Voltage and Current

Employing conditioning circuits during the impedance measurement system aims to extract undesired measurable signals such as components of the switching frequency. Another implementation purpose is to restrict the measured voltages for the onboard ADC's signal acquisition (the voltage range of the ADC from 0 V to 1.8 V).

The vital conditioning measurement is to remove undesired ripples created by the converter. It is well known that when power electronic converters are used, currents and voltages contain high-frequency ripples. Assuming that a constant switching frequency is set to operate the converters, those components particularly appear at the switching frequency and integer multiples of the switching frequency. If the switch operates at a frequency of around one

kilohertz, all of components will typically perform in the high-frequency range (as compared to frequencies of AC perturbations) where the lowest frequency boundary equals the switching frequency of the converter. In order to extract those switching frequency components (for voltage and current measurements), traditional filtering techniques could be adapted. A first-order low-pass filter is the most straightforward implementation, which is capable of removing high-frequency components efficiently, as shown in Figure 4.8. Fortunately, the filtering property can cooperate with voltage division in term of simplifying monitoring circuits and controlling cost.

Voltage divisions are required by the monitoring circuit because the ADC's maximum accepted voltage is 1.8 V. Here, the acquired voltages consist of two voltage elements: cell terminal voltage and current transducer's output voltage. During battery signal acquisitions, the maximum and the minimum voltages are applicable to the full voltage of about 3.9 V (100% SOC) and the lowest operating voltage of 3.18 V (20% SOC).

Unfortunately, both battery terminal voltages exceed the maximum ADC allowable voltage of 1.8 V. Likewise, the excess range situation happens in the current measurement. Discharge currents were arranged in the tests with various levels because the dependency of the current rate is one of the interests focused on in this thesis. During the measurements, there were two different levels (presented in C rate) for the discharge current: 0.5 C and 0.3 C. The maximum values of discharge currents in response to the aforementioned levels are approximate 1.7 A and 1.0 A.

A current transducer LTS 6-NP was chosen to measure the current signal of the battery. It offers a wide bandwidth of 100 kHz to the measurement as the gain-magnitude varies from 0 to -0.5 dB. Importantly, the reason for choosing this type of current transducer is that it has an adjustable measurement sensitivity (most

sensitive to below 2.0 A currents). A linear relationship between the measured current and output voltage is given by:

$$I_{trans} = 3.2V_{trans} - 8 \tag{4.10}$$

where I_{trans} represents the primary current and the measured voltage of the current transducer is V_{trans}.

The LTS 6-NP has desired measurement accuracy (±0.2% at room temperature of 25 °C) and cost efficiency (at around £17), which respects the purpose of reducing the cost and size of the system. Its operating voltage of the current transducer is 5 V and the current consumption is around 28 mA, which can be directly powered by the BBB (onboard voltage is 5 V and current reaches 100 mA), so there is no need to use an external power supply to the current transducer. As a result, the current transducer can be integrated with conditioning circuits, which helps reduce the space size of the measurement hardware.

However, the relationship between the primary current and measurement voltage gives an output voltage of the transducer of 2.5 V when the value of the current is 0 A. It should be noted that the value of the output voltage is over 1.8 V. In this case, voltage dividers are implemented with the maximum gains of 0.4 (the ratio of 1.8 to 4.2) and 0.5 for voltage and current measurements, respectively. According to the mentioned requirements for conditioning circuits (regarding high-frequency ripples and dividing high voltages), a typical combination for the circuit, including a voltage divider and a low-pass filter, is shown in Figure 4.9.

The voltages for ADC acquisitions including measured voltages of the battery and the output of the current transducer are divided in the same way with traditional voltage dividers, consisting of resistors R_{1_f} and R_{2_f}. The DC output voltage (V_{out_f}) of the combination circuit is obtained without reactive

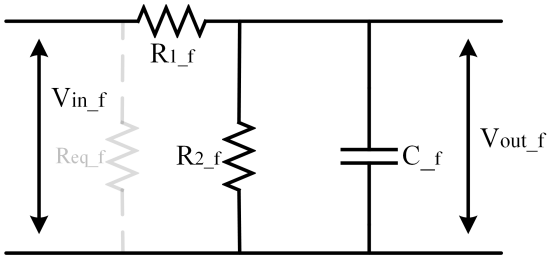

Figure 4.8: Voltage Divider and Filtering Circuit

impedance (or capacitive resistance):

$$V_{out\_f} = \frac{R_{2\_f}}{R_{1\_f} + R_{2\_f}} V_{in\_f} \tag{4.11}$$

where V_{in_f} is the input voltage of the battery or transducer's terminal and V_{out_f} is specific to the ADC measures. Equations (4.12), (4.13) and (4.14) are used in the implementation of the low-pass filter. The resistors are connected in parallel and their equivalent resistance can be analysed by Thevenin's theorem. So the equivalent resistor R_{eq_f} (shown in Figure 4.7 in dashed line) of the circuit can be given as the capacitive impedance is neglected.

$$R_{eq\_f} = R_{1\_f} || R_{2\_f} \tag{4.12}$$

Hence, the cut-off frequency (f_c) of the filter can be expressed as:

$$f_c = \frac{1}{2\pi R_{eq\_f} C_{\_f}} \tag{4.13}$$

Determining the bandwidth of the filter depends on the maximum perturbation frequency. The maximum frequency of AC perturbations can be created at 1.32 kHz by the real-time control system in this work, which will be discussed in Section 4.2.4. It means that the cut-off frequency of the filter should be larger than 1.32 kHz. Table 4.3 and 4.4 show the theoretical values and practical values

Table 4.3: COMPONENT VALUES OF DIVIDER AND LOW-PASS FILTER FOR SINGLE CELL

Designator	Theoretical Value	Real Value	Unit
R_{1_f}	90	99.6	$k\Omega$
R_{2_f}	60	54.6	$k\Omega$
$C_{\_f}$	2.2	-	nF

Table 4.4: COMPONENT VALUES OF DIVIDER AND LOW-PASS FILTER FOR MULTIPLE CELLS

Designator	Theoretical Value	Real Value	Unit
R_{1_f}	334	328	$k\Omega$
R_{2_f}	40	38.8	$k\Omega$
$C_{\_f}$	2.2	-	nF

for preventative components of the first-order filters. The symbol '-' means no measurement for the value identification. As the same capacitor is used in the filter, the equivalent resistances are also identical so the cut-off frequencies are equal. Therefore, the cut-off frequency of the filters is obtained at 2.0 kHz, where the passband sufficiently covers the maximum frequency of perturbations.

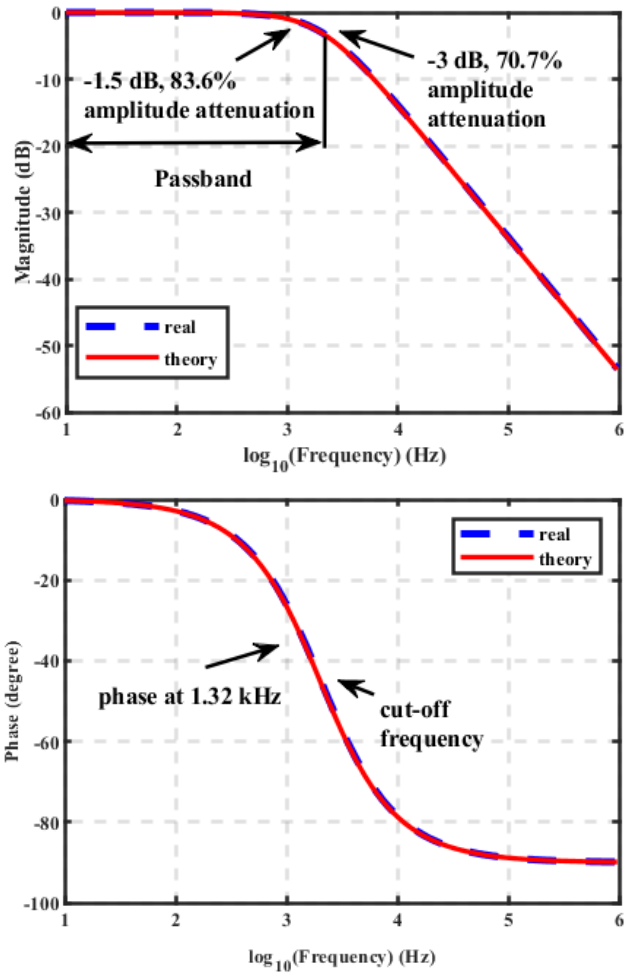

Figure 4.9: Bode Plot for First-Order Low-Pass Filter, Showing Theoretical and Real Performances

Analytically, the output voltage of the filter at the frequency of 1.32 kHz is 1.21 V as the voltage of 1.44 V (the 3.6 V battery nominal voltage is divided by the voltage divider with a division ratio of 0.4 in theory; but in practice, the ratio of 0.354 is considered in data normalisation) is input.

Despite a small voltage attenuation for the output voltage of the filter at 1.32 kHz, an acceptable gain of -1.5 dB (83.6%, which is larger than -3 dB

(70.7%)) for the output is still achieved at the corresponding frequency, as shown in Figure 4.9.

Relative calculations for the voltage gain are expressed by (4.15) and (4.16). It is worth addressing that the switching frequency components will be attenuated if they are taken into account for the proposed measurement. Those components display at integer multiples of the switching frequency ($66kHz$, $log_{10}66k$ equals approximately 5). At these frequencies, the amplitude is much smaller than -35dB, which means that the amplitude is completely attenuated ($-35dB$ approximately equals 0.018, which is almost zero). In this situation, the switching frequency components are so small that they can be considered negligible in the measurement.

In Figure 4.9, it is also observed that the phase shift at the frequency of 1.32 kHz is about 38° (around 45° at the cut-off frequency). It means that the output signal would lag the input signal with a constant phase difference of 38° at the given frequency, which leads to an apparent error in the battery impedances.

$$X_{c\_f} = \frac{1}{2\pi f C_{\_f}} = \frac{1}{2 \times \pi \times 1.32k \times 2.2n} = 54.8k\Omega \tag{4.14}$$

$$V_{out\_f} = V_{in\_f} \frac{X_{c\_f}}{\sqrt{R_{eq\_f}^2 + X_{c\_f}^2}} = \frac{54.8k}{\sqrt{36k^2 + 54.8k^2}} V_{in\_f} = 0.836 V_{in\_f} \tag{4.15}$$

Where X_{c_f} is the capacitive impedance at the frequency of 1.32 kHz.

Particularly, in the single-cell measurements, the same low-pass filters (with the same resistors and capacitor) were used for voltage and current acquisitions. In theory, the same phase shift can be obtained in both signal acquisitions, which will be eliminated in the impedance calculation. Actually, the tolerance of the resistor and capacitor results in a slight difference between the filters, which leads to the difference of the cut-off frequency between the design and the test. More details will be discussed in Section 6.2.

It is worthy of notice that the voltage performances in response to current perturbations are not included in the discussion due to the amplitude of AC voltage responses depending on Ohm's law, which cannot be depicted by a certain expression (several assumptions on the battery ohmic behaviour have been discussed in Section 2.3).

For the output voltage of the current transducer processed by the same conditioning circuit, the battery discharges with the mixed current, including the DC offset of 1.7 A and the oscillation of 0.085 A. After this mixed current passes the current transducer, the current is measured and converted to the voltage measurement. The 1.7 A current is measured by the transducer that results in a voltage of approximately 3.06 V. After the conditioning circuit properly processes the output voltage, the acquired voltage by the ADC is around 1.04 V, which is smaller than the voltage limitation of 1.8 V. After the battery discharge voltage and the current are filtered and divided by the conditioning circuits, the maximum values of voltage and current acquired by the onboard ADC are nearly 1.21 V and 1.04 V, respectively.

Again, the AC excitation of the terminal voltage is not discussed. In general, a higher level of quantisation used in analog signal measurements brings more accurate result, but the ADC sampling rate would be significantly reduced. Balancing quantisation level and sampling rate acts as the substantial rule in this work, which will be explained in the following section.

4.2.3 Onboard Analog-to-Digital Converter

BeagleBone Black has assembled an 8-channel SAR (successive approximation register) ADC on the board. The SAR ADC works with a low power consumption and is frequently used for medium-to-high-resolution applications (a common

Table 4.5: MAXIMUM CIOCK SPEED FOR INTERFACING MULTIPLE ADCs

No. of ADCs	Max. Clock Speed
1	24 MHz
2	20 MHz
3	16.67 MHz
4	14.29 MHz
5	12.25 MHz
6	11.11 MHz

resolution range is 8 to 16 bits). Notably, the BBB shows its compatibility regarding the peripheral ADCs while the maximum clock speed for ADCs would be reduced in the TSC_ADC subsystem (see Figure 4.10) as the number of ADCs increases [133]. The relationship between the number of ADCs and the maximum clock speed is shown in Table 4.5.

Particularly, as only one ADC is active, the clock speed of the onboard ADC reaches 24 MHz. In this situation, the maximum sampling rate of ADC could be obtained at full throughput (200 ksps). In practice, considerable signals (voltage and current signals) can be adequately acquired by a single ADC, so there is no need to add other ADCs to the BBB.

On the other hand, the ADC sampling rate is closely related to several active channels. This is due to the sampling consistency of active channels. Thus, it is necessary to decide how many signals should be measured in the proposed system in priority. Firstly, in term of calculating the battery AC impedance, as expressed by (3.12), at least two channels need to be active to measure the battery terminal voltage and the discharge current. Secondly, temperature as a key factor should be of interest in all relevant measurements, especially in the EIS tests. So, the temperature measurement is included.

For temperature measurements, two categories of measurement methods can be used: one for battery surface measurement and another for battery core temperature detection. The surface thermal measurement is an easy-measure method that has been widely used. However, this method results in a low accuracy on the monitoring temperature for a long-time measurement [24].

The second method is measuring the battery core temperature. This method provides a more accurate trace of the battery temperature dynamic during long-term operation. However, detecting battery core temperature is difficult. The core temperature detection needs to plug a temperature sensor into the battery. If this step is followed, the battery would have irreversible damage, which leads to a potentially unsafe operation for the measurements.

To guarantee a safe operating condition for the battery, an non-invasive approach is employed. The approach is detecting surface temperature of the battery in less 50 seconds, which was observed in [24], depending on the temperature similarity between the surface and core of the battery when battery works with a short time. By this way, a significant effect on the internal temperature of the battery can be avoided when a long-time measurement happens.

So, the surface temperature is measured by an analog thermal sensor, representing the 'core' temperature. In total, three ADC channels are required to be set in the proposed measurement system.

ADC Conversion Process

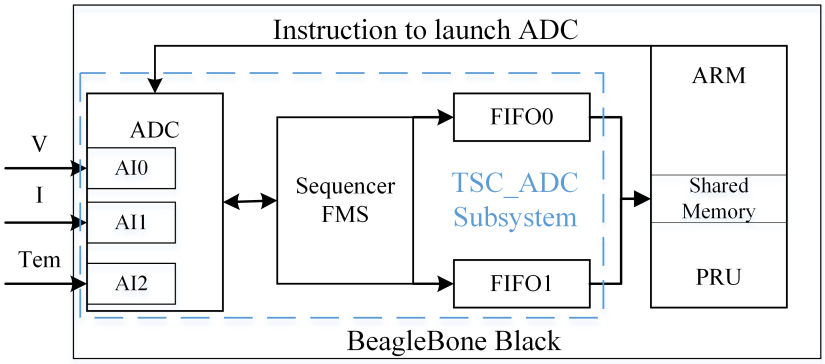

Figure 4.10: Diagram of ADC Operation

The onboard ADC is typically governed by the core processor (ARM) of the BBB. In the ADC application, the ARM sends an initialised signal to the ADC to launch the conversion process, as presented in Figure 4.7. After the Enable (pin's name) receives the start signal from the ARM, the ADC allows the signal to pass the converter, and then the first conversion is launched, as shown in Figure 4.10. It is worth noticing that the IDLE step configuration always enables the Fast-Multiple Sampling (FMS) mechanism, which cannot be avoided. The ADC has to experience the initial IDLE state, following the IDLE configuration in the first conversion process. After that, the ADC could operate with the actual configuration. Thus, it is necessary to monitor the perturbation before it is used in the measurement system in terms of removing the effect of the IDLE activity.

Onboard ADC Sampling Rate

The sampling rate of the ADC is determined by the total number of clock cycles. How many clock cycles used for the conversion depends on the ADC configuration. The main considerations in the configuration include the maximum ADC clock speed, sampling delay, open delay, clock divider, averaging sampling and the

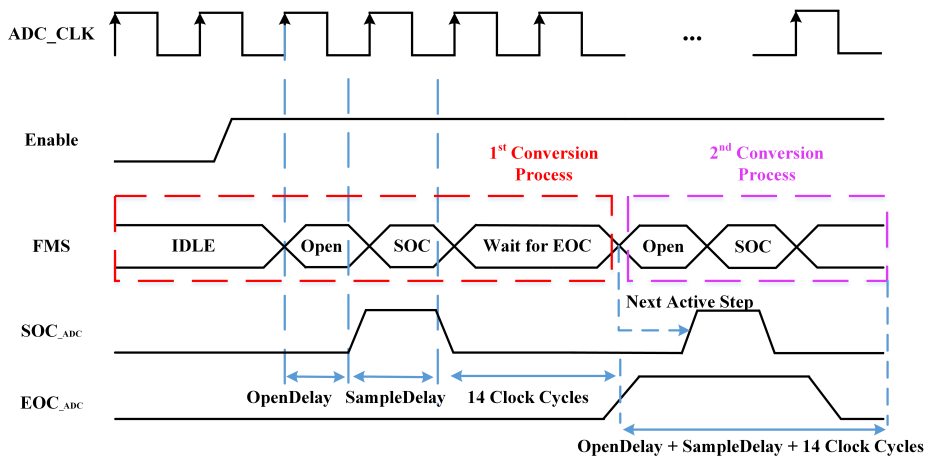

Figure 4.11: Timing Diagram for Sequencer FMS

number of active channels. Next, the number of clock cycles used in the process of the conversion is discussed.

Traditionally, the conversion process spends an identical execution time to convert analog signals in an ADC. However, the conversion process of the onboard ADC is a bit different. As mentioned before, during the fist conversion process shown in Figure 4.11, the ADC works with the IDLE configuration where the execution time is larger than the expected set for the ADC.

A number of clock cycles are allocated to different conversion states. The open delay ($OpenDly$) exists before the start of conversion. It is normally used to increase the waiting time before the conversion begins.The start of conversion (SOC_{ADC}) focuses on the conversion part. The conversion is terminated until the state approaches the end of conversion (EOC_{ADC}). The next conversion only occurs when the (EOC_{ADC}) sends the signal to the FMS. During this process, the FMS skips to the sample delay ($SampleDly$) state from the open delay state which uses the minimum of one clock cycle, and the ADC completes sampling the channel data in 13 cycles. Statistically, the sum of open delay and sample delay together with fixed cycles of 14 is the execution period for the individual channel of the ADC.

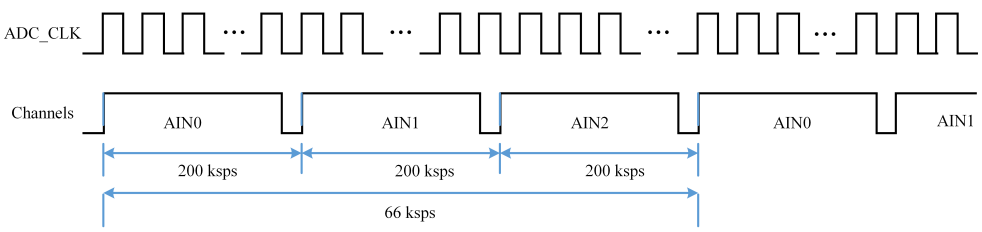

Figure 4.12: Timing of Clocks Across Three Active Channels of ADC

After the ADC finishes the first default process of the IDLE, the conversion moves to the next stage and follows the ADC set to convert signals. In the second stage, there is no IDLE step to extend conversion time so the sampling rate of the ADC from this process begins to follow the configuration. Hence, the sampling rate can be calculated as the averaging sampling is taken into account.

$$f_s = \frac{24MHz}{clk\_div \times 2 \times channels \times (Opendly + Avg \times (14 + SampleDly))} \quad (4.16)$$

Where clk_div is the ADC clock divider and represented as a number to the power of two [146, 147]. The average configuration for samples only happens to sampling time that increases the total sampling duration of active channels due to sampling processes being iterated when the average is called. In the ADC implementation, the clock divider is 4, and the open delay is set at 5, resulting in a sampling frequency for 3-channel active ADC at the full throughput frequency of 200 kHz. The operating frequency of the ADC is valued by one-third of the full throughput of 66 ksps. This is due to active channels being allocated by the same sampling duration and the active channels acquiring the signals in sequence, as shown in Figure 4.12.

Due to the sequent sampling mechanism of the ADC, acquiring battery signals has the problem of the time delay of the sampling, resulting in a phase shift. Figure 4.13 shows a related phase difference between two sinusoidal signals in the time domain. For a sinusoidal signal, two common assumptions are used

to mark the start of the cycle: (1) the point approaches the maximum value; (2) the point occurs at the values changing from positive to negative zero-crossing. Correspondingly, two presentations for the phase difference between two sinusoidal signals can be deployed, as shown in Figure 4.13(a). The phase difference is caused by the sampling latency t_d. The onboard ADC samples battery signals (voltage and current for impedance calculation) at 200 ksps with two channels, AIN0 and AIN1, which means that the latency between channels is caused as those channels sample signal in series. In this case, the theoretical phase shift (ϕ_{t_d}, in degrees) can be calculated as:

$$\varphi_{t_d} = \frac{t_d}{T_s} \times 360 \tag{4.17}$$

where the latency is t_d and T_s denotes the period of the sinusoidal signal.

Figure 4.13(b) shows a ADC acquisition test with two active channels at the sampling rate of 100 ksps. It can be observed that time delay between the voltage (in blue) and current (in red) at the measurement frequency of 1 kHz. The time shift in the illustration is 10 μs, resulting in phase shifts of 3.6 degrees ($(10us/1ms) \times 360 = 3.6$). This test can provide an evidence that phase delay effect of ADC is caused by the time delay, and the time shift equals to sampling rate between two closed channels of the ADC.

Therefore, in the proposed measurement, the minimum period of the sinusoidal signal (AC perturbation) is approximately 0.75 milliseconds (1.32 kHz, discussed in Section 4.2.4), leading to about 2.37° phase difference ($(5\mu s/0.75ms) \times 360 = 2.37$) when the sampling rate is set at 200 ksps. This phase shift caused by the sampling time delay is certained and it acts as a systematic error in the impedance measurement, which means it is possible to compensate for it in the measurement calculation. The true phases of battery signals are obtained by an extra phase shift calculation as the ADC sampling rate is fixed (see Section 4.2.5).

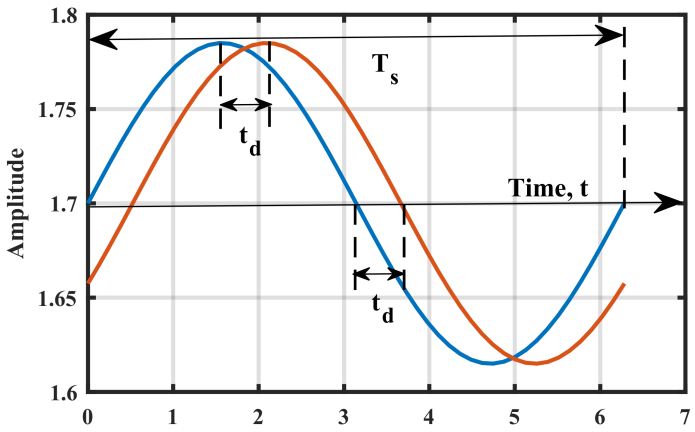

(a)

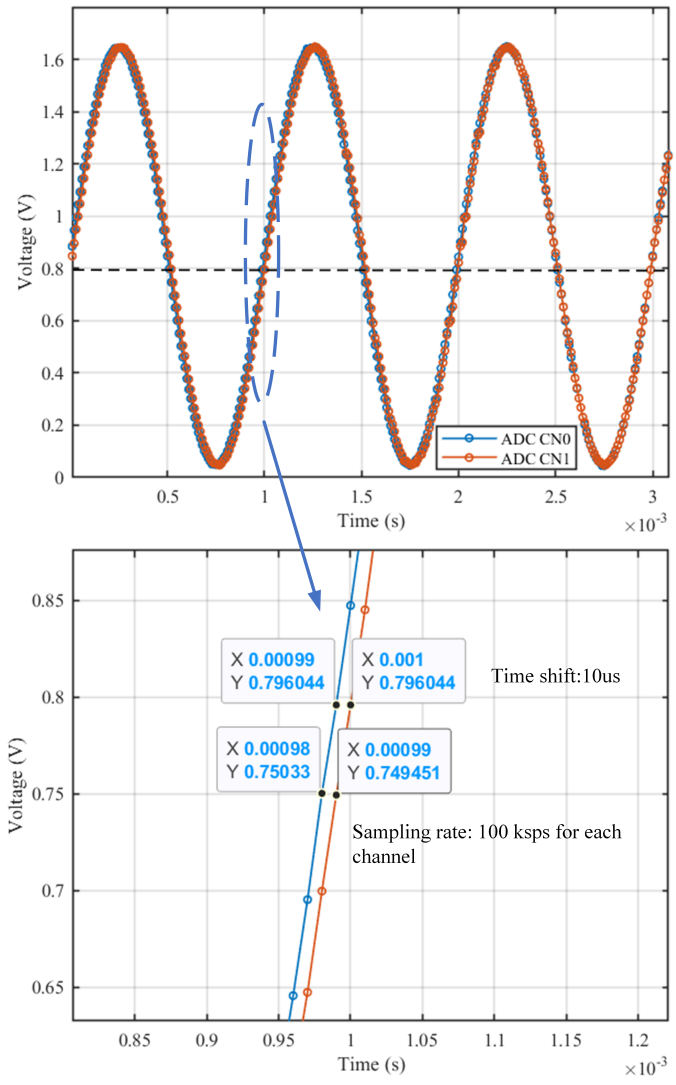

(b)

Figure 4.13: Voltage and Current Waveforms with A Relative Phase Difference

(a) the time scale is arbitrary; (b) two active ADC channels acquiring 1 kHz sinusoidal signal at the sampling rate of 100 ksps.

Onboard ADC Quantisation

The ADC of the BBB has optional levels of the quantisation: 10-bit and 12-bit. As previously discussed, a larger bit of quantisation leads to a smaller quantisation error. Consequently, measurement performance can be reformed. In practice, the onboard ADC performs as the 12-bit quantiser, yielding nominally 4096 (2^{12}) quantification levels for the inputs of all active channels. Hence, the voltage resolution (ΔV) of the ADC under the 1.8 V reference voltage and the 12-bit quantisation level, is given by:

$$\Delta V = \frac{1.8V}{2^{12} - 1} \approx 0.44mV \tag{4.18}$$

Accordingly, the corresponding quantisation error is less than 0.22 mV as rounding and truncations occur in the quantisation that refers to the half values of the quantisation resolution equalling the absolute of quantisation error, as expressed by (3.21). In fact, battery signals consist of two parts: DC and AC. For the DC part, the battery nominal operating voltage is around 3.6 V, and the minimum working voltage is located at the cut-off voltage of 3.0 V. Besides, the current measurement results obtained from the current transducer are over 2.5 V (it is the minimum value measured directly from the current transducer). All values of measured voltages will be processed for the onboard ADC acquisitions below 1.8 V (discussed in Section 4.2.2). The analysis of quantisation performance on the proposed measurement will be given in Chapter 5.

On the contrary, for the AC part, the amplitude of the AC current perturbation is restricted within 5% of the DC set. If the DC set of battery discharge current is 1.7 A, the peak-to-peak value is 0.17 A. The voltage response (in peak-to-peak value) in this condition would be around 0.17 mV as the battery impedance is assumed at 1 $m\Omega$, which is almost close to the quantisation error

(if equal to the quantisation error, it results in 100% error). Actually, the impedance values of the lithium-ion battery used in this thesis are 40x higher than those traditionally quoted for a new Lithium-ion battery used in transportation [2, 13, 107, 120]. It means that the error for signal acquisition is less than 2.5%. Even though the voltage signal is filtered by the first-order filter, the quantisation error would not exceed 6.25% (under the 0.4-rated dividing condition), which can be accepted for the measurement based on low-cost devices. Therefore, the onboard ADC shows a reasonable accuracy for the proposed measurement system.

Other factors, including $\pm 2LSB$ gain error, $\pm 0.5LSB$ differential non-linearity, $\pm 1LSB$ integral non-linearity, and $\pm 2LSB$ offset error (all values are typical values), contribute to the overall errors of ADC [129]. During the measurement, the offset error does not affect the AC measurement and therefore it does not affect the impedance measurement. On the contrary, the gain error influences the amplitude of measured signal but it can be neglected when the signal is small. Besides, the differential non-linearity and integral non-linearity affect measurement value directly so those two errors are kept in this work [148]. In this case, the error reference of ADC of 1 LSB is used (this is the maximum error among quantisation error, differential non-linearity and integral non-linearity). In the future, those errors will be minimised when the largest bit of ADC of 16 is implemented.

4.2.4 Perturbation Setting Values for PI controller

A direct storage method was implemented on loading the perturbed current setting values to the PI controller in the PRU. As the introduction on the BBB's physical memories in Section 3.5.1, shared RAMs act as data tubes, connecting to two critical units: PRU and ARM, which yields data to communicate interactively and efficiently. The shared RAM has a 12 kB memory size, which is sufficient

to contain a few samples for the PI control's AC perturbation setting. If 50 samples for constructing an AC perturbation is set as unsigned short integers (2 bytes memory space occupied) in the C program, only 100 bytes memory size is demanded. When comparing with the full memory size of 12 kB, no more than 1.0% of the storage size of the shared RAM is used to reserve those samples.

Here, 50 samples were used to construct the perturbation in a single period. The frequency of the AC perturbation is created by the proposed real-time system. This construction process is similar to sampling analog signals by ADCs. In practice, every sample is read with a constant time interval in the PRU of the BBB. So, the frequency f_p of perturbation is defined by the system's frequency f_{system} multiplied by the coefficient of $1/N_{samples}$ where $N_{samples}$ denotes number of samples for the perturbation setting in the PI control algorithm. The definition of the frequency f_p of an AC perturbation is given as:

$$f_p = f_{system} \times \frac{1}{N_{samples}} \tag{4.19}$$

The more samples are configured to the perturbation, the more accurate sinusoidal waveform is constructed. Nevertheless, for the proposed measurement, more samples are read by the real-time system, meaning that a lower frequency of perturbation is obtained. This frequency variation significantly affects the maximum frequency of the AC perturbation for the measurement, whereas it does not limit the minimum frequency of the AC perturbation.

As the real-time system operates at 66 kHz, 50 samples read by the system individually results in the maximum excitation frequency at 1.32 kHz ($f_p = \frac{66k}{50} = 1.32kHz$) and the minimum frequency is temporarily set at 0.05 Hz (with a frequency divider $n_{frequency\_divider} = 26666$, $f_p = \frac{66k}{50}/26666 = 0.05Hz$). In this condition, the frequency bandwidth (from 50 mHz to 1.32 kHz) covers

the vast majority of electrochemical characteristics: mass-transport effects (in the low-frequency range from millihertz to hertz), charge-transfer and double-layer effect (within the middle-frequency margin between hertz and kilohertz) and resistive effect (at over kilohertz frequencies), which meets the purpose in the frequency range for the EIS measurement.

Next, discrete-time values of the perturbation are employed as references in the PI controller. When the current-mode control is taken into account, only the AC current perturbation needs to be set in the control algorithm. In practice, the current is sensed by the current transducer and then acquired by the ADC. Thus, two data conversions exist in the current acquisition. If the battery discharges with the configuration on the discharge current rate of 0.5 C, in agreement with 5% of the AC amplitude limitation, the operating current of the battery will consist of the DC base of 1.7 A and the AC component of 0.085 A, as shown in Figure 4.14(a) by red circles. Besides, the sensed current is shown in Figure 4.14(b) by blue circles.

In the same situation, the current acquisition exceeds the ADC's measurement limitation because the output voltage of the transducer is initialised at 2.5 V and increases linearly with positive current clamping. As a gain of 0.4 of the voltage divider was set (in order to meet the requirement of the ADC on the voltage measurement range from 0 V to 1.8 V), the measured current (by the transducer) varies in an acceptable voltage range from 1.04 V to 1.22 V (for the onboard ADC acquisition), corresponding to a battery discharge current rates of 0.3 C and 0.5 C, respectively. Afterwards, the ADC can acquire it directly. When the ADC completes the signal acquisition (including sampling and conversion), the current data (in12-bit digital formula) is transferred to the CPU (of the BBB) and then used by the PI controller algorithm. Thus, it is necessary to keep the AC setting in the same data formula for the control algorithm. The current perturbation is presented by the 12-bit ADC conversion, as illustrated in Figure 4.14(c).

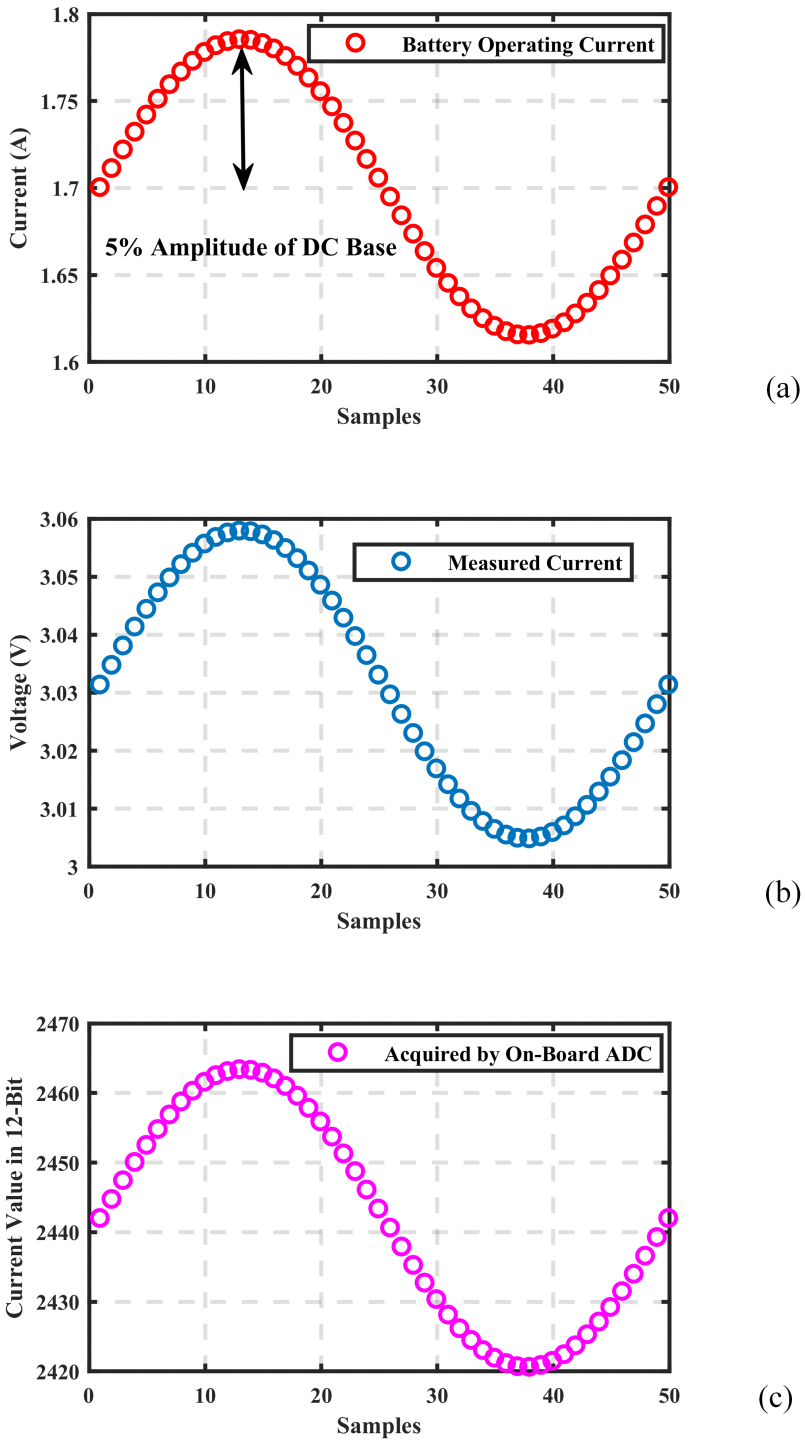

Figure 4.14: Settings for the PI Controller Based on I-V Conversion and 12-bit Perturbation Setting Values for the PI Controller

4.2.5 Data Length Implementation for Single Tone Detection in Online Impedance Measurement

In this thesis, the "online" battery impedance measurement method is deployed. During the impedance measurement, the online system operates continuously and periodically without any interruption on the impedance measurement. The flexible data length is decided to be used in the measurement in order to accelerate the measurement. This measurement speed has a significant influence on the operating duration of the EIS-based state estimations for lithium-ion batteries (discussed in Section 5.6).

Data Length Consideration for the Goertzel Algorithm

Figure 4.15 shows the flowchart of the online impedance measurement in the non-real-time operating environment of the BBB. The flowchart includes four processes of fixed data length for the proposed measurement. The first relevant process is data selection. Selecting data occurs in the ARM at the beginning of the measurement in terms of guaranteeing that all the data comes from the system underlying the steady-state condition. In practice, accounting the selection duration can be replaced by counting the data length because of the constant speed of data transfer between the PRU and the ARM.

If the fixed data length of ($L_{data\_selection}$) is set for the data selection, the time of the data selection ($t_{data\_selection}$) equals the ratio of the data selection length ($L_{data\_selection}$) to the frequency of the real-time system (f_{system}), which is expressed as:

$$t_{data\_selection} = \frac{L_{data\_selection}}{f_{system}} \tag{4.20}$$

During the selection period, data can be transferred from the PRU but does

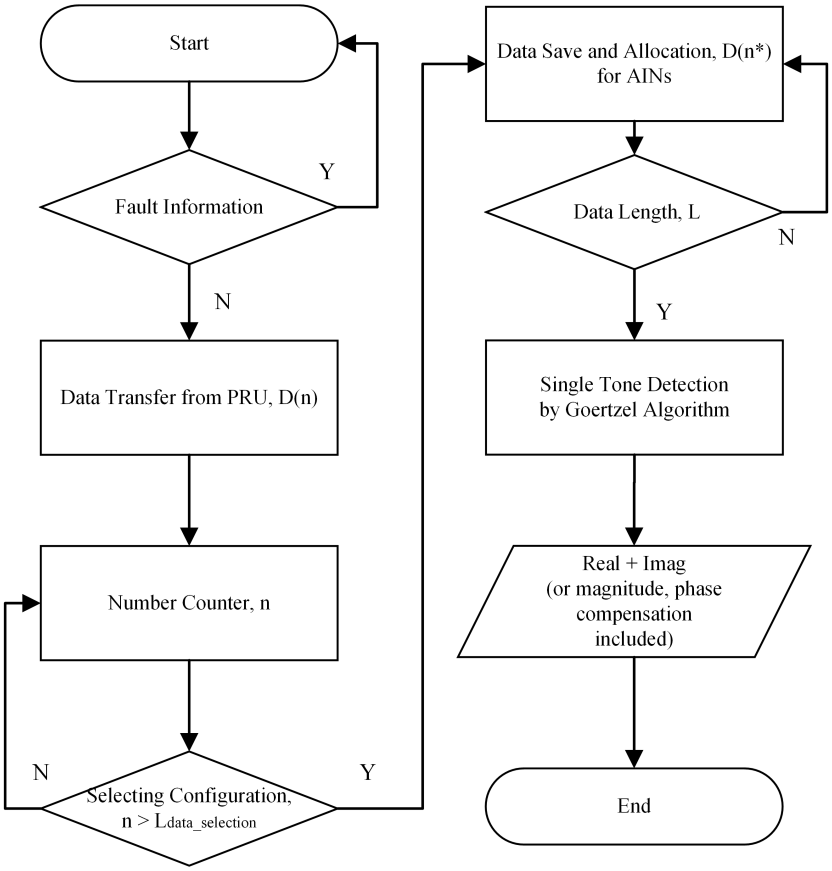

Figure 4.15: Flowchart for the impedance algorithm in ARM

not allow to be saved by the data array in the ARM. Once the measurement approaches static battery operation, measurable data starts to be sent to the impedance calculation through the ring buffer. In the data transfer process, these data should be classified properly due to ADC subsequent acquisition.

As presented in Figures 4.9, the ADC data is transferred from the PRU to the ARM via shared memory, following the order from first to last, which is similar to the order of storing data in the FIFO buffer. Besides, data are saved in sequence in the FIFO with the order: AIN0, AIN1, AIN2. To classify those data into ADC channels, the data allocation is used prior to saving data into the data array.

It is worth addressing that the data length acts as an important vector in the impedance measurement, which affects the impedance accuracy and the impedance calculation speed (which therefore affects the speed of the whole measurement system). In theory, a larger data length brings a higher accuracy for the domain-transfer calculation. However, a larger data length results in a longer duration not only for the transfer calculation but also for the data transfer. In order to balance the data length issue for impedance measurements at different frequencies, a constant measurement time window (this is an initial decision and more tests are still on-going) is deployed.

Additionally, a fixed data number setting is applied to the data allocation in order to guarantee the number of data required by the transfer algorithm. This setting allows the data length stored in arrays to be a bit bigger than the actual requirement of data length L. In this case, the data length L is a flexible identification. Theoretically, determining data length is related to two items: the excitation frequency and the sampling frequency of the ADC. If the excitation frequency is f_p and sampling frequency is f_s, the data length L of a measurement

time window can be given as:

$$L = \frac{f_s}{f_p} \tag{4.21}$$

In addition, the data length is used for a single channel (of the ADC), including at least two measurement time windows. By this way, the domain transfer algorithm can average the amplitude of the tone spectrum, so that a more accurate result can be gained. As a consequence, the data length (L) is more than twice as the total data length stored in the ring buffer. Finally, the result of the battery impedance at the given frequency can be obtained by the posted Goertzel algorithm.

Tone Detection in the Full-Scale Amplitude Spectrum

Since the definition of the data length L is confirmed, how to detect the tone frequency is critical. According to the proposed algorithm, some intermediate processing is completed with the independent sample, and the actual tone detection happens every kth sample. When compared to the FFT on the k-sample consideration, the proposed algorithm on the target frequency demands only k calculations, whereas FFT demands a larger number of $klog2k$ to result in full-scale frequencies. In practice, the single-frequency injection method is utilised for impedance measurements, so only a single spectrum at a certain frequency is concerned.

As shown in Figure 4.16, five frequency elements are chosen for examples, including 50 Hz, 120 Hz, 200 Hz, 300 Hz and 400 Hz. The sampling rate of 1000 sps and the data length of 100 are applied to the Goerztel algorithm and FFT. Consequently, the detected frequency of 120 Hz can be found at the number of 13 ($k_{target} = 13$) in all 50 frequency samples (blue circles shown in Figure). The

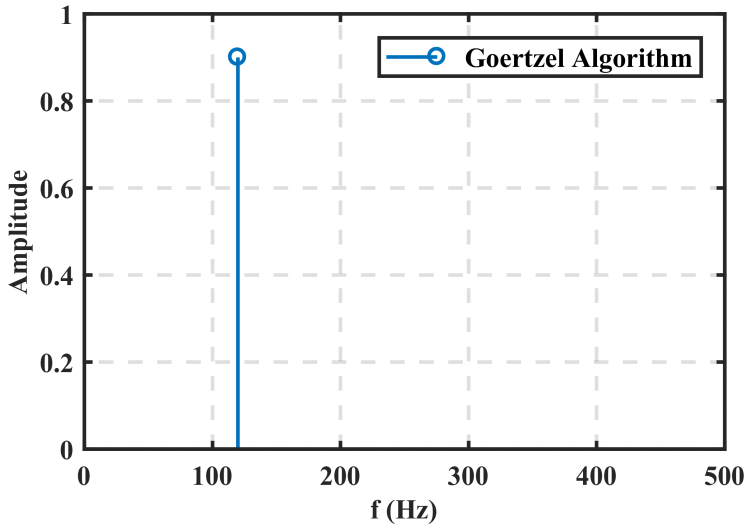

(a)

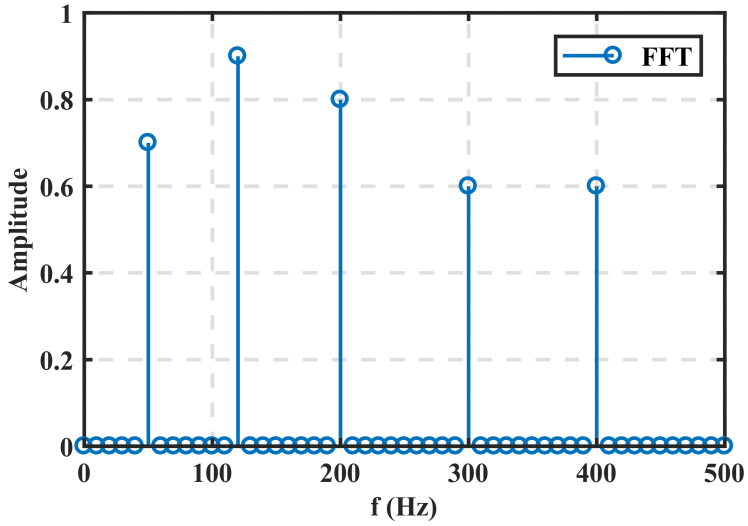

(b)

Figure 4.16: Goertzel Algorithm vs FFT At Five Exampled Frequencies

The transformed targets are multiple sinusoidal signals with five frequency components of 50 Hz, 120 Hz, 200 Hz, 300 Hz and 400 Hz; their corresponding amplitudes are 0.7, 0.9, 0.8, 0.6 and 0.6.

detected number k_{target} is given as:

$$k_{target} = \frac{f_T}{(f_s/L)} + 1 \tag{4.22}$$

where f_T is the target frequency. Particularly, the single frequency detection algorithm is developed from the FFT algorithm (discussed in the next section). An external 1 is added to the derivation because of the DC component (0 Hz) of the spectrum being involved. It is noteworthy that the ratio of sampling frequency f_s and the data length L indicates the frequency resolution in the FFT spectrum. Moreover, the full scale of frequency presented in the spectrum is half of the sampling frequency based on the single side amplitude implementation for the FFT. Therefore, the single frequency detection algorithm (or Goertzel algorithm) can correctly estimate the frequency component of interest.

Programmable Implementation for the Goertzel Algorithm

The Goertzel algorithm is a way of calculating an individual Fourier coefficient. It turns calculating a Fourier coefficient into implementing a second-order filter and using that filter for a fixed number of steps. Figure 4.17 shows the direct form of the second-order filter implementation [149] for the Goertzel algorithm. When considering the z-domain transfer function (3.54) of the Goertzel algorithm in the filter application, three different time states are relevant to the function. The current time activity ($c(n)$) is governed by three factors, called the last time state (Z^{-1}), the two times ago state (Z^{-2}) and the input sample $x(n)$, which can be represented in the program by three variables, $P0$, $P1$, and $P2$.

$$P_0 = coeff \times P_1 - P_2 + x(n) \tag{4.23}$$

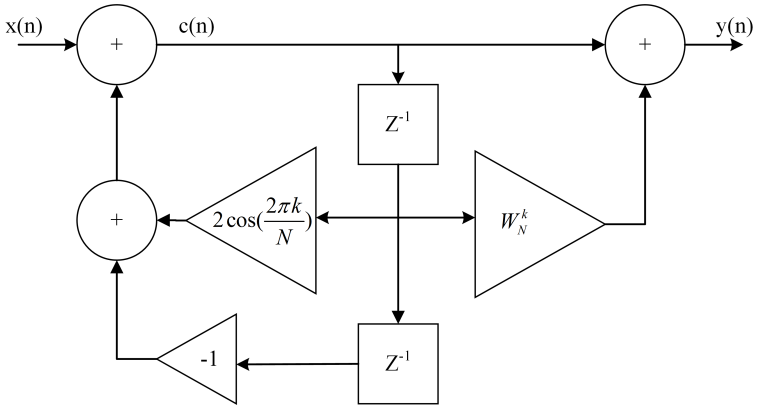

Figure 4.17: Direct Form of IIR Filter Implementation Base on the Transfer Function in (3.54)

The constant coefficient ($coeff$) is equal to $2\cos(\frac{2\pi k}{N})$, where k is the detected number of the target frequency as derived by (4.23). N is the total data samples (or data length L) used by the algorithm. However, time states are not constant due to the time moving forward without any interruption in the measurement. It means the previous current-time state ($P0$) changes to the last-time state ($P1$) and the original last-time state ($P1$) turns to the last two-time state ($P2$). Accordingly, the time-passing states can be defined in the application.

$$P_2 = P_1 \tag{4.24}$$

$$P_1 = P_0 \tag{4.25}$$

Before the start of computing different time states, apposite constant parameters that contribute to determining $coeff$ and k should be initialised, such as sampling rate f_s, sample number N (or data length L) and the target frequency f_T. In addition, the past time performances on $P1$, and $P2$ should be defaulted to zero, corresponding to the zero activity of IIR during the past time ($t < 0$) before the start time ($t = 0$). After the algorithm runs N times, the

numerical real and imaginary parts can be obtained:

$$real = P_1 - P_2 \cos(\frac{2\pi k}{N}) \tag{4.26}$$

$$imag = P_2 \sin(\frac{2\pi k}{N}) \tag{4.27}$$

If the magnitude of the tone is desired, two optional ways can be used:

$$magnitude = real^2 + imag^2 \tag{4.28}$$

$$magnitude = \sqrt{P_1^2 + P_2^2 - P_1 P_2 coeff} \tag{4.29}$$

Finally, the initial phase (φ) calculations for battery signal measurements are expressed, which can be deployed to remove the phase difference caused by the time delay of the ADC sampling.

$$tan(\varphi) = \frac{imag}{real} \tag{4.30}$$

The *atan* function provides a straightforward way to obtain φ in the C program. For the voltage phase (φ_V) calculation, the phase definition (4.31) is directly used for the initial phase for the voltage measurement. But for the current phase calculation (φ_I), an additional sum should be added to the calculation (4.31) in order to fetch the initial phase ($\varphi_{I\_initial}$). This is because the phase shift moves in the right direction, as shown in Figure 4.13, which means that the phase shift of about 2.37° is added to the current signal at 1.32 kHz (in mathematics, $\varphi_{I\_initial} = \varphi_I + 2.37$). Alternatively, the phase shift can be eliminated in the impedance calculation. A simple compensation for phase calculation ($\varphi_{impedance}$) is set in the impedance calculation at 1.32 kHz, given by:

$$\varphi_{impedance} = arctan(\frac{imag}{real}) - 2.37 \tag{4.31}$$

Other phase shifts, responding to impedance measurements at different frequencies, will be discussed in Section 5.2.

4.3 Experimental Prototype Setup

A poof-of-concept prototype is built in the laboratory in order to validate the proposed online impedance measurement method. The prototype provides a possibility to estimate battery SOC online. The experimental prototype consists of only one kind of cylindrical lithium-ion battery of 3.3-Ah 18650-size, a bespoke DC-DC boost converter and a resistive load.

The switching frequency of the DC-DC boost converter is synchronous with the ADC operating frequency. As three ADC channels are used for signal acquisition, the operating frequency of the ADC operates at 66 kHz. Notice that the operating frequency equals to the switching frequency of the converter, and in this case, only one ADC sample is captured during a switching period.

Figure 4.18 shows the flowchart of the proposed online impedance measurement system. This flowchart is split into two parts. The first part (a) depicts the complete real-time processes of the BBB on the signal acquisition, the PI digital control and the soft PWM (set by the GPIO). In this part, a small sinusoidal perturbation of the current is defined to the PI controller in terms of updating the duty cycle of the power converter that starts the impedance measurement operation. The acquired data by the ADC is read from the FIFO and then written into a fixed-size ring buffer dynamically. The time resolution of the buffer writing between samples synchronising to the period of the real-time loop is 15 microseconds.

The second part operating in the ARM describes the online impedance

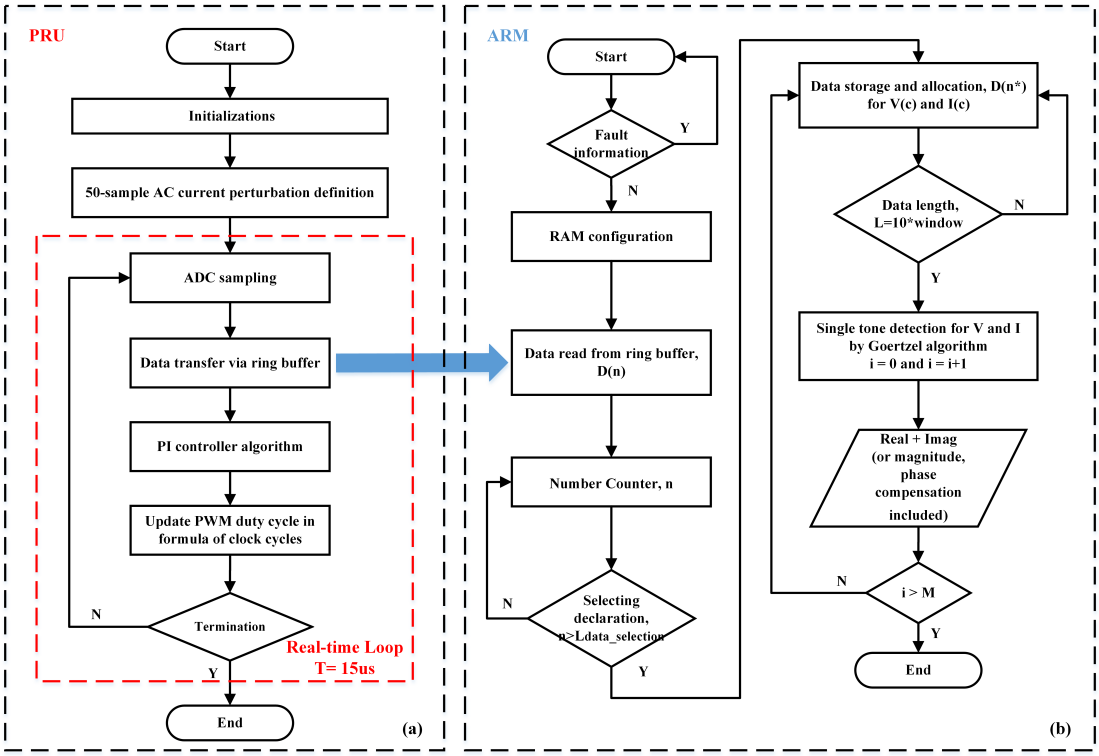

Figure 4.18: Flowchart of the Proposed Online Impedance Measurement System

(a) complete real-time signal acquisitions and controllers in the PRU; (b) online data transfer and impedance calculation in the ARM.

calculation process. This part mainly shows a short-time strategy for data processing for the Goertzel algorithm in order to achieve a fast impedance evaluation. After the data is read from the ring buffer, the data selection abandons the first number of data. The number of the data elements obtained is at the trade-off between the impedance measurement accuracy and the time that the impedance measurement process takes. If a larger number is set for the data selection, it will expand the total time on the data transfer, leading to a slower online measurement speed.

The data allocation happens after the data selection, which is set to allocate the transferred data into three categories: current, voltage and temperature. The lengths of data are utilised to the measurement depending on how many windows are configured for the Geortzel algorithm. As discussed previously, at least two periodic data length should be employed by the algorithm in order to average the amplitude to reduce random errors in the measurement. According to this method, if two measurement time windows are configured for the Goertzel algorithm, the measured signal can be averaged in amplitude at the detected frequency (A measurement time window contains the constant length of data where the length is defined by the ratio of sampling frequency f_s and perturbation frequency f_p). Another averaging impedance technique is applied to the online measurement system, which enhances the accuracy of the measurement. Conventionally, one periodic perturbation (f_p) can be calculated to obtain numerical impedance in complex format. Nevertheless, the battery voltage ($V_{real} + jV_{imag}$) and current ($I_{real} + jI_{imag}$) are measured in practice over M (more than one) consecutive measurements, aiming that the system is not operating in a transient condition and reduce the random measurement errors during the measuring process. A relevant investigation on the measurement cycles M [13], where they chose the value M of 5 to achieve the trade-off between the measurement accuracy and speed, is referenced in the experimental prototype, as shown in Figure 4.16.

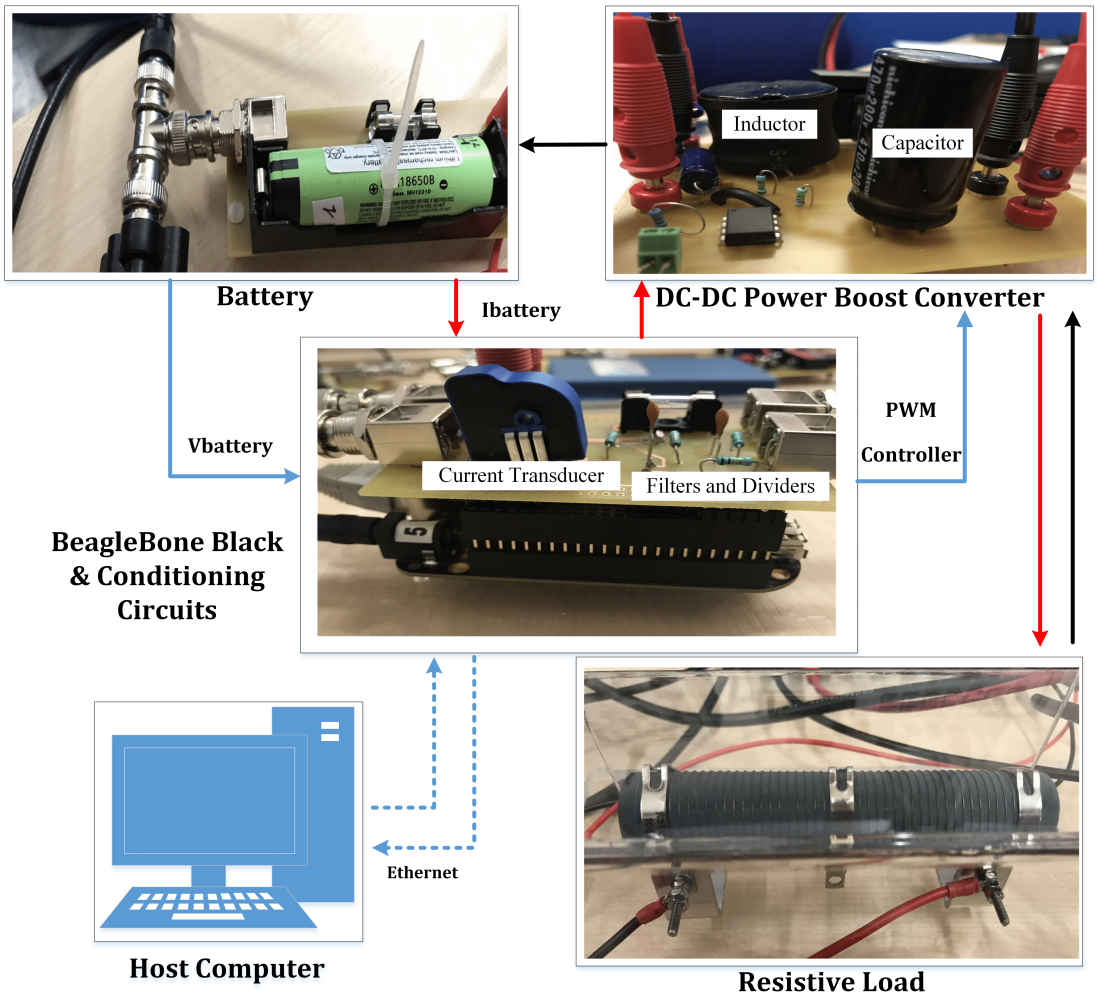

Figure 4.19: Photographs of the Experiment Setup, Voltage Measurement in Blue and Current Measurement in Red

Photographs of the prototype are shown in Figure 4.19. A single cell is directly connected to a bespoke DC-DC converter and drives a resistive load. In addition, the data communication between the BBB and the PC is achieved via Ethernet.

The visible inductor in the illustration is the 1.0 mH designed for a 66 kHz switching frequency and the capacitor in the illustration is the 470 uF implemented with a wide rated voltage range (from 6.3 V to 450 V). The control strategy of the electronic switch is provided by a comprehensive input/output system, where the computer controls the BBB's RPU, ADC and GPIO remotely via Eclipse IDE (Integrated Development Environment). The control algorithm contained in the system is employed in the 200 MHz real-time processor unit of the BBB. The cell current is measured by a Hall effect current transducer, the bandwidth of which is up to 100 kHz. Besides, the output voltage and the battery voltage are processed by the conditioning circuits, the ratio of voltage division and the cut-off frequency of which are 0.35 and 2.0 kHz, respectively.

Afterwards, the processed signals are captured by the 12-bit onboard ADC of the BBB with 6.6×10^4 samples-per-second sampling rate. Meanwhile, those data can be transferred to the non-real-time platform in the BBB's ARM so that the calculations for impedance are accelerated. Finally, the impedance results excluding phase shift (caused by the sampling delay) can be displayed on the computer's screen.

It is worth noting that for the commercial implementation on battery AC impedance measurements, many measurement circuits are integrated in the instrumentation already. So based on this method, the measurement circuits were integrated and embedded on the PCB (Printed Circuit Board), as shown in Figure 4.18. Therefore, the cost and space size of battery AC impedance measurement is reduced.

4.4 Chapter Summary

In this chapter, hardware designs and implementations are mainly discussed for the proposed impedance measurement system. The values of the inductor and capacitor of the DC-DC boost converter are determined based on the design rule on the low ripple and high switching frequency as well as operating specifications of the chosen battery. Oversize voltages (including battery terminal voltage and measured voltage of the current transducer) cannot be directly measured by the ADC because of voltage limitation, so the same conditioning circuits are set in the voltage and current measurements. The benefit of using the same circuit is avoiding the effect of the phase difference on the measurement. Under the same consideration, the theoretical phase difference caused by the time delay of the ADC sampling is included, which only affects the current measurement. Eventually, this phase difference is compensated by the proposed impedance calculation.

Chapter 5

Experimental Prototype Results

This chapter mainly shows the experimental results of the prototype, including the power transfer performance of the bespoke power converter, the real-time controller, and various dependencies of impedance measurement on battery state-of-charge, discharge current rate, and ageing. Meanwhile, the equivalent circuit model developed by fitting these measurable results is included. Finally, measurement duration is exhibited as a critical factor to determine the measurement frequency of the system.

5.1 Measurement System Verifications

The first test was carried out to research the power transfer performance and examine the proposed controller strategy of the bespoke DC-DC boost power converter. In practice, the converter is connected to a lithium-ion battery, operating with a constant discharging current. An AC perturbation at 0.5 Hz is injected into the battery operation. In addition, the switching frequency of

the converter consists in 66 kHz and the controller gains (for proportional and integral items in the control scheme) are $k_p = 1$ and $k_i = 1/900$.

5.1.1 DC-DC Converter Performance of the Proposed Online Measurement System

The performance of the bespoke converter (shown in Section 4.2) is evaluated in an online measurement system where the battery powers a 10 Ω resistive load. In the measurement regarding power transfer performance, a NI USB-6366 (DAQ) was used to monitor the terminal voltage (of the battery), the discharge current (of the battery) and the load current, as shown in Figure 5.1.

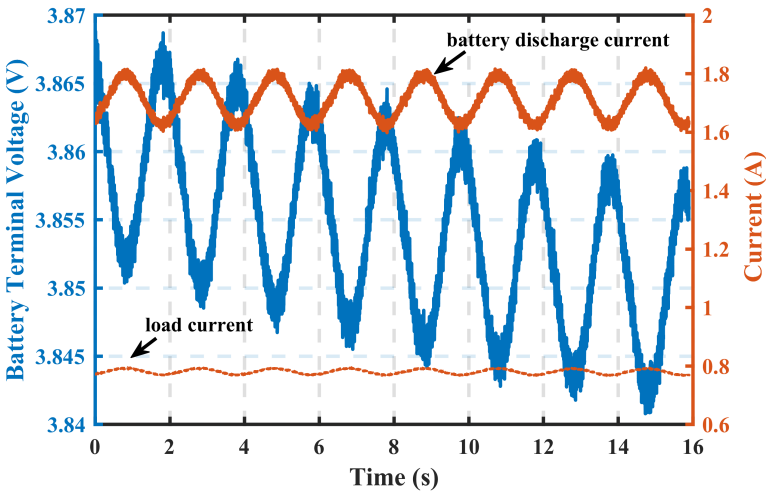

Figure 5.1: Measurements for Calculating Power Efficiency of the Bespoke Converter

Statistically, the cell voltage holds a DC base of around 3.855 V, and the input current performs with the DC value of around 1.7 A at the frequency of 0.5 Hz. In addition, the DC value of the load current is approximately 0.78 A. Therefore, the efficiency of the power transfer from the battery to the load can

be roughly calculated with DC value:

$$\frac{(0.78)^2 \times 10}{3.855 \times 1.7} \times 100\% = 92.8\% \tag{5.1}$$

5.1.2 Real-Time Controller Performances of Proposed Measurements

Despite the fact that the nominal value of battery impedance is usually given in the specifications of the battery at the frequency of 1.0 kHz [150–153], the proposed impedance measurement method is used in this work to measure the impedance at multiple frequencies. Frequencies of AC excitations directly determine the frequency of impedance. In practice, AC excitations were generated by the power converter with the real-time controller mechanism, and seventeen frequencies were considered (not limited to these frequencies, except for the maximum frequency) in the measurement system: 0.05 Hz, 0.5 Hz, 1.0 Hz, 2.1 Hz, 4.3 Hz, 6.5 Hz, 10 Hz, 100 Hz, 111 Hz, 121 Hz, 167 Hz, 190 Hz, 220 Hz, 333 Hz, 440 Hz, 660 Hz and 1320 Hz.

The above mentioned frequencies have a close association with the maximum frequency. A common understanding is that values of frequencies are obtained from a maximum frequency value (1320 Hz in the proposed system), dividing it by the frequency divider ($n_{frequency\_divider}$). In fact, the single operating frequency of the system is the baseline for frequency variations. During the measurement based on the single-frequency perturbation method, all frequency behaviours are modified by the single system operating frequency of 66 kHz. As discussed in Section 3.3, the frequency performance can be presented by the time clock cycle due to constant time resolution (5.0 nanoseconds) of the PRUs of the BBB. The clock cycles are counted from the first instruction of ADC acquisition to the completion of the PWM off state. Theoretically, the total number of clock

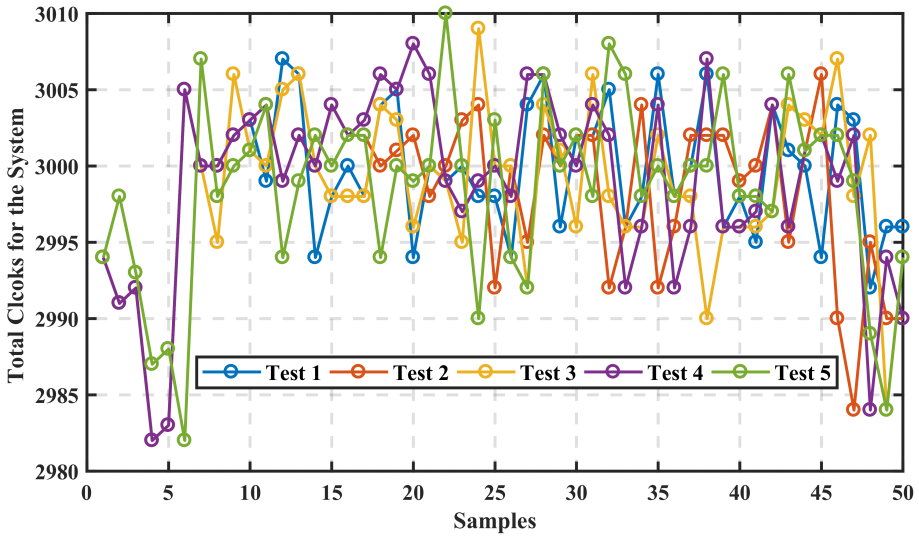

Figure 5.2: Real-Time Control Based on Timing-Clock-Counting Method

cycles of 3000 should be measured. Corresponding clock cycles for the maximum frequency of 1320 Hz are recorded by a single system operation in five experiments. There are 50 measurable targets shown in the illustration for a single test due to 50 individual samples for the AC reference setting in the PI controller. The illustration also portrays that the vast majority of cases maintain approximately 3000 clock cycles, but a few cases act around 2980 clock cycles. This is caused by the clock cycle resolution in the PRU. Besides, the number of clock cycles in five tests are around 3000, which determines the frequency at 1.32 kHz ($66kHz/50 = 1.32kHz$), meeting the expected result of the maximum frequency.

Analytically, some samples hold observed differences as compared to the desired number of clock cycles in Figure 5.2. The observations show that clock cycles for the real-time system slightly vary within the value range from 2980 to 3010, and the maximum variations are 18 cycles at around the fifth sample. Consequently, these discrepancies would cause the real-time performance of the system with an error of no more than 0.6% ($\frac{18}{3000} \times 100\% = 0.6\%$). On the one

hand, the vast majority of clock cycles vary within the range from 2990 to 3010 because the minimum resolution of 10 cycles is developed to compensate for PWM execution time under the C operating condition, shown in Figure 5.3(c). For the differences over 10 clock cycles, in the most possibility, this is due to the floating-point controller algorithm. In Figure 5.3(a), data are read from ADC to PRU with static execution time (266 or 265 clock cycles, equalling 1.33 microseconds), but variable numbers of clock cycles are consumed by the PI controller algorithm. Thus, such performance of the clock cycle in the PWM compensation is obtained in response to those varieties. Even though PI controller algorithm and PWM activity need to face reported tiny variations of clock cycles, their operating frequency still meet with each other due to the unique time performance of the real-time system.

In theory, clock cycles for the fixed-point behaviour (such as add and subtract computations) in a fixed-point processor should be stable. Nevertheless, the operation of fractional multiplications (such as integral coefficient of 1/900 in the PI controller algorithm and other fractional coefficients in the PWM compensation algorithm) are employed to the fixed-point operating condition. They require more complicated codes to maintain the fixed-point position from the floating-point position, so various numbers of clock cycles are needed. In fact, slight frequency variations would not mark significant effects on the frequency determination, which is identified by the representations of AC excitations in the frequency domain, as shown in Section 5.1.2. If it is desired to improve the stability performance of the clock cycle, a floating-point processor could be used, but the cost of the improvement increases.

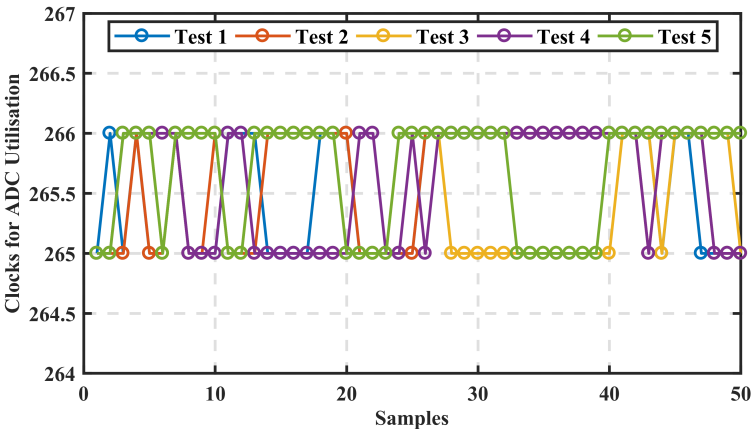

(a)

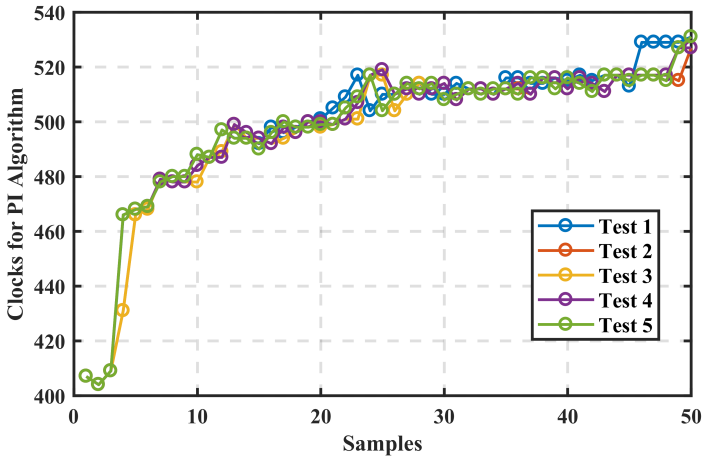

(b)

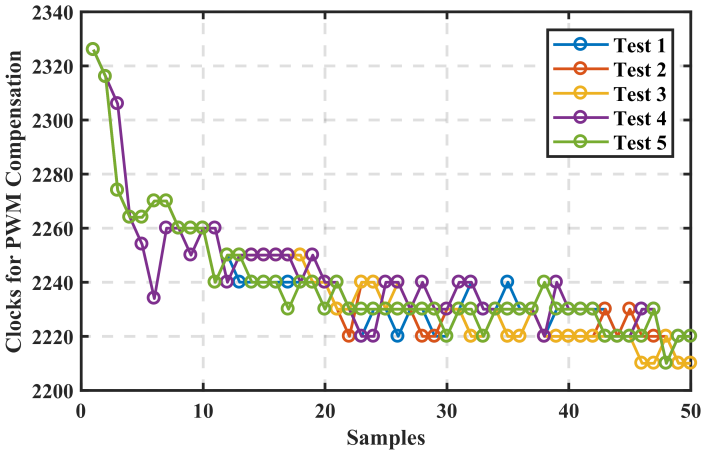

(c)

Figure 5.3: Counting PRU's Clocks in Five Tests for Different Functions: (a) Signal Acquisitions via ADC; (b) PI Controller; (c) PWM Compensation

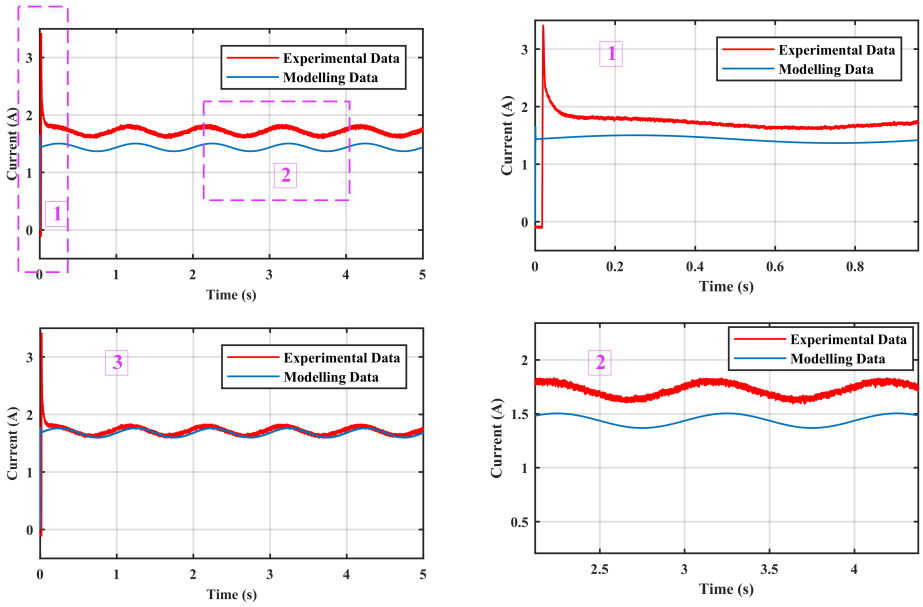

Figure 5.4: Performance of Current-Mode PI Controller At Perturbation Frequency of 1.0 Hz; Sub-plots No.1 and 2 are used to represent the control in transient and state conditions; The sub-plot No.3 shows the different set on proportional parameter of the PI controller, $kp = 10$, where the integral parameter does not change.

Current-Mode Controller Performance Baesd on DC-DC Boost Converter

The performance of the proposed real-time current-mode control strategy for the online battery impedance measurement is compared to the simulation result. The averaged method of DC-DC converter modelling and a traditional PI control were deployed to model the proposed control strategy (as discussed in Section 4.2.1). The experimental data was collected under the condition where the current reference for the control strategy includes DC current base of 1.7 A and 0.085 A (5% DC current base) AC excitation. Besides, the frequency of the AC excitation is 1.0 Hz and the battery operating voltage works at around 3.88 V with a 10 Ω resistive load, resulting in the duty cycle varying at around 0.52. Likewise, the modelling data was collected in the corresponding condition.

Both sets of data are presented in Figure 5.4. It can be observed that the experimental data has a matched performance with the theoretical result (modelling result) when the system approaches its steady state at around 75 milliseconds. In the time range from 0 to 75 milliseconds, as shown in the sub-plot No.1 both results include transient responses, such as the overshoot. Notably, the value of the overshoot collected from experiments is apparently larger than the model's. When the converter model is compared to the prototype, the differences between them consists of resistive losses of passive electronic components (such as inductor and capacitor) and battery effects. The resistive losses only impact power dispersion, while the battery effects such as capacitance would affect transient responses. Thus, based on the above analysis, the apparent discrepancies should be caused by the effect of the battery capacitance (that can boost the transient responses as its state is suddenly changed).

In another sub-plot No.2, the experimental result shown in the illustration is expected. The AC perturbation has an amplitude of 0.085 A, performing with the current base of 1.7 A, which is in agreement with the control purpose. The modelling data was collected under the same parameter configuration (see Table 4.2). The amplitude of the AC perturbation is approximately 0.085 A, matching the control setting. Both amplitudes (of the model and experiment) are not attenuated. The frequencies of AC perturbations are of the interest (reported in Section 2.2), covering the range form millihertz to kilohertz. However, the model acts with a smaller current base (at around 1.5 A) than the expectation due to a smaller proportional parameter of PI controller. As shown in the sub-plot No.3, this difference decreases as the proportional parameter increases.

5.1.3 AC Perturbations for Impedance Measurements

Although the maximum frequency of AC perturbation is limited, it still contains the main discharge dynamics as reviewed in Chapter 2 within the frequency range from 1.0 Hz to 1.0 kHz. As mentioned above, seventeen frequency candidates have been shown for the proposed measurement. When the battery dynamic characteristics distribute at low, middle, and high frequencies, corresponding impedance measurements should meet the requirement on the frequency region from millihertz to kilohertz. Ideally, it is necessary to measure all frequencies to reconstruct the electrochemical impedance spectrum for lithium-ion batteries. But in practice, especially during the online measurement, if all frequency components are measured, the duration of the measurement will last for several hours, which cannot be accepted by small-scale battery applications. To tackle this issue, the multiple-point impedance spectrum method can be adapted. In this method, the impedance spectrum is reconstructed by partial spectrum components in the proposed frequency range (discussed in Section 5.2).

In general, a battery operates at the nominal condition as the baseline for comparison. So, the tests were arranged with a single cell powering a 10 Ω resistance load at the nominal voltage value of around 3.55 V (equalling the SOC level at 60%) at a room temperature of 22-23°C. To monitor the impedance spectrum, waveforms of terminal voltage and discharge current were obtained at the mentioned frequencies in tests. The frequency values, including 0.05 Hz, 1.0 Hz and 1320 Hz, are selected as examples and illustrated in Figure 5.5 (a), (b) and (c).

As discussed previously, the battery operating current is sinusoidally controlled at multiple frequencies, which varies around its steady-state DC base of around 1.7 A (in response to 0.5 C current rate). In the illustrations (Figure 5.5(a) and Figure 5.5(b)) at low frequencies (0.05 Hz and 1.0 Hz), the DC base is

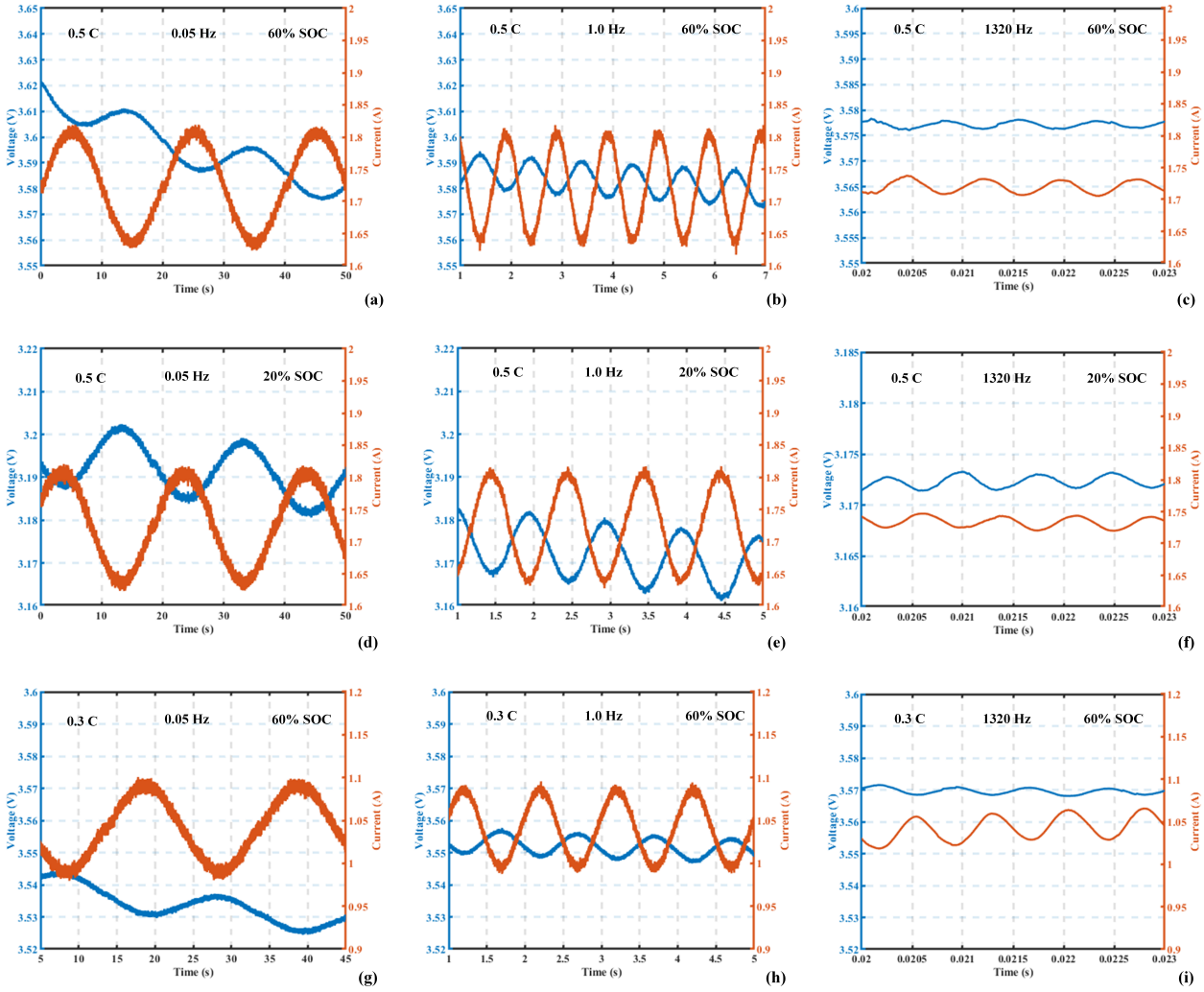

Figure 5.5: Monitoring Battery Signals at Example Frequencies Under Different Measurement Conditions; (1) 60% and 0.5 C :(a) 0.05 Hz, (b) 1.0 Hz and (c) 1.32 kHz; (2) 20% and 0.5 C: (d) 0.05 Hz, (e) 1.0 Hz and (f) 1.32 kHz; (3) 60% and 0.3 C: (g) 0.05 Hz, (h) 1.0 Hz and (i) 1.32 kHz; All signals were monitored during battery steady-state operation (operating time exceeds 0.075 seconds)

valued at the discharge current of around 1.7 A (or 0.5 C discharge current rate based on the battery capacity), and the peak amplitude of the current oscillation is 0.085 A (5% DC base). Therefore, the value of the current varies between 1.65 A and 1.82 A in a sinusoidal manner. Corresponding terminal voltage values of the battery can be obtained between 3.55 V and 3.61 V, performing with amplitudes of approximate 0.01 V and 0.008 V, respectively. Additionally, the remaining sinusoidal waveform illustrated at the maximum frequency (1320 Hz), works with a smaller current variation (peak-to-peak value less than 0.1 A). As a consequence, the amplitude of the voltage response at 1320 Hz is much smaller than the previous discussed voltage behaviours at low frequencies.

A larger peak-to-peak amplitudes of current oscillations (than the expected value of 0.17 A) can be observed at low frequencies in the illustration because the noise measurements are included. This noise may come from the off-the-shelf board, conditioning circuits, or the current transducer. In fact, noise components would not influence the impedance results as proper processing with a domain transfer algorithm is used. For example, the single tone detection algorithm will be employed to deal with experimental data from the time domain to the frequency domain, as a consequence only the main frequency components are targeted in the impedance calculation.

On the contrary, a smaller current amplitude is shown at 1320 Hz, which is an expected phenomenon (caused by the frequency responses of the PI controller and the low-pass filter as shown in Figure 4.4 and Figure 4.6) as the fixed control parameters and first-order filtering technology were deployed. In theory, the amplitude attenuation would not affect the result of the impedance measurement. This is because the same filter results in current and voltage attenuations identically, which can be eliminated in the impedance calculation. Besides, the PI controller only impacts the amplitude of current executions. A smaller current amplitude would receive a smaller voltage response. The result

of the battery impedance would not vary with the current amplitude variation as the measurement occurs at the given frequency.

Another worthily notable measurement phenomena at different frequencies is voltage drift. As shown in Figure 5.5(a), Figure 5.5(b) and Figure 5.5(c), the voltage decrease during the monitoring duration is around 0.035 V at 0.05 Hz in the measurement duration of 50 seconds. However, the voltage drops are nearly 0.015 V at 1.0 Hz in 6 seconds and almost zero at 1320 Hz in 0.003 seconds. These measurement results indicate that a long-term measurement leads to a larger power consumption so a larger voltage drift responds to this regard. For the online impedance measurement system, terminal voltage variation is a severe problem that significantly influences on the accuracy of the impedance measurements. More details regarding the effect caused by voltage drift will be discussed in Chapter 6.

In addition, the long-time battery operation would cause an increment of the internal temperature of the battery [24], which results in negative effects to the measurements. As a consequence, impedance measurements at extremely low frequencies are avoided as far as possible in practice.

Waveform Dependency on SOC and Current Rate

In general, the dependency of the electrochemical impedance spectrum is investigated on the SOC and the current rate in many studies [24, 27, 53, 72, 99]. These studies have pointed out that the SOC variation leads to a significant change in impedance values and the spectrum responds to that variation uniquely in the specific frequency region[7, 154, 155]. For the current rate dependency, relative works show that different current rates would not trigger such crucial variation to the impedance spectrum [13, 107]. In order to examine the influences of SOC

variation and current rate on the impedance of battery, the lowest healthy SOC value of 20% and a lower current rate of 0.3 C were chosen as a comparison. For more details, experiments were set with two underlying battery operating conditions: the SOC value of 20% (terminal voltage of about 3.18 V, shown in Figure 4.2) for the current rate of 0.5 C and the SOC value of 60% for the current rate of 0.3 C. The former would provide a comparison with normal battery operation (60% SOC and 0.5 C) to identify SOC dependency of the impedance spectrum. The latter would provide a reference to analyse the effect of current rate on the impedance spectroscope in the concerned frequency range.

Figure 5.5(d), Figure 5.5(e) and Figure 5.5(f) demonstrate the examples of sinusoidal excitations under the 20% SOC and 0.5 C measurement condition. Similarly, the sinusoidal perturbation values of the battery current were set with 1.7 A DC base and 0.085 A AC variation, obeying the 0.5 C measurement rule. But the terminal voltage of the battery reduces to 3.18 V in response to 20% SOC. It can be observed that the effect of the frequency response of the PI controller also attenuates the amplitude of the current at the maximum frequency. The voltage drift is about 0.02 V at the frequency value of 0.05 Hz with measurement duration of 50 seconds. Besides, the voltage drift value of 0.01 V meets at the frequency value of 1.0 Hz in the measurement time of 5 seconds. They are slightly different from the reported values of the voltage drift at the corresponding frequencies (0.05 Hz and 1.0 Hz) under the same measurement duration (50 seconds and 5 seconds, respectively) and current rate (of 0.5 C). The reason behind this difference may be a lower sensitivity of the battery to OCV changes at a lower SOC.

Moreover, a lower current rate of 0.3 C (about 1.0 A) was set in terms of investigating the effect of current rate on impedance measurements, as shown in Figure 5.5(g) and Figure 5.5(h) and Figure 5.5(i). The lower current rate (less than 1.7 A) could cause a lower amplitude of AC excitation (due to the amplitude

limitation of AC perturbation followed in this thesis: 10% DC current base) and a lower voltage drift (if the measurement duration is identical).

In this case, the amplitude of current perturbations was also configured at 5% of the 0.3 C current rate. It means that the AC amplitude of excitations reduces to 0.05 A. Under this measurement condition, voltage drifts can be observed at two frequencies: 0.05 Hz and 1.0 Hz, the values of which (about 0.012 V and 0.005 V) perform in the same time scale much smaller than the values (about 0.03 V and 0.01 V) obtained in the nominal current rate (0.5 C) measurements. Other measurements regarding battery impedance will be shown in the following sections.

5.2 Online Impedance Measurement Results

In this section, the results of the online impedance measurements under nominal battery operation (0.5 C and 60% SOC) are discussed in priority. Impedance-related signals were measured at seventeen frequency elements in response to the aforementioned frequencies in Section 5.12.

It is worth noting that the physical connection resistance ($R_{connection}$, the pure resistance) would be included in the measurement due to the resistivity of metal materials (such as connectors of the battery holder and traces of the PCB), as shown in Figure 5.7. These connection resistances result in a voltage difference ($V_{difference}$) between the object ($V_{\_object}$) and the measurement port ($V_{\_measurement}$).

Table 5.1 gives voltage differences in five repeated tests (where the battery was replaced by a DC source because the object voltage should be stable during the tests). An assumption was put forward that the voltage of the battery remains the same in AC conditions. It is worth noting that the mean voltage difference is

Table 5.1: CONNECTION RESISTANCE FOR SINGLE CELL

No.	$I_{\_load}$ (A)	$V_{\_object}$ (V)	$V_{\_measurement}$ (V)	$V_{difference}$ (V)	$R_{connection}$ (Ω)
1	1.754	9.55	9.48	0.07	0.0399
2	1.754	9.55	9.48	0.07	0.0399
3	1.754	9.55	9.48	0.07	0.0399
4	1.754	9.55	9.48	0.07	0.0399
5	1.754	9.55	9.48	0.07	0.0399

All tests happened under the same measurement was condition where the 9.55 V DC power supply connected with a 5 Ω load resistor, and the operation lasted for a few minutes; A RS PRO RS14 Handheld Digital Multimeter was used to measure voltages and the load current.

around 0.072 V and the mean connection resistance is 0.0399 Ω. For an accurate impedance representation, the 0.0399 Ω connection resistance will be subtracted from the calculated impedance results.

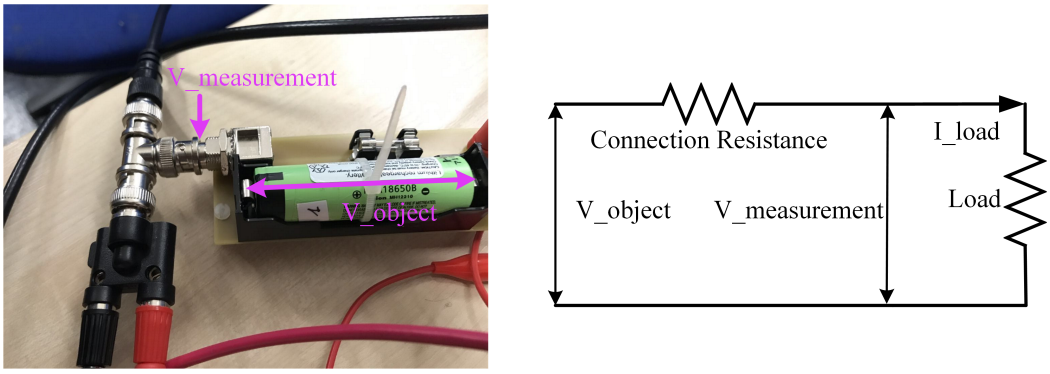

Figure 5.6: Battery Current and Voltage Performance for Identifying Steady-State Operation, Monitored by NI USB-6366

Impedance calculations have a close relationship with the battery terminal voltage and current, as expressed in (3.12) and (3.13). During the measurement, the data of voltage and current were acquired by the onboard ADC and then

sent to the impedance calculation (including a domain transfer algorithm). Two kinds of data lengths affect the impedance measurement accuracy, as discussed in Section 4.2. One exists in the data selection, which was used to guarantee that all the measured data was collected in the battery steady-state operation. In terms of protecting all measurable signals from transient influences, a constant waiting period method for the data selection was deployed.

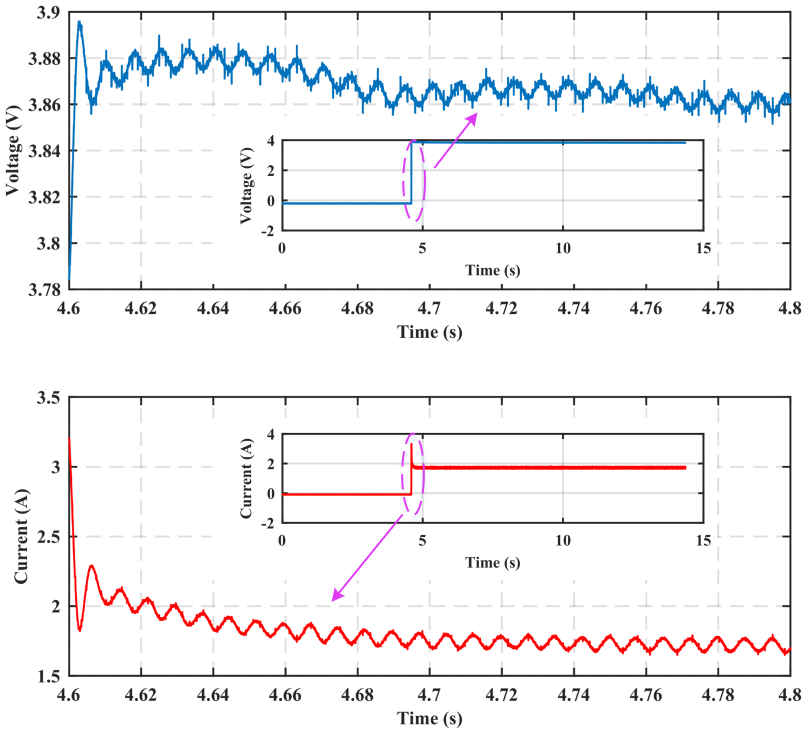

Figure 5.7: Battery Current and Voltage Performance for Identifying Steady-State Operation, Monitored by NI USB-6366

Figure 5.7 shows the current performance and corresponding voltage behaviour. Meeting the stable operating condition means the current should vary around the control setting of 1.7 A and the voltage response needs to be sinusoidal. According to the illustration, the current approaches its steady state at around 4.675 s (including about 4.60 s operating time without battery) and

the expected response of the voltage nearly starts from 4.62 s (including the same operating time without battery).

In theory, a longer waiting time can protect the measurement form transient influences. However, it would lead to several problems during the battery operation, such as a bigger voltage drift and a higher temperature rise. Therefore, the threshold of the waiting time of 0.075 ($4.675 - 0.075 = 0.075$) seconds is decided to be used in this work, which could minimise such effects.

The other type of the data length considered in the measurement is the actual data length applied to the domain transfer algorithm. As is well known, the data length of the transfer algorithm relates to the frequency resolution as the sampling rate is fixed. In general, a larger data length can access more precise resolution for identifying the target frequency.

However, in the online impedance measurement, processing massive data means that not only an extremely high ability of CPU and large space of the memory are required but also a long duration for the measurement is needed. In order to balance the accuracy of the impedance calculation and the data length (see Section 5.6), the fixed measurement time window method for controlling data length was used.

The data length used in the domain transfer algorithm is related to the measurement time window. A measurement time window focuses on the constant number of data for a specific sinusoidal signal. The total length of data covered by a single window equals the ratio of sampling rate to the frequency of sinusoidal perturbation, as expressed in (4.19). When the number of measurement time window of 10 is used in measurements at frequencies: 1320 Hz and 440 Hz, and a single measurement time window is employed in the measurement at the frequency

of 0.05 Hz, the lengths of data of 10×50, 10, and 1 correspond to the frequencies of 1320 Hz, 440 Hz, and 0.05 Hz, respectively.

The phase compensation algorithm is also taken into account for the domain transfer algorithm. As discussed in Section 4.2.5, the sampling delay would cause a phase shift to the battery signal acquisition (for the current). When seventeen frequency candidates are used in the measurement, it means that seventeen phase compensations are required. Those compensations (in degree) can be calculated via (4.15): 2.37 (for 1320 Hz), 1.19 (for 660 Hz), 0.79 (for 440 Hz), 0.59 (for 333 Hz), 0.40 (for 222 Hz) and etc.. With the frequency decreasing, the phase shift declines. Therefore, the maximum phase shift in the measurements is 2.37 degrees at 1320 Hz and the minimum phase shift (of around 9×10^{-5}) occurs at 0.05 Hz.

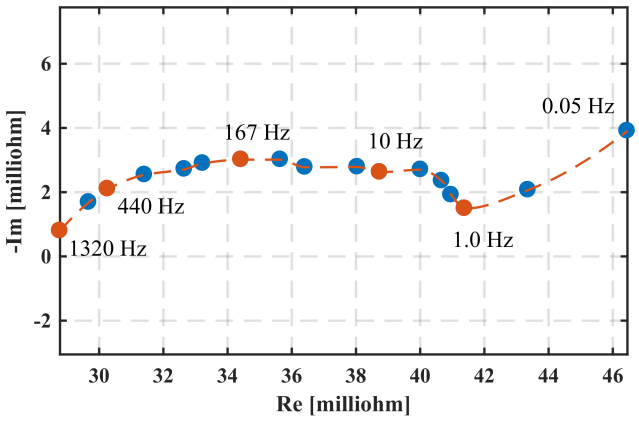

Figure 5.8: Nyquist Plot of Impedance Measurements of a Single Lithium-Ion Battery at 60% SOC and 0.5 C, rebuilding the impedance spectrum with seventeen frequency candidates (marked by blue filled circles); The 5-point reconstructing method is shown here by orange circles; A shape-preserving interpolant algorithm is employed and the fitting result is presented by the dash line.

Figure 5.8 shows the Nyquist plot impedance measurements of a single lithium-ion cell at a nominal voltage of 3.6 V and the current rate of 0.5 C. All

data were acquired in the battery steady-state operation by the BBB's ADC and processed for impedance calculations with a 10-window size of the data length (except for 0.05 Hz that processed with the data length in a single window). A common detected number k ($k = 11$) for the vast of majority of targeted frequencies could be configured in the transfer algorithm (the detected number for 0.05 Hz is 2, corresponding to a single-window configuration for the data length). It should point out that even though a minimum data length was set for the measurement at 0.05 Hz, the measurement duration still exceeds the measurement duration limitation of 50 seconds. So, the impedance result at 0.05 Hz is only presented in this section and will be removed from the remaining measurements in order to reach the temperature constancy purpose, as studied from [24].

In the illustration, the spectrum is reconstructed by seventeen frequency candidates. Besides, the low-frequency range from 0.05 Hz to 1.0 Hz shows that the spectrum in this area mostly has a straight tail of which slope is smaller than 1 (equalling 45 degrees in phase). When the frequency increases, the negative imaginary value of the spectrum gradually climbs up to the maximum value which occurs at 167 Hz frequency and then moves down to the minimum value of around zero at the frequency of 1320 Hz. According to the spectrum changes at middle and high frequencies, the spectrum can be described by a nearly smooth curve. Typically, this curve cannot be verified by a single semi-circle because the half difference of real parts between 1.0 Hz and 1320 Hz does not equal to the imaginary value of impedance at the frequency of 167 Hz. This finding provides evidence for identifying the equivalent circuit model of the lithium-ion battery in which at least two RC branches are included (discussed in Section 5.3).

The variations of magnitude and phase of the impedance are also taken into account. As shown in Figure 5.9(a), the value of the impedance magnitude declines from about 47 $m\Omega$ to 29 $m\Omega$ in the given frequency region. Besides, the phase performances are obtained in the same frequency range, as shown in

Figure 5.9(b). The phase increases as the frequency rises in the first frequency stage (from 0.05 Hz to 1.0 Hz). Afterwards, it falls sharply with the frequency rise in the zoom between 1.0 Hz and 167 Hz; finally, a significant phase increase is achieved as the frequency grows (from 167 Hz). These results regarding the magnitude and phase dynamics in the proposed frequency range are in agreement with [44, 156, 157].

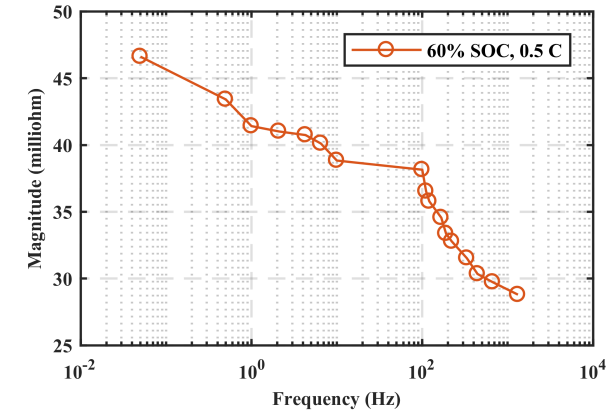

(a)

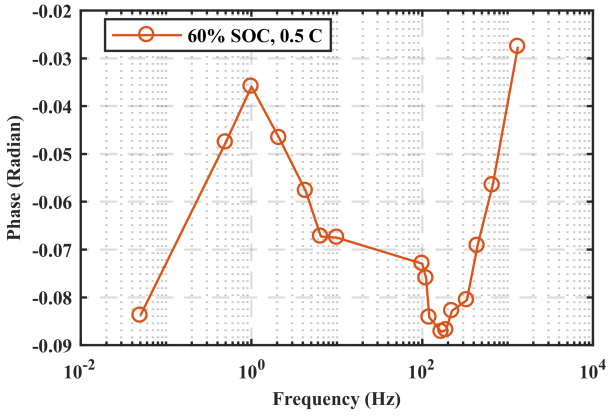

(b)

Figure 5.9: Battery Impedance Variations with Frequencies on the Amplitude (a) and Phase (b)

5.3 Equivalent Circuit Model

In general, the equivalent circuit model is used to predict battery performance and provide SOC and SOH estimations within online battery monitoring applications. In most studies [73, 92, 104, 158, 159], the model of a single cell is conventionally employed as the base. If several single-cell models are connected in series or parallel, the new model is therefore capable of representing the performance of multiple cells for a large-scale battery package.

For online SOC and SOH estimates (shown in Chapter 6), the equivalent circuit model supplies a memory-saving way to map massive EIS data in the embedded battery measurement systems [103]. As introduced in Section 2.3, equivalent circuit models are also evolved to reflect electrical equivalents of sophisticated dynamics inside the battery. An efficient and simplified combination between dynamics and electrical performances of the battery by the structure-based equivalent circuit has been reported in [1]. This thesis focuses on a cell structural version of the impedance model, which points out a direction to design customised ECM in this subsection.

The baseline of ECM corresponds to the impedance measurement under the fundamental measurement condition of 60% SOC and 0.5 C, as shown in Figure 5.8. The illustration unveils the characteristics of the impedance spectrum: at least two semi-circles and a straight trail consist of the spectrum in the given frequency margin. In order to fit the result captured from the basic impedance measurement, the first assumption is put forward to developing the ECM so that two RC branches are considered into the equivalent circuit model in response to the characteristic of the impedance spectrum shown in Figure 5.8. The RC-branch is supposed to model slow effects, for example, diffusion, as studied from [158, 159].

Figure 5.10 shows a redesigned second-order RC equivalent circuit for the lithium-ion battery. Unlike the complex model described in [1], the evolved model provides further simplifications on the replaced variables where Faradaic impedance (caused by lithium ion activities, such as gathering on the surface of the electrode [1]) and solid-phase diffusion impedance are validated by using the Warburg element (Z_w), taken from the Randel circuit as studied from [2]. It also extracts the less critical inductance due to the relatively low frequency (when compared to extremely high frequencies, for instance ten or hundred kilohertz, as shown in [95, 107]).

In RC branches, different values of resistance (R_1 and R_2) and capacitance (C_1 and C_2) are applicable to electrodes due to the different reflections of electrodes on discharge dynamics inside of the battery. The concerned reflections involve the growth of solid electrolyte interface and the change of double-layer capacitance, which are significantly associated with the proposed estimations on SOC and ageing, as explained in Chapter 2.

Moreover, the same Warburg element is involved by the model in order to indicate low-frequency electrochemical dynamics on both electrodes, such as ion diffusion and transport. To easily model those dynamics, the assumption that Warburg element is same on both electrodes is made[1, 2]. In this case, the ECM presented in Figure 5.10 only consists of an anode impedance (Z_{anode}), a cathode impedance ($Z_{cathode}$), and a pure ohmic resistor (R_0). Here, the pure ohmic resistance R_0 is used to typically represent the compositions inside of the cell: electrolyte, separator, and current collectors.

$$Z_{battery} = R_0 + Z_{anode} + Z_{cathod} \tag{5.2}$$

$$Z_{anode} = (R_1 + Z_w)||C_1 \tag{5.3}$$

$$Z_{cathode} = (R_2 + Z_w)||C_2 \tag{5.4}$$

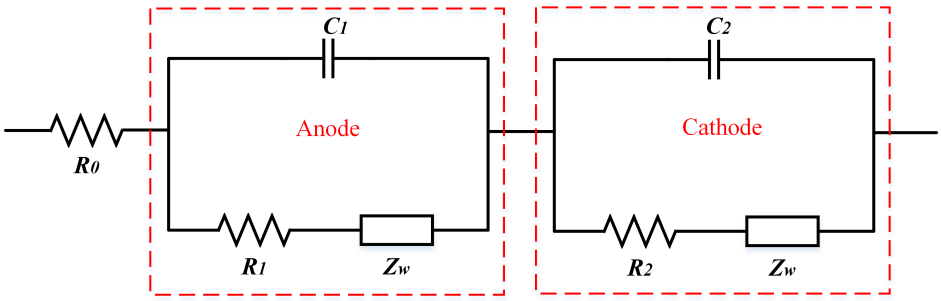

Figure 5.10: 2-RC Full Battery Cell Impedance Model, Modified from [1, 2]

For the sake of determining the parameter values of the ECM, the non-linear least square fitting method was deployed. By this method, the model result can optimally match the experimental data. In addition, the trust-region regression is one of the best optimisations for the non-linear problems [160, 161], which involves a constrained minimisation of a quadratic subject to one non-linear constraint [162]. When compared to another popular regression, called Levenberg-Marquardt regression, the previous regression is more suitable for small size of the sample (such as five samples used in this work). Notably, the regression was used on only the real part of the impedance to minimise percentage error at proposed frequencies.

Table 5.2: VALUES OF COMPONENTS IN THE BATTERY CELL IMPEDANCE MODE

R_0 (Ω)	R_1 (Ω)	C_1 (F)	R_2 (Ω)	C_2 (F)	A_w ($m\Omega/s^{0.5}$)
0.0286	0.007	0.0625	0.0052	2.5	1.39

Table 5.2 includes all component values for the battery cell impedance model. It should be noted that the mathematical expression of the Warburg element (Z_w) has been shown in Eq.(2.4), where the Warburg coefficient (A_w) is fixed in this work (therefore, only five parameters (R_0, R_1, R_2, C_1 and C_2) need to be calculated).

Figure 5.11 shows validation of the model for a single lithium-ion battery at the frequencies of 1.0 Hz, 10 Hz, 167 Hz, 440 Hz and 1320 Hz. Five results respond to five unknown parameters of the ECM, which can be used to reconstruct the impedance spectrum in the expected frequency range, as presented in Figure 5.8. Those impedance measurements correspond to five unknown ECM parameters (as the Warburg coefficient keeps constant). In this case, the whole impedance measurement can be accelerated, and eventually, a short period for the whole process (including impedance measurement and state estimation) is proposed. This is an important goal that the online impedance measurement system desires to reach in small-scale battery powered devices.

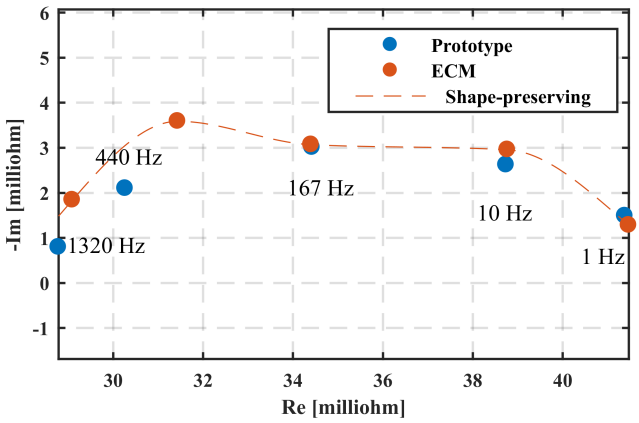

Figure 5.11: Point-Fitting Regression for Panasonic 18650 Cell at 60% SOC, 0.5 C

In Figure 5.11, all available test data (at specific frequencies) are utilised in the optimisation process and the performance of the ECM is therefore expected. Two RC-branch hypotheses for the equivalent model could be reasonably approved in the given frequency range (from 1.0 Hz to 1320 Hz). It should be noted that the spectrum at lower frequencies such as 0.05 Hz and 0.5 Hz are not used for the fitting algorithm due to instability of SOC caused by prolonged measurements at these two frequencies. Besides, obvious differences between the prototype and

modelling can be found at 440 Hz and 1320 Hz, which may arise from the accuracy of the proposed measurement system regarding domain transfer algorithm with relatively short data length (for battery signals at high frequencies).

Still, the regression is capable of reasonable matching, and obtained component values instead of the data for all frequency candidates (discussed in Section 5.1.2) can be used as a time-efficient way not only to track battery internal processes but also to estimate battery states (discussed in Chapter 6).

5.4 Dependency of Impedance Spectrum Characteristic on SOC, Aging and Current Rate

5.4.1 Impedance Spectrum Characteristic on SOC and Aging

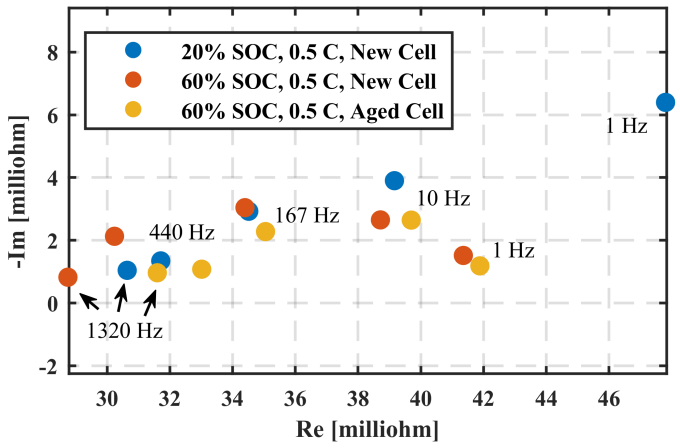

Figure 5.12: Impedance Measurements at different SOCs and Ages

Figure 5.12 shows electrochemical impedance various (including magnitude and phase changes) obtained under different measurement conditions where 20% and 60% SOCs, as well as brand-new and 3-year aged cells are included. When the value of SOC declines from the nominal level of 60% to the minimum level of 20% (in this work), the impedance spectrum at given frequencies shifts to the right in the Nyquist plot. The minimum rise (of about 0.1 $m\Omega$) of the real part of the impedance appears at 167 Hz, whereas the maximum rise (of around 5 $m\Omega$) of the impedance in real part is held at 1 Hz. This says that long-term electrochemical dynamics (of which frequencies perform around 1 Hz, as discussed in Chapter 2) dominantly affect SOC values. A possible reason can be that the reducing number of ions causes weak ion diffusion and transport [44].

Likewise, the real part of the impedance of aged cell increases slightly, varying from near 31 $m\Omega$ to 42 $m\Omega$ in the given frequency range, as compared to the brand-new cell impedance performances under the same SOC and current-rate measurement condition. This is an expected result because the impedance magnitude tends to rise as the cell becomes aged, as reported by [44, 163]. In an ageing progress, battery electrodes would be degraded, especially on the electrodes' surfaces [163]. Both degradations can increase the increase of the charge transfer resistance, and eventually increases overall the impedance of the battery [163].

In advanced offline applications within the lower frequency region, the obvious variations of amplitude at low frequencies as SOC varies are deeply concentrated by some studies where impedance variations at the low-frequency range have been applied as one of the critical indicators to predict SOC values [69, 87]. However, for the online SOC estimations, the impedance measurements at lower frequencies have to face the problem that measurements require a long duration to obtain a whole period of AC excitation, which eventually results in the proposed system performing with a low speed to estimate SOC values.

Additionally, if the EIS-based method is only applied to estimate SOC at lower frequencies, the problem could be exposed in practice that almost the same impedance spectrum obtained in the frequency range of 10 Hz to 1320 Hz, which is difficult to distinguish the dominant effect caused by SOC or ageing (further research will focus on this problem). However, battery degradation is applied to examine the proposed measurement system in this thesis, the confusing issue would not appear in the SOC estimation (discussed in the next chapter) where only brand-new cells were used in all cases.

5.4.2 Dependency of Impedance Measurement on Current Rate

Figure 5.13 shows the other experiment on exploring the effects of the current rate on the impedance measurement for lithium-ion batteries. Results at five frequencies is demonstrated in Figure 5.13(a) at 0.5 C and 0.3 C rates.

In most cases, they shows the differences between different current rates are smaller than 0.001 Ω in both parts (including real and imaginary parts) of the impedance. This says, the magnitudes and phases perform with a high- level similarity at the concerned frequencies, as shown in Figure 5.13(b) and Figure 5.13(c).

This finding would help to implement the EIS-based state estimation in the real word such as EVs and mobile robots in which the influence of discharge current can be neglected. Besides, the current rate has a close relationship with the amplitude of AC perturbations during the proposed measurement (5% DC base for configuring AC perturbation). The almost identical impedance spectrum can indicate that amplitudes of AC excitations would not influence the impedance spectrum in the given frequency range, which can be approved by [164].

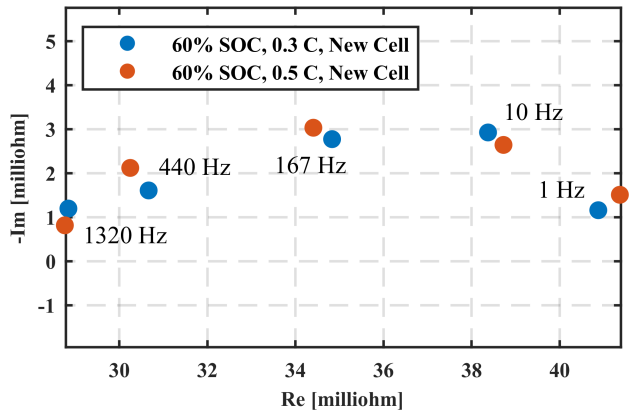

(a)

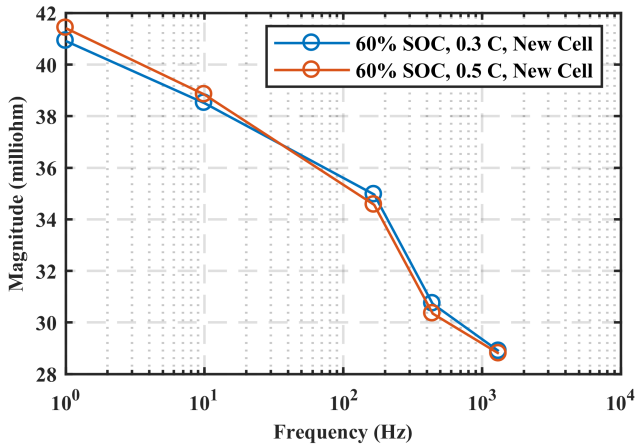

(b)

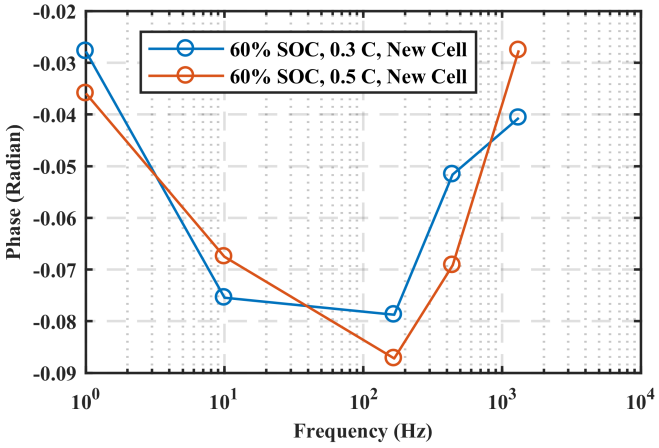

(c)

Figure 5.13: (a) Impedance Measured at 60% SOC and Different C-Rates of 0.3 C and 0.5 C; Comparisons on Magnitude (b) and Phase (c) in Bode Plot

However, when the current rate declines from 0.5 C to 0.3 C, it means the amplitude of AC perturbation reduces from 0.085 A to 0.05 A, as shown in Figure 5.5 (a) and (g) (or Figure 5.5(b) and (h), or Figure 5.5(c) and (i)). This change would bring a challenge to the bit-fixed ADC, which may impact the measurement accuracy, especially for the quantisation of the ADC (discussed in Chapter 6).

5.5 Impedance Measurement of Multiple Cells Connected in Series

As mentioned above, a single cell has a low voltage and a low power capacity, which cannot satisfy the load's requirements for high voltage and long time operation. To solve those issues, a battery package is normally used, which increases the output voltage and expands the power capacity. In a battery package (consisting of at least two cells), batteries are connected in series and parallel. In this section, the impedance measurement is taken into account in many multiple-cell applications.

The impedance performances in those applications (including series-connected and parallel-connected batteries) can be predicted theoretically (as the equivalent circuit model is known). However, several factors (caused by multiple cells and connections) significantly affect the prediction, such as unbalanced SOC, inconsistency of batteries and physical connections between batteries, which lead to measurement results larger than expected in magnitude.

These effects (especially arising from the series-connected cells) are of interest regarding EIS-based state estimations for lithium-ion batteries in the real world. So the proposed impedance measurement system can be employed to explore those interesting problems. Notably, the parallel connection for two cells

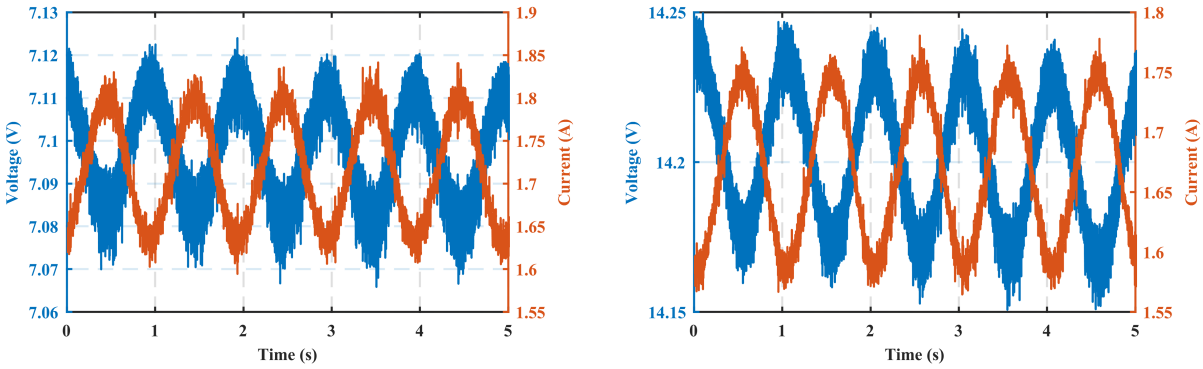

Figure 5.14: AC Coupled Waveforms for Two Cells (Left) and Four Cells (Right) in Series Connection at around 1.0 Hz and 60% SOC, Monitored by NI USB-6366

is neglected in tests due to a high-level operating risk that is caused by relatively high current transient responses.

A consistent impedance measurement was considered in tests where two and four cells were connected in series, and a single power converter was used to generate AC perturbations to the proposed measurements at the frequency of 1.0 Hz. In the experiments, the single power converter method is different from many other studies in which multiple converters are employed to obtain an independent EIS result for each cell. In this condition, the cost efficiency and control consistency can be guaranteed in the applications where a high voltage is demanded. In order to compare the impedance performance at nearly 60% SOC (7.1 V for two series-connected cells and 14.2 V for four series-connected cells), batteries are restricted to operate at those voltages. Both amplitudes of AC perturbations for the tests are around 85 mA, equalling 5% of the DC base of the battery operating current (0.5 C), as presented in Figure 5.14. It should be clarified that the value of the resistive load profile increased to 12 Ω due to the input voltage increase of the converter. So, the duty cycle can vary within the constraint caused by the real-time system (less than the maximum duty cycle of 0.7).

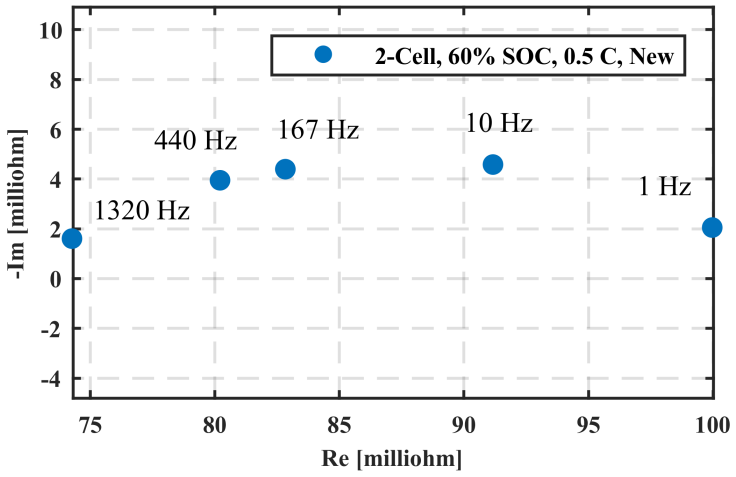

Figure 5.15: Nyquist Plot for Two Series-Connected Cells Under 60% SOC, 0.5 C and Brand-New Measurement Condition

Figure 5.15 shows the experimental results in the Nyquist plot at five frequencies: 1.0 Hz, 10 Hz, 167 Hz, 440 Hz, and 1320 Hz. Notably, the physical connection resistance (around 86.9 $m\Omega$) of two cells in series connection has been excluded (the connection resistance was measured by the same method (discussed in Section 5.2)). In the 60% SOC situation, the impedance of two cells in series presents that the real part of the impedance varies from around 75 $m\Omega$ to nearly 100 $m\Omega$ as the frequency declines. Besides, the imaginary part (absolute value) changes between around 2 $m\Omega$ and 5 $m\Omega$ in the given frequency range. When comparing the magnitude (including real and imaginary part) of the impedance in series connection with it in the single cell activity, as shown in Figure 5.16, the magnitude of series-connected cells is more than two times larger (about two and half times) than the single-cell's at all shown frequencies. Ideally, the impedance magnitude of two homogeneous cells connected in series should be doubled. The possible reasons may arise from SOC inconsistency due to an imbalanced discharged string and cell inconsistency.

On the one hand, the ideal battery string is assembled of identical cells with

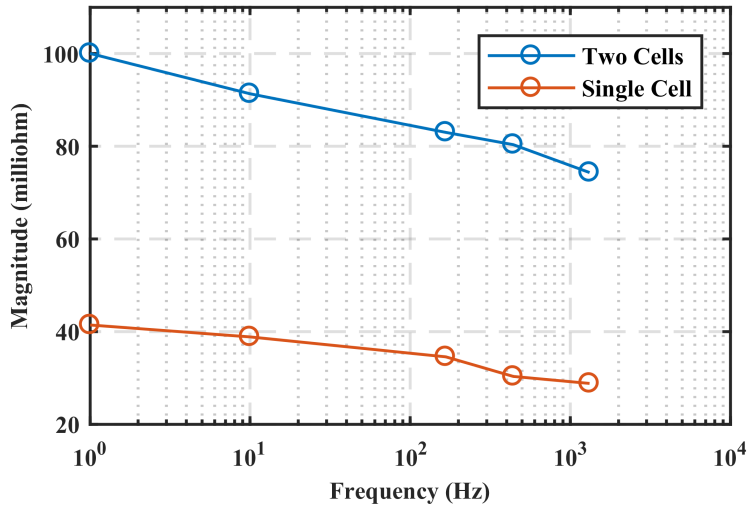

Figure 5.16: Comparison Between Different Measurements with Single Cell and Two Cells in Magnitude

the same initial SOC. In this scenario, the overall cell string SOC is the same as the value of SOC of the single cell, and ultimately, the battery gives the capacity coinciding with the nominal capacity of the cell during the discharging process. However, in the test, there was no specific voltage balanced circuit used to control each cell's voltage, so the same value cannot guarantee the level of SOC for the single cell. As a consequence, the corresponding impedance at a lower voltage (or SOC) causes that concerned difference [165]. Apart from this, cell inconsistency is taken into account, which is dominantly caused by manufacture process and materials. In general, the cell inconsistency would not make such a significant difference between two identical cells as the same factory manufactures them. Therefore, it is necessary to assemble a balanced SOC controller to a single battery as multiple cells are applied to portable devices. In this case, the cell enables the balancing technique to operate within a safe and healthy environment.

On the other hand, the accuracy of the instrumentation may be the reason why there is a difference of approximately 10 $m\Omega$ between single-cell and multiple-cell applications. This discrepancy mainly presents in the real part, as

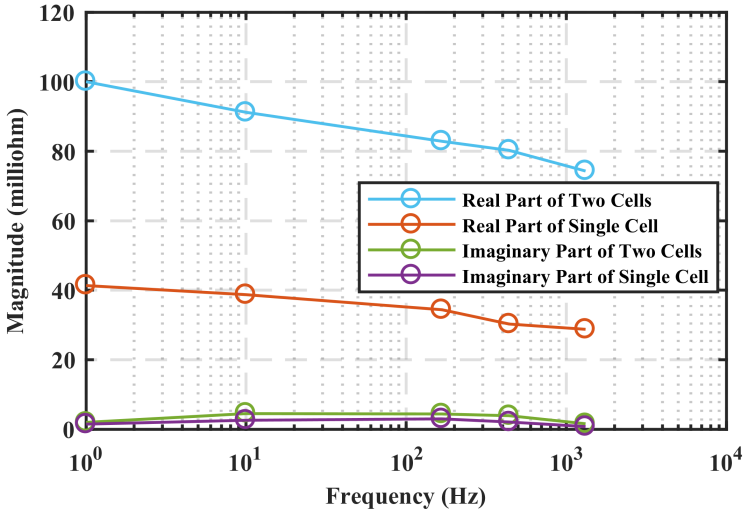

Figure 5.17: Comparison Between Different Measurements with Single Cell and Two Cells in Real and Imaginary Magnitudes

shown in Figure 5.17. In practice, a PCB mechanically supports and electrically connects several cells through conductive tracks and pads. Even though the vast majority of the connection resistance can be roughly measured by the voltage-drift measurement method, more accurate measurement could not be achieved by only using a simple multimeter (the DC voltage resolution of which is only 10 mV whilst its DC current resolution approaches 1 mA). Therefore, the voltage measurement has a lower accuracy than the current measurement. An obvious voltage difference may be obtained in the tests, and eventually it would lead to an apparent impedance difference.

Accordingly, monitoring the impedance of each cell with high accurate instrumentation for multiple-cell applications is suggested. The proposed system based on the BBB can do so (probably together with some signal conditioning circuits to convert the differential voltages of each battery into single-end voltages).

Within optimised measurements, the voltages and one current in the series

connection can be monitored simultaneously, and the voltage of each cell and the measured current can be acquired for four-cell (even for seven-cell) applications at the same time. The maximum number of voltage signals (seven) can be potentially reached by the system. However, once the number of measurable signals increases, more ADC channels should be active. Correspondingly, a lower sampling frequency (less than 66 kHz) is obtained.

5.6 Execution Time of Data Transfer and Processing

The purpose of presenting time performance is to explore the speed of the online measurement. This is a point worth considering for the EIS system, which would be used for commercial areas. The time behaviour determines how long the duration of the proposed measurement system and provides a reliable timing reference for battery state estimations. In general, the time performance is impacted by two factors in this work: the speed of data transfer from the PRU and the ARM of the BBB, as well as the number of samples (also called measurement time window).

A ring buffer mechanism is used to transfer data from the PRU to the ARM of the BBB (discussed in Chapter 3). Theoretically, the frequency of data transfer synchronises with the frequency of the real-time system operation. A fixed frequency is set to the real-time system, which means that a fixed transfer speed can be obtained, as shown in Figure 5.18. In this case, only the data length needs to be considered in this work. As is well known, the data length is usually determined by the measurement time window in the domain transfer algorithm. If a long time window is demanded, a large number of data can be used for the algorithm.

Consequently, a small frequency resolution can be achieved as the sampling rate is constant, which makes it possible to improve the spectrum accuracy. However, a long time constant leads to a slower time response of the measurement system, which causes battery state changes (discussed in Chapter 6) and additional room reflections (such as temperature). These changes would result in a low accurate impedance measurement. Therefore, a low accurate state estimation for the battery is obtained. According to this analysis, ten measurement time windows are decided to be used for this preliminary exploration on the time performance.

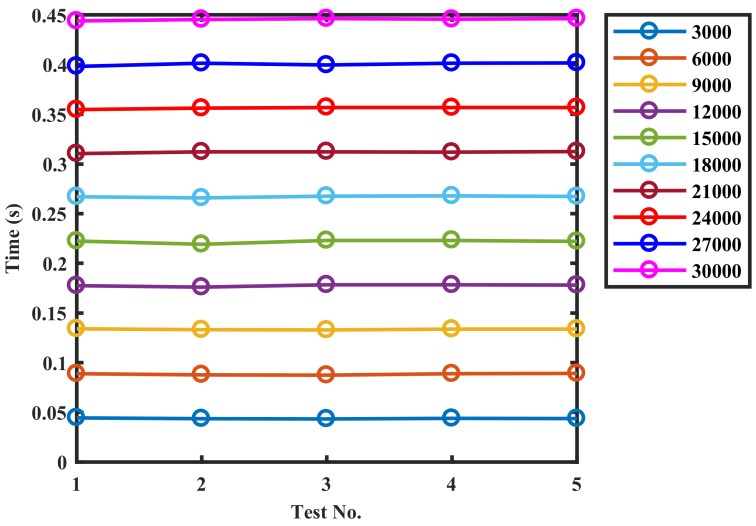

Figure 5.18: The Time Performance of Different Samples Sent from PRU to ARM

The time behaviour of data transfer was examined within the ARM (non-real-time processor), so it is possibly affected by other existing tasks in the processor, such as the Linux OS. In order to reduce those effects, the mean time method was applied.

All tests were repeated five times, and the average of the five-time performances is calculated as the data transfer usable time. The results can be observed in the exhibition that the transfer time behaves regularly for all tests

at the same number of samples, and the mean time performances for the fixed number of samples are linear, as shown in Figure 5.19. This means that the transfer duration for every single sample from the PRU to the ARM is almost identical.

With a numerical performance for the transfer, the averaging time of transferring a single sample from the PRU to the ARM is approximately 15 ms, equalling the real-time operating time of the proposed system.

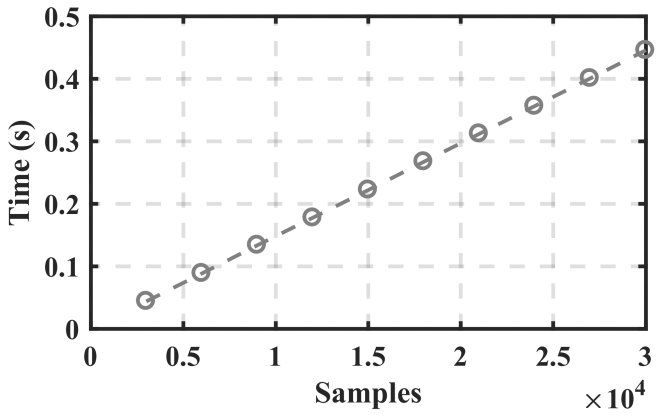

Figure 5.19: The Mean Data Transfer Speed

Additionally, the time activity of the processing data from the time domain to the frequency domain by a single tone algorithm is flexible. This is inconsistent data lengths were allocated to the processing AC excitations at different frequencies. Table 3 lists the time values of data processing at seven frequencies. With the number of samples increasing, the processing duration rises significantly. If all frequencies are devoted to the SOC estimation, the system will last a relatively long time (over 20 seconds).

Alternatively, if the measurements are only concerned in the SOC prediction at a higher frequency range from 1.0 Hz to 1.32 kHz, a relatively shorter measurement duration of approximate 3.5 seconds can be obtained. When the

Table 5.3: TIME PERFORMANCES IN THE TESTS

Frequency (Hz)	Number of Period	Number of Samples	Time for Data Processing (s)
0.05	1	1320000	7.82
0.5	10	1320000	7.82
1.0	10	660000	2.89
10	10	66000	0.39
167	10	4000	0.22
440	10	1500	0.04
1320	10	500	0.04

measurement system cooperates with other applications, such as SOC estimation (shown in Chapter 6), the composed system holds the most probability to meet (or exceed) current frequency calibration of around a few hertz on the OCV-SOC commercial implementations [13].

5.7 Chapter Summary

In this chapter, the results of the proposed measurement are illustrated. The impedance measurements can be obtained over a wide frequency range from 0.05 Hz to 1.32 kHz under the real time operating frequency at 66 kHz and the control's referencing samples at 50. The measurement comparisons are discussed with different lithium-ion battery states, current rates and ages. Battery states and ages can lead to almost the same impedance spectrum changes in the given frequency margin, which should be distinguished in the EIS-based estimation method. However, the exploration of the current rate indicates that no significant impedance spectrum changes respond to the current rate variation in the proposed

frequency range (from 0.05 Hz to 1.32 kHz). Multiple cells in series connection are also taken into account because they are widely used in many portable devices in order to boost the output voltage and power capacity of the battery package. The impedance spectrum of the series-connected cells shows a larger numerical performance than expected values, which needs further work to clarify this phenomenon. Finally, the timing performance of the proposed measurement system is preliminarily investigated, which is mainly determined by the data length of the domain transfer algorithm.

Chapter 6

Performances on the Online Measurement System and Preliminary State Estimation

In this chapter, the contents include validating the performances of the proposed online impedance measurement system and using impedance measurement data to estimate battery states (such as SOC and SOH). The quantity of AC excitations and the comparison between a prototype and a commercial system (called Bio-Logic) area also focused on. Moreover, the measurement uncertainty is taken into account to accurate battery state estimations. Finally, potential optimisation methods extending and refining the research in further work are contained.

6.1 Comparison to a Commercial Measurement System

In order to validate the performances of the prototype, the measurement results obtained from the prototype are compared to the achieved data from the commercial system (Bio-Logic VSP). For the implementation of Bio-Logic VSP, the standard electrode connection mode developed from potentiostat technology (based on the operational amplifier implementation) was used. The mode provides a recommended connection that the positive electrode of the battery connects to working and reference electrodes, and that the negative electrode of the battery connects to the counter electrode. Based on this connection, a bias voltage between working and reference electrodes can be maintained. Besides, voltage measurements in this case, are obtained at three parts, including the working electrode, reference electrode and counter electrode, whilst the working current is measured only at the working electrode.

Moreover, dependencies of the impedance measurements, such as SOC, current rate and battery age, are tested with the same values in the Bio-Logic VSP system. The SOC was set at 60% and 20%, corresponding to the proposed measurements at the open circuit voltage of 3.55 V and 3.18 V, respectively. Magnitudes of AC perturbations were 0.085 A (5% of current rate at 0.5 C) and 0.05 A (5% of current rate at 0.3 C). Furthermore, experimental cells were tested in two age levels: brand-new and 3-years old. Unlike the cell exposed in the natural environment in the prototype, an oven was used to contain the object (including a battery, battery holder and the connection circuits (for voltage and current measurements, as shown in Figure 4.18). In this case, the ambient temperature is maintained at 25 °C, which minimises the effect caused by the ambient temperature variation on the impedance measurement.

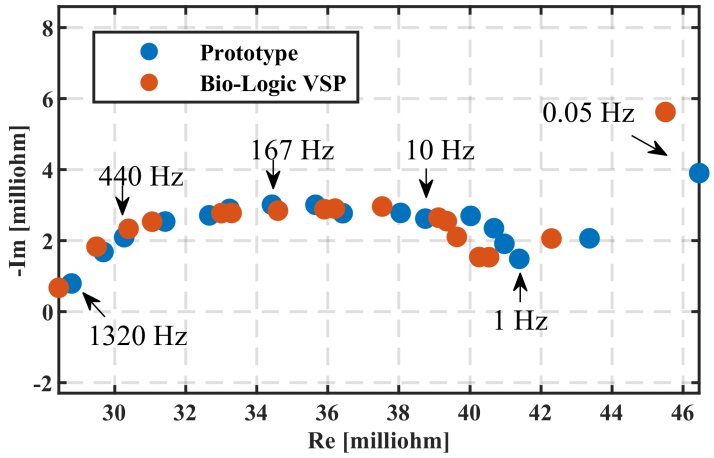

Figure 6.1: Comparison of Prototype and the Bio-Logic VSP Under the Measurement Condition: 60% SOC, 0.5 C and Brand-New Cell

Figure 6.1 shows the impedance measurement differences between the prototype (in blue) and Bio-Logic VSP (in orange) at seventeen frequencies (discussed in Chapter 5). It can be seen that the impedance data captured by the prototype system is in agreement with the reference measurement for the vast majority of frequencies (over 10 Hz). However, there are apparent differences between those two systems in the frequency range from 0.05 Hz to 1 Hz, which normally exist in the comparison between online measurement platforms and potentiostat [2].

Figure 6.2 gives more insight into these discrepancies in magnitude and phase. At lower frequencies (less than 10 Hz), a maximum magnitude discrepancy of 4% can be found at 0.05 Hz, which decreases with increasing frequency. Likewise, the measurement at the lowest frequency (of 0.05 Hz) shows the maximum phase difference of around 0.04 radians. These findings imply that measurements at lower frequencies (less than 10 Hz) in the real battery operation (where the battery state decreases) are different from the operation under the

ideal condition (where the state is almost maintained). The main reason may arise from the battery voltage drop. In practice, the battery normally works with its state (such as SOC) changes due to a power dissipation (the battery terminal voltage declines as the operating current of the battery under control). However, the reference system (Bio-Logic) provides an ideal operating condition for EIS measurements in which the voltage drop of the battery almost disappears (for example, around 22 μV voltage drop and measurement duration of 800 seconds were configured in the measurement), benefiting from the embedded electrochemical interface (potentiostat).

In practice, an efficient way to reduce voltage drop is shortening the measurement duration. Figure 5.5 (a) and (c) show evidence that a longer measurement time results in a larger voltage variation (the voltage dips nearly 50 mV in the measurement time of 50 s while it approaches 0 during the measurement duration of 85 ms). Because of this finding, the measurements at extremely low frequencies (such as 0.05 Hz and 0.5 Hz) are no longer considered in this work, which leads to larger battery state variations for EIS measurements.

6.2 Possible Sources of Measurement Uncertainty

In the prototype, several factors would influence the measurement accuracy, such as PI controller, low-pass filter, and ADC finite resolution. Firstly, both integrator and physical low-pass filters have chances to directly lag measurable signals. While the integrator behaviour only works on the measurable current, the filters lag voltage and current signals at the same time. However, magnitude and phase differences cannot be caused in the tests by using the same filters for measurable objects. This is due to the impedance calculation where the divider effect and

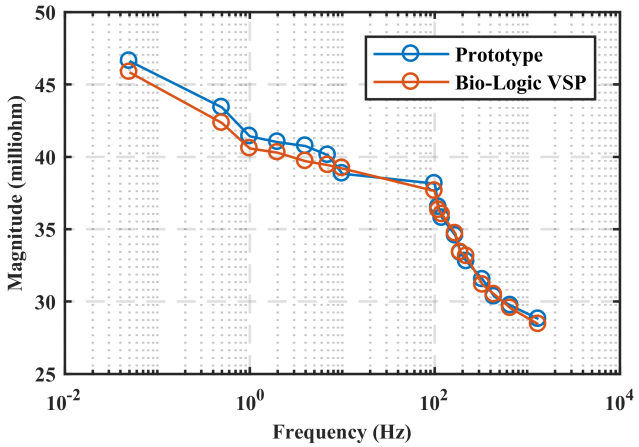

(a)

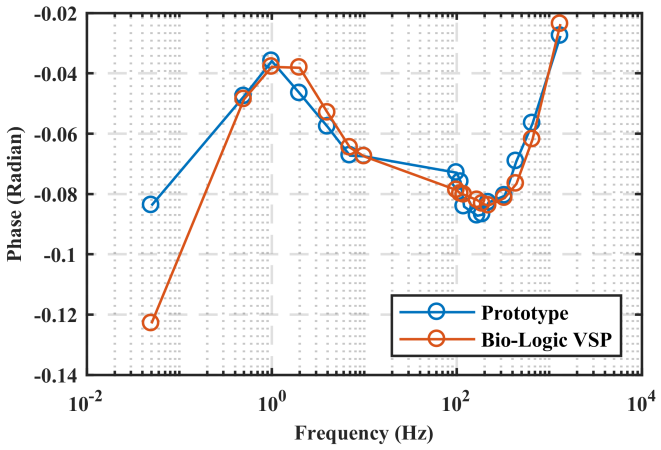

(b)

Figure 6.2: Comparison of Prototype and the Commercial Measurement Instrument on Magnitude (a) and Phase (b) at 60 % SOC and 0.5 C

phase shift on battery voltage and current can be eliminated in the end. More importantly, the finite resolution (12-bit) of the ADC leads to measurement errors (the maximum quantisation error of 0.44 mV, corresponding to the maximum error of ADC of 1 LSB). This error affects the accuracy of the measured samples, which in particular occur at the highest frequency of 1320 Hz. For example, the error of the voltage measurement of 4.4% ($0.44mV/10mV \times 100 = 4.4\%$) is obtained at the frequency of 1320 Hz (see Figure 5.5(c)), whilst it is 0.88% ($0.44mV/50mV \times 100 = 0.88\%$) at the frequency of 0.05 Hz (see Figure 5.5(a)). The current measurements have errors at 0.05 Hz and 1320 Hz (0.8% at 0.05 Hz, $0.44mV/(50mV) \times 100 = 0.8\%$, and 5.5% at 1320 Hz, $0.44mV/(8mV) \times 100 = 5.5\%$). As a result, the error in the voltage measurement is dominant, which cause the maximum error of around 5.5% in the impedance calculations.

If it is desired to increase the accuracy of the impedance measurements, two feasible ways can be deployed. The first approach is to increase the perturbation magnitude of the AC perturbation setting for impedance measurements at high frequencies, which yields larger voltage magnitude in the responses. As a result, the expanded magnitude can be well quantified by the 12-bit ADC. Another method is to configure a larger bit to the ADC, so that the quantisation levels are capable of significantly increasing, but this has the disadvantage of decreasing the sampling rate.

Other factors, including current transducer sensitivity, the tolerance of resistor and the difference (less than 2 °C) in an ambient temperature between the two systems, may slightly influence the measurement discrepancy, which can be neglected when compared to the main impact of the voltage variation. For more details, the measurement error of the current transducer is ±0.2%. Thus, this current difference does not have a significant effect on the impedance measurement, which can be neglected in the measurement.

As discussed previously (in Section 4.2.2), for the tolerance of the resistor, it is generally neglected in theory if the same filters (including the same resistors and capacitors) are employed. However, the use of those components are considered in practice with their tolerances, especially with tolerances of resistors (the conventional tolerances: 1%, 5% and 10%). In this work, all resistors were used in conditioning circuits with the tolerances of 1% or 5%. These tolerances lead to the differences of the cut-off frequency of approximately 1% (for the tolerance of resistor of 1%, calculated via (4.14)) or 5% (for the tolerance of resistor of 5%, calculated via (4.14)). When considering their effects on the voltage gain (see (4.16)), the gain varies with the resistor's tolerances within 1% (calculated via (4.15) and (4.16)). So they can be neglected in the measurement. Finally, the temperature discrepancy is less than 2 °C, the effect of which is also ignored in the measurement.

6.3 Comments on Data Selection

Several papers [11, 33, 44, 92, 166] have investigated the dependency of electrochemical impedance measurements, such as SOC, current rate and ageing, but the consistent duration of reaching lithium-ion battery stable operation has not been achieved yet. In the proposed impedance measurement system, the application of data selection was developed form the direct current resistance (DCR) technique, and the purpose of selecting data is to prevent measurable signals of the battery from transient responses of the system. To achieve this goal, extending the waiting time method has been employed in this thesis.

Depending on the proportional relationship between the time performance of data transfer and the length of data (introduced in Section 5.6), the method focuses on the length of data to control the waiting time. In general, transient

responses could be caused by sudden DC and AC variations in the system, while the considerable waiting durations for these two variables are significantly different. For example, in a direct resistance measurement, the change of the DC current need a long-time (from a few hundred milliseconds to several seconds, such as 1.0 to 20 seconds in EV [167, 168]) to trigger the voltage response (contains an immediate voltage drop and a further voltage drop [44]). If the transient responses caused by DC current are mainly considered in this work, the waiting time of a single measurement could be constantly set at 20 seconds, corresponding to the number of data of around 20*66000.

Nevertheless, a long waiting time is not suitable for the online impedance measurement due to the terminal voltage variation of the battery. By contrast, if AC current causing transient responses is considered, the time needed to approach steady-state operating conditions may be short and flexible due to multiple frequencies of AC perturbations. This is the main reason that data selection chose the flexible data length method to reach a stable system operation. As discussed in Chapter 4, a flexible data length has been introduced to the tests in which all data length covers integer period(s) of the AC excitation. Correspondingly, the different waiting time has been discussed with respect to AC perturbations at different frequencies. The minimum duration of data transfer could be investigated at higher frequencies due to a smaller data length. It should be pointed out that the fixed data length method has been explained in the previous chapter but it was only deployed in the proposed measurement at the frequency range from 1.0 Hz and 1320 Hz. At lower frequencies (less than 1 Hz), a larger measurement time window means a longer measurement time, which expands the whole measurement time. This measurement time is an important factor in the online measurements. So, the trade-off between data length and impedance calculation accuracy is an interesting topic that will absorb more attention in the further.

6.4 Battery State Estimations

In this section, impedance measurement data combined with the equivalent circuit model is used to estimate battery states (SOH and SOC) via the most-sensitive parameter method. In this method, the measurement data (measured with different SOC and ageing levels) is firstly fitted by a 2-RC ECM (see Figure 5.10) and then the parameter sensitivities of the ECM are compared in order to find out the most sensitive indicators for SOC and SOH, respectively.

6.4.1 Measurement Uncertainty

The measurement uncertainty should be given at the beginning in terms of the estimation accuracy. All measurement systems have some degrees of uncertainty that may arise from environmental impacts such as uncontrollable variations of the measured object, and random factors such as instrument resolution. The systematic factors are also worth considering such as offset, gain error, etc., which are usually caused by the instrument.

The uncertainty level defines the sensitivity of the proposed measurement. Two types of measurement uncertainty are discussed in many studies. Type-A uncertainty is inferred from the statistical analysis of a series of measurements, treating measurement data in the mean value and standard deviation (or extended deviation). Type-B uncertainty offers scientific judgements using relevant sources of information, which may include an instrument manufacturer's specifications, a calibration certificate or reference values published in handbooks.

In practice, the measurement could be caused by uncontrolled variations, including interval variations of the cell and possible variations of the ambient environment (such as humidity and temperature). Type-A uncertainty is able to

evaluate these random effects during a series of measurements in quantification. With the type-A certainty, the numerical estimations of uncontrolled variations provide a good chance to analyse impedance measurement variations correctly. This is of interest to ECM-based state estimations of the battery.

Figure 6.6(a) presents five repeated measurements at five frequencies under Type-A uncertainty statistic. The mean values (crosses, averaged by 5) of the real part of the impedance at five targeted frequencies provide the best prediction of the cell impedance. Besides, the standard deviation (as shown by circles in the illustration) is only calculated based on the real part of the impedance (dominant value in amplitude, as discussed in Section 5.6), which gives an estimation of the associated uncertainty.

The certainty estimations at higher frequencies (such as 440 Hz and 1320 Hz) are much larger than at lower frequencies (such as 1.0 Hz and 10 Hz), given that more measurement variations happen at those high frequencies. This may be caused by a lower number of samples used for the domain algorithm, which weights the uncertainty. However, if a larger number of samples is used to the measurement, it may cause a long measurement duration, which in turn increases the measurement uncertainty.

Figure 6.6(b) illustrates a comparison between the model impedance (shown by purple filled circles) and the measured data. All cases of the model impedance in the frequency range from 1 Hz to 1320 Hz were obtained by the trust-region algorithm and the measured data were acquired from five repeated measurements (corresponding to the Type-A uncertainty) . It can be observed that the compatibility between model and experimental data can be acceptable at the targeted frequencies, which approves the model validity for the purpose of this work. The range of impedance measurement results that covers the true value in the real part of battery impedance (m) is $m \pm 0.002\Omega$. The uncertainty level

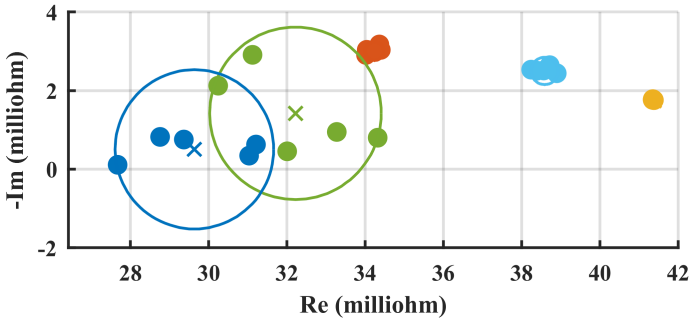

(a)

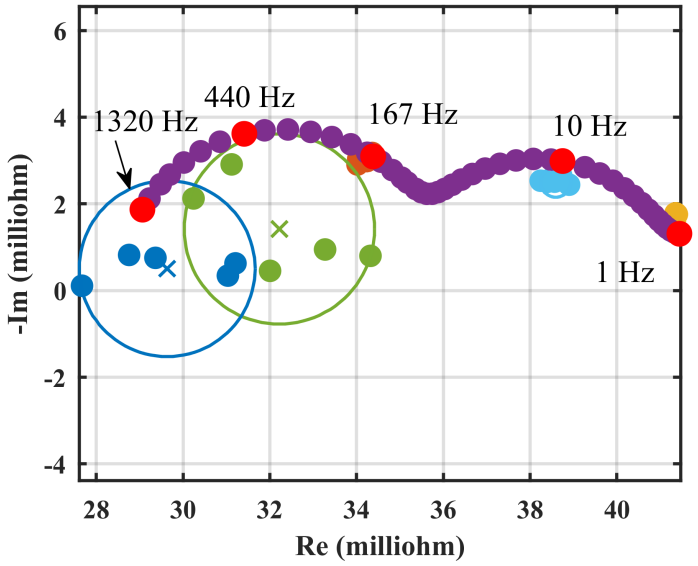

(b)

Figure 6.3: Type-A Uncertainty (the coverage factor of 3 (99.7% probability), shown by circles) at Five Frequencies Under 60% SOC and 0.5 C Measurement Condition; (a) Type-A Measurement Uncertainty at Five Measurement Frequencies: 1 Hz, 10 Hz, 167 Hz, 440 Hz and 1320 Hz; (b) the Measurement Uncertainty for the ECM-Based State Estimation for Batteries (targeted frequencies in red filled circles)

of 0.002 Ω determines the sensitivity of the proposed impedance measurement system for lithium-ion batteries. When ohmic resistances vary above these thresholds, it can be confirmed that a sudden increase or decrease of the battery impedance indicates abnormal battery operation, such as high temperature or short circuit [108]. As a result, the potentially dangerous operation of the battery can be detected in advance so the measurement uncertainty is able to provide reliable monitoring to ensure that the battery is operating under safe conditions.

Type-B uncertainty is also taken into account in this work. This uncertainty comes from the systematic errors (mainly considered in this thesis) such as the ADC acquisition error and the first-order filter error as discussed in Section 6.2. When comparing systematic errors to random errors (Type-A uncertainty included), the systematic errors can be roughly calculated (shown in Section 6.2), which are typically smaller than the Typy-A uncertainty. So the Type-A uncertainty is typically employed to battery state estimations, discussed in the following section.

6.4.2 ECM Based State Estimation

Battery state estimations based on the most sensitive parameter method are discussed in this subsection. As explained in Section 5.3, the proposed ECM only consists of five unknown parameters, including R_0, R_1, C_1, R_2 and C_2. In theory, each of them would have an independent reflection in the state variation. Depending on the reflection level, the most sensitive parameter can be used to indicate the state variation. Then, with a proper fitting algorithm, the state variation can be expressed by the most sensitive parameter.

In general, SOC varies within a limited range. In order to clarify this range, apart from before mentioned tests at 20% SOC and 60% SOC (a safe SOC

Table 6.1: ECM PARAMETERS FOR SOC ESTIMATION

SOC (%)	R_0 (Ω)	R_1 (Ω)	C_1 (F)	R_2 (Ω)	C_2 (F)	A_w ($m\Omega/s^{0.5}$)
100	0.0266	0.0043	0.0875	0.0095	1.05	1.39
60	0.0286	0.007	0.0625	0.0052	2.5	1.39
20	0.0308	0.005	0.15	0.0135	5.255	1.39

Table 6.2: ECM PARAMETERS FOR SOH ESTIMATION

Cell	R_0 (Ω)	R_1 (Ω)	C_1 (F)	R_2 (Ω)	C_2 (F)	A_w ($m\Omega/s^{0.5}$)
brand-new	0.0286	0.007	0.0625	0.0052	2.5	1.39
3-year	0.0313	0.0042	0.0105	0.0055	1.2	1.39

operating range from 100% to 20%), an additional measurement with the full value (100%) of SOC was completed, which identifies an upper band for the SOC estimation (the lower band identified by 20% SOC). Table 6.1 lists parameter values at different SOC levels and the fitting performances at those SOC levels are shown in Figure 6.4.

Besides, SOH is a kind of evaluation of the battery life span, which is significantly affected by the material degradation of the battery. This degradation increases with the battery becoming older. So, brand-new and 3-year batteries were employed in the measurements. Table 6.2 gives the parameter values obtained from the fitting results (the fitting results at 20% SOC and 100% SOC are shown in Figure 6.4).

Figure 6.5 demonstrates ECMs at three SOC levels and the numerical performances of the ECM parameters. The Nyquist plot in the demonstration

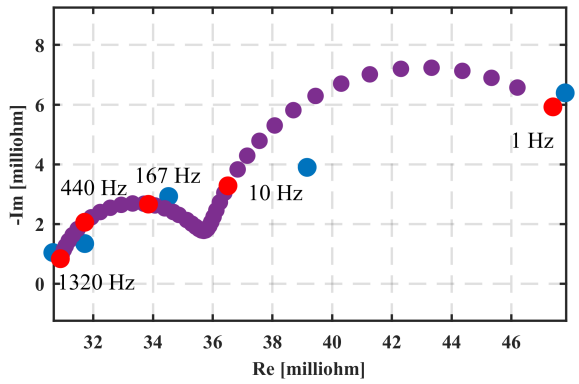

(a)

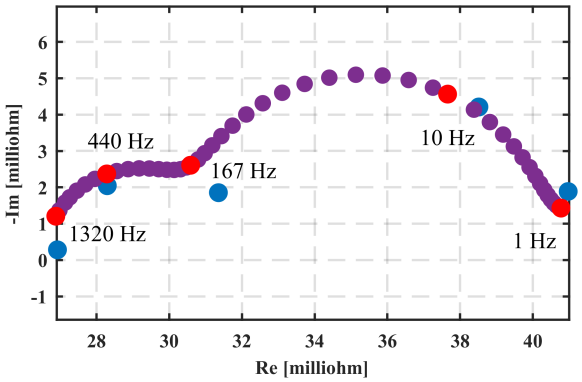

(b)

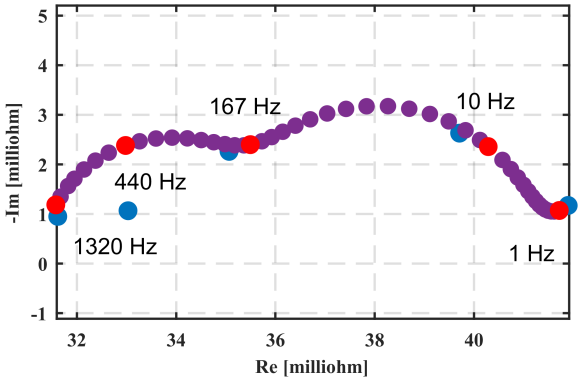

(c)

Figure 6.4: The Fitting Performances (measured data and estimated data shown by blue filled circles and read filled circles, respectively); (a) and (b) for the measurement dependency on two SOC levels:20% SOC and 100% SOC under the measurement condition of 0.5 C and brand-new cell; (c) for the measurement dependency on the battery age; the Frequency Range of the Proposed Model (shown by purple filled circles) from 0.05 Hz to 1.32 kHz

shows impedance spectrum variations in the proposed frequency range from 1.0 Hz to 1.32 kHz. With the value of SOC decreasing, the pure ohmic resistance (the imaginary part is zero) apparently rises, and the left semicircle gradually enlarges. These changes indicate that the electrochemical characteristics of the battery such as electrolyte decomposition and SEI increment of the anode are affected by SOC variables.

The right semicircle shows two observed dynamics in the given frequency region. On the one hand, from the full level of SOC to 60% SOC, the diameter of the right semicircle becomes small. On the other hand, when the value of SOC tends from 60% to 20%, the radius of the semicircle rises. The dynamics of both semicircles with SOC variations indicate that the electrochemical characteristics (mainly including SEI and double-layer capacitance) are obtained from the both electrolyte, which is in agreement with the assumption that put forward to modelling the lithium-ion battery.

In Figure 6.5, the measured data were fitted to the proposed model (see Figure 5.10). The resistance R_0 associated with the electrolyte decomposition and other structural resistive responses (except for electrodes) fitted at different SOCs, decreases linearly as SOC rises. About 16% resistance reduction happens within the given SOC range. The rate of loss of resistance is much lower than the rate of fading of capacity, implying that the pure ohmic resistance does not obviously vary with SOC, as is found in one publication [69].

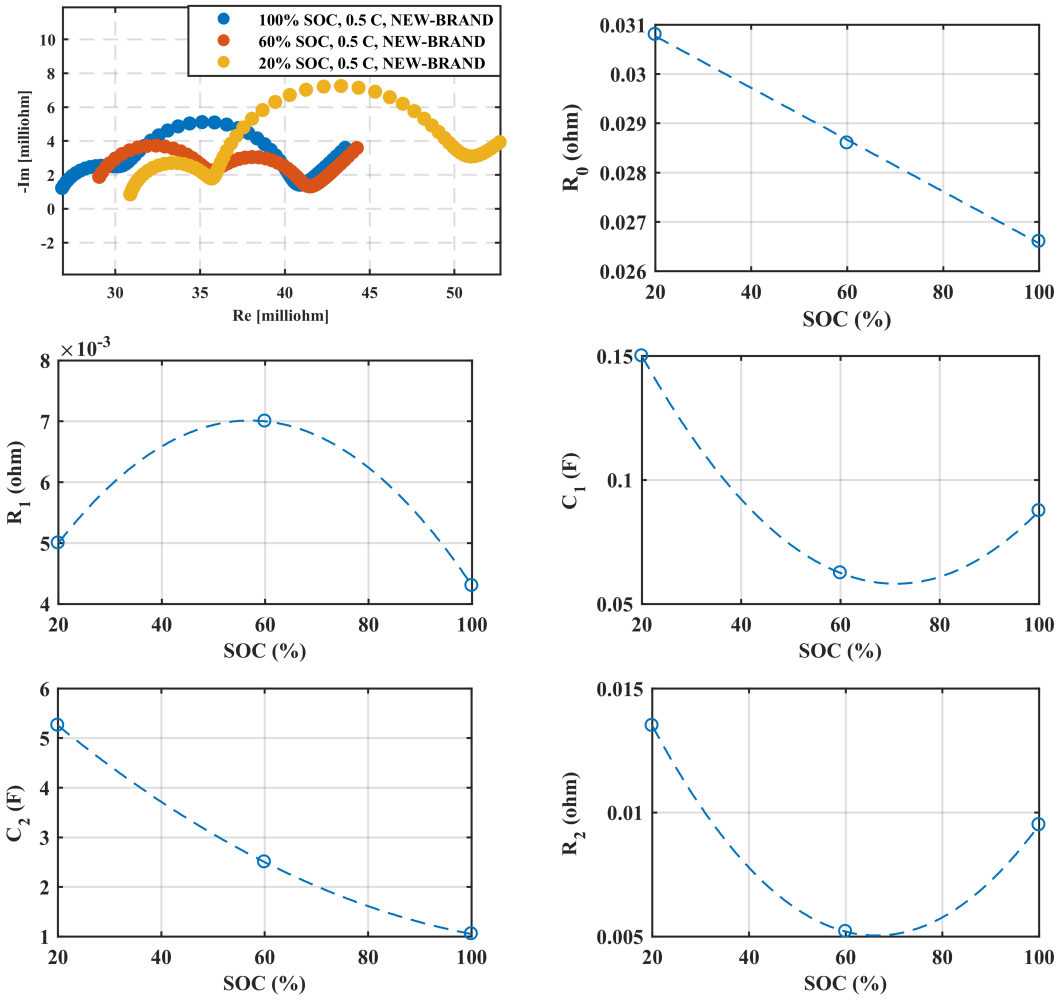

Figure 6.5: ECM Parameter Sensitivities for SOC (dashed line – fitted, circle – applied)

As discussed previously, the left semicircle reflects SOC variations with a small variation, so R_1 and C_1 hold narrow varying margins that are undesirable as applied indicators to predict SOC. By contrast, the right semicircle sensitively responds to SOC changes. In the illustration, with SOC increment, the value of R_2 declines from around 6.5 F to about 1.0 F, and R_2 reduces to 10 $m\Omega$ from 150 $m\Omega$, giving that the SOC variations affect the battery electrical characteristics mainly at the cathode. Based on this finding, R_2 and C_2 are equally possible

indicators for the SOC estimation. It should be noted that C_2 has a very similar response to battery degradation, which conflicts with SOC variations. In Figure 6.6, the parameters of ECM on aging variation are presented. As explained in Chapter 2, the battery faces a loss of chemical performance over time and use. In this case, the most indicative factor of ECM is capable of properly detecting this loss. The illustration shows a suitable detector C_2 as compared with other observations of factors. The detector C_2 responds to the ageing changes, varying from around 2.4 F to 1.2 F, which equals about 50% capacitance reduction. A common understanding of this reduction is that the battery has suffered a loss of capacity property due to material degradation over a long time scale. When considered to SOC and ageing estimations, the final determination is that R_2 is used to estimate SOC. However, the factor C_2 may be applied to indicate ageing but needs more data to distinguish the impact of SOC variation and ageing variation. Hence, corresponding relationships can be obtained by a quadratic fitting only for the SOC only in the range ($20\% \leqslant SOC \leqslant 100\%$).

$$SOC = \begin{cases} 0.67 + (25.4R_2 - 0.11)^{0.5} & OCV > 3.6V \\ 0.67 - (25.4R_2 - 0.11)^{0.5} & OCV \leq 3.6V \end{cases} \tag{6.1}$$

However, in (6.1), SOC has optional solutions in the quadratic calculation. To overcome this issue, the value of the terminal voltage of the battery can be referred in order to determine which value of SOC is suitable. For example, 75% SOC and 45% SOC are simultaneously obtained in the SOC estimation. Meanwhile, the value of the terminal voltage (or OCV) is currently 3.8 V. As the value of voltage is larger than 3.6 V, the value of SOC should be over 50% (without any degradation). Thus, the value of SOC of 75% is determined to BMS. Besides, R_2 rises with the age increasing, resulting in an ohmic increment of 0.1 $m\Omega$ per year. However, this ohmic increase can be neglected when compared to the R_2 significant change with SOC.

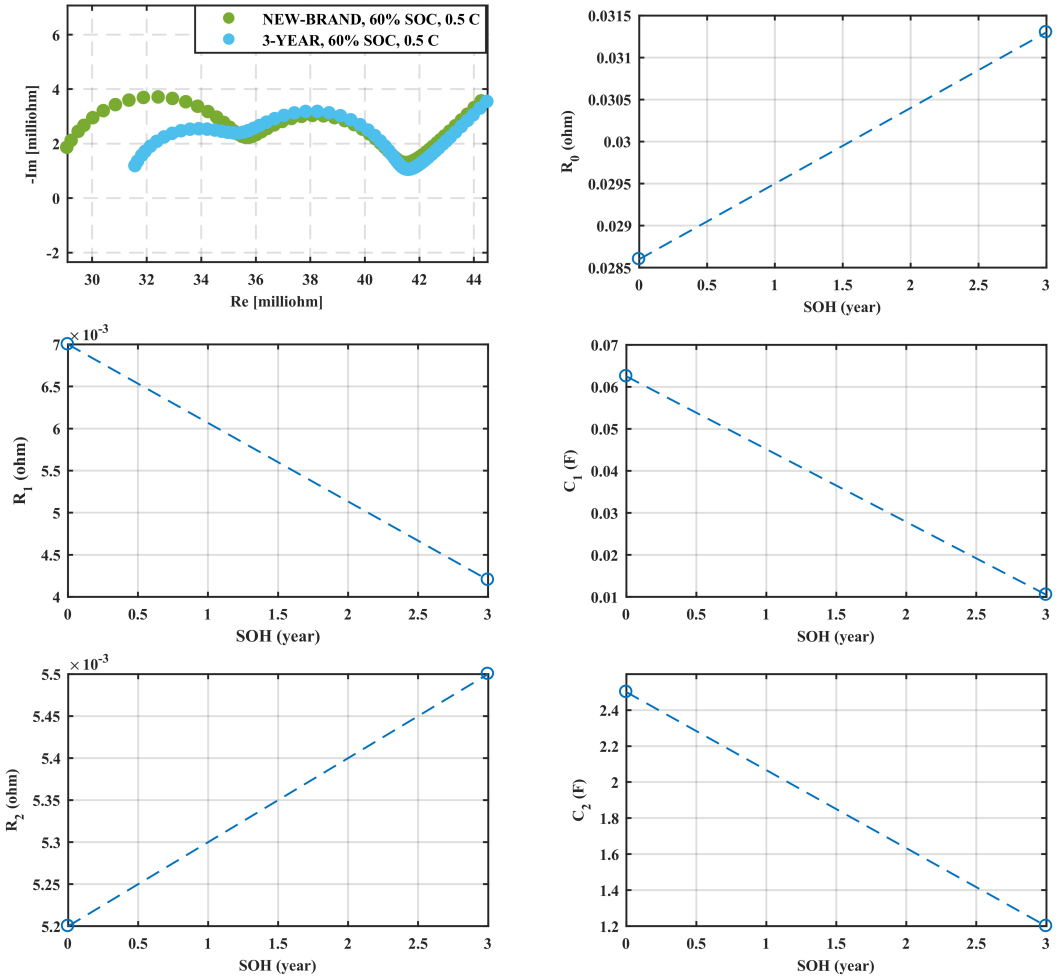

Figure 6.6: ECM Parameter Sensitivities for SOH (dashed line – fitted, circle – applied)

For the SOH definition, as studied from [69], impedance-based parameters at different states are exploited. In relevant studies, the determination of SOH relates to three state factors: measurable (current) factor, initial factor, and ageing factor. These factors can be used as a threshold to show the best and worst conditions of the cell. Besides, the measurable parameter examines the recent state of the battery. In Figure 6.5 and 6.6, R_2 and C_2 could be applied to indicate SOC and ageing, respectively. The remaining factors of ECM, R_1, C_1, and R_0, need to be fully considered. R_1 and C_1 gives their reflections with

quite a narrow range on ageing variation. Therefore, we assume that they would not respond sensitively to SOH changes. R_0 reasonably responds to SOC and ageing with the change of 5 $m\Omega$ and 3 $m\Omega$, respectively. In this case, there is a hypothesis for R_0 to obtain reasonable changes in different states. Besides, the pure ohmic resistance R_0 expresses linear correlations (due to a small volume of experimental data) to those states, which can be easily modelled in further investigations. Therefore, the linear SOH estimation is developed from the study as:

$$SOH = |\frac{R_{0(M)} - R_{0(N)}}{R_{0(A)} - R_{0(N)}}| \times 100\% \tag{6.2}$$

Where $R_{0(A)}$ and $R_{0(N)}$ are real values of impedances of new and ageing cells at the frequency of 1320 Hz. Besides, $R_{0(M)}$ denotes the real value of impedance obtained at the same frequency. Accordingly, the SOH calculated from (6.2) is 100%, indicating that the cell is totally fresh. On the contrary, the SOH reaches 0%, meaning that the cell meets the ageing (or end of life) condition.

It should be noted that a special representation of R_0 is implemented by using the real part of impedance at the maximum frequency. This is due to the limitation of the proposed measurement system on the frequency of AC perturbation. However, with this implementation, R_0 would face the fact that its value would act with a tiny error (less than 0.5 $m\Omega$), as shown by the error bars in Figure 6.7. The minimum impedances at different SOC levels are worthy noting in the illustration because their corresponding frequencies increase as SOC declines, which has been concluded by publications [155, 169, 170]. Besides, unlike the real part of the impedance application to SOH, the frequency of the minimum impedance enables to reflect the healthy change of the battery, acquiring from [69]. With regard to these findings, the pure ohmic resistance R_0 employed in the SOH prediction is realisable.

Nevertheless, the mentioned measurement uncertainty is critically taken

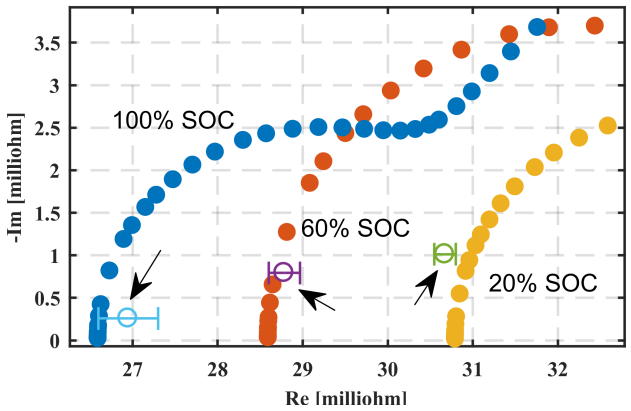

Figure 6.7: Real Parts of the Impedance Measurement (circle) Obtained at 1320 Hz and Compared with the Fitting R_0 of ECM (filled circles); The frequency of interest expanded from 0.05 Hz to 10 kHz;

into account in the $R_{0(M)}$-based SOH estimation. Thus, the measured value of $R_{0(M)}$ is liable to deviate from its actual value. As the measurement uncertainty of 0.002 Ω is used to (6.2), the expression of the SOH estimation can further to determine the estimation uncertainty U_{SOH}, given by:

$$SOH = |\frac{(R_{0(M)} \pm 0.002) - R_{0(N)}}{R_{0(A)} - R_{0(N)}}| \times 100\% \tag{6.3}$$

$$U_{SOH} = |\frac{0.002}{R_{0(A)} - R_{0(N)}}| \tag{6.4}$$

6.5 Further Work

Many opportunities exist in the research that may further extend and refine the measurement system. The results collected from the system have identified that the prototype has the ability to sensitively detect tiny variations of battery discharge signals (voltage and current). However, the small-signal voltage and current perturbations could affect the battery powering the load and in the

end cause notable issues to the load, such as accelerating energy dissipation and then causing battery temperature rise by more heat being generated [171]. In addition, SOC estimations based on the ECM method are limited by the current fitting algorithm, which consequently restricts transferring this technology to commercial applications. Moreover, the impedance measurements shown in the framework were stressed with multiple frequencies that distributed over the desired frequency range, but the total duration of those measurements lasted for about 3.5 seconds. Thus, it can be believed that those initial results warrant further research. Firstly, an efficient approach can be applied to average the amplitudes of AC perturbation to zero that uses two of the same DC-DC boost power converters with a phase shift of 180 degrees to two individual perturbation references, as found in [13, 107]. Secondly, if the fitting algorithm does not entirely match online artificial prediction for the RC factors of the ECM, as an alternative way, it is possible to reuse the database with a comparison method to estimate SOC, which is currently not yet applied to the online EIS measurement due to measurement duration and cost. The proposed low-cost system can offer this comparison method because only a few frequency points are needed so it would not require a large memory space to store the data. Finally, for a more reasonable measurement duration based on the 5-point spectrum method, more tests are needed here to seek a trade-off between measurement duration and the frequencies of battery electrochemical dynamics.

6.6 Chapter Summary

The concept of this chapter mainly includes the performance evaluation between commercial and proposed systems, as well as battery state estimation based on the most sensitive parameter method. The prototype can be realised to measure

battery impedance at the frequency range of 1 Hz to 1320 Hz for online EIS-based state estimations of a lithium-ion battery. However, it is hard to obtain an accurate measurement at extremely low frequencies such as 0.05 Hz due to an apparent voltage drop that leads to battery state instability. Two ECM parameters, R_1 and R_0, have the most sensitive reflections on the SOC and SOH variations, which were therefore used to indicate battery states. With the help of quadratic and linear algorithms, two simple relationships were given to quantify SOC and SOH using the above mentioned parameters.

Chapter 7

Conclusion

This work has presented an online impedance measurement system for lithium-ion batteries in response to the requirements of commercial EIS measurements about cost-efficiency, space-saving, and ease of programming. A bespoke DC-DC power converter, connected to the battery, was used to introduce AC perturbations onto the battery current. This implementation depends on the DC-DC power boost converter that not only allows impedance measurements to work with normal battery operations (discharge with voltage decrease) but also provides an enhanced voltage output for a high operating voltage need at the load. Besides, a BeagleBone Black board as a suitable hardware solution was used to control the converter, acquire and process the measurement signals (voltage and current signals) in the time and frequency domains, and then calculate the impedance values. This is because the board has several properties that depend on the hard real-time programmable units and a powerful core processor.

A novel solution was discussed by using the counting clock cycle method to control the power converter in real-time, which can create AC perturbations in a desired frequency range from 0.05 Hz to 1.32 kHz. The measured signals of

the battery were acquired by an active onboard ADC, which works at a sampling frequency of 66 kHz synchronously with the operating frequencies of the PI control algorithm and the PWM controller. Moreover, impedance calculations could be completed within ARM operating environment (non-real-time operation), which relies on the combination of a general-purpose the ARM processor and real-time micro-controllers with the ring buffer technique. As a consequence, the requirement of dedicated and sophisticated commercial instrumentations for the EIS measurement can be eliminated, leading to lower cost, reduced design complexity, and smaller size of the overall system.

The proposed online measurement system showed an innovative real-time control solution for the DC-DC power converter, delivering a clock cycle error of 0.6% and a wide frequency range of the generated AC perturbations. The critical electrochemical dynamics of the battery can be well covered within the obtained frequency range. Depending on these achievements, the differences in electrochemical dynamics were detected by the impedance spectrum under several battery operating conditions, such as SOC, the current rate and ageing.

The impedance in Nyquist representations and Bode plots showed a slight measurement difference (less than 0.001 Ω) between the prototype and a reference measurement obtained from state-of-the-art instrumentation in the frequency range from 1 Hz to 1.32 kHz. In contrast, the impedance at low frequencies such as 0.05 Hz and 0.5 Hz posed a relatively large discrepancy (over 0.001 Ω) for all cases as compared to the measurement with the integrated commercial system. The main reason for this difference is that more energy is consumed in a long-time measurement, so the battery terminal voltage cannot stay constant. The experiment has identified the interpretation that a lower C-rate configuration delivered a lower voltage drop at the same value of SOC. In addition, the consequences obtained from experiments on different battery operations, including SOCs and ages, deliver different impedance changes in

the frequency domain, which are in agreement with the findings reported by the publications [27, 56, 143]. Furthermore, the time behaviour of the online measurement system has been revealed to define the speed of the impedance calculation with a fixed measurement time window method (in the frequency from 1.0 Hz to 1320 Hz). If an online parameter estimation of the ECM guarantees its execution time to be below a millisecond, the proposed measurement system will complete 5-point impedance measurements within seconds, which is capable of approaching recent commercial applications on the battery monitoring [113]. However, an unbalancing battery issue occurred as two cells were connected in series to test the cost-efficient impedance measurement approach with only a single DC-DC power converter. One of the possible solutions has been reported by using a balancing circuit to control cell operation, which will be used to large-scale battery powered devices.

A practical five-point offline estimation method for lithium-ion batteries has been proposed in this thesis based on fitted parameters of the second-order RC ECM. By this method, it is not necessary to measure the impedance spectrum over a long measurement duration, and there is also no need to utilise a large memory space to store historical EIS information. Experimental results have firstly revealed the most sensitive parameters of ECM of R_2 and R_0 in response to changes in SOC and SOH, respectively. Furthermore, the measurement uncertainty of 0.002 Ω took a crucial role not only to diagnose the battery operating fault but also to determine the estimation accuracy, especially for SOH estimation. In the future, the current offline fitting method will be developed for the online application in terms of embedding EIS information to serve a battery management system for portable devices.

In general, developing improved, simpler and cheaper approaches that have access to complete online EIS measurement provides the opportunity to use off-the-shelf BeagleBone Black for further research and developments that

potentially can lead to more accurate state estimations in the battery management system. The main contribution of this work favours further developments in such a direction.

References

[1] S. E. Li, B. Wang, H. Peng, and X. Hu, "An electrochemistry-based impedance model for lithium-ion batteries," *Journal of Power Sources*, vol. 258, pp. 9 – 18, 2014.

[2] E. Din, C. Schaef, K. Moffat, and J. T. Stauth, "A scalable active battery management system with embedded real-time electrochemical impedance spectroscopy," *IEEE Transactions on Power Electronics*, vol. 32, no. 7, pp. 5688–5698, 2017.

[3] H. Ritchie and M. Rosery. (23th April 2020) Energy. [Online]. Available: https://ourworldindata.org/energy

[4] Enerdata. (23th April 2020) Electricity domestic consumption. [Online]. Available: https://yearbook.enerdata.net/electricity/electricity-domestic-consumption-data.html

[5] F. L. Robert L. Seale and et al. (29th April 2020) Energy conversion. [Online]. Available: https://www.britannica.com/technology/energy-conversion/Internal-combustion-engines

[6] T. C. Commission. (23th April 2020) Environmental and sustainability policy. [Online]. Available: https://www.gov.uk/government/publications/environmental-and-sustainability-policy

[7] X. Yang, Y. Song, G. Wang, and W. Wang, "A comprehensive review on the development of sustainable energy strategy and implementation in china," *IEEE Transactions on Sustainable Energy*, vol. 1, no. 2, pp. 57–65, 2010.

[8] Deloitte. (29th April 2020) Deloitte centre for energy solution. [Online]. Available: https://www2.deloitte.com/content/dam/Deloitte/us/Documents/energy-resources/us-er-electric-storage-paper.pdf

[9] T. Chen, Y. Jin, H. Lv, and et al, "Applications of lithium-ion batteries in grid-scale energy storage systems," *Transactions of Tianjin University*, vol. 26, p. 208–217, 2020.

[10] X. Hu, C. Zou, C. Zhang, and Y. Li, "Technological developments in batteries: A survey of principal roles, types, and management needs," *IEEE Power and Energy Magazine*, vol. 15, no. 5, pp. 20–31, 2017.

[11] Y. Li, K. Liu, A. M. Foley, A. Zulke, M. Berecibar, E. Nanini-Maury, J. V. Mierlo, and H. E. Hoster, "Data-driven health estimation and lifetime prediction of lithium-ion batteries: A review," *Renewable and Sustainable Energy Reviews*, vol. 113, p. 109254, 2019.

[12] A. Hoke, A. Brissette, K. Smith, A. Pratt, and D. Maksimovic, "Accounting for lithium-ion battery degradation in electric vehicle charging optimization," *IEEE Journal of Emerging and Selected Topics in Power Electronics*, vol. 2, no. 3, pp. 691–700, 2014.

[13] W. Huang and J. A. Abu Qahouq, "An online battery impedance measurement method using dc–dc power converter control," *IEEE Transactions on Industrial Electronics*, vol. 61, no. 11, pp. 5987–5995, 2014.

[14] P. Shi and Y. Zhao, "Application of unscented kalman filter in the soc estimation of li-ion battery for autonomous mobile robot," in *2006 IEEE International Conference on Information Acquisition*, 2006, pp. 1279–1283.

[15] C. Wu and R. Ferrero, "A flexible real-time measurement and control system for enhanced in-situ battery monitoring," in *2019 IEEE 10th International Workshop on Applied Measurements for Power Systems (AMPS)*, 2019, pp. 1–6.

[16] M. Debasish, L. Jianlin, N. Shrikant, W. David, and D. Claus, "Understanding the structure and structural degradation mechanisms in high-voltage, lithium-manganese–rich lithium-ion battery cathode oxides: A review of materials diagnostics," *MRS Energy amp; Sustainability*, vol. 2, p. E15, 2015.

[17] U.K. Government. (10th May 2020) UK becomes first major economy to pass net zero emissions law. [Online]. Available: https://www.gov.uk/government/news/uk-becomes-first-major-economy-to-pass-net-zero-emissions-law

[18] G. Qian, X. Liao, Y. Zhu, F. Pan, X. Chen, and Y. Yang*, "Designing flexible lithium-ion batteries by structural engineering," *ACS Energy Lett.*, vol. 3, pp. 690–701, 2019.

[19] P. Kurzweil and K. Brandt, *Chapter 3 - Overview of Rechargeable Lithium Battery Systems*, J. Garche and K. Brandt, Eds. Elsevier, 2019, ISBN: 978-0-444-63777-2.

[20] L. Gaines, "The future of automotive lithium-ion battery recycling: Charting a sustainable course," *Sustainable Materials and Technologies*, vol. 1-2, pp. 2 – 7, 2014.

[21] J. B. Dunn, L. Gaines, M. Barnes, J. L. Sullivan, and M. Wang, "Material and energy flows in the materials production, assembly, and end-of-life stages of the automotive lithium-ion battery life cycle," 6 2012.

[22] C. Daniel and J. Besenhard, *Thermodynamics and Mechanistics*. WILEY-VCH, 2011, ISBN: 9783527637188.

[23] S. Dou, "Review and prospect of layered lithium nickel manganese oxide as cathode materials for li-ion batteries," *J Solid State Electrochem*, vol. 17, pp. 911–926, 2013.

[24] R. R. Richardson and D. A. Howey, "Sensorless battery internal temperature estimation using a kalman filter with impedance measurement," *IEEE Transactions on Sustainable Energy*, vol. 6, no. 4, pp. 1190–1199, 2015.

[25] S. Gang, Z. Wei, H. Zhonghua, and L. Shanshan, "Estimation of battery soc based on improved ekf algorithm," in *2016 IEEE Information Technology, Networking, Electronic and Automation Control Conference*, 2016, pp. 151–154.

[26] L. Zhi, Z. Peng, W. Zhifu, S. Qiang, and R. Yinan, "State of charge estimation for li-ion battery based on extended kalman filter," *Energy Procedia*, vol. 105, pp. 3515 – 3520, 2017.

[27] C. Yi-Ping, C.-S. Moo, K. S. Ng, and Y.-C. Hsieh, "Enhanced coulormb counting method for estimating state of charge (soc) and state of health (soh) estimation of lithium-ion batteries," *Journal of Applied Energy*, vol. 86, no. 9, pp. 1506–1511, 2009.

[28] S. Jonsson, Lennart (Sverige, "Method of monitoring the internal impedance of an accumulator battery in an uninterruptible power supply, and an uninterruptible power supply," *United States Patent*, 1995.

[29] P. A. Lindahl, M. A. Cornachione, and S. R. Shaw, "A time-domain least squares approach to electrochemical impedance spectroscopy," *IEEE Transactions on Instrumentation and Measurement*, vol. 61, no. 12, pp. 3303–3311, 2012.

[30] M. Einhorn, F. V. Conte, C. Kral, and J. Fleig, "A method for online capacity estimation of lithium ion battery cells using the state of charge and the transferred charge," *IEEE Transactions on Industry Applications*, vol. 48, no. 2, pp. 736–741, 2012.

[31] X. Wei, X. Wang, and H. Dai, "Practical on-board measurement of lithium ion battery impedance based on distributed voltage and current sampling," *Energies*, vol. 11, no. 1, 2018.

[32] D. I. Stroe, M. Swierczynski, A. I. Stan, V. Knap, R. Teodorescu, and S. J. Andreasen, "Diagnosis of lithium-ion batteries state-of-health based on electrochemical impedance spectroscopy technique," in *2014 IEEE Energy Conversion Congress and Exposition (ECCE)*, 2014, pp. 4576–4582.

[33] C. Fleischer, W. Waag, H.-M. Heyn, and D. U. Sauer, "On-line adaptive battery impedance parameter and state estimation considering physical principles in reduced order equivalent circuit battery models: Part 1. requirements, critical review of methods and modeling," *Journal of Power Sources*, vol. 260, pp. 276 – 291, 2014.

[34] A. Barai, K. Uddin, W. Widanage, A. McGordon, and P. Jennings, "A study of the influence of measurement timescale on internal resistance characterisation methodologies for lithium-ion cells," *Sci Rep.*, vol. 8, pp. 1–13, 2018.

[35] J. Zhu, Z. Sun, X. Wei, and H. Dai, "Battery internal temperature estimation for lifepo4 battery based on impedance phase shift under operating conditions," *Energies*, vol. 11, no. 1, pp. 1–17, 2017.

[36] J. Sun, G. Wei, L. Pei, K. Song, C. Wu, and C. Zhu, "Online internal temperature estimation for lithium-ion batteries based on kalman filter," *Energies*, vol. 8, pp. 4400–4415, 2015.

[37] J. Zhu, Z. Sun, X. Wei, and H. Dai, "A new lithium-ion battery internal temperature on-line estimate method based on electrochemical impedance spectroscopy measurement," *Journal of Power Sources*, vol. 274, pp. 990 – 1004, 2015.

[38] F. Lijing, F. Zhang, and G. Liu, "A battery state-of-charge estimation method with extend kalman filter," *IEEE/ASME Conference on Advance Intelligent Mechatronics*, pp. 1008–1013, 2008.

[39] Z. Lu, X. Yu, L. Zhang, X. Meng, L. Wei, and L. Jin, "Experimental investigation on the charge-discharge performance of the commercial lithium-ion batteries," *Energy Procedia*, vol. 143, pp. 21 – 26, 2017.

[40] S. M. Rakiul Islam and S.-Y. Park, "Precise online electrochemical impedance spectroscopy strategies for li-ion batteries," *IEEE Transactions on Industry Applications*, vol. 56, no. 2, pp. 1661–1669, 2020.

[41] Y.-D. Lee, S.-Y. Park, and S.-B. Han, "Online embedded impedance measurement using high-power battery charger," *IEEE Transactions on Industry Applications*, vol. 51, no. 1, pp. 498–508, 2015.

[42] J.-G. Chen, Y.-D. Lee, and S.-Y. Park, "Adaptive pi gain control to realize sinusoidal ripple current charging," in *2015 9th International Conference on Power Electronics and ECCE Asia (ICPE-ECCE Asia)*, 2015, pp. 2582–2589.

[43] U. Westerhoff, K. Kurbach, F. Lienesch, and M. Kurrat, "Analysis of lithium-ion battery models based on electrochemical impedance spectroscopy," *Energy Technology*, vol. 4, no. 12, pp. 1620–1630, 2016.

[44] W. Waag, S. Käbitz, and D. U. Sauer, "Experimental investigation of the lithium-ion battery impedance characteristic at various conditions and aging states and its influence on the application," *Applied Energy*, vol. 102, pp. 885 – 897, 2013.

[45] C. Zhao, J. Sun, and Q. Wang, "Thermal runaway hazards investigation on 18650 lithium-ion battery using extended volume accelerating rate calorimeter," *Journal of Energy Storage*, vol. 28, p. 101232, 2020.

[46] BioLogic. (23th April 2020) Vsp. [Online]. Available: https://www.biologic.net/product_category/essential-potentiostats/

[47] G. instruments. (23th April 2020) Eis box. [Online]. Available: https://www.gamry.com/potentiostats/eis-boxl

[48] P. research. (23th April 2020) Wavedriver200 eis bipotentiostat/galvanostat. [Online]. Available: https://pineresearch.com/shop/potentiostats/wavedriver-series

[49] J. M. Tarascon and M. Armand, "Issues and challenges facing rechargeable lithium batteries," *Nature*, vol. 414, pp. 359–367, 2001.

[50] A. Patil, V. Patil, D. W. Shin, J.-W. Choi, D.-S. Paik, and S.-J. Yoon, "Issue and challenges facing rechargeable thin film lithium batteries," *Materials Research Bulletin*, vol. 43, no. 8, pp. 1913 – 1942, 2008.

[51] A. Väyrynen and J. Salminen, "Lithium ion battery production," *The Journal of Chemical Thermodynamics*, vol. 46, pp. 80 – 85, 2012.

[52] M. Hibino, *SECONDARY BATTERIES – LITHIUM RECHARGEABLE SYSTEMS — Positive Electrodes: Vanadium Oxides*, J. Garche, Ed. Amsterdam: Elsevier, 2009, ISBN: 978-0-444-52745-5.

[53] A. K. Padhi, "Phospho-olivines as positive-electrode materials for rechargeable lithium batteries," *Journal of The Electrochemical Society*, vol. 144, no. 4, pp. 1188–1194, 1997.

[54] Z. Abdin and K. R. Khalilpour, *Chapter 4 - Single and Polystorage Technologies for Renewable-Based Hybrid Energy Systems*, K. R. Khalilpour, Ed. Academic Press, 2019, ISBN: 978-0-12-813306-4.

[55] A. Ritchie and W. Howard, "Recent developments and likely advances in lithium-ion batteries," *Journal of Power Sources*, vol. 162, no. 2, pp. 809 – 812, 2006.

[56] V. Pop, H. J. Bergveld, P. H. L. Notten, and P. P. L. Regtien, "State-of-the-art of battery state-of-charge determination," *Measurement Science and Technology*, vol. 16, no. 12, pp. R93–R110, oct 2005.

[57] P. SANYO Energy (U.S.A.) Corp. (2012) Lithium ion ncr18650b datasheet. [Online]. Available: https://www.imrbatteries.com/content/panasonic_ncr18650b-2.pdf

[58] J. T. Warner, *Chapter 3 - Lithium-ion battery operation*, J. T. Warner, Ed. Elsevier, 2019, ISBN: 978-0-12-814778-8.

[59] D. Freudiger, M. D'Arpino, and M. Canova, "A generalized equivalent circuit model for design exploration of li-ion battery packs using data analytics," *IFAC-PapersOnLine*, vol. 52, no. 5, pp. 568 – 573, 2019.

[60] M. Kassem and C. Delacourt, "Postmortem analysis of calendar-aged graphite/lifepo4 cells," *Journal of Power Sources*, vol. 235, pp. 159 – 171, 2013.

[61] A. Jossen, "Fundamentals of battery dynamics," *Journal of Power Sources*, vol. 154, no. 2, pp. 530 – 538, 2006.

[62] K. S. Ng, C.-S. Moo, Y.-P. Chen, and Y.-C. Hsieh, "Enhanced coulomb counting method for estimating state-of-charge and state-of-health of lithium-ion batteries," *Applied Energy*, vol. 86, no. 9, pp. 1506 – 1511, 2009.

[63] W.-Y. Chang, "The state of charge estimating methods for battery: A review," *Hindawi*, vol. 2013, no. 953792, pp. 1–8, 2013.

[64] M. Coleman, C. K. Lee, C. Zhu, and W. G. Hurley, "State-of-charge determination from emf voltage estimation: Using impedance, terminal voltage, and current for lead-acid and lithium-ion batteries," *IEEE Transactions on Industrial Electronics*, vol. 54, no. 5, pp. 2550–2557, 2007.

[65] F. Sun, X. Hu, Y. Zou, and S. Li, "Adaptive unscented kalman filtering for state of charge estimation of a lithium-ion battery for electric vehicles," *Energy*, vol. 36, no. 5, pp. 3531 – 3540, 2011.

[66] S. Lee, J. Kim, J. Lee, and B. Cho, "State-of-charge and capacity estimation of lithium-ion battery using a new open-circuit voltage versus state-of-charge," *Journal of Power Sources*, vol. 185, no. 2, pp. 1367 – 1373, 2008.

[67] J. Chiasson and B. Vairamohan, "Estimating the state of charge of a battery," *IEEE Transactions on Control Systems Technology*, vol. 13, no. 3, pp. 465–470, 2005.

[68] Li Ran, Wu Junfeng, Wang Haiying, and Li Gechen, "Prediction of state of charge of lithium-ion rechargeable battery with electrochemical impedance spectroscopy theory," in *2010 5th IEEE Conference on Industrial Electronics and Applications*, 2010, pp. 684–688.

[69] H. Yuan and L. Dung, "Offline state-of-health estimation for high-power lithium-ion batteries using three-point impedance extraction method," *IEEE Transactions on Vehicular Technology*, vol. 66, no. 3, pp. 2019–2032, 2017.

[70] S. Rodrigues, N. Munichandraiah, and A. Shukla, "A review of state-of-charge indication of batteries by means of a.c. impedance measurements," *Journal of Power Sources*, vol. 87, no. 1, pp. 12 – 20, 2000.

[71] S. Sato and A. Kawamura, "A new estimation method of state of charge using terminal voltage and internal resistance for lead acid battery," in *Proceedings of the Power Conversion Conference-Osaka 2002 (Cat. No.02TH8579)*, vol. 2, 2002, pp. 565–570.

[72] D. Jiani, L. Zhitao, W. Youyi, and W. Changyun, "A fuzzy logic-based model for li-ion battery with soc and temperature effect," in *11th IEEE International Conference on Control Automation (ICCA)*, 2014, pp. 1333–1338.

[73] F. Huet, "A review of impedance measurements for determination of the state-of-charge or state-of-health of secondary batteries," *Journal of Power Sources*, vol. 70, no. 1, pp. 59 – 69, 1998.

[74] J. Xu, C. C. Mi, B. Cao, J. Deng, Z. Chen, and S. Li, "The state of charge estimation of lithium-ion batteries based on a proportional-integral observer," *IEEE Transactions on Vehicular Technology*, vol. 63, no. 4, pp. 1614–1621, 2014.

[75] A. A. Hussein, N. Kutkut, and I. Batarseh, "A hysteresis model for a lithium battery cell with improved transient response," pp. 1790–1794, 2011.

[76] Y. Li, H. Sheng, Y. Cheng, D.-I. Stroe, and R. Teodorescu, "State-of-health estimation of lithium-ion batteries based on semi-supervised transfer component analysis," *Applied Energy*, vol. 277, p. 115504, 2020.

[77] T. Ashwin, A. McGordon, and P. Jennings, "Electrochemical modelling of li-ion battery pack with constant voltage cycling," *Journal of Power Sources*, vol. 341, pp. 327 – 339, 2017.

[78] R. Xiong, J. Tian, H. Mu, and C. Wang, "A systematic model-based degradation behavior recognition and health monitoring method for lithium-ion batteries," *Applied Energy*, vol. 207, pp. 372 – 383, 2017.

[79] G. Bai, P. Wang, C. Hu, and M. Pecht, "A generic model-free approach for lithium-ion battery health management," *Applied Energy*, vol. 135, pp. 247 – 260, 2014.

[80] A. Nuhic, T. Terzimehic, T. Soczka-Guth, M. Buchholz, and K. Dietmayer, "Health diagnosis and remaining useful life prognostics of lithium-ion batteries using data-driven methods," *Journal of Power Sources*, vol. 239, pp. 680 – 688, 2013.

[81] Y. Li, M. Abdel-Monem, R. Gopalakrishnan, M. Berecibar, E. Nanini-Maury, N. Omar, P. van den Bossche, and J. V. Mierlo, "A quick on-line state of health estimation method for li-ion battery with incremental capacity curves processed by gaussian filter," *Journal of Power Sources*, vol. 373, pp. 40 – 53, 2018.

[82] Z. He, M. Gao, G. Ma, Y. Liu, and S. Chen, "Online state-of-health estimation of lithium-ion batteries using dynamic bayesian networks," *Journal of Power Sources*, vol. 267, pp. 576 – 583, 2014.

[83] E. Samadani, S. Farhad, W. Scott, M. Mastali, L. E. Gimenez, M. Fowler, and R. A. Fraser, "Empirical modeling of lithium-ion batteries based on electrochemical impedance spectroscopy tests," *Electrochimica Acta*, vol. 160, pp. 169 – 177, 2015.

[84] L. Gagneur, A. Driemeyer-Franco, C. Forgez, and G. Friedrich, "Modeling of the diffusion phenomenon in a lithium-ion cell using frequency or time domain identification," *Microelectronics Reliability*, vol. 53, no. 6, pp. 784 – 796, 2013.

[85] A. Nyman, "An experimental and theoretical study of the mass transport in lithium-ion battery electrolytes," *Kungliga Tekniska Högskolan (KTH) Chemical Science and Engineering*, vol. PhD Thesis, 2011. [Online]. Available: https://www.diva-portal.org/smash/get/diva2:392067/FULLTEXT01.pdf

[86] P. Personnettaz, S. Landgraf, M. Nimtz, N. Weber, and T. Weier, "Mass transport induced asymmetry in charge/discharge behavior of liquid metal batteries," *Electrochemistry Communications*, vol. 105, p. 106496, 2019.

[87] Q. Zhang, D. Wang, B. Yang, X. Cui, and X. Li, "Electrochemical model of lithium-ion battery for wide frequency range applications," *Electrochimica Acta*, vol. 343, p. 136094, 2020.

[88] P. Verma, P. Maire, and P. Novák, "A review of the features and analyses of the solid electrolyte interphase in li-ion batteries," *Electrochimica Acta*, vol. 55, no. 22, pp. 6332 – 6341, 2010.

[89] P. Kurzweil, *Chapter 19 - Electrochemical Double-layer Capacitors*, P. T. Moseley and J. Garche, Eds. Amsterdam: Elsevier, 2015, ISBN: 978-0-444-62616-5.

[90] N. Kularatna, *3 - Dynamics, models, and management of rechargeable batteries*, N. Kularatna, Ed. Boston: Academic Press, 2015, ISBN: 978-0-12-407947-2.

[91] A. Moya, "Identification of characteristic time constants in the initial dynamic response of electric double layer capacitors from high-frequency electrochemical impedance," *Journal of Power Sources*, vol. 397, pp. 124 – 133, 2018.

[92] N. A. Cañas, K. Hirose, B. Pascucci, N. Wagner, K. A. Friedrich, and R. Hiesgen, "Investigations of lithium–sulfur batteries using electrochemical impedance spectroscopy," *Electrochimica Acta*, vol. 97, pp. 42 – 51, 2013.

[93] Lijun Gao, Shengyi Liu, and R. A. Dougal, "Dynamic lithium-ion battery model for system simulation," *IEEE Transactions on Components and Packaging Technologies*, vol. 25, no. 3, pp. 495–505, 2002.

[94] S. Buller, M. Thele, E. Karden, and R. W. D. Doncker, "Impedance-based non-linear dynamic battery modeling for automotive applications," *Journal of Power Sources*, vol. 113, no. 2, pp. 422 – 430, 2003.

[95] M. J. Brand, M. H. Hofmann, S. S. Schuster, P. Keil, and A. Jossen, "The influence of current ripples on the lifetime of lithium-ion batteries," *IEEE Transactions on Vehicular Technology*, vol. 67, no. 11, pp. 10 438–10 445, 2018.

[96] R. Subramanian, P. Venhovens, and B. P. Keane, "Accelerated design and optimization of battery management systems using hil simulation and rapid control prototyping," in *2012 IEEE International Electric Vehicle Conference*, 2012, pp. 1–5.

[97] R. Gu, Z. Ma, T. Cheng, Y. Lyu, A. Nie, and B. Guo, "Improved electrochemical performances of licoo2 at elevated voltage and temperature with an in situ formed spinel coating layer," *ACS Applied Materials & Interfaces*, vol. 10, no. 37, pp. 31 271–31 279, 2018.

[98] Y. Xie, J. Li, and C. Yuan, "Mathematical modeling of the electrochemical impedance spectroscopy in lithium ion battery cycling," *Electrochimica Acta*, vol. 127, pp. 266 – 275, 2014.

[99] J. Kim, S. Lee, and B. H. Cho, "Complementary cooperation algorithm based on dekf combined with pattern recognition for soc/capacity estimation and soh prediction," *IEEE Transactions on Power Electronics*, vol. 27, no. 1, pp. 436–451, 2012.

[100] R. W. J. M. Huang, F. Chung, and E. M. Kelder, "Impedance simulation of a li-ion battery with porous electrodes and spherical li intercalation particles," *Journal of The Electrochemical Society*, vol. 153, no. 8, p. A1459, 2006.

[101] D. Li, L. Yang, and C. Li, "Control-oriented thermal-electrochemical modeling and validation of large size prismatic lithium battery for commercial applications," *Energy*, vol. 214, p. 119057, 2021.

[102] J. Vetter, P. Novak, M. Wagner, C. Veit, K. Moller, J. Besenhard, M. Winter, M. W. Mehrens, C. Vogler, and A. Hammouche, "Ageing mechanisms in lithium-ion batteries," *Journal of Power Sources*, vol. 147, no. 1, pp. 269 – 281, 2005.

[103] X. Zhou, Z. Pan, X. Han, L. Lu, and M. Ouyang, "An easy-to-implement multi-point impedance technique for monitoring aging of lithium ion batteries," *Journal of Power Sources*, vol. 417, pp. 188 – 192, 2019.

[104] H. Dai, B. Jiang, and X. Wei, "Impedance characterization and modeling of lithium-ion batteries considering the internal temperature gradient," *Energies*, vol. 11, no. 1, 2018. [Online]. Available: https://www.mdpi.com/1996-1073/11/1/220

[105] F. Saidani, F. X. Hutter, R.-G. Scurtu, W. Braunwarth, and J. N. Burghartz, "Lithium-ion battery models: a comparative study and a model-based powerline communication," *Advances in Radio Science*, vol. 15, pp. 83 – 91, 2017.

[106] A. S. Andersson, B. Kalska, L. Häggström, and J. O. Thomas, "Lithium extraction/insertion in lifepo4: an x-ray diffraction and mössbauer spectroscopy study," *Solid State Ionics*, vol. 130, no. 1, pp. 41 – 52, 2000.

[107] J. A. A. Qahouq and Z. Xia, "Single-perturbation-cycle online battery impedance spectrum measurement method with closed-loop control of power converter," *IEEE Transactions on Industrial Electronics*, vol. 64, no. 9, pp. 7019–7029, 2017.

[108] G. Dotelli, R. Ferrero, P. G. Stampino, S. Latorrata, and S. Toscani, "Pem fuel cell drying and flooding diagnosis with signals injected by a power converter," *IEEE Transactions on Instrumentation and Measurement*, vol. 64, no. 8, pp. 2064–2071, 2015.

[109] Q. Yang, J. Xu, X. Li, D. Xu, and B. Cao, "State-of-health estimation of lithium-ion battery based on fractional impedance model and interval capacity," *International Journal of Electrical Power & Energy Systems*, vol. 119, p. 105883, 2020.

[110] W. Li, Q.-A. Huang, C. Yang, J. Chen, Z. Tang, F. Zhang, A. Li, L. Zhang, and J. Zhang, "A fast measurement of warburg-like impedance spectra with morlet wavelet transform for electrochemical energy devices," *Electrochimica Acta*, vol. 322, p. 134760, 2019.

[111] M. Itagaki, M. Ueno, Y. Hoshi, and I. Shitanda, "Simultaneous determination of electrochemical impedance of lithium-ion rechargeable batteries with measurement of charge-discharge curves by wavelet transformation," *Electrochimica Acta*, vol. 235, pp. 384–389, 2017.

[112] D. Klotz, M. Schönleber, J. Schmidt, and E. Ivers-Tiffée, "New approach for the calculation of impedance spectra out of time domain data," *Electrochimica Acta*, vol. 56, no. 24, pp. 8763–8769, 2011.

[113] R. Ferrero, C. Wu, A. Carboni, S. Toscani, M. De Angelis, H. George-Williams, E. Patelli, and P. A. Pegoraro, "Low-cost battery monitoring by converter-based electrochemical impedance spectroscopy," in *2017 IEEE International Workshop on Applied Measurements for Power Systems (AMPS)*, 2017, pp. 1–6.

[114] R. Koch, R. Kuhn, I. Zilberman, and A. Jossen, "Electrochemical impedance spectroscopy for online battery monitoring - power electronics control," in *2014 16th European Conference on Power Electronics and Applications*, 2014, pp. 1–10.

[115] R. Koch, C. Riebel, and A. Jossen, "On-line electrochemical impedance spectroscopy implementation for telecommunication power supplies," in *2015 IEEE International Telecommunications Energy Conference (INTELEC)*, 2015, pp. 1–6.

[116] A. Waligo and P. Barendse, "A comparison of the different broadband impedance measurement techniques for lithium-ion batteries," in *2016 IEEE Energy Conversion Congress and Exposition (ECCE)*, 2016, pp. 1–7.

[117] L. A. Middlemiss, A. J. Rennie, R. Sayers, and A. R. West, "Characterisation of batteries by electrochemical impedance spectroscopy," *Energy Reports*, vol. 6, pp. 232 – 241, 2020.

[118] L.-R. Chen, S.-L. Wu, D.-T. Shieh, and T.-R. Chen, "Sinusoidal-ripple-current charging strategy and optimal charging frequency study for li-ion batteries," *IEEE Transactions on Industrial Electronics*, vol. 60, no. 1, pp. 88–97, 2013.

[119] R. Hasan and J. Scott, "Impedance measurement of batteries under load," in *2019 IEEE International Instrumentation and Measurement Technology Conference (I2MTC)*, 2019, pp. 1–5.

[120] D. A. Howey, P. D. Mitcheson, V. Yufit, G. J. Offer, and N. P. Brandon, "Online measurement of battery impedance using motor controller excitation," *IEEE Transactions on Vehicular Technology*, vol. 63, no. 6, pp. 2557–2566, 2014.

[121] R. P. Aguilera, P. Acuna, G. Konstantinou, S. Vazquez, and J. I. Leon, "Chapter 2 - basic control principles in power electronics: Analog and digital control design," in *Control of Power Electronic Converters and Systems*, F. Blaabjerg, Ed. Academic Press, 2018, pp. 31 – 68, ISBN: 978-0-12-805245-7.

[122] Z. Xia and J. A. Abu Qahouq, "High frequency online battery impedance measurement method using voltage and current ripples generated by dc-dc converter," in *2020 IEEE Applied Power Electronics Conference and Exposition (APEC)*, 2020, pp. 1333–1338.

[123] R. S. Gemmen, "Analysis for the Effect of Inverter Ripple Current on Fuel Cell Operating Condition ," *Journal of Fluids Engineering*, vol. 125, no. 3, pp. 576–585, 06 2003.

[124] B. Wahdame, L. Girardot, D. Hissel, F. Harel, X. Francois, D. Candusso, M. C. Pera, and L. Dumercy, "Impact of power converter current ripple on the durability of a fuel cell stack," in *2008 IEEE International Symposium on Industrial Electronics*, 2008, pp. 1495–1500.

[125] A. Sandschulte, R. Ferrero, L. Hardwick, and E. Patelli, "Approach to wide-frequency battery impedance measurements in commercial applications," in *2019 IEEE 10th International Workshop on Applied Measurements for Power Systems (AMPS)*, 2019, pp. 1–6.

[126] L. Guo, J. Y. Hung, and R. M. Nelms, "Evaluation of dsp-based pid and fuzzy controllers for dc–dc converters," *IEEE Transactions on Industrial Electronics*, vol. 56, no. 6, pp. 2237–2248, 2009.

[127] O. Diene and A. Bhaya, "Design of discrete-time adaptive pid controllers for a class of linear integrator systems," *IFAC Proceedings Volumes*, vol. 44, no. 1, pp. 11 344 – 11 349, 2011.

[128] L. C. Stevanatto, V. J. Brusamarello, and S. Tairov, "Parameter identification and analysis of uncertainties in measurements of lead–acid batteries," *IEEE Transactions on Instrumentation and Measurement*, vol. 63, no. 4, pp. 761–768, 2014.

[129] TEXAS INSTRUMENTS Technical Documents. (23th July 2020) Am335x sitara processors. [Online]. Available: https://www.ti.com/lit/ds/sprs717l/sprs717l.pdf

[130] TEXAS INSTRUMENTS. (23th April 2020) Flexible interface (pru-icss) reference design for simultaneous, coherent daq using multiple adcs. [Online]. Available: https://www.ti.com/lit/ug/tidudn4a/tidudn4a.pdf

[131] A. Alanwar, F. M. Anwar, Y.-F. Zhang, J. Pearson, J. Hespanha, and M. B. Srivastava, "Cyclops: Pru programming framework for precise timing applications," in *2017 IEEE International Symposium on Precision Clock Synchronization for Measurement, Control, and Communication (ISPCS)*, 2017, pp. 1–6.

[132] S. M. Kuo, B. H. Lee, and W. Tian, *Real-Time Digital Signal Processing, Implementations and Applications*, 2007, 2nd ed.

[133] X. Zhao, D. M. Laverty, A. McKernan, D. J. Morrow, K. McLaughlin, and S. Sezer, "Gps-disciplined analog-to-digital converter for phasor measurement applications," *IEEE Transactions on Instrumentation and Measurement*, vol. 66, no. 9, pp. 2349–2357, 2017.

[134] D. Molloy, "Chapter 15 - real-time interfacing with the pru-icss," in *Exploring BeagleBone Black Tools and Techniques for Building with Embedded Linux*. WILEY, 2019, ISBN: 9781118935125.

[135] M. Kuipers, P. Schroer, T. Nemeth, H. Zappen, A. Blömeke, and D. U. Sauer, "An algorithm for an online electrochemical impedance spectroscopy and battery parameter estimation: Development, verification and validation," *Journal of Energy Storage*, vol. 30, 2020.

[136] R. Beck, A. G. Dempster, and I. Kale, "Finite-precision goertzel filters used for signal tone detection," *IEEE Transactions on Circuits and Systems II: Analog and Digital Signal Processing*, vol. 48, no. 7, pp. 691–700, 2001.

[137] Z. Gao, P. Reviriego, X. Li, J. Maestro, M. Zhao, and J. Wang, "A fault tolerant implementation of the goertzel algorithm," *Microelectronics Reliability*, vol. 54, no. 1, pp. 335 – 337, 2014.

[138] K. Uddin, A. D. Moore, A. Barai, and J. Marco, "The effects of high frequency current ripple on electric vehicle battery performance," *Applied Energy*, vol. 178, pp. 142 – 154, 2016.

[139] S. Piller, M. Perrin, and A. Jossen, "Methods for state-of-charge determination and their applications," *Journal of Power Sources*, vol. 96, no. 1, pp. 113 – 120, 2001.

[140] S. Li, C. Zou, M. Küpper, and S. Pischinger, "Model-based state of charge estimation algorithms under various current patterns," *Energy Procedia*, vol. 158, pp. 2806 – 2811, 2019.

[141] G. L. Plett, "Extended kalman filtering for battery management systems of lipb-based hev battery packs: Part 1. background," *Journal of Power Sources*, vol. 134, no. 2, pp. 252 – 261, 2004.

[142] W. Choi, J. Howze, and P. Enjeti, "Development of an equivalent circuit model of a fuel cell to evaluate the effects of inverter ripple current," *Journal of Power Sources*, vol. 158, no. 2, pp. 1324 – 1332, 2006.

[143] R. Ferrero, M. Marracci, and B. Tellini, "Single pem fuel cell analysis for the evaluation of current ripple effects," *IEEE Transactions on Instrumentation and Measurement*, vol. 62, no. 5, pp. 1058–1064, 2013.

[144] G. Dotelli, R. Ferrero, P. G. Stampino, S. Latorrata, and S. Toscani, "Low-cost pem fuel cell diagnosis based on power converter ripple with hysteresis control," *IEEE Transactions on Instrumentation and Measurement*, vol. 64, no. 11, pp. 2900–2907, 2015.

[145] A.J.Forsyth and S. Mollov, "Modelling and control of dc-dc converters," *POWER ENGINEERING JOURNAL*, pp. 229–236, 1998.

[146] S. Barrett and D. Pack, *Hardware Organization and Software Programming*, M. A. Thornton, Ed. Morgan and Claypool, 2019, ISBN: 9781681736266.

[147] A. Ray and K. Bhurchandi, *Basic Peripherals and their Interfacing with 8086/88*. The Taia Mcgraw-Hill Co., 2006, ISBN: 1-25-900613-1.

[148] Measurement Computing, "Analog to digital conversion," vol. 508, no. 946-5100, pp. 1–7, 2016.

[149] K. Banks. (20th May 2020) The goertzel algorithm. [Online]. Available: https://www.embedded.com/the-goertzel-algorithm

[150] F. Tenergy Corp. (16th June 2020) Ca tenergy cylindric lithium-ion cell 30005-0 datasheet. [Online]. Available: https://www.shorepowerinc.com/media/wysiwyg/files/Tenergy-30005-0-datasheet.pdf

[151] AA Portable Power Corp. (20th April 2020) Production specification of lithium ion polymer battery. [Online]. Available: http://www.batteryspace.com/Prod-specs/A055275-21Ah.pdf

[152] Batteryspace. (28th April 2020) Polymer lithium-ion battery product specification. [Online]. Available: http://www.batteryspace.com/prod-specs/4108.pdf

[153] LG Chem. (26th April 2020) Rechargeable lithium ion battery product specification, icr18650 s3 2200mah. [Online]. Available: http://www.batteryspace.com/prod-specs/4869.pdf

[154] P. Osswald, S. Erhard, A. Noel, P. Keil, F. Kindermann, H. Hoster, and A. Jossen, "Current density distribution in cylindrical li-ion cells during impedance measurements," *Journal of Batteries and Supercaps*, vol. 2, pp. 37–48, 2019.

[155] J. Zhu, Z. Sun, X. Wei, and H. Dai, "A new lithium-ion battery internal temperature on-line estimate method based on electrochemical impedance spectroscopy measurement," *Journal of Power Sources*, vol. 274, pp. 990 – 1004, 2015.

[156] P. Osswald, S. Erhard, A. Noel, P. Keil, F. Kindermann, H. Hoster, and A. Jossen, "Understanding the reaction interface in lithium-oxygen batteries," *Journal of Power Sources*, vol. 314, pp. 93 – 101, 2016.

[157] X. Zhou, J. Huang, Z. Pan, and M. Ouyang, "Impedance characterization of lithium-ion batteries aging under high-temperature cycling: Importance of electrolyte-phase diffusion," *Journal of Power Sources*, vol. 426, pp. 216 – 222, 2019.

[158] E. P. Randviir and C. E. Banks, "Electrochemical impedance spectroscopy: an overview of bioanalytical applications," *Anal. Methods*, vol. 5, pp. 1098–1115, 2013. [Online]. Available: http://dx.doi.org/10.1039/C3AY26476A

[159] S. Cho, I. Lee, J. Baek, and G. Moon, "Battery impedance analysis considering dc component in sinusoidal ripple-current charging," *IEEE Transactions on Industrial Electronics*, vol. 63, no. 3, pp. 1561–1573, 2016.

[160] T. M. Le, B. Fatahi, H. Khabbaz, and W. Sun, "Numerical optimization applying trust-region reflective least squares algorithm with constraints to optimize the non-linear creep parameters of soft soil," *Applied Mathematical Modelling*, vol. 41, pp. 236 – 256, 2017.

[161] Y. Wang, A. Yagola, and C. Yang. Springer-Verlag Berlin Heidelberg, 2011, ISBN: 978-3-642-13742-6.

[162] F. V. Berghen, "Levenberg-marquardt algorithms vs trust region algorithms," in *PhD Thesis*. Universit e Libre de Bruxelles, 2004.

[163] A. Guha and A. Patra, "Online estimation of the electrochemical impedance spectrum and remaining useful life of lithium-ion batteries," *IEEE Transactions on Instrumentation and Measurement*, vol. 67, no. 8, pp. 1836–1849, 2018.

[164] X. Wang, X. Wei, Q. Chen, J. Zhu, and H. Dai, "Lithium-ion battery temperature on-line estimation based on fast impedance calculation," *Journal of Energy Storage*, vol. 26, p. 100952, 2019.

[165] A. Christensen and A. Adebusuyi, "Using on-board electrochemical impedance spectroscopy in battery management systems," in *2013 World Electric Vehicle Symposium and Exhibition (EVS27)*, 2013, pp. 1–7.

[166] R. Srinivasan, B. G. Carkhuff, M. H. Butler, and A. C. Baisden, "Instantaneous measurement of the internal temperature in lithium-ion rechargeable cells," *Electrochimic Acta*, vol. 56, no. 17, pp. 6198 – 6204, 2011.

[167] S. Wang, M. Verbrugge, J. S. Wang, and P. Liu, "Power prediction from a battery state estimator that incorporates diffusion resistance," *Journal of Power Sources*, vol. 214, pp. 399 – 406, 2012.

[168] G. L. Plett, "High-performance battery-pack power estimation using a dynamic cell model," *IEEE Transactions on Vehicular Technology*, vol. 53, no. 5, pp. 1586–1593, 2004.

[169] U. Krewer, F. Roder, E. Harinath, R. D. Braatz, B. Bedurftig, and R. Findeisen, "Review—dynamic models of li-ion batteries for diagnosis and operation: A review and perspective," *Journal of The Electrochemical Society*, vol. 165, pp. 3656–3673, 2018.

[170] S. Erol, "Electrochemical impedance spectroscopy analysis and modeling of lithium cobalt oxide/carbon batteries," *UNIVERSITY OF FLORIDA*, vol. PhD Thesis, 2015.

[171] H. Zhang, *Impact of Current Ripple on Electric Vehicle Charging Equipment*. Atlantis Press, 2016/01, ISBN: 978-94-6252-185-8. [Online]. Available: https://doi.org/10.2991/iccte-16.2016.161